



**NAVAL
POSTGRADUATE
SCHOOL**

MONTEREY, CALIFORNIA

THESIS

**CORROSION AND THERMAL PROCESSING IN COLD
GAS DYNAMIC SPRAY DEPOSITED AUSTENITIC
STAINLESS STEEL COATINGS**

by

John A Luhn

June 2016

Thesis Advisor:
Co-Advisor:

Sarath K. Menon
Luke N. Brewer

Approved for public release; distribution is unlimited

THIS PAGE INTENTIONALLY LEFT BLANK

REPORT DOCUMENTATION PAGE			Form Approved OMB No. 0704-0188
<p>Public reporting burden for this collection of information is estimated to average 1 hour per response, including the time for reviewing instruction, searching existing data sources, gathering and maintaining the data needed, and completing and reviewing the collection of information. Send comments regarding this burden estimate or any other aspect of this collection of information, including suggestions for reducing this burden, to Washington headquarters Services, Directorate for Information Operations and Reports, 1215 Jefferson Davis Highway, Suite 1204, Arlington, VA22202-4302, and to the Office of Management and Budget, Paperwork Reduction Project (0704-0188) WashingtonDC20503.</p>			
1. AGENCY USE ONLY <i>(Leave blank)</i>	2. REPORT DATE June 2016	3. REPORT TYPE AND DATES COVERED Master's thesis	
4. TITLE AND SUBTITLE CORROSION AND THERMAL PROCESSING IN COLD GAS DYNAMIC SPRAY DEPOSITED AUSTENITIC STAINLESS STEEL COATINGS		5. FUNDING NUMBERS	
6. AUTHOR(S) John A. Luhn			
7. PERFORMING ORGANIZATION NAME(S) AND ADDRESS(ES) Naval Postgraduate School Monterey, CA 93943-5000		8. PERFORMING ORGANIZATION REPORT NUMBER	
9. SPONSORING /MONITORING AGENCY NAME(S) AND ADDRESS(ES) Office of the Secretary of Defense Corrosion Policy and Oversight		10. SPONSORING/MONITORING AGENCY REPORT NUMBER	
11. SUPPLEMENTARY NOTES. The views expressed in this thesis are those of the author and do not reflect the official policy or position of the Department of Defense or the U.S. Government. IRB Protocol number <u>N/A</u> .			
12a. DISTRIBUTION / AVAILABILITY STATEMENT Approved for public release; distribution is unlimited		12b. DISTRIBUTION CODE	
13. ABSTRACT (maximum 200words)			
<p>This thesis presents research on the corrosion properties and effects of heat treatment on austenitic stainless steel coatings produced by the cold gas dynamic spray process on 316L stainless steel substrates. Previous work on the use of the low-pressure cold spray process to spray austenitic stainless steel was reproduced and validated. Heat treatment of the coatings was found to reduce porosity and evidence was found of recrystallization of the coatings. No significant changes in elemental distribution were found to occur during heat treatment. Corrosion testing was conducted by salt fog testing and anodic polarization. Coatings in the as-sprayed condition were found to be less corrosion resistant than bulk 316L stainless steel. Heat treated samples were observed to show corrosion resistance even worse than as-sprayed coatings. In fact, all heat treated samples exhibited little or no passivation behavior. Grain boundary sensitization is suspected to a probable cause for poor corrosion resistance in some samples and the presence of ferrite in the powder and coatings may also be a cause of corrosion resistance that is worse than the fully austenitic substrate.</p>			
14. SUBJECT TERMS cold spray, stainless steel, salt fog testing, potentiostatic testing			15. NUMBER OF PAGES 179
			16. PRICE CODE
17. SECURITY CLASSIFICATION OF REPORT Unclassified	18. SECURITY CLASSIFICATION OF THIS PAGE Unclassified	19. SECURITY CLASSIFICATION OF ABSTRACT Unclassified	20. LIMITATION OF ABSTRACT UU

THIS PAGE INTENTIONALLY LEFT BLANK

Approved for public release; distribution is unlimited

**CORROSION AND THERMAL PROCESSING IN COLD GAS DYNAMIC
SPRAY DEPOSITED AUSTENITIC STAINLESS STEEL COATINGS**

John A. Luhn
Lieutenant, United States Navy
B.S., University of California, Davis, 2008

Submitted in partial fulfillment of the
requirements for the degree of

MECHANICAL ENGINEER

from the

NAVAL POSTGRADUATE SCHOOL
June 2016

Approved by: Sarah K. Menon
Thesis Advisor

Luke N. Brewer
Co-Advisor

Garth V. Hobson
Chair, Department of Mechanical and Aerospace Engineering

THIS PAGE INTENTIONALLY LEFT BLANK

ABSTRACT

This thesis presents research on the corrosion properties and effects of heat treatment on austenitic stainless steel coatings produced by the cold gas dynamic spray process on 316L stainless steel substrates. Previous work on the use of the low-pressure cold spray process to spray austenitic stainless steel was reproduced and validated. Heat treatment of the coatings was found to reduce porosity and evidence was found of recrystallization of the coatings. No significant changes in elemental distribution were found to occur during heat treatment. Corrosion testing was conducted by salt fog testing and anodic polarization. Coatings in the as-sprayed condition were found to be less corrosion resistant than bulk 316L stainless steel. Heat treated samples were observed to show corrosion resistance even worse than as-sprayed coatings. In fact, all heat treated samples exhibited little or no passivation behavior. Grain boundary sensitization is suspected as the probable cause for poor corrosion resistance in some samples, and the presence of ferrite in the powder and coatings may also be a cause of corrosion resistance that is worse than the fully austenitic substrate.

THIS PAGE INTENTIONALLY LEFT BLANK

TABLE OF CONTENTS

I.	INTRODUCTION.....	1
A.	MOTIVATION	1
B.	THE COLD SPRAY MATERIAL DEPOSITION PROCESS.....	4
C.	CORROSION.....	6
D.	OBJECTIVES	8
II.	COLD SPRAY OF AUSTENITIC STAINLESS STEEL	9
A.	INTRODUCTION.....	9
B.	REPRODUCTION OF PREVIOUS WORK	12
C.	SAMPLE PREPARATION FOR CURRENT WORK	22
III.	EFFECT OF HEAT TREATMENT ON SPRAYED COATINGS.....	25
A.	INTRODUCTION.....	25
B.	EXPERIMENTAL METHODS	27
C.	RESULTS AND DISCUSSION	28
IV.	CORROSION TESTING OF COLD SPRAYED AUSTENITIC STAINLESS STEEL POWDERS	63
A.	INTRODUCTION.....	63
B.	EXPERIMENTAL METHODS	68
1.	Salt Fog Testing.....	69
2.	Polarization Testing.....	72
C.	SALT FOG RESULTS AND EVALUATION	72
D.	POLARIZATION TESTING RESULTS	91
E.	DISCUSSION	97
V.	CONCLUSION	105
APPENDIX A.	CHARACTERIZATION.....	107
A.	COATING MICROGRAPHS.....	107
B.	EDS MAPS	119
APPENDIX B.	FOG CHAMBER RESULTS	131
A.	SAMPLE PHOTOGRAPHS.....	131
B.	SURFACE PROFILES.....	139
LIST OF REFERENCES.....	151	
INITIAL DISTRIBUTION LIST	157	

THIS PAGE INTENTIONALLY LEFT BLANK

LIST OF FIGURES

Figure 1.	Comparison of general temperature and particle velocity range for coating spray techniques. Source: [3].	2
Figure 2.	Schematic of the cold spray deposition process. Source: [8].	5
Figure 3.	Schematic mechanism of pitting corrosion. Source: [29].	7
Figure 4.	Low magnification optical micrographs of coatings sprayed with helium gas at 1.7 MPa and 230°C; 40 mm standoff distance. (a) 5001; (b) 5002; (c) PG-AMP-10.	15
Figure 5.	High magnification optical micrographs of coating sprayed with helium gas at 1.7 MPa and 230°C; 40 mm standoff distance. (a) 5001; (b) 5002; (c) PG-AMP-10.	16
Figure 6.	Typical micrographs of PG-AMP-10 powder sprayed with N ₂ gas at 1.7 MPa and 450°C showing improved coating quality (decreased porosity) at 40 mm standoff distance. 16 mm standoff (top); 40 mm distance (bottom).	17
Figure 7.	Coating detachment phenomena observed during spaying of 3 rd pass with 5001 powder. He gas, 1.7 MPa at 230°C.	19
Figure 8.	Coating detachment phenomena observed in 5002 powder sprayed with helium gas at 1.7 MPa, 230°C. Increasing magnification (a) to (c).	21
Figure 9.	High magnification optical micrographs of as-sprayed coatings showing qualitatively dense coating structure with limited porosity. (a) 5001 powder; (b) 5002 powder; (c) PG-AMP-10 powder.	29
Figure 10.	High magnification optical micrographs showing changes in porosity with heat treatment. 5001 powder. (a) as sprayed; (b) 950°C/1hr; (c) 800°C/2hrs; (d) 600°C/8 hrs.	31
Figure 11.	Backscatter electron images of 5001 powder samples showing porosity reduction following heat treatment. (a) as sprayed; (b) 950°C/1hr; (c) 800°C/2hrs; (d) 600°C/8 hrs.	32
Figure 12.	Backscatter electron images of 5002 powder samples showing porosity reduction following heat treatment. (a) as sprayed; (b) 950°C/1hr; (c) 800°C/2hrs; (d) 600°C/8 hrs.	33
Figure 13.	Backscatter electron images of PG-AMP-10 powder samples showing porosity reduction following heat treatment. (a) as sprayed; (b) 950°C/1hr; (c) 800°C/2hrs; (d) 600°C/8 hrs.	34
Figure 14.	Typical point EDS measurement of possible precipitate.	35

Figure 15.	High resolution secondary election images of micro-porosity in 950°C/1 hr samples. 5002 powder, in lens detector (left); PG-AMP-10 powder, secondary electron detector (right).	36
Figure 16.	Typical EDS elemental distribution map. 5001 powder, 600°C/8hrs heat treatment.....	38
Figure 17.	EDS map of as sprayed PG-AMP-10 powder showing chromium rich areas likely associated with ferrite phase grains.....	40
Figure 18.	EDS maps showing evidence of elemental redistribution in 5002 powder, 950°C/1 hrs (left) and 800°C/2hrs (right). Note different scale.....	41
Figure 19.	EDS maps showing evidence of elemental redistribution in PG-AMP-10 powder, 950°C/1 hrs (left) and 800°C/2hrs (right).	42
Figure 20.	EDS maps of 5002 powder, 950°C/1 hr heat treatment at 500X (left) and 1.5KX (right) showing inconsistency in observed elemental distribution.....	44
Figure 21.	EDS maps of 5002 powder, 800°C/2 hrs heat treatment at 500X (left) and 1.5KX (right) showing inconsistency in observed elemental distribution.....	45
Figure 22.	EDS maps of PG-AMP-10 powder, 950°C/1 hr treatment at 500X (left) and 1.5KX (right) showing inconsistency in observed elemental distribution.....	46
Figure 23.	EDS maps of PG-AMP-10 powder, 800°C/2 hrs treatment at 500X (left) and 1.5KX (right) showing inconsistency in observed elemental distribution.....	47
Figure 24.	Chromium distribution in ferrite grains and process artifacts in PG-AMP-10 coating.....	48
Figure 25.	Time-Temperature sensitization curve for 304 stainless steel alloy with varying carbon contents. Source: [41].	50
Figure 26.	EDS maps of high nickel particle in 5002 as-sprayed powder sample.....	51
Figure 27.	X-ray diffraction spectra from 5001 powder samples.	53
Figure 28.	X-ray diffraction spectra from 5002 powder samples.	54
Figure 29.	X-ray diffraction spectra from PG-AMP-10 powder samples.	54
Figure 30.	EDS maps of chromium distribution in PG-AMP-10 powder samples showing high chromium areas likely associated with ferrite grains. (a) as sprayed; (b) 950°/1hr; (c) 800°C/2hrs; (d) 600°C/8 hrs.....	56
Figure 31.	Backscatter micrographs of 950°C/1 hr heat treated samples showing evidence of recrystallization and grain growth. Note annealing twins	

visible in 5001 and 5002 samples. (a) 5001; (b) 5002; (c) PG-AMP-10.....	57
Figure 32. Backscatter micrographs of 800°C/2 hrs heat treated samples showing evidence of recrystallization and grain growth. (a) 5001; (b) 5002; (c) PG-AMP-10.....	58
Figure 33. Average coating hardness. Results from Schiel [3] included for comparison.....	60
Figure 34. Typical polarization curve showing passivation behavior of 316L stainless steel in 0.05M H ₂ SO ₄ . Adapted from: [56].	67
Figure 35. Schematic diagram of a typical polarization testing cell. Source: [56].....	68
Figure 36. Method of supporting samples in salt fog chamber	70
Figure 37. Observed weekly salt fog sample mass loss.....	73
Figure 38. Mass loss measured after 1000 hrs salt fog exposure and cleaning of samples with 10% nitric acid	74
Figure 39. Example optical profiler output. (a) initial; (b) 525 hrs exposure; (c) 1005 hrs exposure, cleaned with ethanol and deionized water only; (d) 1005 hrs exposure, cleaned with 10% nitric acid. Note that color is normalized to the individual sample and varies between samples.....	76
Figure 40. Observed area fraction of sample pitting during weekly sample inspection.....	77
Figure 41. Observed sample pit density during weekly sample inspection.....	78
Figure 42. Observed average pit area during weekly inspection.....	79
Figure 43. Pit area fraction measured after 1000 hrs salt fog exposure and cleaning with nitric acid.....	80
Figure 44. Pit density measured after 1000 hrs salt fog exposure and cleaning with nitric acid.....	81
Figure 45. Average pit area measured after 1000 hrs salt fog exposure and cleaning with nitric acid.....	82
Figure 46. Maximum pit depth observed following 1000 hrs salt fog exposure and cleaning with 10 wt % nitric acid.....	83
Figure 47. Photographs of samples showing corrosion deposits on sample surface. PG-AMP-10 group 1. (a) initial; (b) 495 hrs; (c) 1000 hrs, cleaned with deionized water and methanol. (d) 1000 hrs, cleaned with 10% nitric acid.....	85
Figure 48. Profiler output and generated texture showing erroneous measurement of sample slope as peaks and valleys. 5002 powder,	

800°C / 2 hrs heat treatment. Profile following 1000 hrs exposure and nitric acid cleaning	89
Figure 49. Example resolved valley profile showing pitted regions with unresolved centers (blue circled regions). 5002 powder, 950°C / 1 hr heat treatment. Profile following 1000 hrs exposure and nitric acid cleaning.....	90
Figure 50. Anodic polarization curves for 5001 powder samples.....	92
Figure 51. Anodic polarization curves for 5002 powder samples.....	93
Figure 52. Anodic polarization curves for PG-AMP-10 powder samples.....	93
Figure 53. Anodic polarization curves for as-sprayed samples.....	94
Figure 54. Anodic polarization curves for 950°C/1 hr heat treated samples.....	94
Figure 55. Anodic polarization curves for 800°C/2 hrs heat treated samples.....	95
Figure 56. Polarization curves for bulk 316L substrates.....	96
Figure 57. Photographs of samples following 1000 hours salt fog chamber exposure and cleaning with deionized water/methanol showing evidence of corrosion on coating sides. Top 5001; middle 5002; bottom PG-AMP-10.....	103
Figure 58. Low resolution optical micrographs of 5001 coating: As sprayed (top left); 950°C/1 hr (top right); 800°C/2 hrs (bottom left); 600°C/8 hrs (bottom right).....	107
Figure 59. High resolution optical micrographs of 5001 coating: As sprayed (top left); 950°C/1 hr (top right); 800°C/2 hrs (bottom left); 600°C/8 hrs (bottom right).....	108
Figure 60. Low resolution SEM micrographs of 5001 coating, backscatter mode: As sprayed (top left); 950°C/1 hr (top right); 800°C/2 hrs (bottom left); 600°C/8 hrs (bottom right).....	109
Figure 61. High resolution SEM micrographs of 5001 coating, backscatter mode: As sprayed (top left); 950°C/1 hr (top right); 800°C/2 hrs (bottom left); 600°C/8 hrs (bottom right).....	110
Figure 62. Low resolution optical micrographs of 5002 coating: As sprayed (top left); 950°C/1 hr (top right); 800°C/2 hrs (bottom left); 600°C/8 hrs (bottom right).....	111
Figure 63. High resolution optical micrographs of 5002 coating: As sprayed (top left); 950°C/1 hr (top right); 800°C/2 hrs (bottom left); 600°C/8 hrs (bottom right).....	112
Figure 64. Low resolution SEM micrographs of 5002 coating, backscatter mode: As sprayed (top left); 950°C/1 hr (top right); 800°C/2 hrs (bottom left); 600°C/8 hrs (bottom right).....	113

Figure 65.	High resolution SEM micrographs of 5002 coating, backscatter mode: As sprayed (top left); 950°C/1 hr (top right); 800°C/2 hrs (bottom left); 600°C/8 hrs (bottom right).....	114
Figure 66.	Low resolution optical micrographs of PG-AMP-10 coating: As sprayed (top left); 950°C/1 hr (top right); 800°C/2 hrs (bottom left); 600°C/8 hrs (bottom right).....	115
Figure 67.	High resolution optical micrographs of PG-AMP-10 coating: As sprayed (top left); 950°C/1 hr (top right); 800°C/2 hrs (bottom left); 600°C/8 hrs (bottom right).....	116
Figure 68.	Low resolution SEM micrographs of PG-AMP-10 coating, backscatter mode: As sprayed (top left); 950°C/1 hr (top right); 800°C/2 hrs (bottom left); 600°C/8 hrs (bottom right)	117
Figure 69.	High resolution SEM micrographs of PG-AMP-10 coating, backscatter mode: As sprayed (top left); 950°C/1 hr (top right); 800°C/2 hrs (bottom left); 600°C/8 hrs (bottom right)	118
Figure 70.	EDS Maps of 5001 powder as sprayed.....	119
Figure 71.	EDS Maps of 5001 powder, 950°C/1 hr heat treatment.....	120
Figure 72.	EDS Maps of 5001 powder, 800°C/2 hrs heat treatment.....	121
Figure 73.	EDS Maps of 5001 powder, 600°C/8 hrs heat treatment.....	122
Figure 74.	EDS Maps of as sprayed 5002 powder.....	123
Figure 75.	EDS Maps of 5002 powder, 950°C/1 hr heat treatment.....	124
Figure 76.	EDS Maps of 5002 powder, 800°C/2 hrs heat treatment	125
Figure 77.	EDS Maps of 5002 powder, 600°C/8 hrs heat treatment	126
Figure 78.	EDS Maps of as sprayed PG-AMP-10 powder.....	127
Figure 79.	EDS Maps of PG-AMP-10 powder, 950°C/1 hr heat treatment	128
Figure 80.	EDS Maps of PG-AMP-10 powder, 800°C/2 hrs heat treatment	129
Figure 81.	EDS Maps of PG-AMP-10 powder, 600°C/8 hrs heat treatment	130
Figure 82.	5001 Group 1 Photographs. As sprayed (left), 950°C/1 hr (center), 800°C/2 hrs (right)	131
Figure 83.	5001 Group 2 Photographs. As sprayed (left), 950°C/1 hr (center), 800°C/2 hrs (right)	132
Figure 84.	5001 Group 3 Photographs. As sprayed (left), 950°C/1 hr (center), 800°C/2 hrs (right)	133
Figure 85.	5002 Group 1 Photographs. As sprayed (left), 950°C/1 hr (center), 800°C/2 hrs (right)	134

Figure 86.	5002 Group 2 Photographs. As sprayed (left), 950°C/1 hr (center), 800°C/2 hrs (right)	135
Figure 87.	PG-AMP-10 Group 1 Photographs. As sprayed (left), 950°C/1 hr (center), 800°C/2 hrs (right)	136
Figure 88.	PG-AMP-10 Group 2 Photographs. As sprayed (left), 950°C/1 hr (center), 800°C/2 hrs (right)	137
Figure 89.	Bare Substrate Photographs. As sprayed (left), 950°C/1 hr (center), 800°C/2 hrs (right)	138
Figure 90.	5001 As-sprayed sample #1 surface profile and texture analysis	139
Figure 91.	5001 As-sprayed sample #2 surface profile and texture analysis	139
Figure 92.	5001 As-sprayed sample #3 surface profile and texture analysis	140
Figure 93.	5001 950°C/1 hr sample #1 surface profile and texture analysis	140
Figure 94.	5001 950°C/1 hr sample #2 surface profile and texture analysis	141
Figure 95.	5001 950°C/1 hr sample #3 surface profile and texture analysis	141
Figure 96.	5001 800°C/2 hrs sample #1 surface profile and texture analysis	142
Figure 97.	5001 800°C/2 hrs sample #2 surface profile and texture analysis	142
Figure 98.	5001 800°C/2 hrs sample #3 surface profile and texture analysis	143
Figure 99.	5002 As-sprayed sample #1 surface profile and texture analysis	143
Figure 100.	5002 As-sprayed sample #2 surface profile and texture analysis	144
Figure 101.	5002 950°C/1 hr sample #1 surface profile and texture analysis	144
Figure 102.	5002 950°C/1 hr sample #2 surface profile and texture analysis	145
Figure 103.	5002 800°C/2 hrs sample #1 surface profile and texture analysis	145
Figure 104.	5002 800°C/2 hrs sample #2 surface profile and texture analysis	146
Figure 105.	PG-AMP-10 As-sprayed sample #1 surface profile and texture analysis	146
Figure 106.	PG-AMP-10 As-sprayed sample #2 surface profile and texture analysis	147
Figure 107.	PG-AMP-10 950°C/1 hr sample #1 surface profile and texture analysis	147
Figure 108.	PG-AMP-10 950°C/1 hr sample #2 surface profile and texture analysis	148
Figure 109.	PG-AMP-10 800°C/2 hrs sample #1 surface profile and texture analysis	148

Figure 110. PG-AMP-10 800°C/2 hrs sample #2 surface profile and texture analysis.....	149
Figure 111. Bare substrate as-sprayed sample surface profile and texture analysis.....	149
Figure 112. Bare substrate 950°C/1 hr sample surface profile and texture analysis.....	150
Figure 113. Bare substrate 800°C/2 hrs sample surface profile and texture analysis.....	150

THIS PAGE INTENTIONALLY LEFT BLANK

LIST OF TABLES

Table 1.	Commercial powder nominal composition summary. Adapted from: [3].....	10
Table 2.	Summary of commercial austenitic stainless steel powder size. Adapted from: [3].....	10
Table 3.	Summary of commercial austenitic stainless steel powder characteristics. Adapted from: [3].....	10
Table 4.	Summary of cold spray coating characteristics for four commercial austenitic stainless steel powders. Adapted from [3].....	11
Table 5.	Summary of cold spray stainless steel coatings achieved using helium carrier gas at 230°C and 1.7 MPa. Adapted from: [3].....	12
Table 6.	Summary of deposition efficiency and coating thickness per pass for replication of previous work and testing the effect of increased standoff distance.	13
Table 7.	Cold spray machine settings used to grit blast coupons prior to coating deposition.....	22
Table 8.	Cold spray machine settings used for coating preparation.	23
Table 9.	Elemental composition in wt % of cold spray coatings with various heat treatments obtained through EDS.	36
Table 10.	Coating phase composition as determined by X-ray diffraction. Data reported by Schiel [3] included for comparison.	55
Table 11.	Average coating hardness. Results from Schiel [3] included for comparison.....	59
Table 12.	Qualitative corrosion performance of as-sprayed cold spray coating relative to uncoated 316 stainless steel substrate.....	86
Table 13.	Qualitative corrosion performance of heat treated coatings relative to corrosion performance in the as-sprayed condition.	86
Table 14.	Measured open circuit and pitting potential voltages from coating and substrate polarization testing.....	97

THIS PAGE INTENTIONALLY LEFT BLANK

ACKNOWLEDGMENTS

I would like to thank both of my advisors, Dr. Luke N. Brewer and Dr. Sarath Menon, for their generous assistance, technical insight and help through this project. Both of these gentlemen devoted numerous hours to supporting this thesis; without them I would never have been able to complete it.

Likewise, Dr. Chanman Park, Dr. Dragoslav Grbovic and Mr. Max Neumann provided invaluable assistance with operation and training on various instruments, facilities and techniques required to complete this work.

Also, I am indebted to Ms. Miki Ngai at the University of Alabama for her generous assistance in conducting polarization testing. Without her assistance, a major section of this research could not have been completed.

Funding for this project was provided by Mr. Richard Hays, Deputy Director of the Office of the Secretary of Defense Office of Corrosion Policy and Oversight.

Finally, I would like to thank all of the faculty of the Mechanical and Aeronautical Engineering department at the Naval Postgraduate school for their technical expertise and generous assistance whenever and wherever needed. The education and experience I have received with their assistance and guidance will be an invaluable resource in my future career as an Engineering Duty Officer. I am also grateful for the assistance and support of my fellow students in this fine program.

THIS PAGE INTENTIONALLY LEFT BLANK

I. INTRODUCTION

A. MOTIVATION

Many material failures both within the Navy and outside of it occur due to either mechanical wear or corrosion or both. Consequently, a very large amount of effort has been invested over the years in the prevention and repair of wear and corrosion. Prevention of wear can be accomplished through design and operation changes, but also by improved materials. A major goal of material science research has been to develop materials that are harder and/or stronger in order to better resist mechanical wear. Likewise, corrosion is also responsible for significant cost in design and repair of damage; one source [1] gives an annual corrosion cost to the Department of the Navy of roughly \$7 billion.

One common solution to help reduce corrosion or wear is to add a coating of a harder or more corrosion resistant material to a part in order to protect the base material. This approach allows the use of a less corrosion- or wear-resistant base material for structural, economic or other reasons. It is also common to use a material addition process to restore a worn or damaged part surface to the required dimensions. The traditional method for applying a thin uniform coating of a material is to use a thermal spray process. In this process the coating material is applied to the surface as a spray of molten droplets or heated solid particles at high temperature, which cool and solidify on contact with the base metal [2]. The thermal spray method is well developed and has many advantages including relatively low cost, simple use, fast deposition rates and a breadth of knowledge and experience in its use. However, the high temperature of the coating material can cause undesirable oxidation or property changes in the sprayed material as well as heating and possible thermal damage to the substrate material [2].

A recently developed alternative is the cold gas dynamic spray process, which uses kinetic energy of coating particles rather than thermal energy to form a coating. Consequently, the particles of coating material are subjected to much lower temperatures, greatly reducing many of thermal spray's undesirable side effects such as vaporization of

volatile elements, thermal stresses in the coating and oxidation or property changes in the coating and/or substrate materials due to high temperatures [2]. When conducted correctly, the cold spray process also gives a more dense coating due to a plastic peening effect from succeeding particles impacting on the applied coating and from the lack of a “splashing” effect that occurs with the impact of liquid or nearly liquid droplets [2]. The range of application temperatures and velocities used in the cold spray technique as compared to other coating spray technologies is shown in Figure 1.

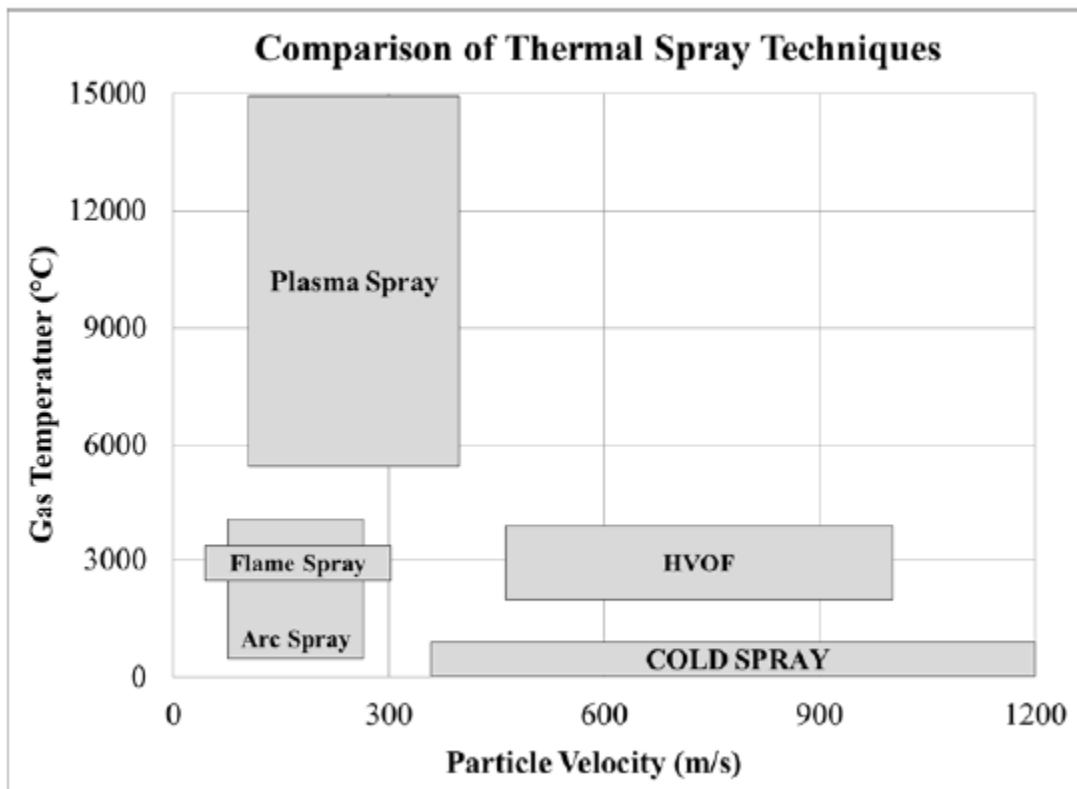


Figure 1. Comparison of general temperature and particle velocity range for coating spray techniques. Source: [3].

There are numerous applications for this coating technology, but those of greatest importance to the department of defense are the repair of damaged parts that cannot readily be repaired by more conventional methods and the application of protective coatings to parts made of corrosion prone materials such as magnesium. Work on the use of a 316L stainless steel coating for corrosion protection on a magnesium alloy, AZ91E

was conducted in 2010 by Spencer and Zhang [4], with the result that the stainless steel coating significantly reduced the corrosion potential of a sample when compared to uncoated magnesium alloy substrates in electrochemical corrosion testing. Their finding showed that any amount of coating had some positive benefit, and a thicker coating approached the behavior of bulk 316 stainless steel showing a pronounced passivation effect. This demonstrates a potential for the use of this coating technique for corrosion protective coatings. Notably, even though the coating has some degree of porosity, the behavior of a sufficiently thick coating suggests that adequate protection of the substrate is still achieved. This is important as the substrate material in this application will almost certainly be anodic to the coating material and hence a small exposed area of the substrate will suffer rapid corrosion due to the large available cathode area of the coating and consequent concentrated corrosion on the small exposed substrate section. The use of an aluminum coating to protect a different magnesium alloy, AZ91D, was demonstrated by Tao et al. [5] in 2010. Their work suggested that the coating reduced the pitting potential on the substrate. Similar work by DeForce et al. in 2011 demonstrated the use of a Al-5 wt % Mg coating on an otherwise active ZE41A-T5 magnesium alloy [6]. Other more exotic combinations have also been investigated; Al-Mangour et al. examined the use of a cold spray Co-Cr coating on 316L stainless and showed marked improvement in the corrosion resistance of the stainless steel [7].

The cold spray process has also been demonstrated as a viable repair process for the restoration of part surfaces that have suffered wear, corrosion or other mechanical damage [8, 9]. To repair this type of damage, new material must be added to the component without causing any detrimental changes in the base component material. For many materials, such as magnesium alloys, traditional material addition techniques such as welding or thermal spray would cause sufficient damage in the base material to render the part unusable. Traditionally, these parts would be scrapped and replaced once a certain wear/damage allowance was exceeded. The cost and operational impacts of this approach can be significant. For these applications the cold spray process offers an economical method of building up the needed material without causing base material damage and hence restoring the components to service. Not only does this offer

potentially significant cost saving, but may also allow a much faster repair, thereby minimizing downtime. P. F. Leyman and V. K. Champagne have demonstrated this use of the cold spray technique in the repair of helicopter mast supports in U.S. Army aircraft, with over 50 successful repairs conducted. These parts would have otherwise been scrapped [8]. Villafuerte and Wright have likewise demonstrated cold spray repair of other aircraft components with the repair meeting all FAA certification requirements [9]. Notably, the repairs demonstrated operationally to date have been to restore a critical dimension, rather than the repair material being used structurally. The use of the cold spray process for structural repair is an area of ongoing research [10–13].

With the current and predicted future tight defense budgets, there is a strong impetus for the U.S. Navy to investigate and develop the most effective and efficient techniques for the repair of mechanical and corrosion damage to ships and aircraft. With a proven record of success in the repair of light alloy structures, the cold spray process may prove to be an economical technique for the repair of steel structures.

B. THE COLD SPRAY MATERIAL DEPOSITION PROCESS

The cold gas dynamic spray process is a relatively recent technology originating from supersonic wind tunnel testing at the Institute of Theoretical and Applied Mechanics of the Siberian Branch of the Russian Academy of Science in Novosibirsk during the 1980s [14]. In this process, particles of the coating material are accelerated by entrainment in a supersonic jet of gas produced by the expansion of a working gas through a converging-diverging (DeLaval) nozzle. Typical particle sizes of 5 to 100 μm are used, and these particles obtain a velocity of 500–1,200 m/s when entrained in the gas jet. This velocity gives sufficient kinetic energy that the particles bond to a substrate upon impact through plastic deformation [4, 15–21]. The critical parameter in the successful adhesion of a particle is its velocity on impact with the substrate. Investigation has shown that there is a “critical velocity” where particles having a velocity in excess of this will adhere and those with a velocity below will not. The velocity achieved by a particular particle is primarily influenced by the choice of working gas and the velocity of the gas jet. The velocity of the gas jet in turn is controlled by nozzle design and the sonic velocity

in the nozzle, which is in turn a function of the upstream gas pressure and temperature. In order to increase this velocity the working gas is typically preheated prior to entering the nozzle. As the gas expands, the temperature decreases so the actual gas temperature at the point of particle entrainment is in the range of -100 to +100°C; hence the name “cold spray” [22–24]. There are two main variants on the overall cold spray process; high pressure and low pressure cold spray systems [24]. In high pressure systems the powder is entrained in the gas stream prior to expansion through the nozzle whereas low pressure systems entrain the powder on the expansion side of the nozzle. Low pressure type system typically operate at a pressure below 2.0 MPa [3] and are more portable [24]. The overall process for a low pressure type cold spray system is illustrated schematically in Figure 2.

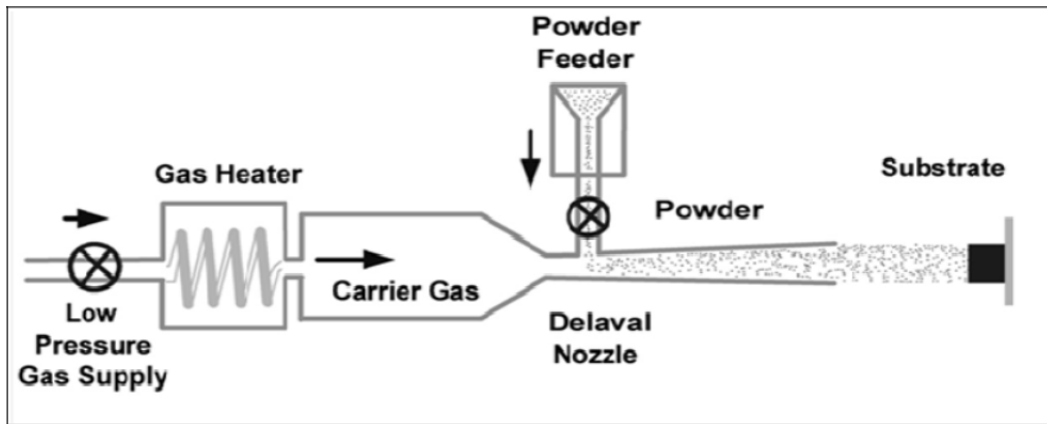


Figure 2. Schematic of the cold spray deposition process. Source: [8].

Selection of the working gas used in the cold spray process has a great deal of effect on quality of the final coating produced [25]. The gas used must be inert to avoid undesirable reactions with the powder or substrate metals. It is desirable to have a high sonic velocity as the final nozzle exit velocity is directly related to the sonic velocity of the gas. Likewise, a high gas density is desirable to achieve the most effective acceleration of the entrained particles. Helium, nitrogen and air are the most commonly used working gasses. Of these, helium typically gives the best performance due to a high

sonic velocity, but is also by far the most costly. Nitrogen is much cheaper to use, but does not offer as good of performance [25].

C. CORROSION

Corrosion is defined as a destructive chemical reaction between a metal or alloy and its environment. It has been described as “extractive metallurgy in reverse,” as the general trend is from the refined metal to return to the lower energy chemical compound of its ore [26]. In almost all cases corrosion reactions are electrochemical in nature; that is, they involve the transfer of electric charge as part of the overall chemical reaction. The electrochemical nature of the reaction means that it may be separated into two physically separate half reactions provided there is an electrical connection between the two. This conductive path is typically proved by a conductive electrolyte which is water with dissolved ions in common environmental corrosion.

Stainless steels are characterized as a steel alloy having at least 10.5 wt% chromium added [27]. The additional chromium promotes the formation of a passive surface layer and gives a material with generally excellent corrosion resistance. However, stainless steels are susceptible to other specific corrosion modes, notably pitting, crevice corrosion and stress corrosion cracking [28]. Pitting and crevice corrosion are both forms of localized corrosion damage resulting from a similar mechanism. At its heart this is a failure of the passivation layer. Chlorine ions cause a local breakdown of the passive film leading to the nucleation of a pit. Local corrosion then leads to deaeration of the water thus forming a local acidic solution and anodic region. The surrounding water becomes alkaline by cathodic reduction of dissolved oxygen and allows the surrounding metal surface to act as an anode. Once a pit is established it forms a sheltered local environment where ferrous ions resulting from the anodic corrosion reaction can react with chlorine ions dissolved in the water to produce ferrous hydroxide and hydrochloric acid. This mechanism for acid production in turn decreases the local pH in turn produces more favorable conditions for galvanic corrosion [26]. This is shown schematically in Figure 3.

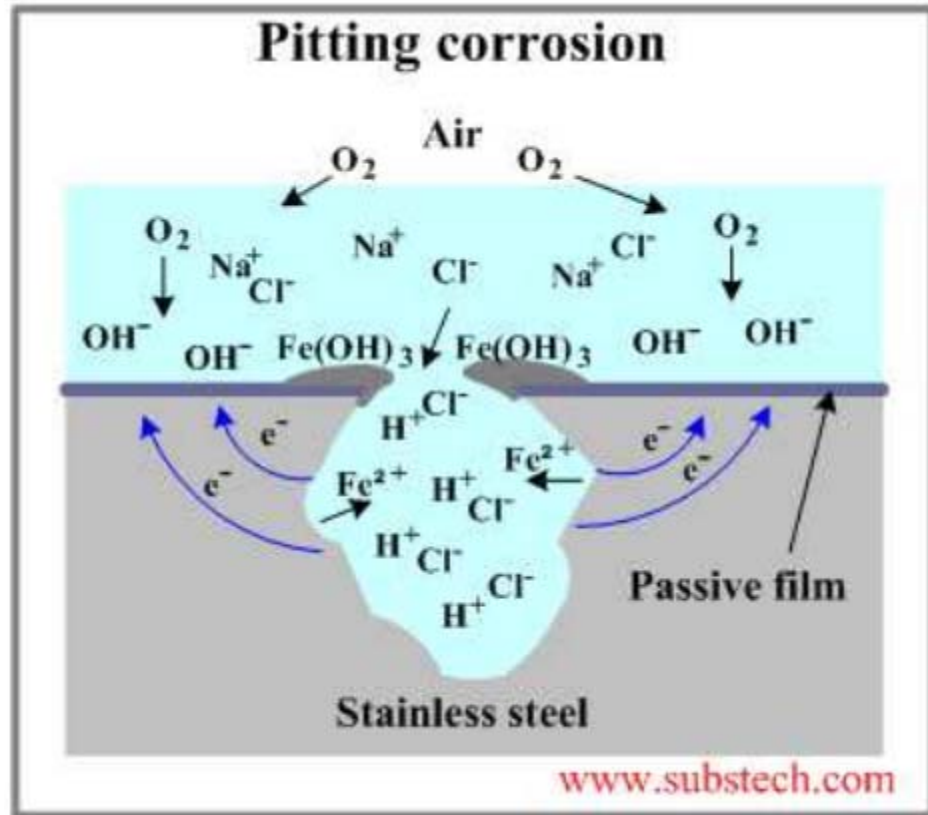


Figure 3. Schematic mechanism of pitting corrosion. Source: [29].

The difference between pitting and crevice corrosion is simply that crevice corrosion occurs at a mechanical feature on the material, such as a seam, void or near biological organisms such as barnacles whereas pitting can occur anywhere upon the surface [26]. Stress corrosion cracking is a form of environmentally induced cracking where a corrosion type reaction from environmental exposure results in material failure through brittle cracking [26]. However, this form of corrosion damage requires the presence of a tensile stress in the material, and since the surface of the cold spray coating is known to have significant compressive residual stress this corrosion mode will not be considered in this study [26].

D. OBJECTIVES

Two main technical objectives were set for this thesis work:

- 1. Investigate the corrosion properties of low pressure cold spray austenitic stainless steel coatings.**

While the corrosion properties of austenitic stainless steel are well known, there is limited work on the corrosion properties of cold spray austenitic coatings, and specifically a lack of work on the properties of low pressure cold spray coatings. The low pressure process generates a coating that may be substantially more porous than the high pressure spray or bulk material, hence it is expected the corrosion properties may be significantly different. This research aims to investigate these properties through salt fog (ASTM B117) and electrochemical polarization testing (ASTM G5) of low pressure cold spray austenitic stainless steel coatings. Several different powders and heat treatments will be applied to investigate the changes in corrosion properties from these treatments.

- 2. Investigate the effects of heat treatment on the microstructure and characteristics of cold sprayed austenitic stainless steel coatings.**

Previous work has demonstrated successful deposition of austenitic stainless steel coatings on stainless steel substrates using both high and low pressure cold spray techniques [3–4, 7, 15–17]. The optimal cold spray parameters for use of certain powders with a low pressure cold spray machine have also been determined and the microstructure of these powders and the resulting coatings have been characterized [3]. There has been work conducted on the microstructure and property changes in austenitic stainless steel coatings applied with the high pressure cold spray technique, however, there is a lack of investigation into the effects of annealing heat treatment on the coating microstructure and properties when a low pressure technique is used to apply the material. This research will aim to reproduce the previously reported successful low pressure austenitic stainless steel cold spray deposits and will attempt to fully characterize the microstructural changes to the coating resulting from annealing heat treatments.

II. COLD SPRAY OF AUSTENITIC STAINLESS STEEL

A. INTRODUCTION

Previous work on the application of austenitic stainless steel coatings was conducted at NPS by Schiel in 2014. In this work, he used 4 austenitic stainless steel powders; one of a nominal 304L stainless steel, one 316 and two 316L. These powders are Centerline “S5001” (SS304L) and “S5002” (SS316L), Inovati KM316 (SS316) and Plasma Giken PG-AMP-10 (SS316L). The manufacturer’s nominal compositions for these powders are given in Table 1. Schiel also characterized the powders using a variety of experimental methods. A summary of his results is shown in Tables 2 and 3 [3]. Analysis of the particle size distribution in the powders found that the 5001 and KM316 powders have a unimodal symmetric distribution of particle sizes while the 5002 and PG-AMP-10 powders have a distinct fraction of larger powder particles. All of the powders except the PG-AMP-10 also were found to have a relatively spherical particle shape; the PG-AMP-10 powder has a mix of irregular shapes [3]. The particle morphology is important in how well the particles are accelerated by the gas stream. A mix of smaller and larger particles is also expected to give lower porosity as the smaller particles more effectively fill the gaps between larger ones [3]. Within the individual power particles the grain size and phase distribution changes the mechanical properties of the material with a smaller grain size being associated with a harder material having lower ductility but greater strength [30]. All of the stainless steel alloys used here are typically almost entirely composed of the austenite phase with a very small amount of ferrite [27]. The properties of these two phases are significantly different, so a large amount of ferrite could result in bulk material properties that are different than expected for these types of stainless steels. Specifically, ferrite is known to be less corrosion resistant than austenite [31]. The grain orientation spread (GOS) is a measure of the plastic deformation experienced by a material. Typical annealed deformation-free crystalline materials can be expected to exhibit a GOS of 0.1–0.3° [32]. The higher values observed here suggest substantial plastic deformation of the particles [3].

Table 1. Commercial powder nominal composition summary. Adapted from: [3].

Powder	Fe	Cr	Ni	Mn	Mo	Si	C
S5001 (304L)	68.4	19.0	10.9	1.0	-	0.6	0.017
S5002 (316L)	65.5	17.2	13.0	1.5	2.2	0.5	0.014
KM 316 (316)	68.2	16.8	10.8	1.3	2.1	0.6	0.02
PG-AMP-10 (316L)	69.0	17.0	12.0	-	2.0	-	-

All elemental contributions are given in weight percent.

Table 2. Summary of commercial austenitic stainless steel powder size. Adapted from: [3].

Powder	Mean Size (μm)	D10 (μm)	D90 (μm)
S5001 (304L)	19.9	12.5	28.4
S5002 (316L)	45.6	18.1	75.2
KM 316 (316)	17.2	6.7	25.5
PG-AMP-10 (316L)	61.3	14.3	164.8

Table 3. Summary of commercial austenitic stainless steel powder characteristics. Adapted from: [3].

Powder	Mean Size (μm)	% Ferrite (XRD)	Crystallite Size (μm)	Average GOS ($^\circ$)
S5001 (304L)	19.9	~0	2.7	1.8
S5002 (316L)	45.6	50	6.4	2.4
KM 316 (316)	17.2	23	4.1	2.4
PG-AMP-10 (316L)	61.3	46	6.0	1.6

Schiel also conducted characterization of sprayed coatings using the above four powders and helium working gas at 1.7 MPa and 230°C. His results are shown in Table 4 [3]. His results verify that a satisfactory low pressure cold spray coating can be achieved with this configuration. His characterization of the coatings indicates that a substantial amount of the ferrite seen in some of the original powder is retained in the coatings produced and the grain size in the coatings is reduced by roughly a factor of 10 to a submicron size in all four powders. The GOS values obtained show that a very high degree of plastic deformation is also present in the coating [3].

Table 4. Summary of cold spray coating characteristics for four commercial austenitic stainless steel powders. Adapted from [3].

Powder	Deposition Efficiency (%)	Thickness per Pass (mm)	% Ferrite (EBSD/XRD)	Crystallite Size (μm)	Average GOS (°)
S5001 (304L)	11.8	0.67	1	0.22	2.3
S5002 (316L)	12.3	0.71	19/48 [†]	0.38	1.7
KM 316 (316)	41.8	0.15	1	0.33	2.4
PG-AMP-10 (316L)	29.4	0.93	27/58 [†]	0.33	2.2/1.3*

Sprayed with helium gas at 230°C and 1.7 MPa. [†] denotes collection via X-Ray diffraction. * denotes the ferrite crystal GOS.

Additionally, Schiel conducted a systematic investigation into the optimal spray conditions for these powders. For this he used both N₂ and helium carrier gas and examined a number of gas pressure and temperature combinations to find those that gave the optimal coating deposition. Quantification of the coatings for this study was conducted by measurement of the deposition efficiency and the coating thickness, with the deposition efficiency being measured as the mass of the final coating divided by the mass of the powder sprayed. The coating mass was determined by measurement of the substrate before and after spraying with the powder mass likewise being the initial mass of powder loaded minus the mass removed from the system following spraying.

From this investigation, Schiel determined that the best conditions for deposition of all four of the stainless steel powders were with helium gas at 230°C and 1.7 MPa. These results are summarized in Table 5. Only the PG-AMP-10 powder was successfully deposited with N₂ carrier gas and this was only achieved at one spray condition, 450°C and 1.7 MPa. A 4.1% deposition efficiency and a 0.26 mm coating thickness was reported with these conditions. [3]

Table 5. Summary of cold spray stainless steel coatings achieved using helium carrier gas at 230°C and 1.7 MPa. Adapted from: [3].

Test No.	1	2	3	4
Powder Material	S5001	S5002	KM316	PG-AMP-10
Working Gas	Helium	Helium	Helium	Helium
Substrate Material	Grey Cast Iron	Grey Cast Iron	Grey Cast Iron	Grey Cast Iron
Gas Temperature (°C)	230	230	230	230
Gas Pressure (MPa)	1.7	1.7	1.7	1.7
Powder Feed Rate (g/min)	60.4	54.8	2.4	19.6
Deposition Efficiency (%)	11.8	12.3	41.8	29.4
Coating Thickness per Pass (mm)	0.67	0.71	0.15	0.93

B. REPRODUCTION OF PREVIOUS WORK

An initial goal of this research was to verify the results reported by Schiel and to ensure a reproducible quality coating could be produced for use in further work. Additionally, some further investigation was conducted into the effects of an increased standoff distance. Schiel developed a mathematical model of the fluid dynamics of the spray jet, which suggests that an increase in standoff distance from the 16 mm used in his optimization work to 40 mm should result in an increase in the average particle velocity [3]. As the particle velocity is the primary controlling factor in the successful deposition of the coating, this result suggests that better coating results should be obtained at an increased standoff distance. Schiel briefly investigates this effect with one powder and reports finding no change in the deposition efficiency or coating thickness, but some evidence of improved coating quality in the form of reduced porosity. This result was investigated further, and some additional testing was conducted using other powders with N₂ carrier gas. Schiel had tested a number of N₂ spray conditions and reported negligible deposition in all but one case, however it was deemed possible that the increase in particle velocity from the increase in standoff distance could be enough to have a sufficient number of particles now exceed the critical velocity and hence achieve a measurable coating.

A number of test sprays were conducted, using both N₂ and helium gas in both cases using a 1.7 MPa gas pressure and temperature of 230°C with helium and 450°C with N₂. Other machine settings used were as listed in Table 8 with the exception of some

sprays using a 16 mm standoff distance vs 40. In all cases 316 stainless steel substrates were used. Substrates were grit blasted using Centerline G0002 grit with machine parameters as listed in Table 7 and were cleaned with ethanol prior to coating deposition. A summary of the coatings produced is shown in Table 6.

Table 6. Summary of deposition efficiency and coating thickness per pass for replication of previous work and testing the effect of increased standoff distance.

Powder	Working Gas	Standoff Distance (mm)	Deposition Efficiency	Coating Thickness per pass (mm)
5001	N2	40	0.0%	0.00
	He	40	12.4%	0.33
5002	N2	40	0.0%	0.00
	He	16	-	0.39
		40	-	0.32
PG-AMP-10	N2	40	0.5%	0.06
	He	16	27.2%	0.36
		40	28.0%	0.80

Deposition efficiency not measured in samples marked by ‘-’

Overall the results achieved agree reasonably well with those reported by Schiel. Even with the increased standoff distance no measurable coating was achieved with N₂ and the 5001 or 5002 powders. The PG-AMP-10 powder was observed to form a measurable coating, but with lower deposition efficiency than reported by Schiel. This may be a measurement error. Deposition efficiency was not accurately measured in several other samples as well. Some variation was noted in the coating thickness. In part this is due to a difference in measurement method; Schiel measured the thickest portion of the coating which typically occurs at the ends of the coated area where the cold spray system would dwell for a short time while the control moved to the next program step. This region would be significantly thicker than the majority of the coating. For this work, the average bulk thickness of the coating was measured as this is the critical dimension for practical application. It was also determined that the coating thickness produced is highly dependent on the actual powder feed rate which cannot be accurately controlled.

The cold spray system used has a nominal feed rate setting, however the actual powder feed rate is also highly dependent on the material level in the feeder and is thus difficult to consistently and accurately set. Schiel's modeling shows that the powder velocity distribution and thus the overall coating quality is not greatly affected by the feed rate; hence the variation in effective powder feed rate due to this inconsistency in feed rate results solely in a variation of coating thickness and not a notable variation in coating quality.

Sections were taken of these samples and polished for optical microscopy. Polishing was conducted on an automatic polishing machine using grinding paper through 1200 (P4000) grit followed by polishing through $0.05\text{ }\mu$ alumina on a cloth wheel. Optical Microscopy was conducted to inspect the coating porosity both within the coating and at the coating/substrate interface. This examination showed a generally consistent dense coating in agreement with Schiel's reported results. Typical micrographs are shown in Figures 4–6.

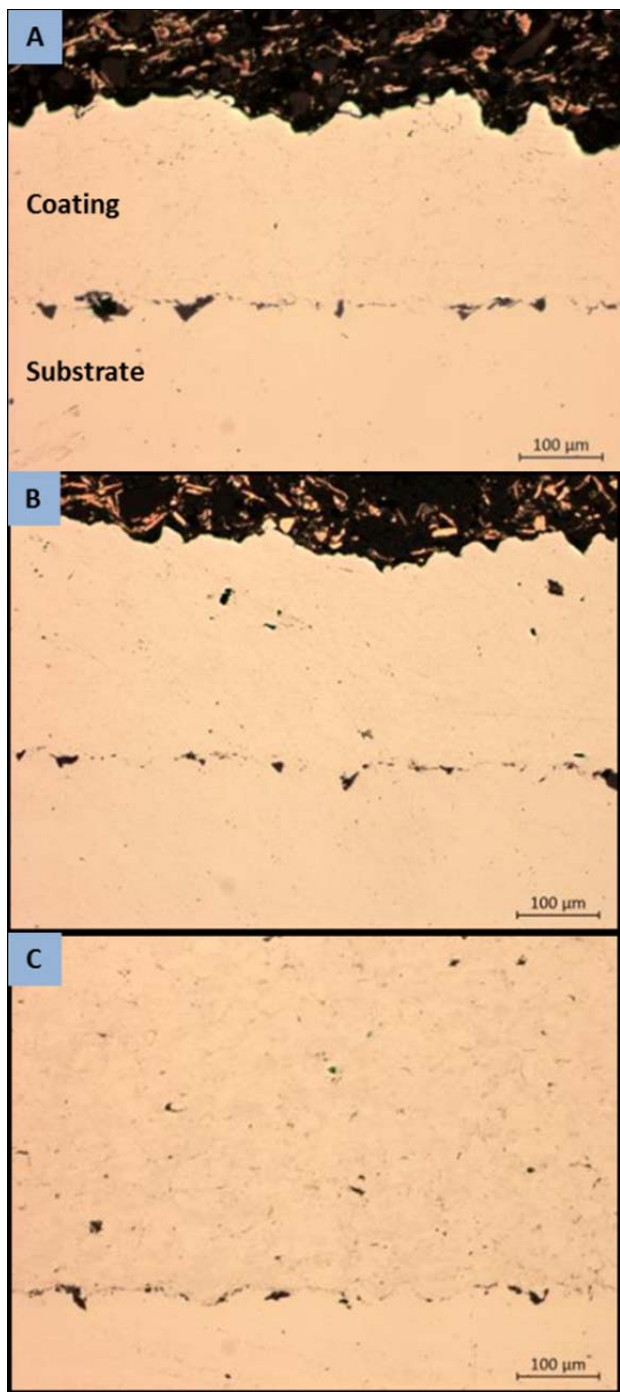


Figure 4. Low magnification optical micrographs of coatings sprayed with helium gas at 1.7 MPa and 230°C; 40 mm standoff distance. (a) 5001; (b) 5002; (c) PG-AMP-10.

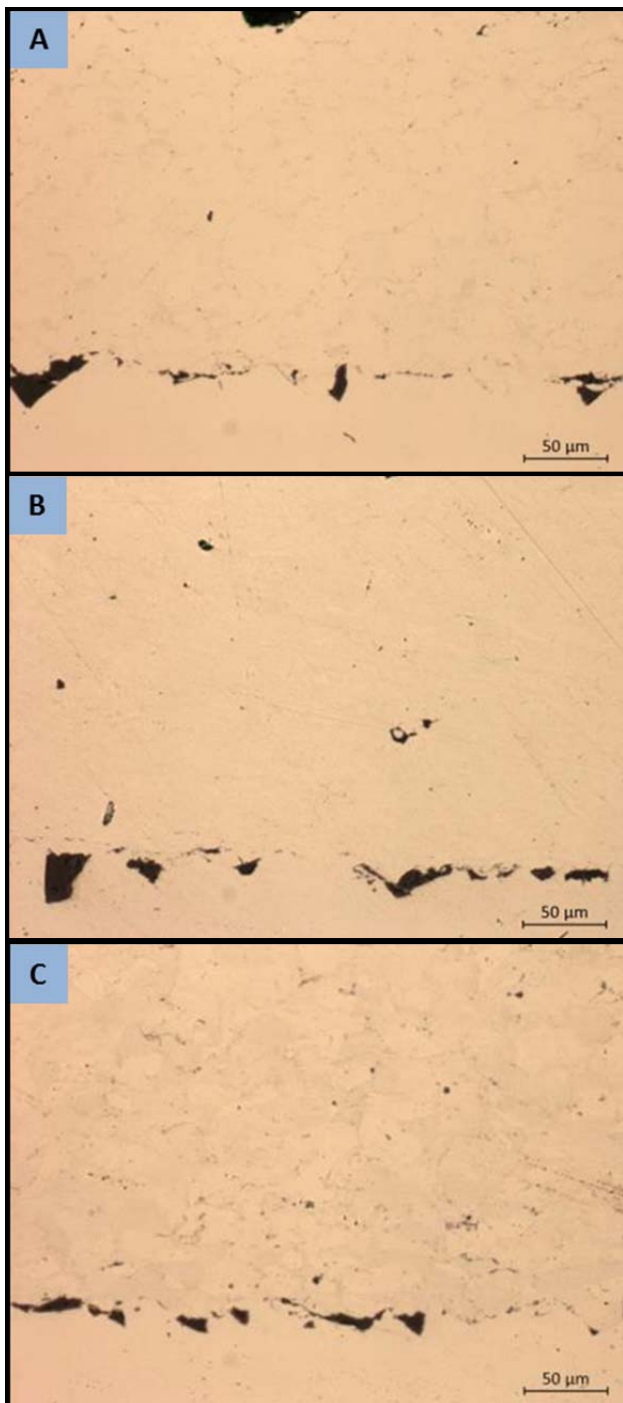


Figure 5. High magnification optical micrographs of coating sprayed with helium gas at 1.7 MPa and 230°C; 40 mm standoff distance. (a) 5001; (b) 5002; (c) PG-AMP-10.

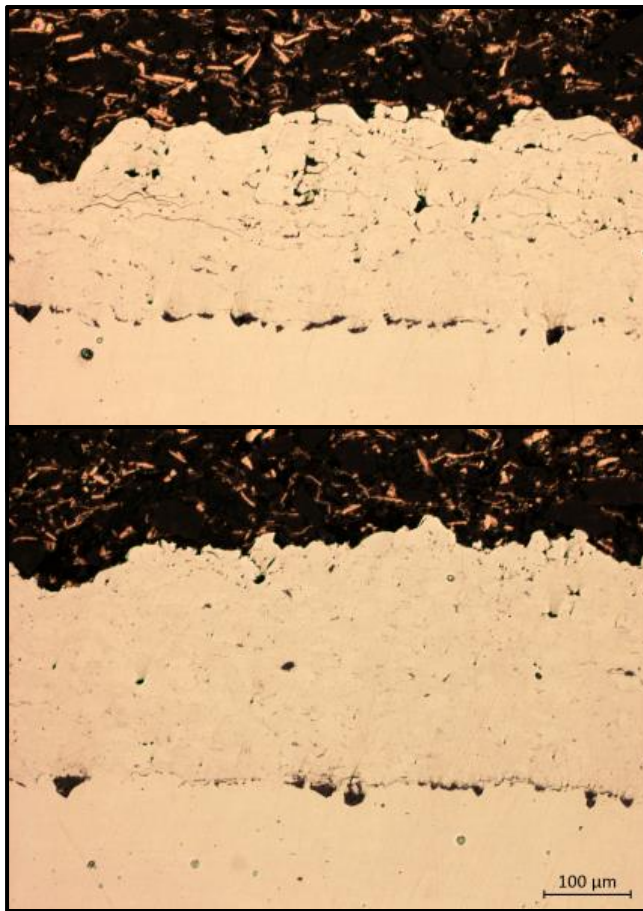


Figure 6. Typical micrographs of PG-AMP-10 powder sprayed with N_2 gas at 1.7 MPa and 450°C showing improved coating quality (decreased porosity) at 40 mm standoff distance. 16 mm standoff (top); 40 mm distance (bottom)

When using helium working gas, no significant differences were found between 16 mm and 40 mm working distances either in coating thickness or quality. There was a measurable difference in thickness as seen in Table 6, however thicknesses were sufficiently inconsistent across all samples that this difference is inconclusive. The coating quality was observed to be consistent across all samples, and generally matches that reported by Schiel. The PG-AMP-10 and 5002 coatings were observed to have qualitatively greater porosity than the 5001. Both still showed high density within the coating however. Notably, Schiel reports evidence of decreased coating/substrate boundary porosity when the standoff distance was increased but this effect was not seen

in this work. PG-AMP-10 samples sprayed with N₂ working gas did show an improvement in coating quality with an increase in standoff distance from 16 to 40 mm as seen in Figure 6. The coating produced at a 40 mm standoff distance shows qualitatively lower porosity within the coating, though with no change in the coating/substrate interface porosity.

In several instances the spraying of an additional layer on a previously well adhered coating was observed to result in the entire coating detaching from the substrate. An example of this phenomena is shown in Figure 7. The sample illustrated is using the 5001 powder with helium gas, however complete detachment was also observed with PG-AMP-10 powder and N₂ gas on the 4th pass. Additionally, multiple other samples exhibited partial detachment where the coating was only attached on one side of the deposit. Partial detachment was observed in samples of all 3 powders. Schiel also reports observing a similar phenomenon during some of his N₂ test sprays. No systematic investigation was conducted, however the general trend observed is that this is primarily associated with a thicker multiple pass coating. The detachment of the coating consistently happened during the spraying operation and no external mechanical force was involved—the coating detachment occurs solely as a result of stresses resulting from the particle impact or thermal effects.

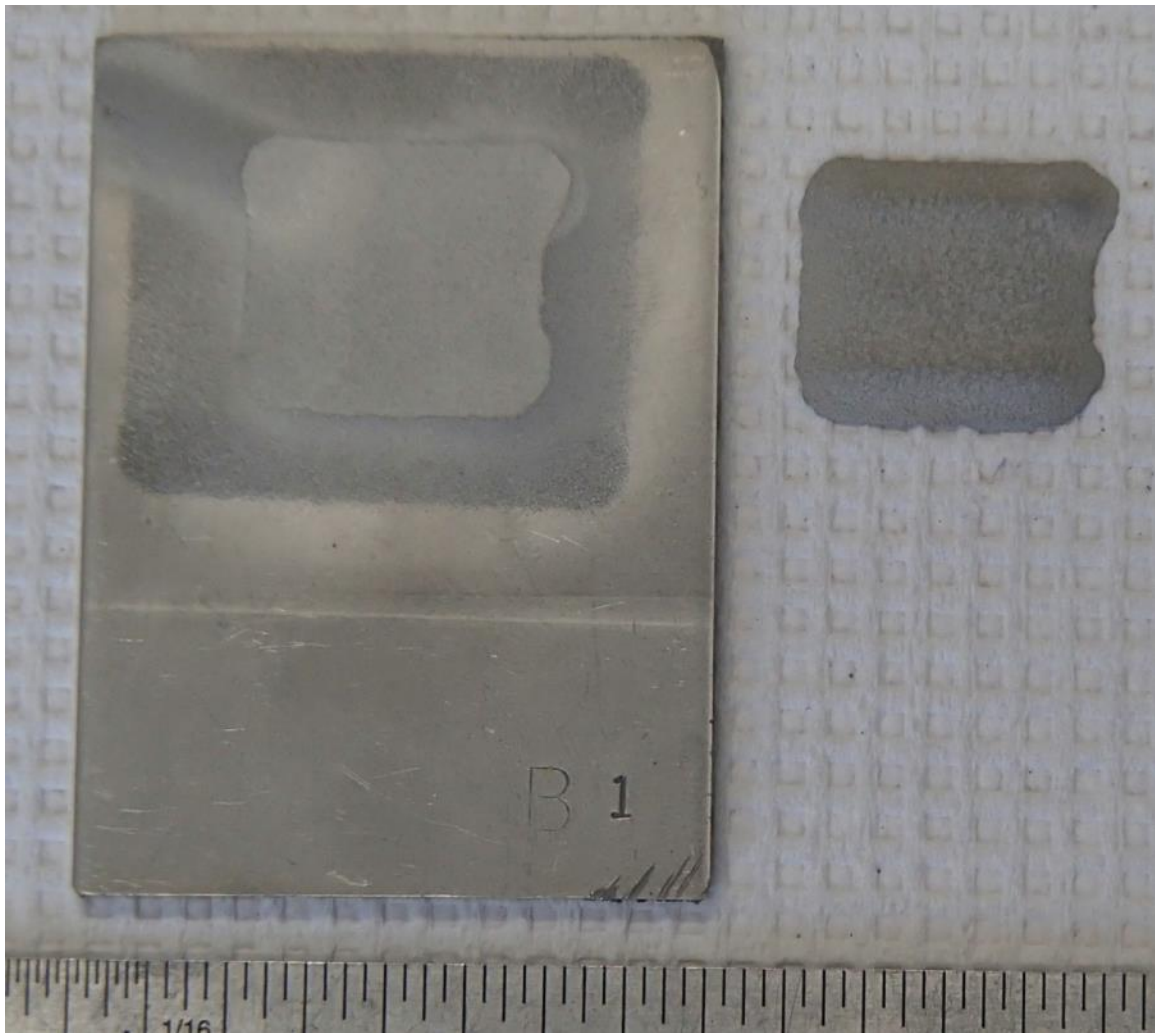


Figure 7. Coating detachment phenomena observed during spraying of 3rd pass with 5001 powder. He gas, 1.7 MPa at 230°C

Examination of micrographs of other samples shows evidence of the mechanism that leads to this detachment. Almost all samples observed showed some degree of porosity at the coating/substrate boundary, but in several samples sections up to several mm in length were seen where the coating was detached from the substrate within an otherwise well adhered coating. This is shown in figure 8. Close inspection of the surfaces in these regions reveals a surface morphology in the coating that closely matches that of the substrate surface, suggesting that the coating was previously adhered to the substrate in these regions and was subsequently pulled up off of the substrate by some force. The gross coating detachment observed may be the result of this small scale

detachment occurring over a large area and resulting in the entire coatings being completely detached from the substrate. The evidence of a force pulling the coating off the substrate suggests that the ultimate cause is a tensile stress in the coating at the substrate/coating boundary. Work conducted on residual stress in cold spray coatings [33, 34] shows that compressive residual stress is found in the coating surface, and a tensile residual stress is common at the coating/substrate boundary; however the magnitude of this stress appears to be dependent on the exact spray parameters used and the substrate/coating material. Notably, results reported in the available literature focus on aluminum and copper coating with no data available on stainless steel coatings. Further investigation is warranted to measure the residual stress in low pressure cold spray stainless steel coatings and determine mitigation measures to prevent the coating detachment problem observed. This problem would prevent the application of a reliable high quality coating and hence makes practical application of the process very difficult. Residual stress studies could show if the ultimate problem is high residual stress in the coating or low bond strength. If the problem lies in a high residual stress then it is possible that a stress relief heat treatment between coating passes could alleviate this problem.

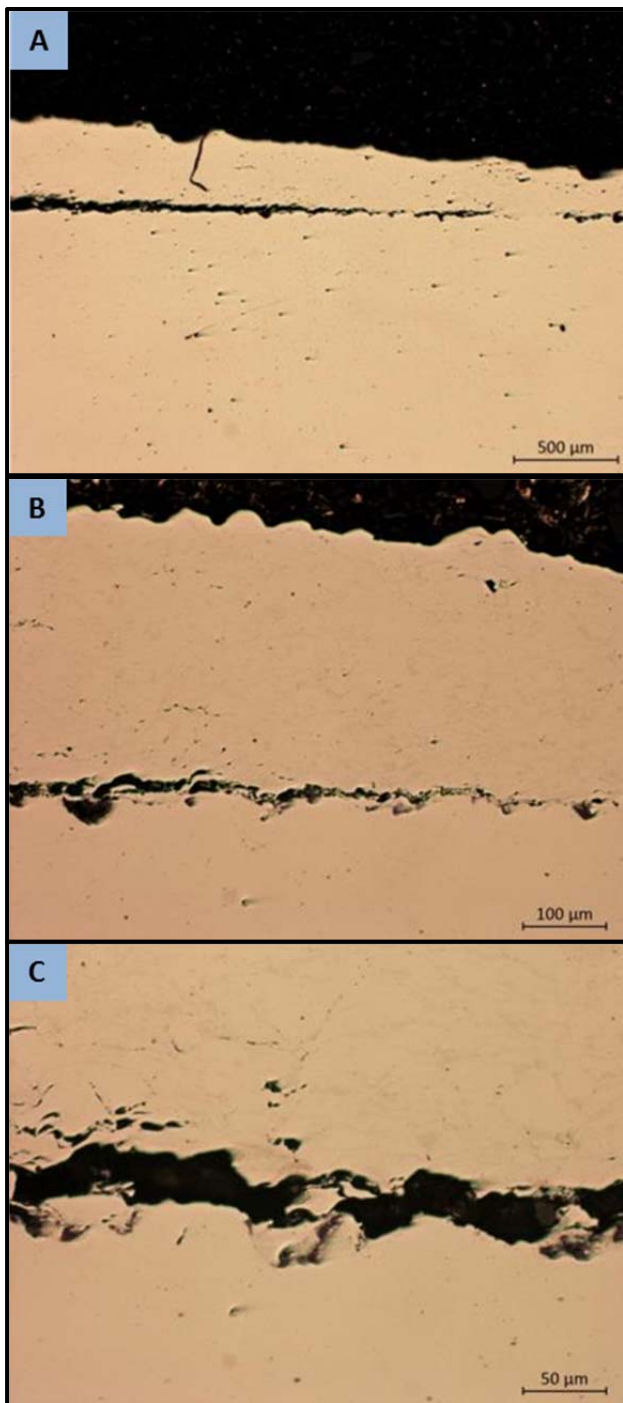


Figure 8. Coating detachment phenomena observed in 5002 powder sprayed with helium gas at 1.7 MPa, 230°C. Increasing magnification (a) to (c).

C. SAMPLE PREPARATION FOR CURRENT WORK

Centerline “S5001” and “S5002” along with Plasma Giken “PG-AMP-10” powders were used for all further investigation work. These powders will henceforth be referred to as “5001”, “5002” and “PG-AMP-10”. All substrate coupons used were commercially available cold rolled unpolished 316 stainless steel strip with nominal dimensions of 76.2 x 50.8 x 3.18 mm (3 x 2 x 1/8”) Coupons were cut from lengths of 50.8 x 3.18 mm (2 x 1/8”) strip using either abrasive or bandsaw cutting. All low pressure cold spray deposits were made using a Centerline (Windsor) Limited SST Model P low pressure cold spray deposition system located at NPS and operating under automatic control. Coupons were grit blasted using Centerline SST-G0002 grit media. This is a 80 grit alumina blasting grit supplied specifically for cold spray substrate preparation with a nominal particle size of 100–300 μm . Machine settings used for grit blasting are shown in Table 7. Substrates were cleaned after grit blasting using ethanol and allowed to air dry prior to coating deposition. Coating deposition was conducted using the machine settings shown in Table 8. Multiple passes were used as needed to give the desired thickness for the testing in question.

Table 7. Cold spray machine settings used to grit blast coupons prior to coating deposition.

Blasting Media	SST-G0002
Gas	Nitrogen
Gun Type	Automatic
Nozzle	WC
Gas Temperature (°C)	125
Gas Pressure (MPa)	1.0 (150)
Nominal Powder Feed Rate (%)	15
Gun Stand-off Distance (mm)	15
Gun Traverse Speed (mm/s)	50
Gun Step Over per Pass (mm)	1.5

Table 8. Cold spray machine settings used for coating preparation.

Powder	5001, 5002, PG-AMP-10
Gas	Helium
Gun Type	Automatic
Nozzle	WC
Gas Temperature (°C)	230
Gas Pressure (MPa)	1.7(250)
Nominal Powder Feed Rate (%)	40
Gun Stand-off Distance (mm)	40
Gun Traverse Speed (mm/s)	40
Gun Step Over per Pass (mm)	1.2

Heat treatments were conducted in a Lincoln “Blue M” radiant type electrically fired furnace fitted with automatic temperature control. The furnace was preheated to the specified temperature prior to samples being inserted, and the treatment time was started upon the insertion of samples into the preheated furnace. The furnace atmosphere was air with no special treatment. Samples were removed from the furnace and allowed to cool in still air. Three heat treatment procedures were used: 600°C for 8 hours (henceforth referenced as “600°C/8 hrs”), 800°C for 2 hours (henceforth referenced as “800°C/2 hrs”), and 950°C for 1 hour (henceforth referenced as “950°C/1 hr”).

THIS PAGE INTENTIONALLY LEFT BLANK

III. EFFECT OF HEAT TREATMENT ON SPRAYED COATINGS

A. INTRODUCTION

Heat treatment is a well-known and commonly used processing technique to change the properties of the material [30]. By heating the material to a temperature below its melting point various processes are either activated or accelerated at the microscopic level resulting in changes to the microstructure and hence the macroscopic material properties. This type of treatment typically consists of a relatively rapid heating of the material to a specified temperature followed by a certain time held at that temperature and a relatively rapid cooling and is commonly known as annealing. Most of the microscopic processes occurring during this treatment occur as a result of diffusion and follow a Arrhenius form rate equation:

$$Rate = Ae^{\frac{-E}{RT}} \quad (1)$$

Here “A” is a pre-exponential term characteristic of the process, “R” is the universal gas constant, “T” is the absolute temperature and “E” is an activation energy associated with the process. In a process of this type there is an activation energy “E” required for the process to occur and an exponential dependence of the process rate on the temperature. From a practical point of view, this means that the process will not occur at a practically useful rate below a specific temperature and will exponentially accelerate in rate with increasing material temperature.

Three stages of annealing are generally defined: recovery, recrystallization and grain growth [30]. Recovery occurs at the lowest temperature of the three and does not typically effect the overall grain structure but does decrease residual stresses through the movement and in some cases annihilation of dislocations within the crystal structure. This treatment typically has little visible macroscopic effect but does improve electrical conductivity and in some cases corrosion resistance.

The next stage of heat treatment is recrystallization. A definitive boundary temperature is difficult to define and changes depending on the degree of cold work of the material but is generally given as 0.4 times the absolute melting temperature (T_m).

The melting temperature of the 3xx stainless steel is approximately 1650K, so recrystallization in this material should occur at around 375°C. Above this temperature diffusion occurs rapidly enough to allow atomic diffusion sufficient for a new unstrained grain structure to nucleate and begin to grow in highly deformed regions. The diffusion rate is still low enough that these new grains remain relatively small and a certain amount of the original grain structure remains. Because the new grains tend to form at high stress regions (i.e., where there are a high concentration of dislocations), this process tends to greatly reduce the number of dislocations in the material and hence result in increased ductility and decreased tensile strength in the material.

At higher annealing temperatures, the diffusion rate becomes even higher and rather than numerous small grains formed during recrystallization, smaller numbers of strain-free nuclei grow rapidly due to the increased diffusion controlled growth rate resulting in a relatively small number of individually large grains. These large grains result in a material with very high ductility and low strength [30].

Several researchers have investigated annealing treatments of austenitic stainless steel cold spray coatings [35–37]. X. M. Meng et al. investigated the effects of annealing at 950°C for 2 hours on 304 stainless steel coatings and found evidence of full recrystallization, a substantial decrease in coating porosity and coating ductility/hardness values equivalent to those of annealed bulk 304 stainless steel [35]. Xian-Ming Meng et al. performed similar annealing treatments on cold sprayed 304 stainless steel coatings using temperatures of 300°C, 600°C, 800°C and 950°C [36]. Sundararajan et al. performed work on cold spray 316L stainless steel coatings using heat treatments at 400°C, 800°C and 1100°C reporting reduced porosity and improved bonding and mechanical properties [37]. Notably, these investigations have all been on coatings produced by the high-pressure cold spray process.

In the as-sprayed condition cold spray coatings are known to have a very high amount of plastic deformation and thus high strength but very low ductility with properties substantially different than bulk stainless steel [34]. In many application this mismatch is likely undesirable. In this context, heat treatment may be a practical method

to improve the properties of the coating and more closely match the coating properties to the substrate.

B. EXPERIMENTAL METHODS

Samples were prepared as described in (II.C). A nominal 12.5 x 19 mm (1/2 x 3/4") deposit was used with two passes being used on 5001 and 5002 samples and one on the PG-AMP-10 samples. Two samples of each powder were prepared, with the average coating thickness being 0.66 mm (0.026") for the 5001 powder, 0.47 mm (0.018") for the 5002 powder and 0.91 mm (0.036") for the PG-AMP-10 powder. Each of the samples was then cut down the long axis of the substrate roughly at the center of the deposit to give two roughly identical size samples with a roughly 12.5 x 9.5 mm (1/2" x 3/8") deposit from each original substrate, for a total of four samples of each powder.

Following heat treatment the samples were cut to give specimens for examination using a Struers metallurgical saw. A transverse cross section and coating surface sample was prepared for microscopy, as well as a surface sample for X-ray diffraction studies. The transverse cross section samples were used for microhardness measurements following the completion of microscopy examination. X-ray diffraction samples were polished through a 1200 (P2500) grit grinding paper using a Buhler automatic polishing machine. Microscopy samples were polished through 1200 (P2500) grit grinding paper and further polished through 0.05 μm alumina powder using polishing cloths on an automatic Buhler polishing machine. Final polishing was initially conducted using 0.05 μm colloidal silica in a vibrator polishing machine however this was determined to be insufficient for reliable EBSD mapping and electro polishing was instead used with a 10% perchloric acid/ethanol electrolyte at -40°C with a 20V potential and 30 second polishing time.

Microstructural characterization of samples was performed using a number of techniques. Optical microscopy was performed using a Nikon Epiphot 200 metallographic microscope equipped with Nikon 'NIS Elements' image capture software. Magnifications of 100x and 200x were used. Optical images were used primarily to characterize large-scale porosity in the coating. Electron microscopy was performed

using a Zeiss Neon 40 scanning electron microscope (SEM) using both secondary electron and backscatter electron imaging modes. Magnifications of 1.5KX and 3KX were used to quantify microscopic porosity and overall microstructure. Energy dispersion spectroscopy (EDS) was used to identify the elemental composition and distribution in the samples. Overall sample composition was measured at a magnification of 300x and EDS mapping was conducted at a magnification of 500X and 1.5KX. In addition to iron, nickel, chromium, silicon and molybdenum concentrations and distribution were measured. Trace elements were not measured. Electron backscatter diffraction mapping (EBSD) was conducted to determine the phase distribution, grain size and grain orientation mismatch. In all cases a 20kv accelerating voltage was used, with a 30 μ m aperture for secondary electron imaging and 60 μ m with high current used for EBSD and EDS work. EBSD mapping was performed at a magnification of roughly 900X to give a scan size of roughly 85 x 300 μ m. X-ray diffraction (XRD) measurements were conducted on a Rigaku MiniFlex 600 instrument with a high speed position sensitive detector using Cu $K\alpha_1$ radiation using 40 kv excitation voltage and 15 ma filament current. A scan of 2 Θ angles from 40°-100° was used with a 0.02° step and a 10° per minute scan rate.

Hardness testing was conducted using a Struers DuraScan-50 microhardness testing machine. A Vickers type indenter was used with a 0.9807 N load (HV 0.1 scale). The load was applied and maintained for 15 seconds. A minimum of 25 individual points were used in each test with a 0.1 mm spacing between points. Individual test points were inspected and any that coincided with large scale porosity were rejected.

C. RESULTS AND DISCUSSION

Examination of the coating microstructure at low magnification shows that all three powders produce a qualitatively dense coating with relatively low porosity as shown in Figure 9. Qualitatively the different powders produce similar amounts of porosity but with a different spatial distribution. The 5002 and 5001 powders tend to have long thin regions while the PG-AMP-10 tends to shows a greater number of smaller porous regions. This is likely due to the powder morphology. As measured by Schiel, the

5001 and 5002 powders have a spherical morphology with generally consistent size while the PG-AMP-10 has a bimodal size distribution and a much more irregular particle shape [3].

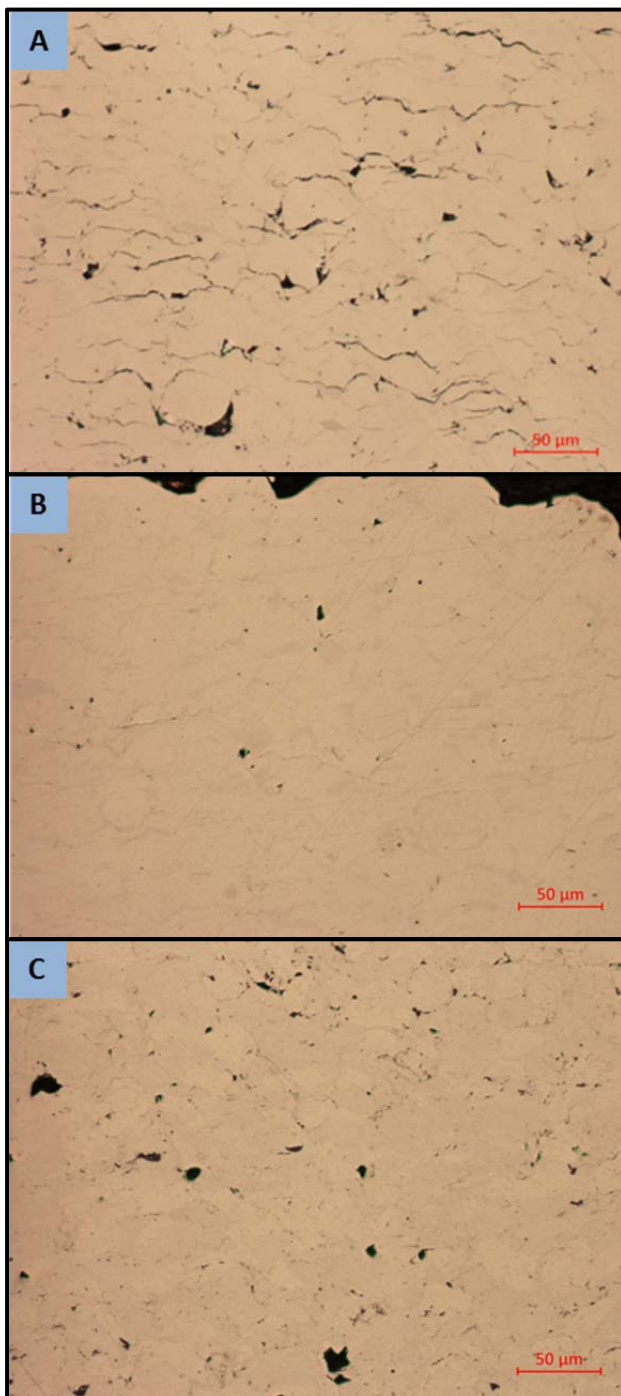


Figure 9. High magnification optical micrographs of as-sprayed coatings showing qualitatively dense coating structure with limited porosity. (a) 5001 powder; (b) 5002 powder; (c) PG-AMP-10 powder.

In the cold spray process a very high degree of deformation occurs during the particle adhesion process resulting in a highly stressed microstructure with very small grains [22]. Rapid recrystallization and recovery can thus be expected during annealing. All three of the heat treatments used in this work are above the generally accepted recrystallization temperature of $0.4T_m$ so evidence of recrystallization can be expected in all heat treatments. For reference, 600°C is $0.53T_m$, 800°C is $0.65T_m$ and 950°C is $0.74T_m$.

The most visible change resulting from heat treatment is in the sample porosity. The lowest energy state is a complete absence of porosity, so the trend is expected to be towards reduced porosity as diffusion rates increase with temperature. Since the complete elimination of porosity would require substantial large scale diffusion this is not likely. As an intermediate lower energy state, the consolidation of numerous smaller porous regions in single larger areas and the conversion of long thin regions to one or more spherical regions can be expected. This behavior is seen in the 5001 samples as seen in Figures 10 and 11. The lower temperature heat treatment shows a structure similar to the as-sprayed sample but in both the higher temperature samples the long thin regions of inter-splat porosity are seen to have consolidated into circular regions. With longer or higher temperature treatment, these would be expected to consolidate further to individually larger but less numerous regions. Similar results are seen in the 5002 and PG-AMP-10 powders as shown in Figures 12 and 13.

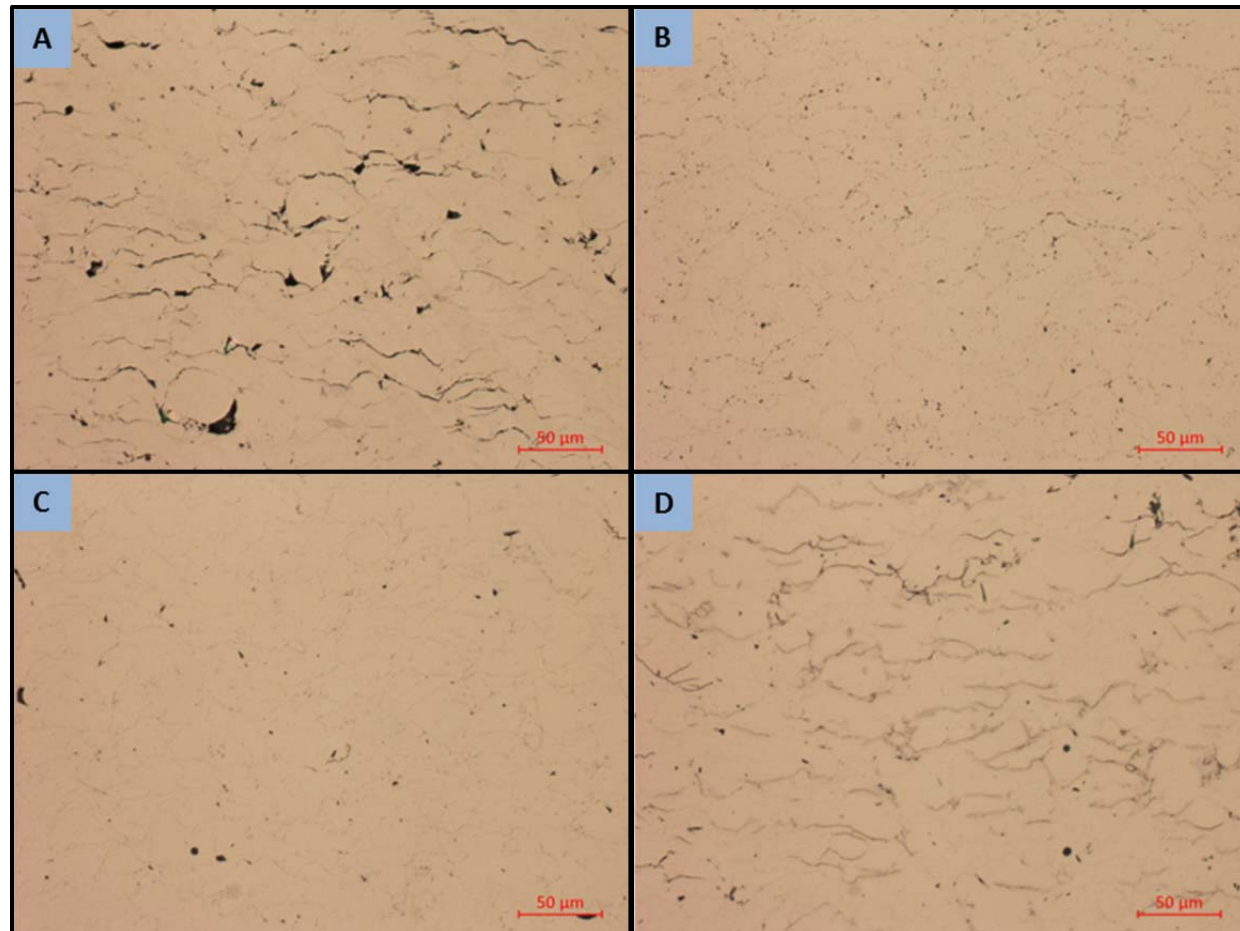


Figure 10. High magnification optical micrographs showing changes in porosity with heat treatment. 5001 powder. (a) as sprayed; (b) 950°C/1hr; (c) 800°C/2hrs; (d) 600°C/8 hrs.

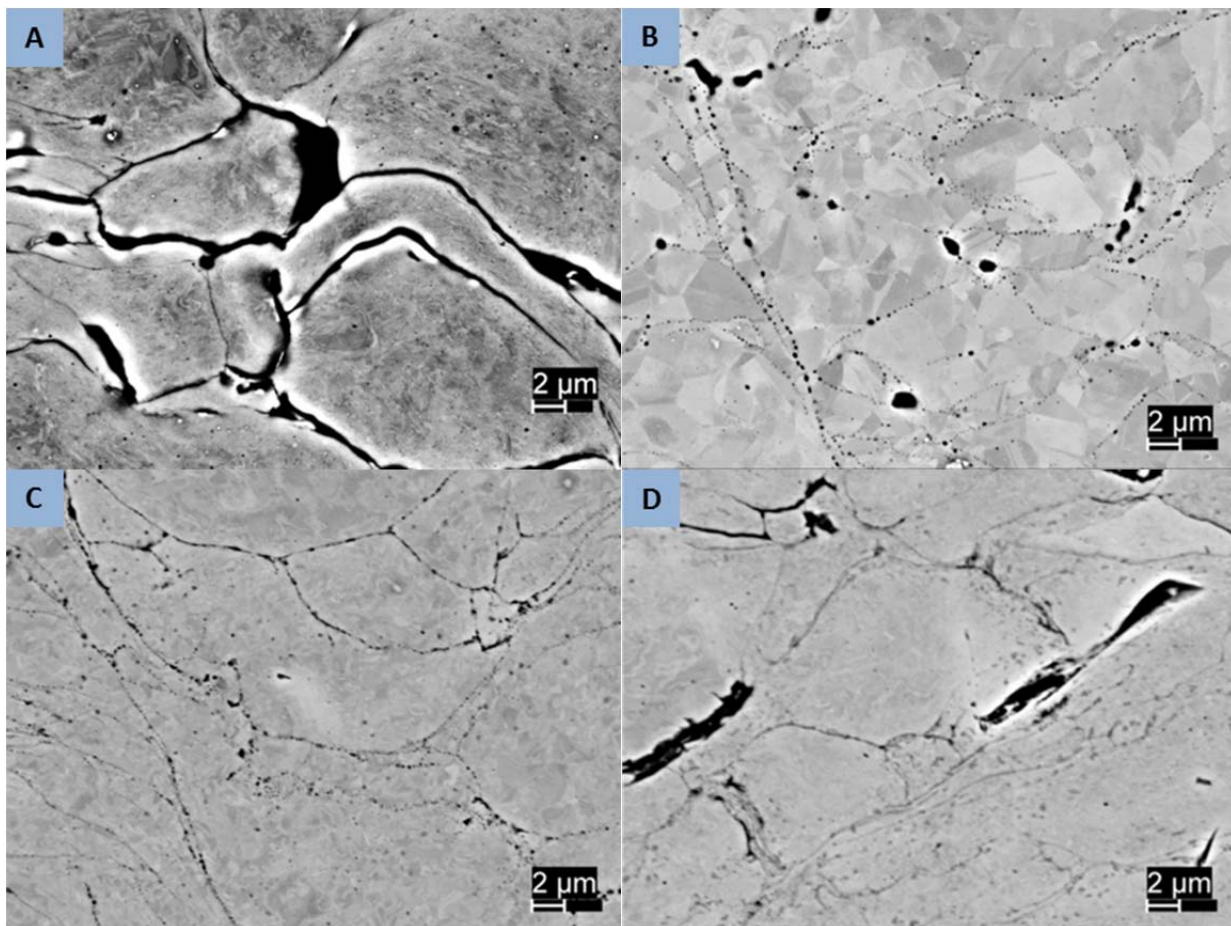


Figure 11. Backscatter electron images of 5001 powder samples showing porosity reduction following heat treatment. (a) as sprayed; (b) 950°C/1hr; (c) 800°C/2hrs; (d) 600°C/8 hrs.

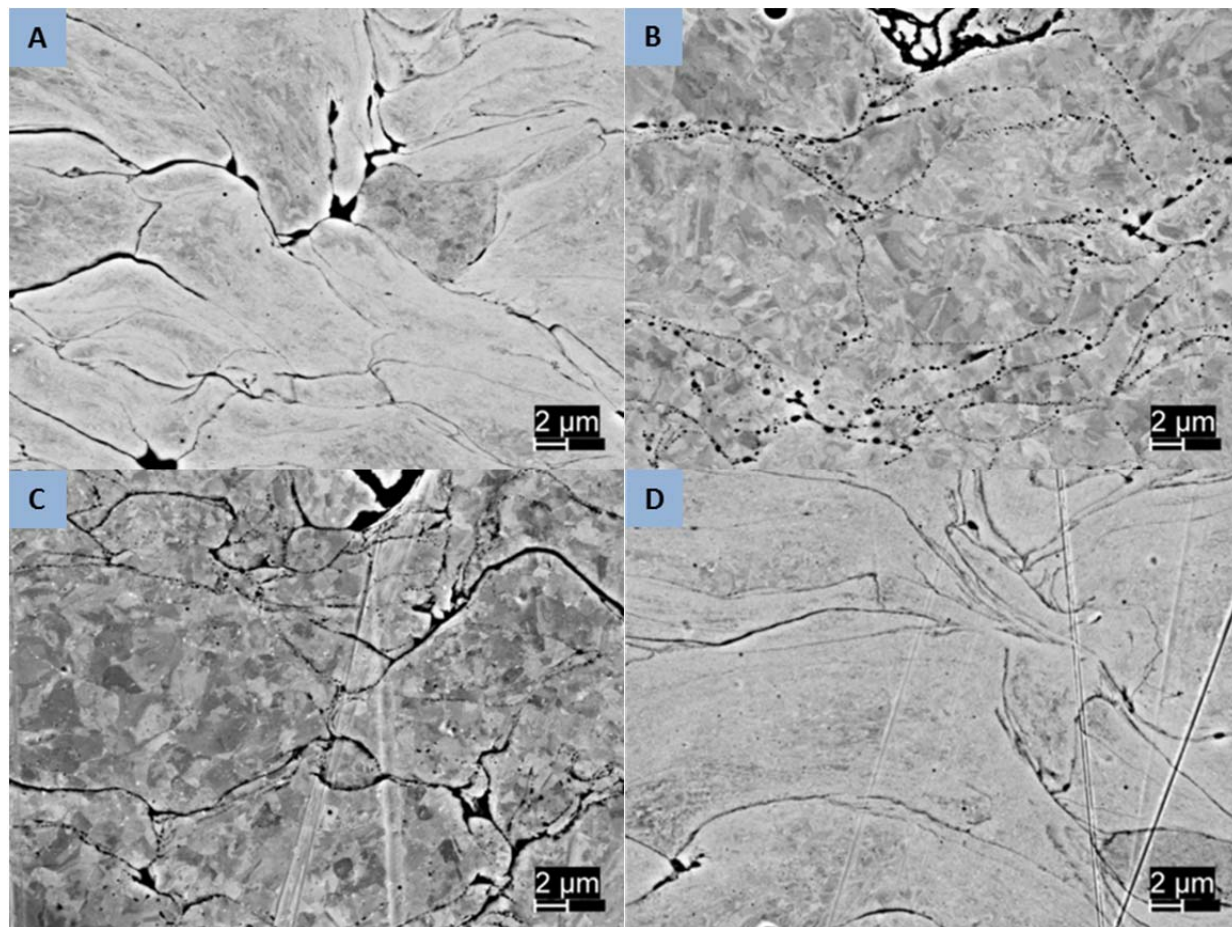


Figure 12. Backscatter electron images of 5002 powder samples showing porosity reduction following heat treatment. (a) as sprayed; (b) 950°/1hr; (c) 800°C/2hrs; (d) 600°C/8 hrs.

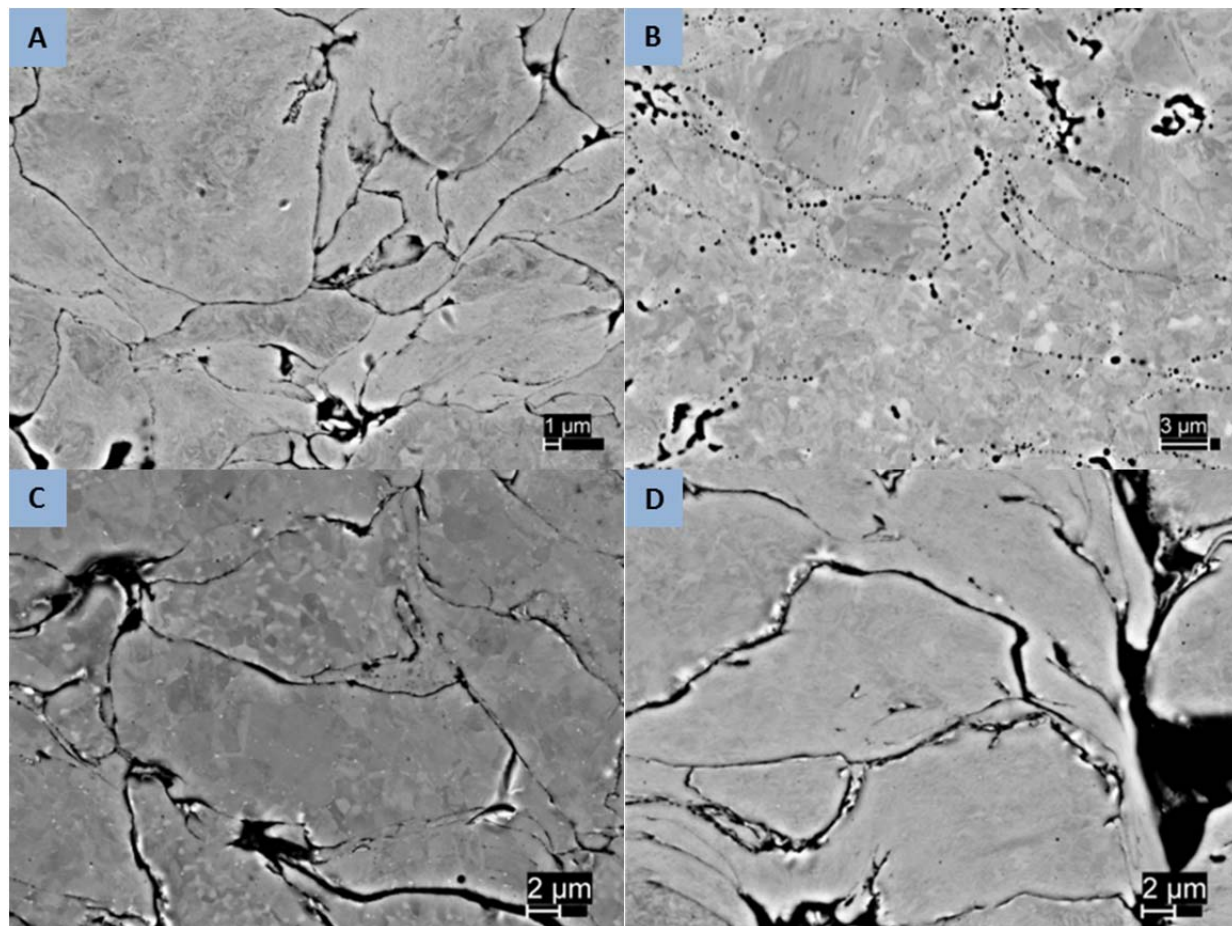


Figure 13. Backscatter electron images of PG-AMP-10 powder samples showing porosity reduction following heat treatment. (a) as sprayed; (b) 950°C/1hr; (c) 800°C/2hrs; (d) 600°C/8 hrs.

In the 950°C/1 hr micrographs small circular dark regions are observed that seem to correspond to inter-splat boundaries. These images were taken using the backscatter detection mode to enhance contrast, however this also has the effect of making it difficult to determine if dark regions are porosity in the sample or precipitates with a lower atomic number than the bulk material. In order to further identify these, high magnification EDS scanning and secondarily electron imaging was conducted in these regions. No evidence of elemental concentration was seen in EDS scanning which suggests that these areas are porosity rather than precipitates. A typical point EDS measurement is shown in Figure 14. In this case, the chromium content is observed to actually be less than the overall coating composition (Table 9).

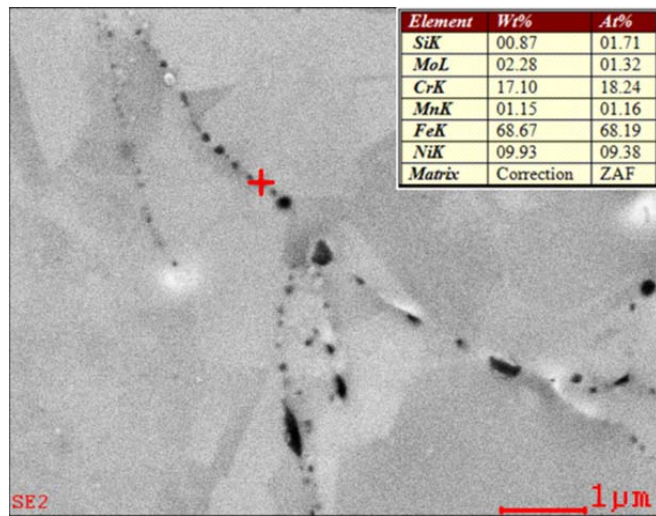


Figure 14. Typical point EDS measurement of possible precipitate.

The resolution of the EDS process may not have been sufficient to show very small precipitates however. SEM imaging at higher magnifications gives the results shown in Figure 15.

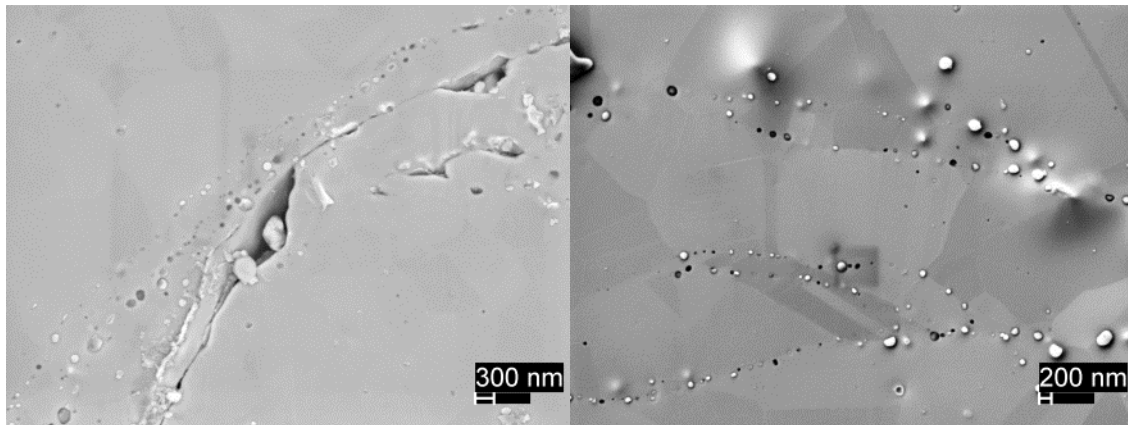


Figure 15. High resolution secondary election images of micro-porosity in 950°C/1 hr samples. 5002 powder, in lens detector (left); PG-AMP-10 powder, secondary electron detector (right).

Both of these images clearly show that there is some micro porosity still present in the samples. Possible nanometer scale precipitates are seen in the 5002 powder (Figure 15 left) and some small circular regions that are clearly porosity are seen in the PG-AMP-10 example (Figure 15 right). It is possible that these areas were actually precipitates and the carbide precipitates have been dislodged during the polishing process leaving behind a crater that appears as porosity.

The overall composition of the coating in each sample was measured by EDS with results shown in Table 9.

Table 9. Elemental composition in wt % of cold spray coatings with various heat treatments obtained through EDS.

	Element								
	Al	Si	P	S	Mo	Cr	Mn	Fe	Ni
304L specification*	-	<1.0	<0.045	<0.03	-	18.0-20.0	2.00		8.0-12.0
316L specification*	-	<1.0	<0.045	<0.03	2.0-3.0	16.0-18.0	2.00		10.0-14.0
5001 as sprayed	0.13	0.74	0.04	0.10	-	19.44	1.53	68.18	9.84
5001 950/1 hr	0.11	0.77	0.02	0.05	-	19.50	1.77	67.90	9.87
5001 800/2 hrs	0.15	0.83	0.03	0.07	-	19.49	1.76	67.86	9.82
5001 600/8 hrs	0.25	1.06	0.05	0.09	-	19.39	1.59	67.63	9.95
5002 as sprayed	0.16	1.09	0.00	-	2.32	17.13	1.27	67.81	10.22
5002 950/1 hr	0.15	0.82	0.02	-	2.31	17.14	1.21	68.39	9.96
5002 800/2 hrs	0.20	1.08	0.04	-	2.43	16.98	1.10	67.95	10.21
8002 600/8 hrs	0.71	0.99	0.06	-	2.41	16.97	1.17	67.70	9.99
PG-AMP-10 as sprayed	0.14	0.96	0.00	-	2.18	17.92	0.23	67.76	10.80
PG-AMP-10 950/1 hr	0.19	1.39	0.03	-	2.31	18.04	0.18	66.83	11.03
PG-AMP-10 800/2 hrs	0.24	1.29	0.00	-	2.25	17.79	0.24	67.49	10.69
PG-AMP-10 600/8 hrs	0.21	1.28	0.00	-	2.15	17.58	0.32	67.73	10.72

*Nominal alloy composition from [27]

The composition measured is similar to that reported by Schiel [3]. Higher amounts of silicon and aluminum were seen in some samples, however this may be due to contamination with abrasive from the polishing process. Trace amounts of calcium and chlorine were seen in all samples also likely due to contamination. Sulfur content in the 316L powders was not measured as it was masked by molybdenum. The overall samples composition is seen to not vary greatly with heat treatment. This is expected since none of the primary alloying elements have high vapor pressure at the temperatures in question and thus are not expected to vaporize. It is similarly unlikely for significant absorption of substances from the furnace environment to occur aside from some degree of surface oxidation.

While the overall composition is relatively constant, the elemental distribution may change with heat treatment due to solid state diffusion resulting in undesirable phase changes, precipitates or depletion of necessary alloying elements and thus changes in the bulk material properties. Of the alloying elements in stainless steels, chromium is perhaps the most important since it is primarily responsible for the corrosion resistance of the material [27]. Molybdenum also has important benefits for pitting resistance in the 316 alloys (5002 and PG-AMP-10 powder) [27]. Chromium, molybdenum and silicon stabilize the ferrite phase in steels, while nickel and manganese stabilize the austenite phase [38]. Consequently, a change in the distribution of these elements may cause or be indicative of a change in the phase structure. This in turn is likely to effect the corrosion and mechanical properties of the material. The distribution of elements within the sample was determined by EDS mapping, with a typical set of elemental distribution maps shown in Figure 16. Complete maps for each sample are included in the appendix.

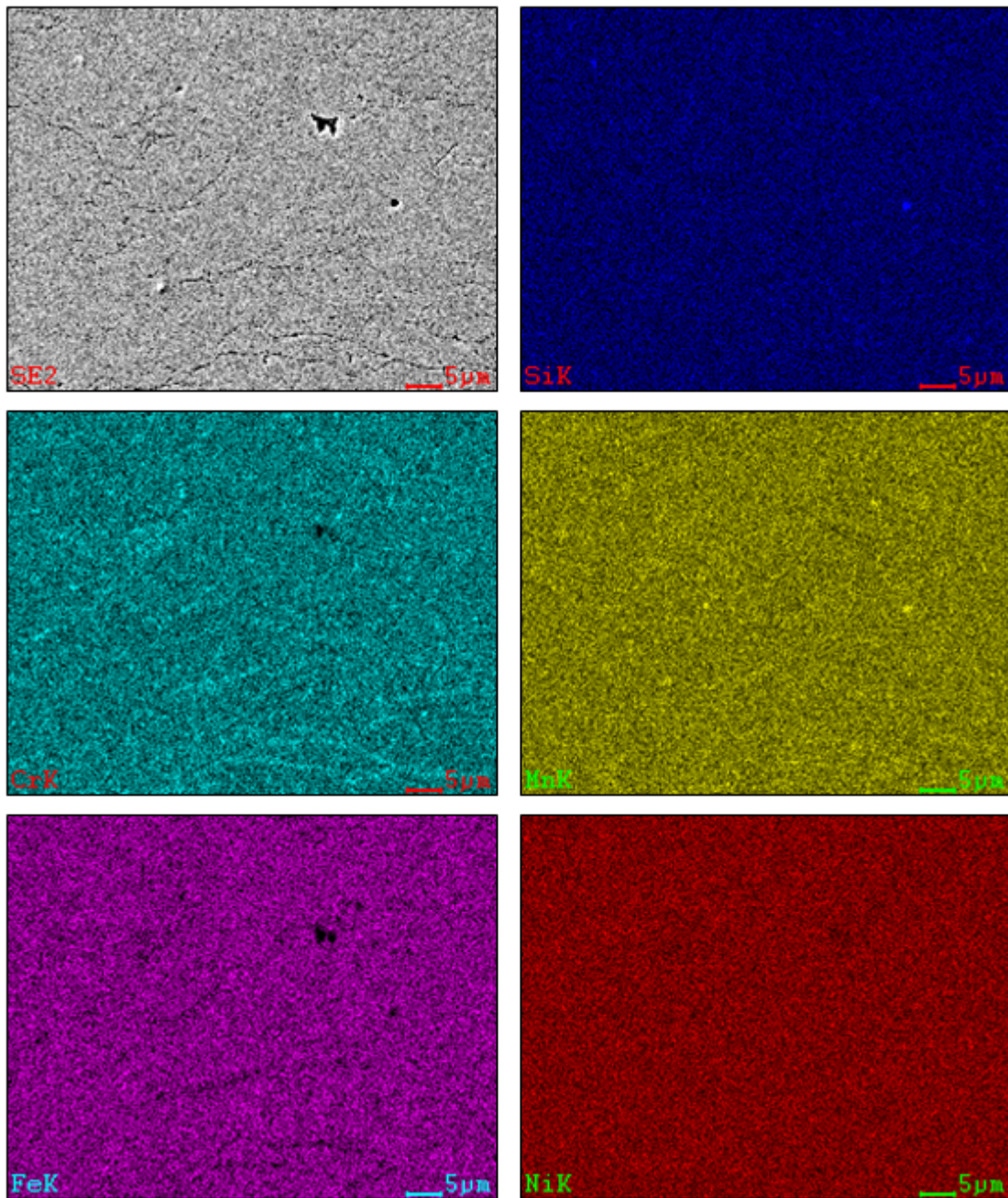


Figure 16. Typical EDS elemental distribution map. 5001 powder, 600°C/8hrs heat treatment.

There are two common detrimental effects caused by chromium redistribution during heat treatment or welding; sensitization and the formation of σ phase iron chromium alloy. The former occurs when chrome carbides form and precipitate. These tend to form preferentially at grain boundaries and result in the depletion of chromium in the area surrounding the precipitate. The primary concern here is corrosion resistance. The chromium carbide precipitate can form a galvanic couple with the surrounding steel and the depletion of chromium in the surrounding area can result in an area of the metal with less than the 12 wt % chromium content associated with the formation of a protective chrome oxide layer and hence the loss of corrosion protection in this area [39]. The concern with the formation of σ phase in contrast is mechanical properties. This phase is a chromium/molybdenum rich intermetallic phase that is very brittle and known to form during heating in the 600–900°C range. Cold working prior to heating and the presence of ferrite are both known to increase the kinetics of σ phase formation [40–42]. Even a small amount of this phase greatly decreases the overall material ductility and toughness.

The distribution of nickel, molybdenum and silicon was found to be relatively even and consistent for all of the powders and heat treatments. In all of the 5001 samples and the 600°C/8hrs heat treatment samples of 5002 and PG-AMP-10 no significant changes were evident in iron, chromium or manganese distribution. The PG-AMP-10 powder shows evidence of uneven chromium distribution in the as-sprayed condition as shown in Figure 17. Schiel reports similar uneven chromium distribution in the raw powder. [3]. The chromium rich areas seen here and in subsequent maps of the PG-AMP-10 powder likely correspond to the ferrite phase. In both the 5002 and PG-AMP-10 samples some evidence is seen of chromium and manganese concentration at particle boundaries in the 800°C/2 hrs and 950°C/1 hr heat treatments. This is most notable in the 5002 powders, and chromium shows the most striking change. This is illustrated in Figures 18 and 19.

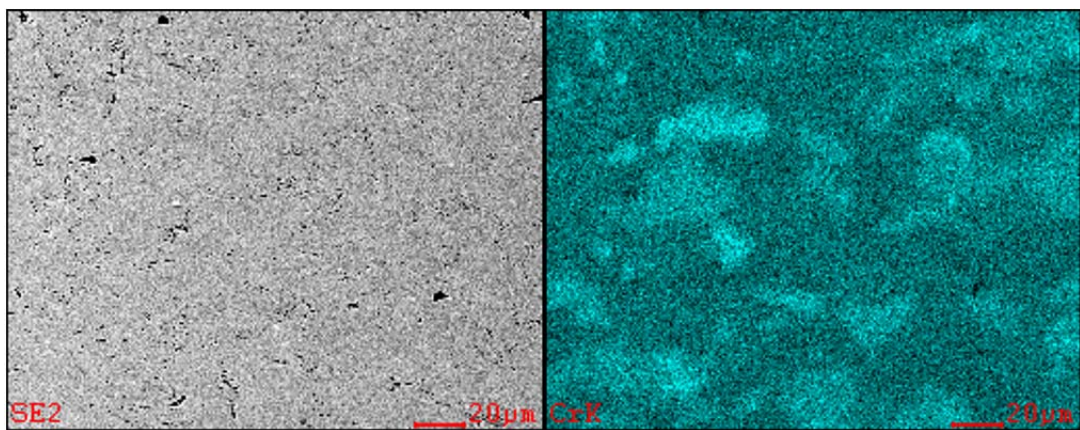


Figure 17. EDS map of as sprayed PG-AMP-10 powder showing chromium rich areas likely associated with ferrite phase grains.

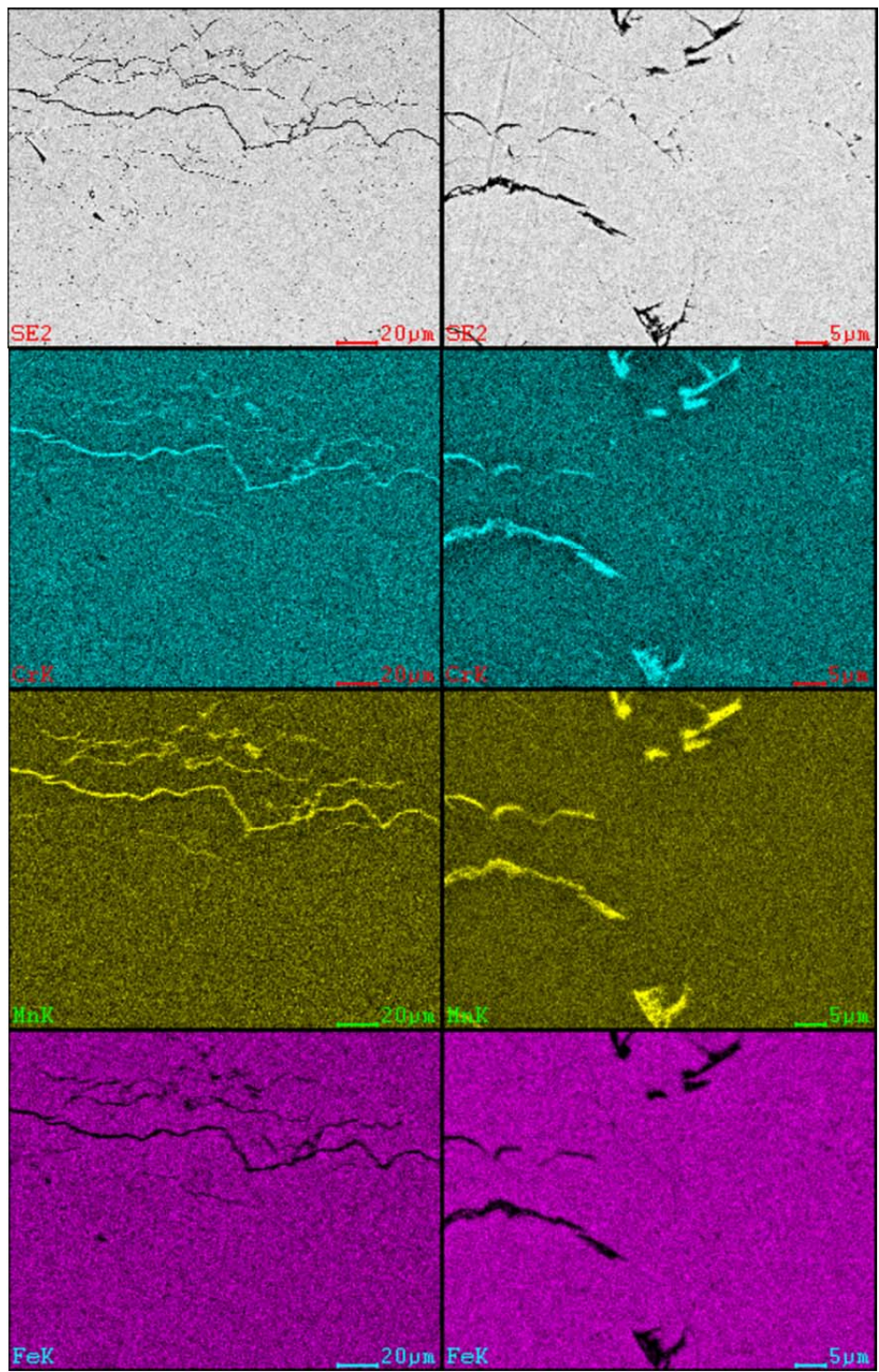


Figure 18. EDS maps showing evidence of elemental redistribution in 5002 powder, 950°C/1 hrs (left) and 800°C/2hrs (right). Note different scale.

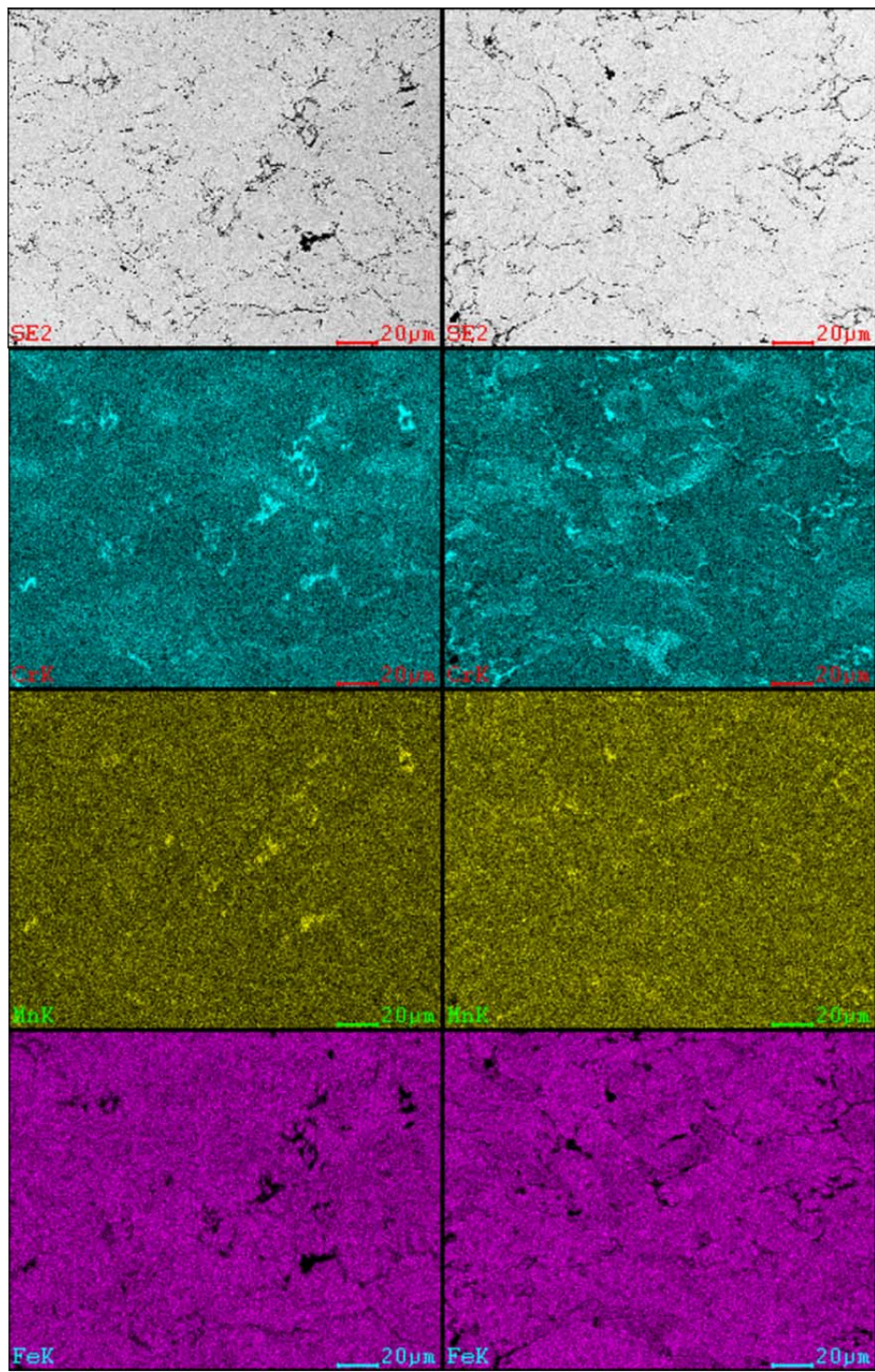


Figure 19. EDS maps showing evidence of elemental redistribution in PG-AMP-10 powder, 950°C/1 hrs (left) and 800°C/2hrs (right).

It is notable however that the striking concentration noted in the 5002 maps shown in Figure 18 was not consistent. Maps were taken at both a high (1.5KX) and low (500X) magnification and in both the 950°C/1 hrs and 800°C/2hrs heat treatments of the 5002 a clear concentration was seen in one set of maps but not the other. Figures 20 and 21 show this occurrence. In both of these samples, the apparent concentration of the elements appears to be associated with porosity in the sample. There is also an apparent complete lack of iron in these regions. Taken together these facts suggest that the apparent concentration seen may be an artifact of the mapping process rather than evidence of an actual elemental redistribution. The PG-AMP-10 powder shows a similar concentration of chromium in porous regions but with more consistency between maps as shown in Figures 22 and 23. An apparent lack of iron in the apparent high chromium regions is seen in these samples as well however, suggesting the same EDS process artifact as is apparent in the 5002 data. Some apparent depletion of iron concentration is to be expected from an increase in chromium concentration, but this should show as a lighter region on the map, not a completely dark region. A large dilution of iron would have to occur to give the very low signal level associated with a completely dark region of the map and this seems unlikely from the apparent chromium increase. It should be noted however that there is also a distribution of chromium in the PG-AMP-10 powder that is likely associated with ferrite grains. These regions are the larger areas that show some apparent concentration of chromium with a lower concentration of iron. There are also regions showing a high concentration of chromium (brighter color) and a corresponding complete lack of iron and visual porosity; these regions are likely artifacts. This is illustrated in Figure 24.

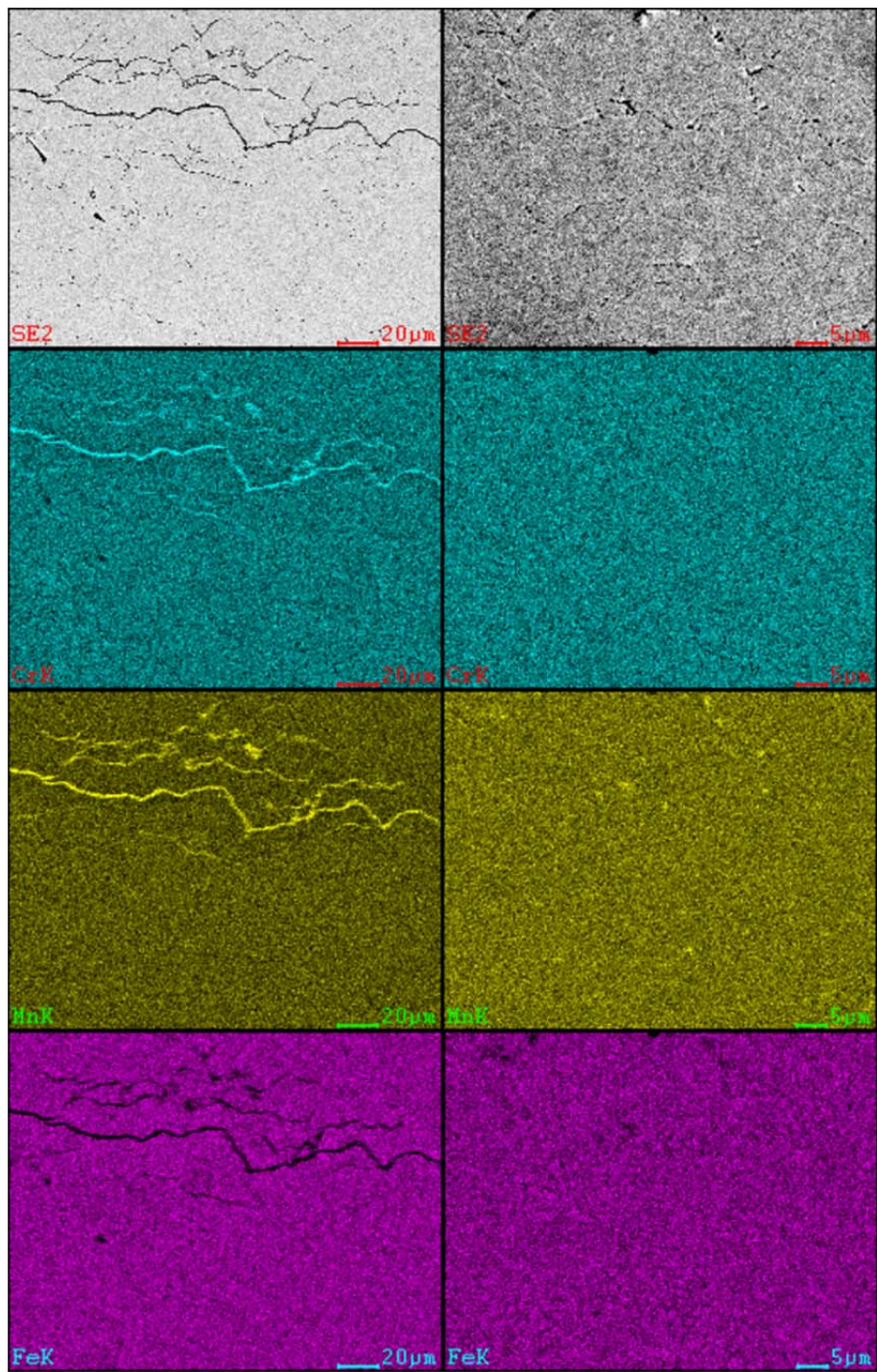


Figure 20. EDS maps of 5002 powder, 950°C/1 hr heat treatment at 500X (left) and 1.5KX (right) showing inconsistency in observed elemental distribution.

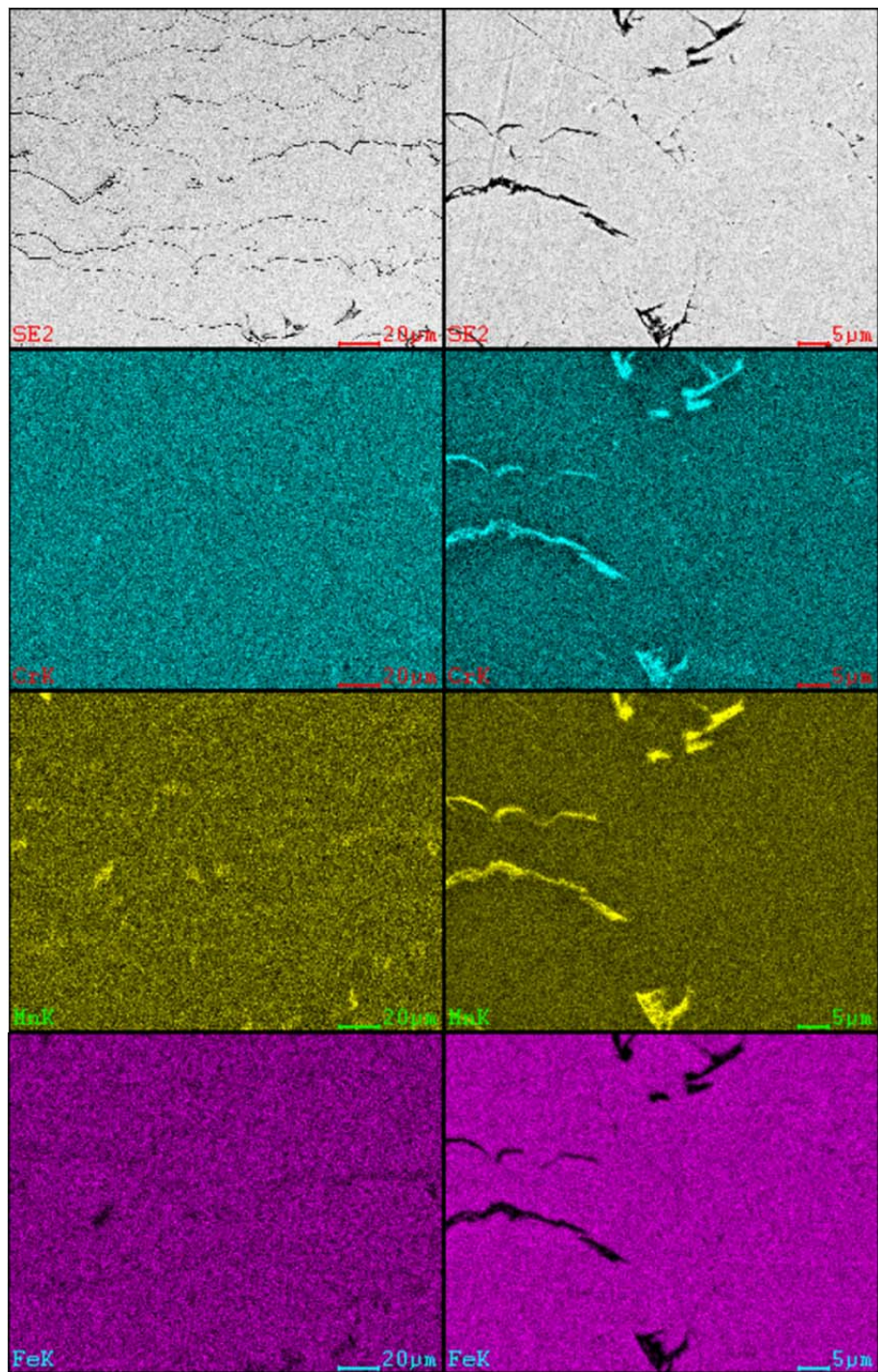


Figure 21. EDS maps of 5002 powder, 800°C/2 hrs heat treatment at 500X (left) and 1.5KX (right) showing inconsistency in observed elemental distribution.

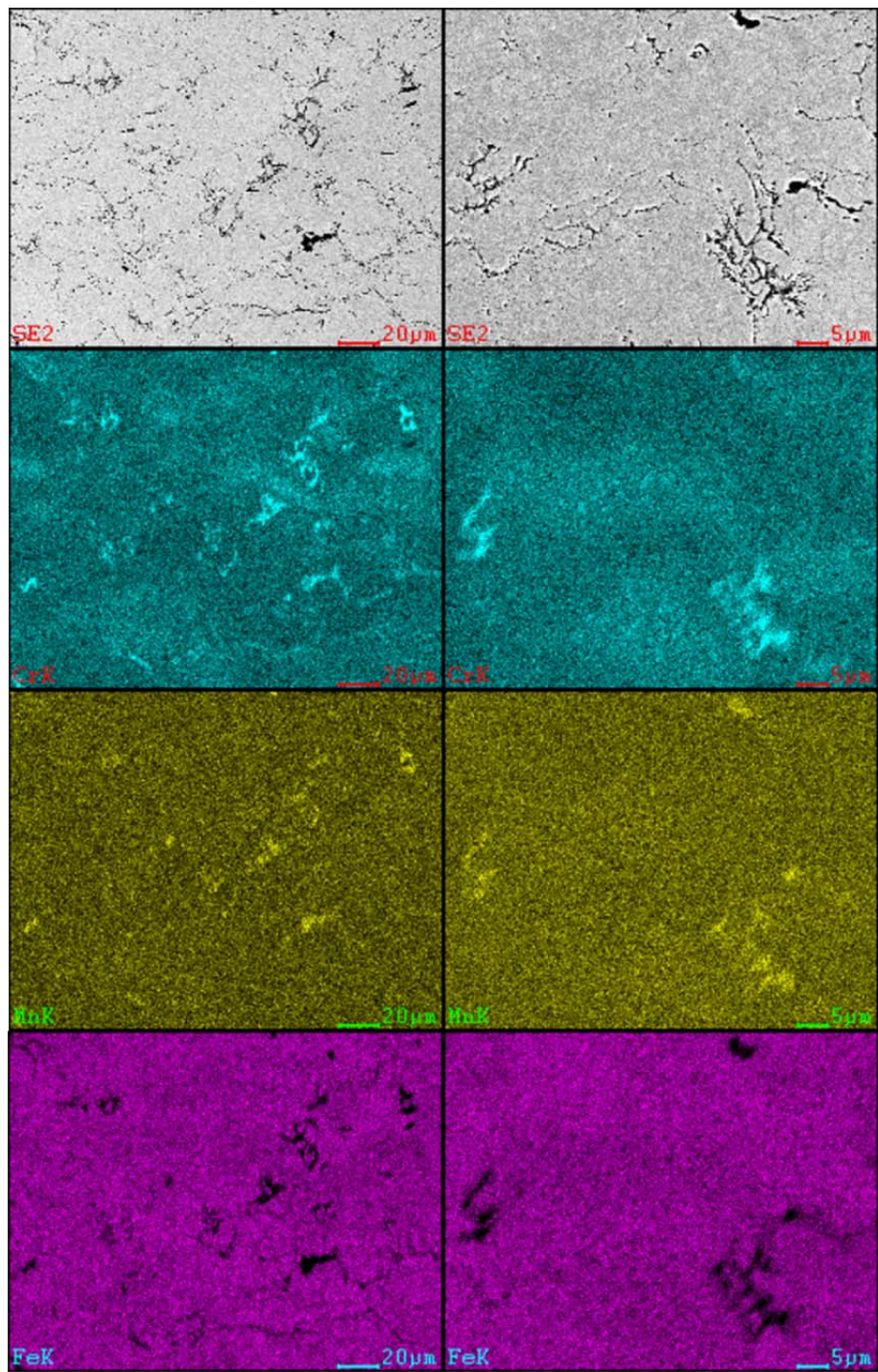


Figure 22. EDS maps of PG-AMP-10 powder, 950°C/1 hr treatment at 500X (left) and 1.5KX (right) showing inconsistency in observed elemental distribution.

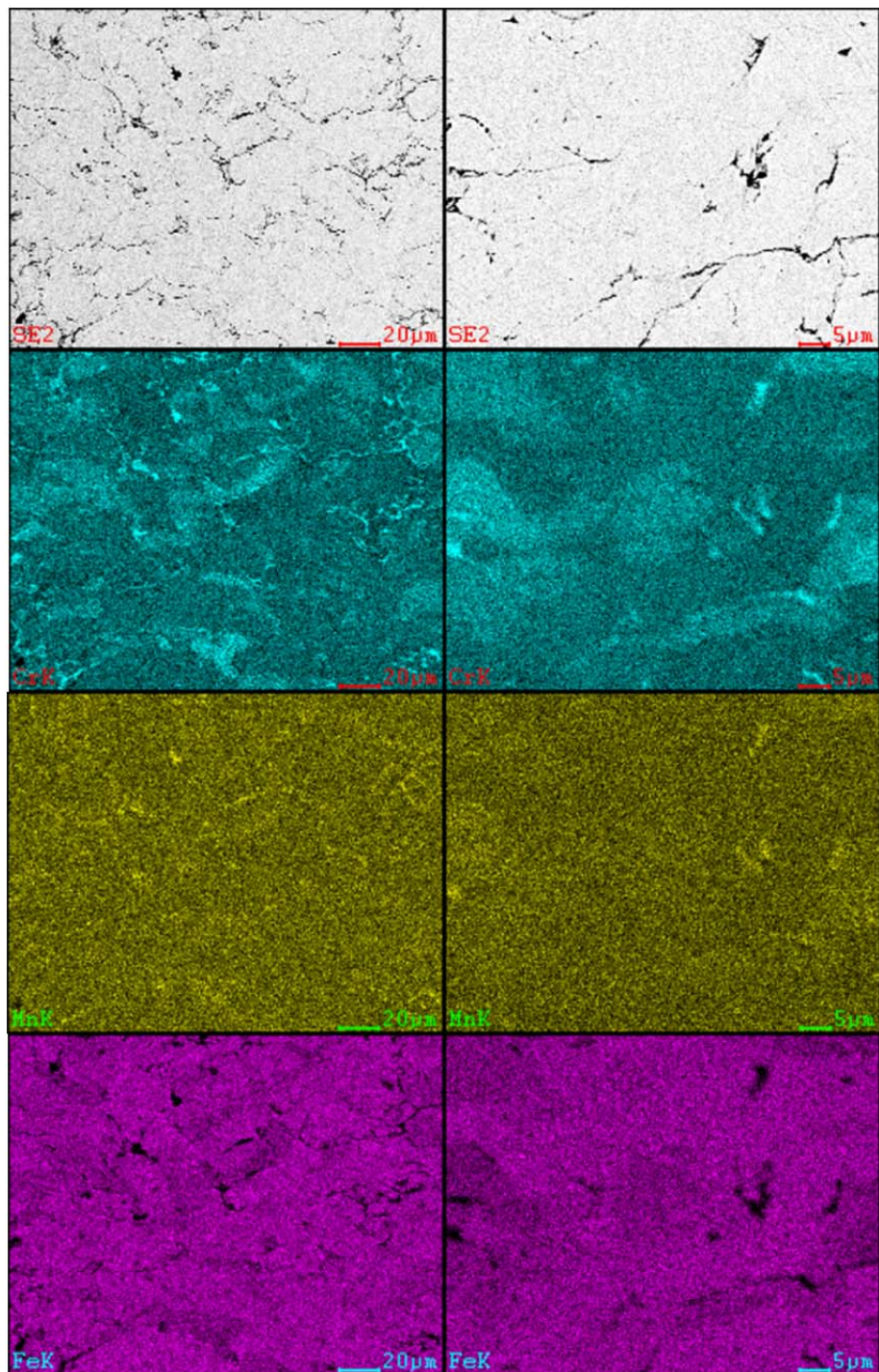


Figure 23. EDS maps of PG-AMP-10 powder, 800°C/2 hrs treatment at 500X (left) and 1.5KX (right) showing inconsistency in observed elemental distribution.

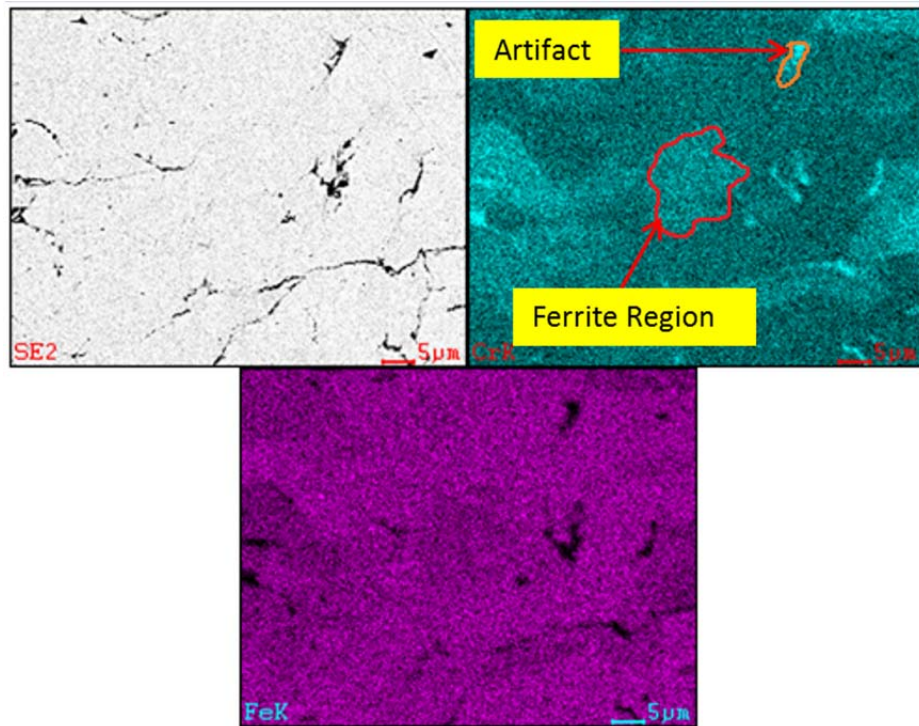


Figure 24. Chromium distribution in ferrite grains and process artifacts in PG-AMP-10 coating.

The σ phase transformation is generally considered to occur in the range of 600–900°C and is known to not occur below approximately 500°C. [39, 40]. This phase also forms preferentially from ferrite, so a high ferrite concentration makes the phase change more likely. At temperatures of 815–925°C regions of σ phase will coalesce reducing the detrimental effect on mechanical properties, and in the 955–1120°C range σ phase will redissolve and transform back to ferrite. σ phase is however generally associated with stainless steels having higher chromium content such as duplex type steels and takes a substantial time to form although a high degree of cold work is known to increase the susceptibility of formation [41, 42].

Sensitization of the metal due to carbide precipitation occurs in roughly the range of 600–850°C [45] though sources give a variety of values from roughly 425°C to 900°C [38, 41, 43]. This is complicated by sensitization being a non-equilibrium phenomena. Sensitization occurs after a certain period, but after a certain additional time desensitization occurs neutralizing the detrimental effects. On a microscopic scale this

reflects the differential between the diffusion rates of carbon and chromium atoms. Sensitization initially occurs as a result of chromium carbide precipitation. The relatively quick diffusion of carbon atoms in the steel matrix results in concentration and favors formation of carbides, however the much slower diffusion of chromium atoms causes a local depleted area around the carbides. With sufficient time however bulk diffusion of chromium will refill this depleted region and return the desired corrosion resistance.

Sensitization is also highly dependent on the carbon content of the stainless steel. A carbon content below 0.03% greatly reduces the susceptibility of the material to sensitization, and this is the origin of the 'L' series stainless steel alloys, ie 304L and 316L [38]. All of the powders and the substrate used in this work are this type of material and are specified to have less than 0.03% carbon. Both the 5001 and 5002 powders in fact have significantly less than this with manufacturer specified carbon content of 0.014 and 0.017%, respectively [3]. The effect of lower carbon concentration is shown in the time-temperature curve in Figure 25. Even at the optimal temperature, it can be seen that nearly 10 hours is required for sensitization in a steel with 0.03% carbon, and over 100 hours for one with 0.019%. Notably, this curve is for a 304 stainless alloy so it is only applicable to the 5001 powder. Available literature suggests that all of the austenitic type steels follow similar patterns of behavior however. [38, 41–42, 44–46].

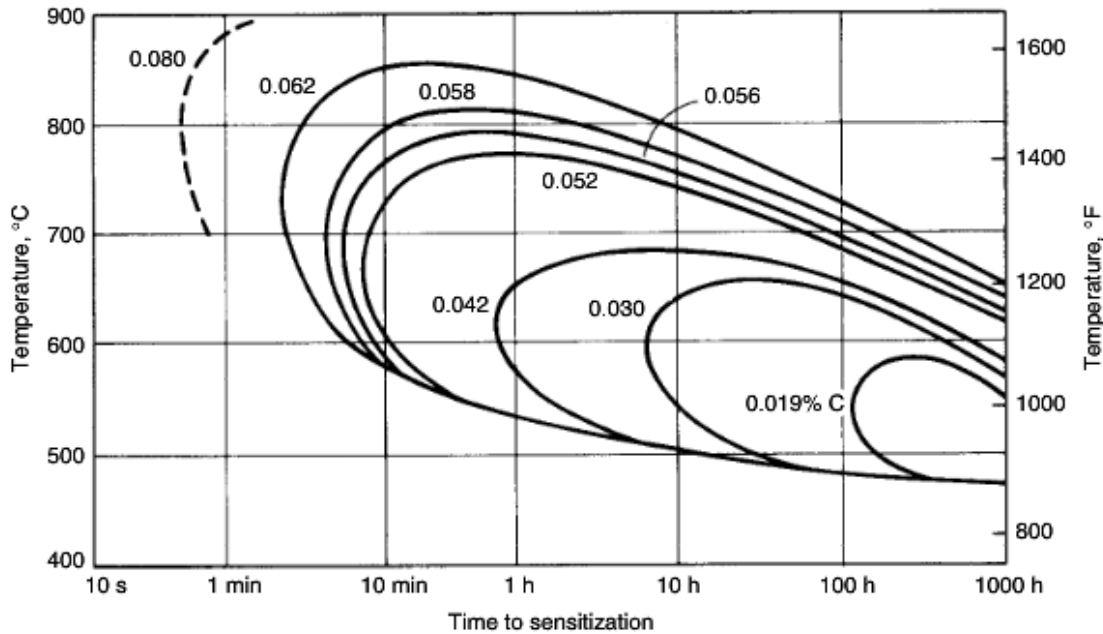


Figure 25. Time-Temperature sensitization curve for 304 stainless steel alloy with varying carbon contents. Source: [41].

In contrast to most literature however, a study conducted by Atanda et al. [47] specifically on 316L sensitization did find evidence of sensitization at times and temperatures that would not be expected to produce this effect. Specifically, chromium depleted zones associated with sensitization were found in 316L steel heat treated for 2 hours at 800°C. This study did not test any temperature lower than 750°C; at this temperature sensitization was very noticeable after a 2 hour heat treatment and not present after 8 hours. This suggests that a treatment of 600°C for 8 hours likely experiences some degree of sensitization. Testing at 950°C in this study found minor sensitization after 30 minutes of heat treatment and none after an hour.

With this background, it can be expected that sensitization is likely to happen in the 600°C/8 hrs heat treatment and possibly in the 800°C/2 hrs treatment. σ phase may occur in the 800°C/2 hrs and 950°C/1 hr heat treatments as well. Time constraints prohibited a complete investigation into these changes, however high magnification inspection of coating grain boundaries was conducted using SEM microscopy and EDS analysis. Both sensitization and σ phase transformation would be expected to show a high

chromium concentration that could be identified by EDS and should have shown as a high contrast region when imaged in the backscatter electron mode. No evidence of either phenomena was seen during examination of samples. A single high nickel particle was found in the 5002 as-sprayed powder. This appears to be a particle of the original powder that formed with high nickel and molybdenum content for some reason.

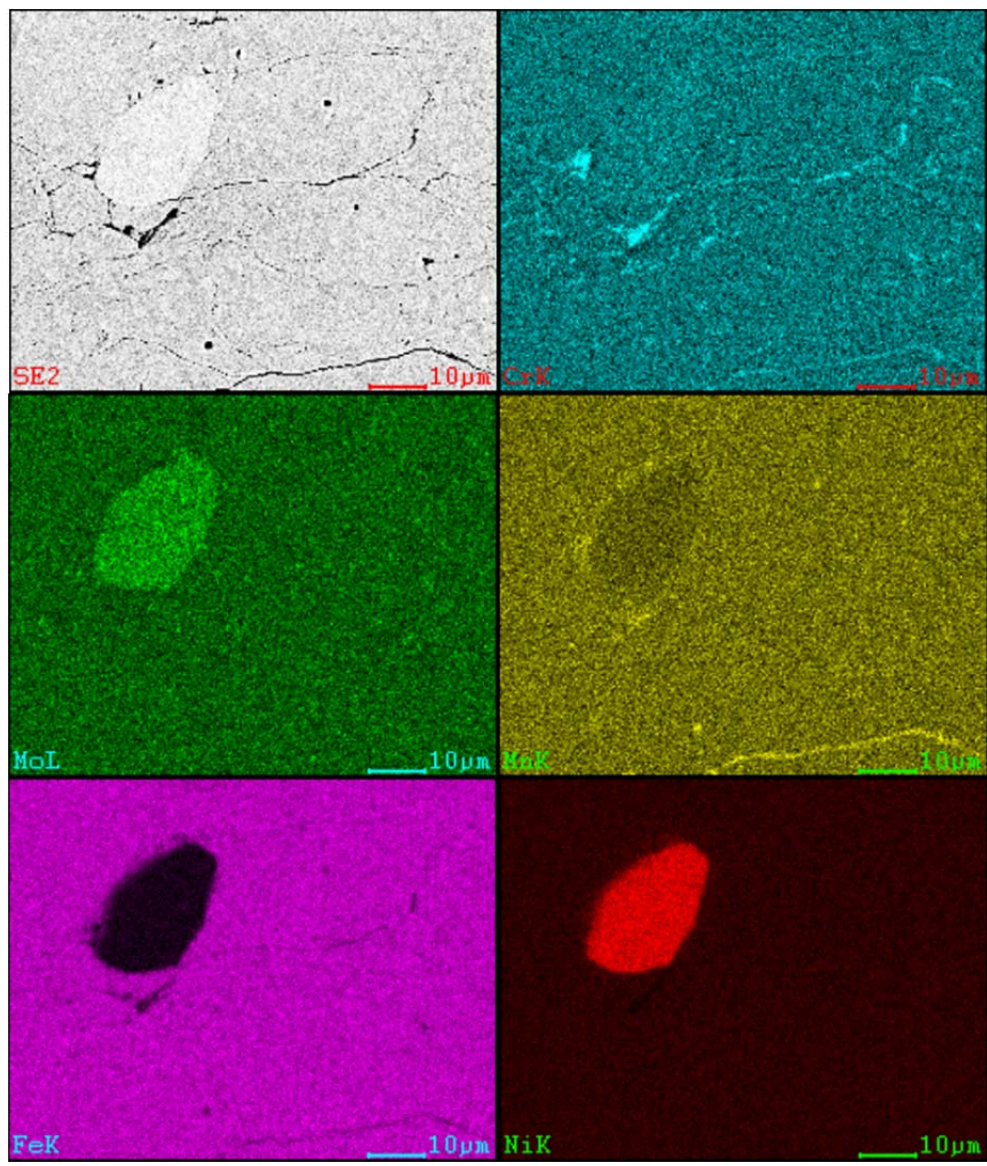


Figure 26. EDS maps of high nickel particle in 5002 as-sprayed powder sample.

It was planned to use EBSD mapping and X-ray Diffraction (XRD) to investigate the grain size and phase distribution in the samples with the objective of determining to what degree the coating recrystallized during heat treatment, the grain size and any phase changes occurring. Schiel found that the 5002 and PG-AMP-10 powders contain roughly 50% ferrite both in the raw powder form and as sprayed while the 5001 is essentially 100% austenite. [3] Mechanical properties are strongly influenced by the grain size, cold working and material phases [30] and corrosion resistance is influenced by cold work and phase, [31] so it is important to characterize any changes in these properties. Austenite is generally more corrosion resistant than ferrite [31] and has desirable properties such as low temperature toughness and weldability [27]. Typically 304 and 316 alloys have only a minimal amount of ferrite with a primarily austenite structure [27]. The high ferrite content of the 5002 and PG-AMP-10 powders is thus rather abnormal for a austenitic stainless steel and is likely due to the manufacturing process used to form the original powder [3]. The gas atomization process used to produce the powders results in a very high cooling rate which promotes the formation of an abnormally large amount of ferrite [48]. EBSD mapping is a technique using the diffraction of backscattered electrons to identify the crystal lattice type, size and orientation in a particular region. By scanning a large area and collecting these patterns a map can be built of the overall grain structure which can be used to find the grain size and the misorientation angle between grains which can be correlated with the degree of deformation of the particles [32]. Unfortunately, despite repeated attempts EBSD data of sufficiently high quality for meaningful analysis proved impossible to obtain in the time available.

X-ray diffraction data was obtained giving some insight into phases changes in the coating. The spectra produced by this process are shown in Figures 27–29. These spectra were then assessed with the known BCC and FCC crystal diffraction patterns to attempt to quantify the austenite (FCC) and ferrite (BCC) phase balance. In addition to the expected FCC and BCC iron peaks, several additional peaks are noted. These are believed to originate from the aluminum sample holder used in the instrument. The high cost of helium spray gas and large number of samples resulted in the decision to use relatively small sample sections for these measurement with the unexpected result that

the sample holder was also measured during XRD. The distance from the sample holder to the focal point of the XRD system results in a positional shift of these aluminum peaks from the normal spectra of aluminum. This effect also likely resulted in the shifts seen in the iron peaks between samples as the thickness of the samples used was not consistent causing a degree of positional shift in each of these. Neither of these effects change the relative ratio of the BCC iron peak intensity to that of FCC iron however, so the phase balance of the material can still be determined [49]. The phase composition obtained from this analysis is tabulated in Table 10 along with the results reported by Schiel for as-sprayed coatings [3].

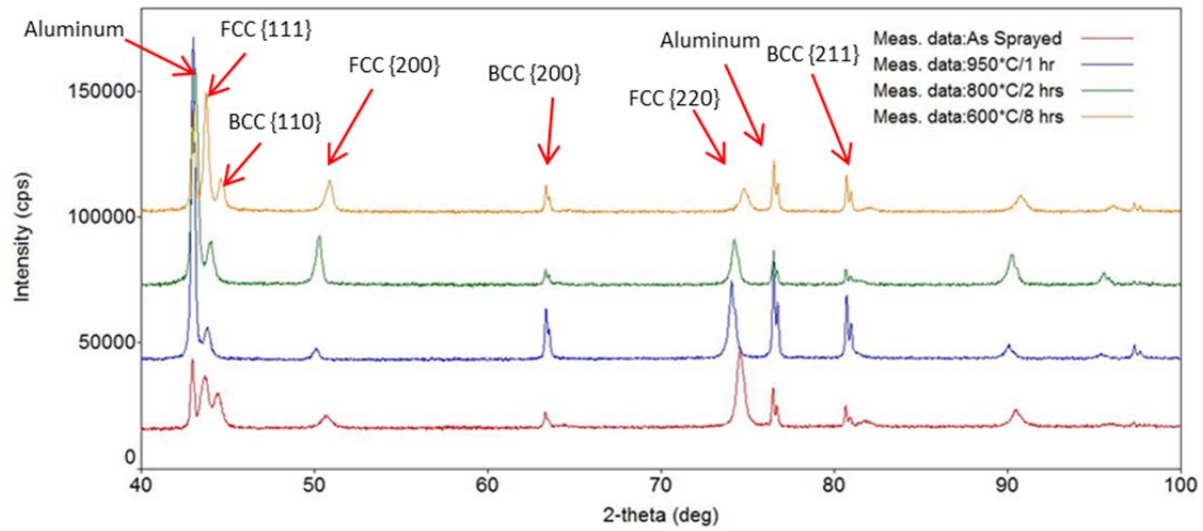


Figure 27. X-ray diffraction spectra from 5001 powder samples.

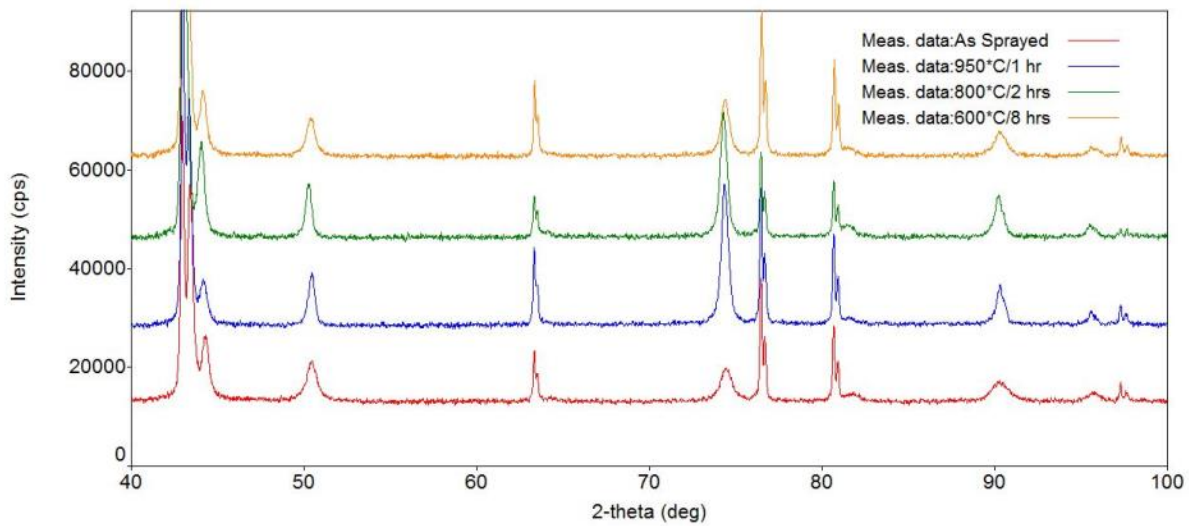


Figure 28. X-ray diffraction spectra from 5002 powder samples.

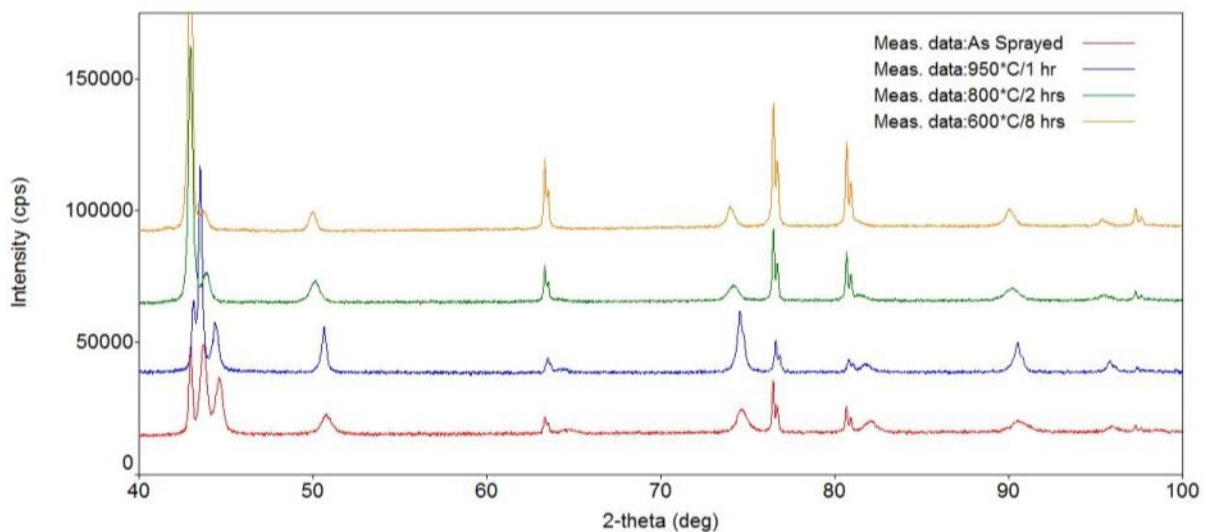


Figure 29. X-ray diffraction spectra from PG-AMP-10 powder samples.

Sample	Ferrite fraction (%)	Austenite fraction (%)
5001, Schiel	1.0	99.0
5001, As sprayed	4.9	95.1
5001, 600°C/8 hrs	18.6	81.4
5001, 800°C/2 hrs	17.6	82.4
5001, 950°C/1 hr	16.0	84.0
5002, Schiel	48.0	52.0
5002, As sprayed	18.9	81.1
5002, 600°C/8 hrs	25.7	74.3
5002, 800°C/2 hrs	15.0	85.0
5002, 950°C/1 hr	10.0	90.0
PG-AMP-10, Schiel	58.0	42.0
PG-AMP-10, As sprayed	30.8	69.2
PG_AMP-10, 600°C/8 hrs	36.3	63.7
PG_AMP-10, 800°C/2 hrs	22.6	77.4
PG-AMP-10, 950°C/1 hr	9.5	90.5

Table 10. Coating phase composition as determined by X-ray diffraction.
Data reported by Schiel [3] included for comparison.

This data shows that substantial changes in the phase balance occur with heat treatment. The 5001 powder shows a trend towards an increased ferrite fraction roughly consistent at 15% in all three heat treatments. The 5002 and PG-AMP-10 powders show less of a clear trend with the 600°C/8 hrs treatment in both cases showing an increase in ferrite over the as-sprayed sample, and the 800°C/2 hrs sample having the lowest ferrite content. Notably, the measured as-sprayed phase balance differs significantly from Schiel's result for both of these powders. From a theoretical point of view, these alloys should be essentially 100% austenite. Ferrite formation results from non-equilibrium cooling, impurities, carbon contamination or other similar non ideal conditions [48]. The substantial ferrite content in the initial powder is thus likely a result of the manufacture process and with heat treatment the ferrite content should greatly diminish. The difference may be due to the heat treatment being insufficient for a full equilibrium condition or possibly from additional unaccounted for ferrite stabilizing elements. It is

noted that the PG-AMP-10 powder shows evidence of chromium distribution likely associated with ferrite grains in all three heat treatments. This distribution is most clearly evident in the as-sprayed samples, and least in the 950°C/1 hr heat treatment. It is suggested that this distribution of chromium stabilizes the ferrite phase locally, and the relatively slow diffusion of chromium results in this uneven distribution and hence higher ferrite content remaining after all 3 treatments. The lowest observed ferrite content in this powder is in the 800°C/2 hrs treatment however, which seems to have a similar chromium distribution to the 950°C/1 hr and 600°C/8 hrs samples which both have a significantly different observed ferrite fraction. The chromium distribution of all four of the PG-AMP-10 samples is shown in Figure 30.

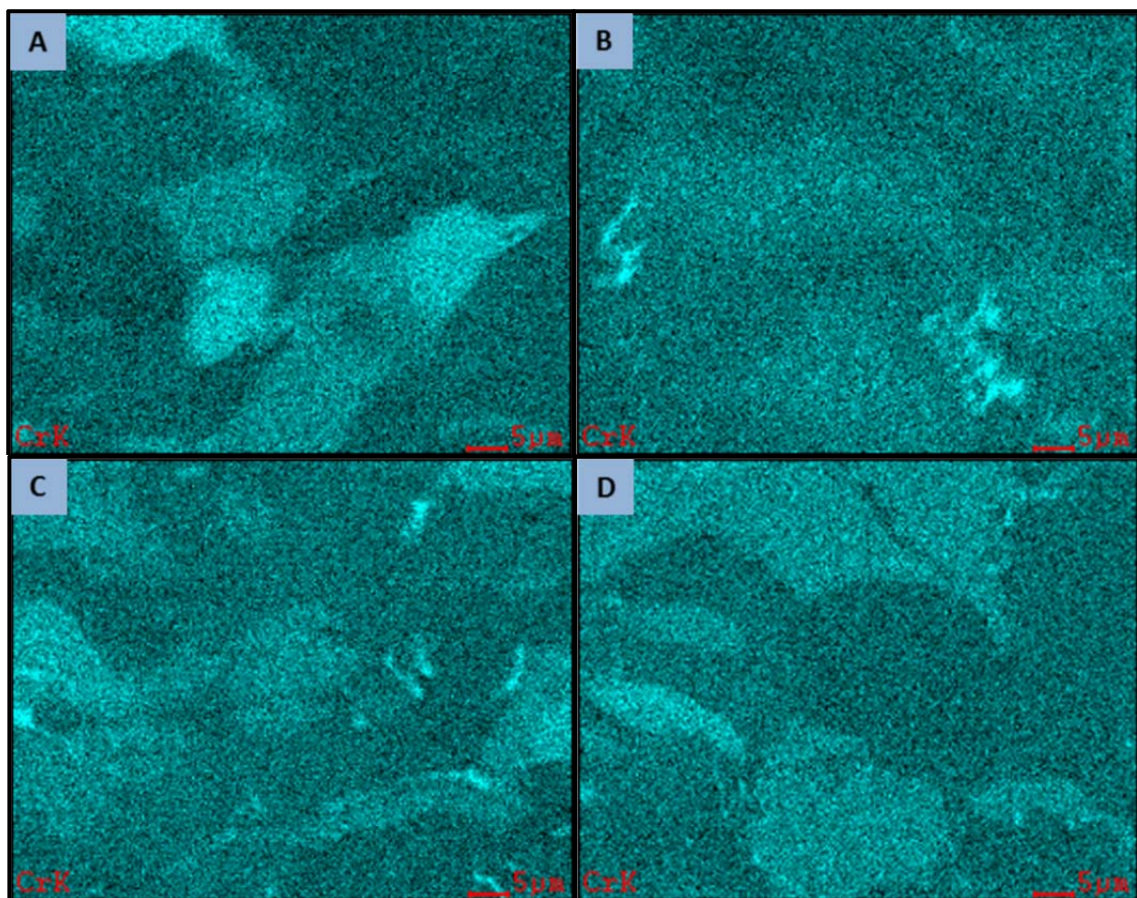


Figure 30. EDS maps of chromium distribution in PG-AMP-10 powder samples showing high chromium areas likely associated with ferrite grains.
 (a) as sprayed; (b) 950°C/1hr; (c) 800°C/2hrs; (d) 600°C/8 hrs.

Examination of SEM images allows some qualitative examination of grain size and distribution. This can be seen in Figures 31 and 32. Both the 950°C/1 hr and 800°C/2 hrs samples appear to show grain growth in all 3 samples although it is most clearly seen in the 5001 950°C/1 hr sample.

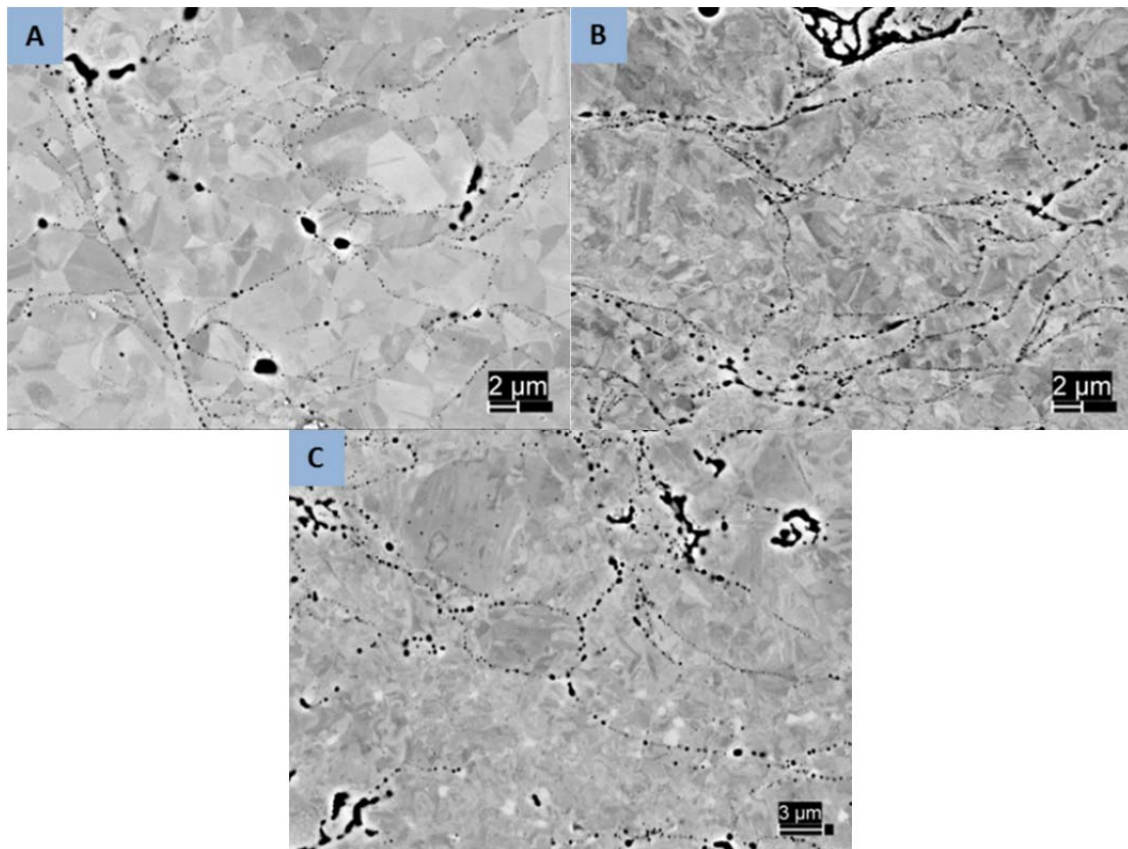


Figure 31. Backscatter micrographs of 950°C/1 hr heat treated samples showing evidence of recrystallization and grain growth. Note annealing twins visible in 5001 and 5002 samples. (a) 5001; (b) 5002; (c) PG-AMP-

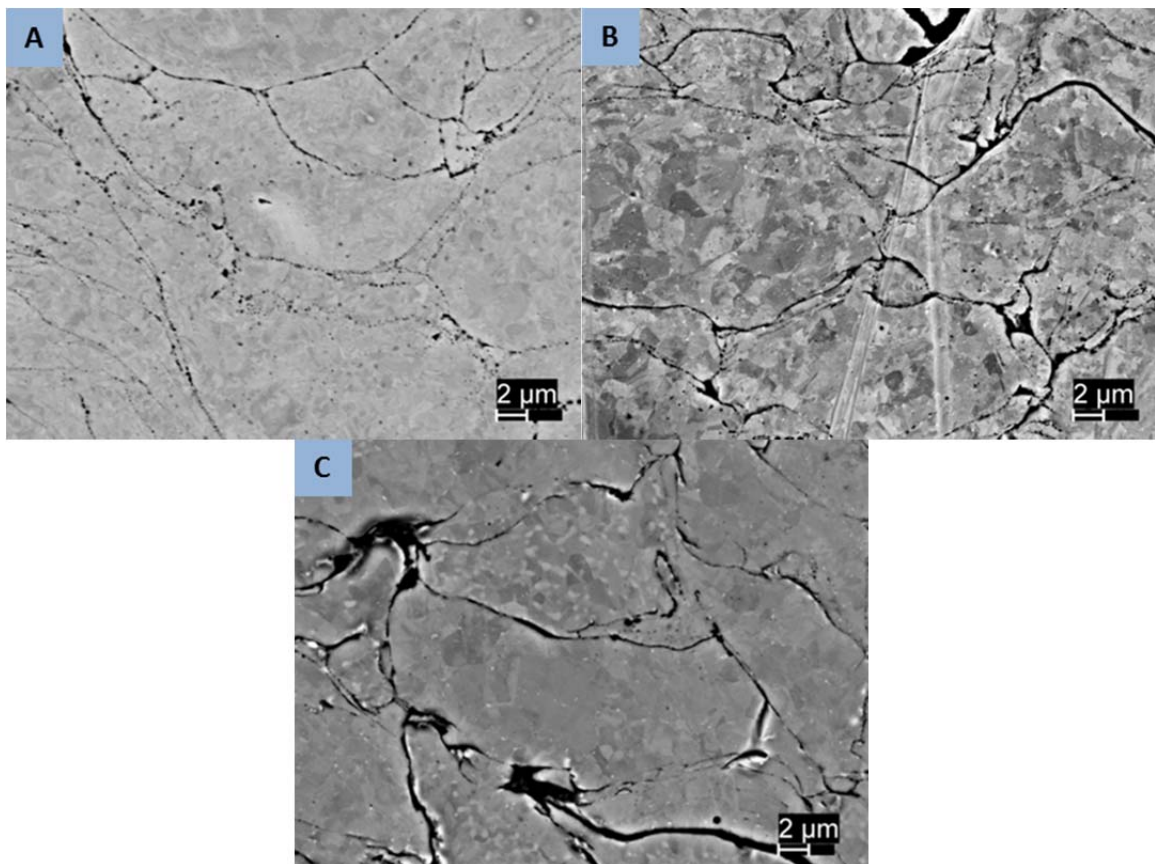


Figure 32. Backscatter micrographs of 800°C/2 hrs heat treated samples showing evidence of recrystallization and grain growth. (a) 5001; (b) 5002; (c) PG-AMP-10

Microhardness testing was also conducted to investigate the coating structure. There is a direct relationship between the measured hardness of the material and its tensile strength, degree of plastic deformation and ductility with a higher hardness value associated with a higher degree of deformation and tensile strength but lower ductility [30]. The as-sprayed coating is known to be quite hard due to a very high degree of plastic deformation caused by the spraying process [3]. It is expected that heat treatment will soften the material due to recovery and recrystallization of the microstructure. The results obtained from micro hardness measurements of coatings are shown in table 11 along with results obtained by Schiel for as-sprayed coatings. This is also shown graphically in figure 33.

Table 11. Average coating hardness. Results from Schiel [3] included for comparison.

Sample	Average Hardness (HV)	Std Deviation
5001, Schiel	317.0	19.0
5001, As sprayed	382.7	34.0
5001, 600°C/8 hrs	345.3	22.6
5001, 800°C/2 hrs	232.2	27.9
5001, 950°C/1 hr	275.7	23.5
5002, Schiel	314.0	44.0
5002, As sprayed	334.5	45.1
5002, 600°C/8 hrs	326.9	20.7
5002, 800°C/2 hrs	343.9	46.0
5002, 950°C/1 hr	231.5	25.1
PG-AMP-10, Schiel	231.0	23.0
PG-AMP-10, As sprayed	272.1	50.0
PG_AMP-10, 600°C/8 hrs	294.5	65.5
PG_AMP-10, 800°C/2 hrs	224.6	38.1
PG-AMP-10, 950°C/1 hr	184.8	22.1
Substrate, Schiel	172.0	4.0
Substrate, non-treated	170.1	6.0
Substrate, 600°C/8 hrs	166.9	6.6
Substrate, 800°C/2 hrs	167.4	4.9
Substrate, 950°C/1 hr	173.5	5.4

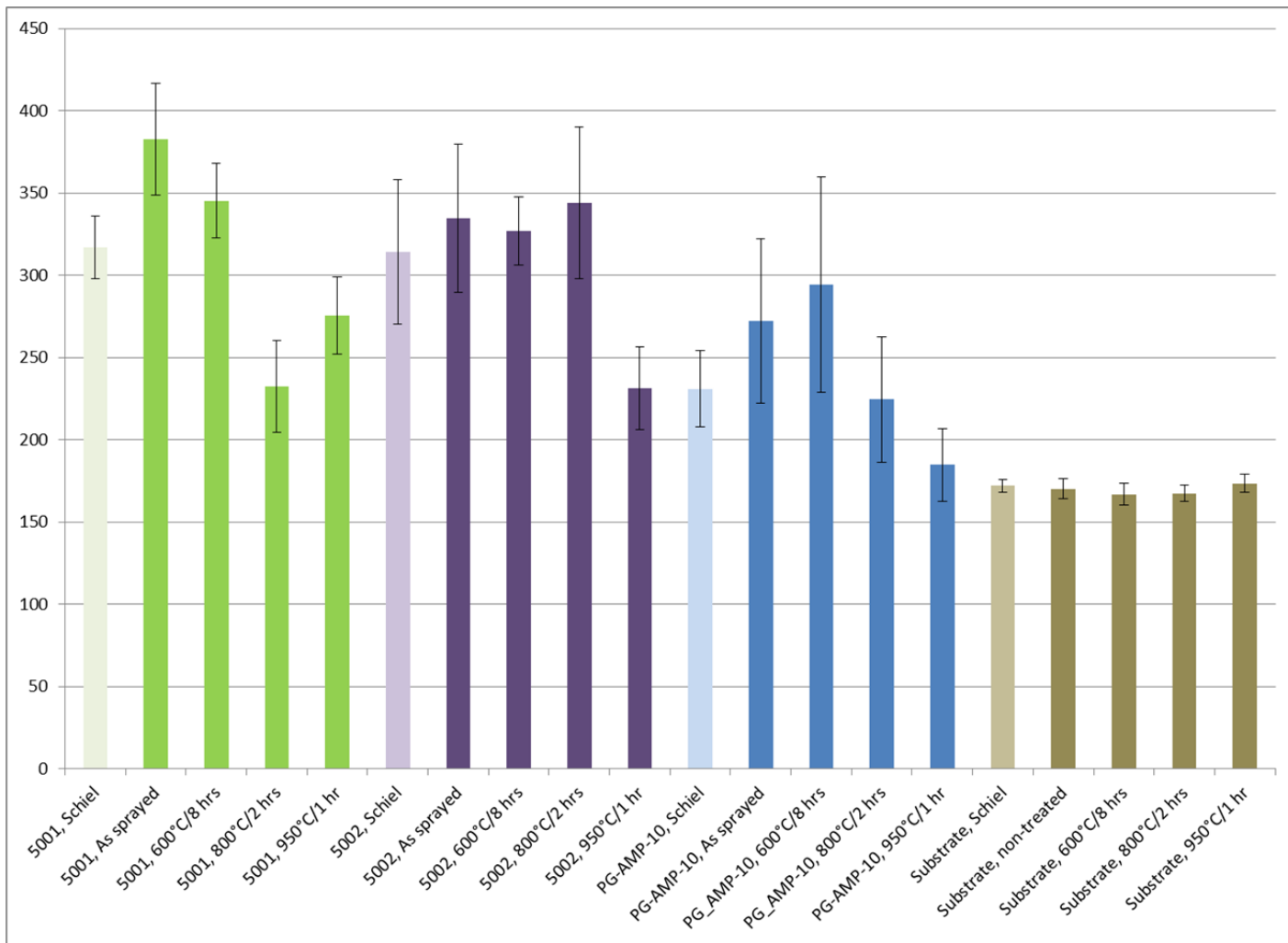


Figure 33. Average coating hardness. Results from Schiel [3] included for comparison.

All of the coatings were found to be harder than the substrate even after heat treatment. Overall a trend is seen towards lower hardness with heat treatment. Both the 800°C/2 hrs and 950°C/1 hr heat treatments clearly reduce the coating hardness in the 5001 and PG-AMP-10 powders while only the higher temperature clearly has the effect in the 5002 powder. In all three powders the 600°C/8 hrs treatment has little effect. This suggests that the recrystallization temperature for these coatings lies somewhere between 600°C and 800°C. Micrographs of the sample microstructure as shown in figures 31 and 32 appear to show that in at least the 5001 powder, the 950°C/1 hr samples have a larger grain size than the 800°C/2 hrs samples which would be expected to result in a lower hardness measured in the 950°C/1 hr samples contrary to what is actually seen. This suggests that there may be a more complex microstructure in these samples than is evident in the micrographs although the hardness data obtained has sufficient scatter that this difference may simply be an artifact of measurement error.

Notably, the hardness measurements have substantial deviation particularly in the PG-AMP-10 powder. This may be a result of the different phase grain structure present in this powder. In all of the samples the porosity of the coating is a significant source of potential error. Care was taken to avoid taking measurements in an area of large scale porosity as much as possible as this would lead to an artificially low hardness measurement, however this was not always possible especially in the PG-AMP-10 powder. Further, microscale porosity would also cause erroneously low hardness values and is much more difficult to avoid.

THIS PAGE INTENTIONALLY LEFT BLANK

IV. CORROSION TESTING OF COLD SPRAYED AUSTENITIC STAINLESS STEEL POWDERS

A. INTRODUCTION

Investigation of the corrosion properties of cold spray coatings was conducted using salt spray (fog) chamber testing and electrochemical polarization testing. Salt spray (fog) testing is the oldest and most widely used laboratory cabinet test used to characterize corrosion resistance of material [50]. This type of testing provides a simple and reliable method to provide information on the overall corrosion behavior of a material in a laboratory environment. The material to be tested is placed in a controlled environment with exposure conditions selected to exaggerate certain corrosion conditions. The salt fog chamber provides an atmosphere of salt (NaCl) fog at an elevated temperature which simulates marine atmospheric exposure but with an accelerated corrosion rate. This test method does not directly correlate to corrosion in service, but can be used as a valid accelerated laboratory test of relative corrosion resistance [50]. The test is governed by ASTM standard B117.

The chamber operates using humid heated air expanding through a nozzle to entrain and vaporize salt water maintaining a saturated salt fog atmosphere in the chamber. The temperature of the chamber is maintained at $35 \pm 2^\circ\text{C}$ ($95 \pm 3^\circ\text{F}$) and a fan is fitted to continually circulate the air/salt fog. The air used to atomize the salt fog is first passed through a humidification tower where it is bubbled through heated water to heat and humidify the air. This tower is typically maintained at a higher temperature so that cooling of the air upon expansion through the nozzle results in a final temperature close to the desired environmental temperature in the chamber. Typical settings are $46\text{--}49^\circ\text{C}$ ($114\text{--}121^\circ\text{F}$). This method of testing provides an environment with a high concentration of chlorine ions and is hence well suited to general characterization of resistance to pitting corrosion as well as general overall corrosion [51].

Uniform overall corrosion is typically quantified by measuring the overall mass loss of the sample [52]. The raw numeric value measured with a balance can be combined with the sample surface area to give a normalized mass loss which is typically reported.

With knowledge of the material density the mass loss can be expressed as a corrosion rate, commonly in MPY (mills per year) or the expected overall loss in the thickness of the sample in 1 year of exposure. This measurement does not account for pitting damage accurately however, as pitting is characterized by generally small localized areas of damage which can reach a sufficient depth and size to lead to local failure long before measurement of simple mass loss would predict failure. In the use of cold spray coatings for corrosion protection of a base metal this is an especially significant concern as a pit reaching the base metal would potentially have catastrophic effects since the base metal is commonly anodic to the coating and the small base material area would suffer rapid corrosion due to concentration effects from the large exposed coating area [26]. The measurement of pitting corrosion is thus critical. Unfortunately it is difficult to definitively measure pitting in a qualitative manner. Traditionally the number and size of pits on a sample was measured manually using an optical microscope and a grid [26]. This is time consuming and subjected to error however. Modern technology has allowed the use of optical profiling methods to automate this measurement, although this still requires a degree on interpretation. The depth and cross section of pits is also critical to measure, as pits may form with a variety of shapes and sizes not readily visible from surface observation [26]. Depth can be measured to some degree with optical profiling methods, but the only definitive methods are destructive and involve either repeated surface machining followed by optical examination or the preparation and examination of numerous cross sections. For this work the optical profiling method is used for measurement and the error inherent in this accepted.

Optical profiling is done using interference microscopy and is functionally very similar to a conventional optical microscope [53]. The difference between the two lies in the use of a beam splitter in the objective lens on the profiler such that a part of the light is reflected off the sample and part off a fixed optically flat reference mirror. When the distance between the splitter and a section of the samples is the same as that from the splitter to the reference mirror, a destructive interference pattern will be formed in the resolved image in those regions of the image corresponding to the regions of the sample having that distance from the objective. By scanning the objective vertically and

monitoring the locations where an interference pattern is seen in the final image a profile of the surface can be constructed. Using a computer system this process can be automated and controlled to high accuracy, giving an accurate and reproducible surface profile measurement system. Like a common optical microscope, the area that can be scanned is inversely proportional to the magnification. Consequently, imaging a large area at high magnification can only be conducted by taking multiple individual exposures and combining them into one overall profile. This is known as a ‘stitched’ profile. A difficulty can arise in this process if the sample surface is not perfectly flat as any variation in the overall surface will be tracked as a deviation from the reference plane. This can be mitigated to a degree by configuring the system to automatically focus prior to each individual measurement as this will recalibrate the reference plane for each measurement to the base plane of the sample in that region. An additional issue is the limited range of sensitivity in the sensor system used when trying to examine a surface with regions of varying reflectivity. A light level calibration sufficient to measure less reflective regions will be overwhelmed by more reflective ones, and one preventing saturation in high reflectivity regions may not pick up adequate signal from less reflective areas. For examination of corrosion this problem occurs in areas with less reflective corrosion products on the sample and regions with limited lighting such as the bottom of pits. This method was previously demonstrated in the study of pitting corrosion at NPS by R. Johnson [54].

Electrochemical polarization testing examines the corrosion behavior of a material by controlling the electrical potential applied to the substance in a controlled environment and measuring the current that results from a given polarization [55]. This current is a direct measurement of the number of electrons exchanged in the electrochemical reaction occurring on the material surface and hence the amount of material that is dissolved by the corrosion reaction. By varying the potential applied, a map of the behavior can be generated, and an estimate can be made of the resistance of the material to corrosion. The electrochemical potential applied to the material in service is a function of the environment and conditions it is exposed to, so a direct conversion of polarization behavior to an in service corrosion rate is difficult, however general behavior

in a specific solution can be measured and this can be used to judge likely performance. Specifically, the open circuit potential (OCV) can be determined which is important in assessing a potential galvanic interaction with other materials and passivation/pitting behavior can be determined. Passivation is the fundamental property that allows the corrosion resistance of many families of metals such as the stainless steels. In a material with this type of behavior, very low corrosion rates are observed within a wide band of oxidizing potentials. This is characterized by a sharp change in the corrosion rate at a certain potential. Below this potential the material behaves actively where a small increase in potential results in a large increase in corrosion rate. At the passivation potential, however a large decrease (typically 10^3 – 10^6) in the corrosion rate is noted and this low rate remains constant as the potential is increased for a certain region [26]. Eventually a potential is reached that is strong enough that the corrosion rate again increases. This potential region is known as the transpassive region and the potential at the start of this region is the pitting potential. Passivation behavior is generally explained through the formation of a stable oxide layer on the surface of the material. This layer serves a protective film greatly retarding the kinetics of the electrochemical corrosion reaction. In the presence of a sufficiently strong oxidizing potential however this oxide film breaks down resulting increased corrosion rates. Pitting occurs due to a localized break down of this film [26]. A typical polarization plot showing passivation behavior is shown in Figure 34.

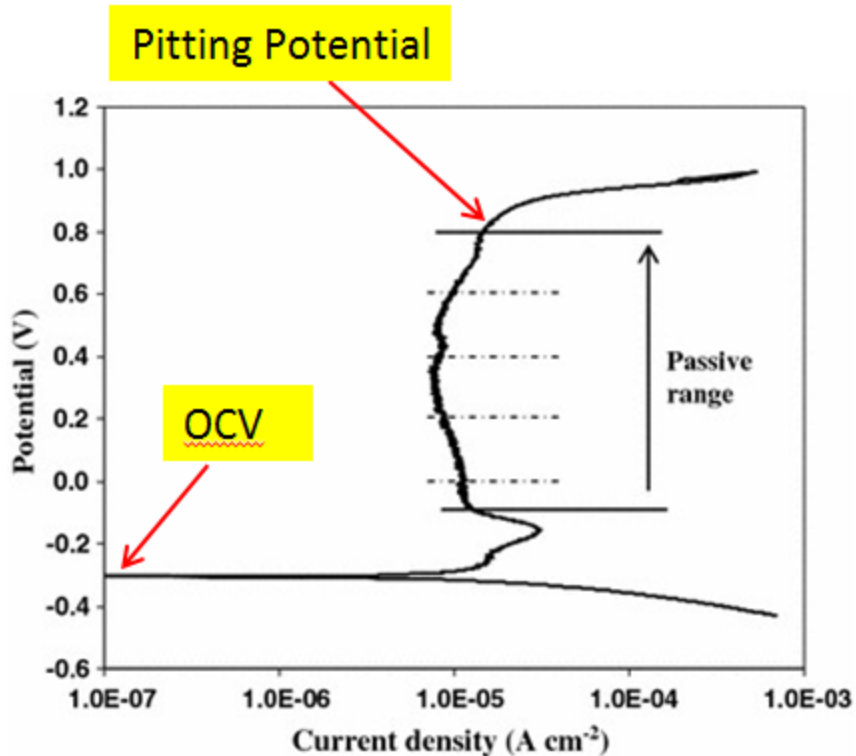


Figure 34. Typical polarization curve showing passivation behavior of 316L stainless steel in 0.05M H_2SO_4 . Adapted from: [56].

The governing standard for polarization testing is ASTM standard G5. The standard testing apparatus consists of special glass beaker with a number of ports. The sample to be tested is held in a holder that is insulated from the electrolyte and configured to only allow a specified sample area to be exposed. A probe with a salt bridge to a reference electrode is set close to but not touching this exposed surface and two or more auxiliary electrodes of a non-reactive metal (typically platinum) are installed as well. The polarizing voltage is applied to the auxiliary electrodes and the reference electrode is used to measure the applied potential at the sample surface. A high precision control system is used to apply the desired voltage and measure the resulting current flowing through the auxiliary electrodes and sample [57]. The apparatus is illustrated in Figure 35.

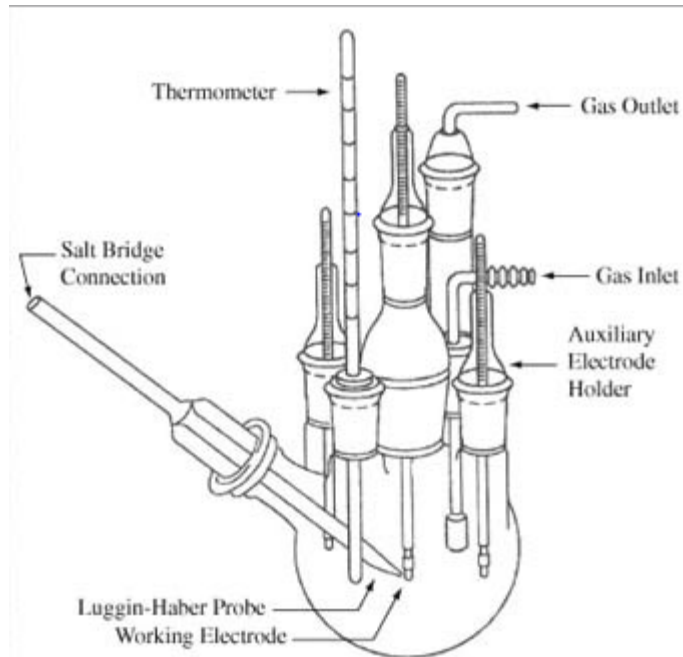


Figure 35. Schematic diagram of a typical polarization testing cell. Source: [56].

B. EXPERIMENTAL METHODS

Samples were prepared using the procedures describing in section (II.C). All salt fog sample substrates were machined to an identical length of 66.7 mm (2-5/8") prior to spraying. Salt fog sample substrates were drilled with a 3.2 mm (1/8") hole at the end opposite from the deposit. This hole was offset 12.5 mm (1/2") from the longitudinal centerline of the substrate and holes were identically located between samples. This offset was intended to ensure that the samples hung at an angle in the fog chamber and prevent standing water on the upper edge of the deposit.

For fog chamber testing, a total of 9 samples were prepared using the 5001 powder along with 6 each of the 5002 and PG-AMP-10 powders. Heat treatments of 950°C for 1 hr and 800°C for 2 hrs were used along with as-sprayed samples. Samples were equally proportioned between treatments for each powder such that a minimum of two samples of each powder with each heat treatment were tested. Three uncoated substrates were also prepared and heat treated identically with the coated samples for a total of 24 individual fog chamber samples. Following heat treatment, the samples were

milled to give a flat deposit surface for measurement. A nominal 12.5 x 12.5 mm (1/2 x 1/2") surface area was attempted, however this was not achieved in all cases as this would have required the removal of an excessive amount of the deposit thickness and left a very thin coating. The surface of the uncoated substrates was milled down expect for a 12.5 x 12.5 mm (1/2 x 1/2") section in roughly the same location as the deposits on other substrates. This was done such that this section was left protruding roughly 0.64 mm (0.025") above the rest of the surface. All samples were then polished to 1200 (P2500) grit using a Buhler automatic polishing machine. Grinding was conducted using a fixed time rather than a qualitative assessment of the surface as would be done for a conventional polishing as the intent was to give a baseline clean flat surface rather than a true polish. Following polishing the deposit thickness was measured. The average coating thickness measured was 0.92 mm (0.036") for the 5001 samples, 0.38 mm (0.015") for the 5002 samples and 1.13 mm (0.044") for the PG-AMP-10 samples.

1. Salt Fog Testing

Corrosion testing was conducted in a salt fog chamber following ASTM specification B117 for 1000 hours. A 5 wt % salt solution was used as specified in ASTM B117, [51] with demineralized water and plain commercial salt being used. The salt used was specified to contain no added anti caking agents or substances other than common table salt, however not chemical analysis was available. The chamber was operated at a nominal 95°F chamber temperature with a 109°F column temperature and 12 psi air supply. The actual temperatures and air supply pressure were checked daily on weekdays during testing. These were observed to vary within the range of 90–95°F for the chamber temperature, 104–108°F for the saturation column and 11–13 psi for the air supply. When initially started the salt fog system did not operate properly, resulting in a period of 60 hours when the chamber was in operation with an atmosphere having a limited salt fog concentration. This was corrected and the initial exposure time is not counted in the exposure time used for evaluation. Samples were suspended from wooden dowels using plastic ‘zip ties’ and hung in the chamber. Samples were verified to not touch each other or the chamber structure when inserted. This is illustrated in Figure 36. The procedure used deviates from ASTM B117 specification in that the pH and salinity of the salt water

used was not measured and there were no collection devices used in the chamber to verify salt fog volume. Visual inspection of the chamber was instead used to verify a visible fog. These deviations were justified due to available equipment and the use of the chamber testing as a qualitative comparative test; any impurities or variation in the fog quality can be assumed to effect all samples equally and hence cause minimal error.



Figure 36. Method of supporting samples in salt fog chamber

Samples were removed once a week for inspection and measurement. This removal was done by groups of six samples with two groups being conducted on one day and the remaining two the next. This was done due to the lengthy time (3–4 hours per group of six samples) required to conduct the full sample measurement process using optical profiling. The time of each group removal and replacement was recorded and the time out of the chamber was accounted for in computation of the total sample exposure time. Each group was removed in the same order so after the first week sample exposure time between examinations was roughly identical across all groups.

Cleaning of samples was conducted by immersion in fresh deionized water placed in an ultrasonic cleaner for five minutes. When completed, samples were visually inspected and if possible any remaining surface corrosion products on the surface were removed by gentle scrubbing with a clean paper towel wetted with deionized water. No attempt was made to completely clean the surface other than the removal of obvious surface deposits that could be easily removed. Samples were immersed in ethanol and

subjected to a further five minutes of ultrasonic cleaning. Samples were then dried with hot air.

Following cleaning and drying, the mass of the samples was measured using a digital balance with an accuracy of 5 mg and photographs were taken of the samples. Pitting and surface corrosion damage was tracked by optical profilometry using a Zygo 'NewView 7100' optical profiling system fitting with a 10X lens. A total nominal area of 16 mm² was scanned during each inspection, generally considering of a 4 x 4 mm square area. Several samples required a 2 x 8 mm or 3 x 6 mm area instead, due to deposit shape or machining damage. Limitation on the field of view of the system required the use of a 'stitching' procedure where 42 separate profile exposures were made and automatically combined into one overall profile. A 20% overlap was used between individual scans and all individual scans were configured to automatically focus prior to scanning to insure a consistent surface baseline despite a surface that was not completely flat or level. An attempt was made to ensure the scan covered the same area of the sample each week. A measurement of the initial sample mass and a profile of the surface was made prior to the start of fog chamber exposure for each sample as well. The initial and first 2 weekly sample profiles were conducted using a scan of 40 µm above and below the reference surface of the sample, and all following measurements used a scan 65 µm above and below the surface.

Upon completion of the nominal 1000 hours of exposure, the samples were cleaned and measured using the above procedure. A substantial amount of corrosion products were observed to remain on the samples after cleaning which hindered measurement of pit depth and was suspected to cause an inaccurately low assessment of the actual sample mass loss. In order to remove these deposits the samples were further cleaned using a solution of 10% nitric acid maintained at 60°C (140°F) as recommended by ASTM G1 and reference literature [26, 52]. Following this cleaning the surface profile and sample mass were again measured.

2. Polarization Testing

Samples were prepared as delineated in section (II.C). Heat treatments of 950°/1 hr and 800°C/2 hrs were used together with as-sprayed samples. A disc type test sample holder was used with a exposed surface area of 1 cm². Test specimens were cut from the sprayed coating using a water jet cutter and polished through 1200 grit silicon carbide grinding paper. Polarization tests were conducted at the University of Alabama corrosion lab using a Gamry PCI 4300–33004 potentiostat system. Testing was conducted in a 5 wt % NaCl solution at 25°C. Samples were allowed to stabilize for 900 seconds prior to measurement of the open circuit potential voltage (OCV). Anodic polarization was conducted beginning 300 mv below the OCV with a scan rate of 0.2 mv per second. Specimens were also cut from the uncoated substrates both with and without heat treatment and were tested similarly.

C. SALT FOG RESULTS AND EVALUATION

The observed mass loss per week is plotted in Figure 37. In generating this plot, the individual measured mass loss from each sample was used with the individual sample deposit surface area to find generate a value for the mass loss in mg/cm² and these values then averaged to give the plotted value. The exception to this is the bare substrate samples for which the entire substrate area was used to find the mass loss and the actual measured value was used as only one sample for each heat treatment was tested. Mass loss from corrosion of the substrate was not accounted for in the sprayed samples as this was assumed to be much lower than the corrosion rate of the coating. Observed mass loss data validates this assumption as shown by the much lower mass loss rate of the uncoated substrates in the plot. Notably, this plot does not include the mass loss determined following cleaning of the samples in nitric acid, only the weekly measurement after cleaning in deionized water and ethanol. The mass loss measured after cleaning samples with 10% nitric acid is shown graphically in Figure 38.

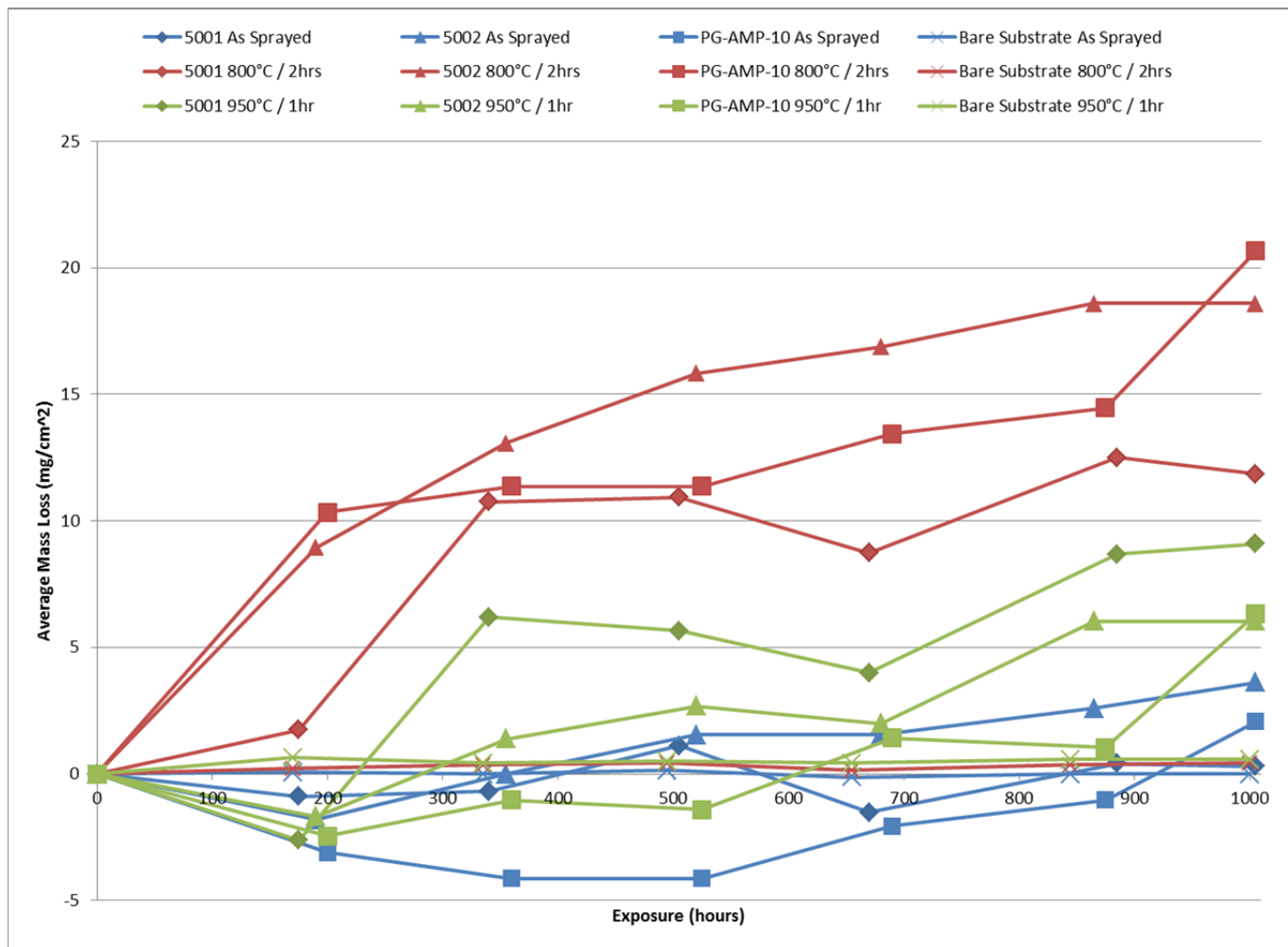


Figure 37. Observed weekly salt fog sample mass loss.

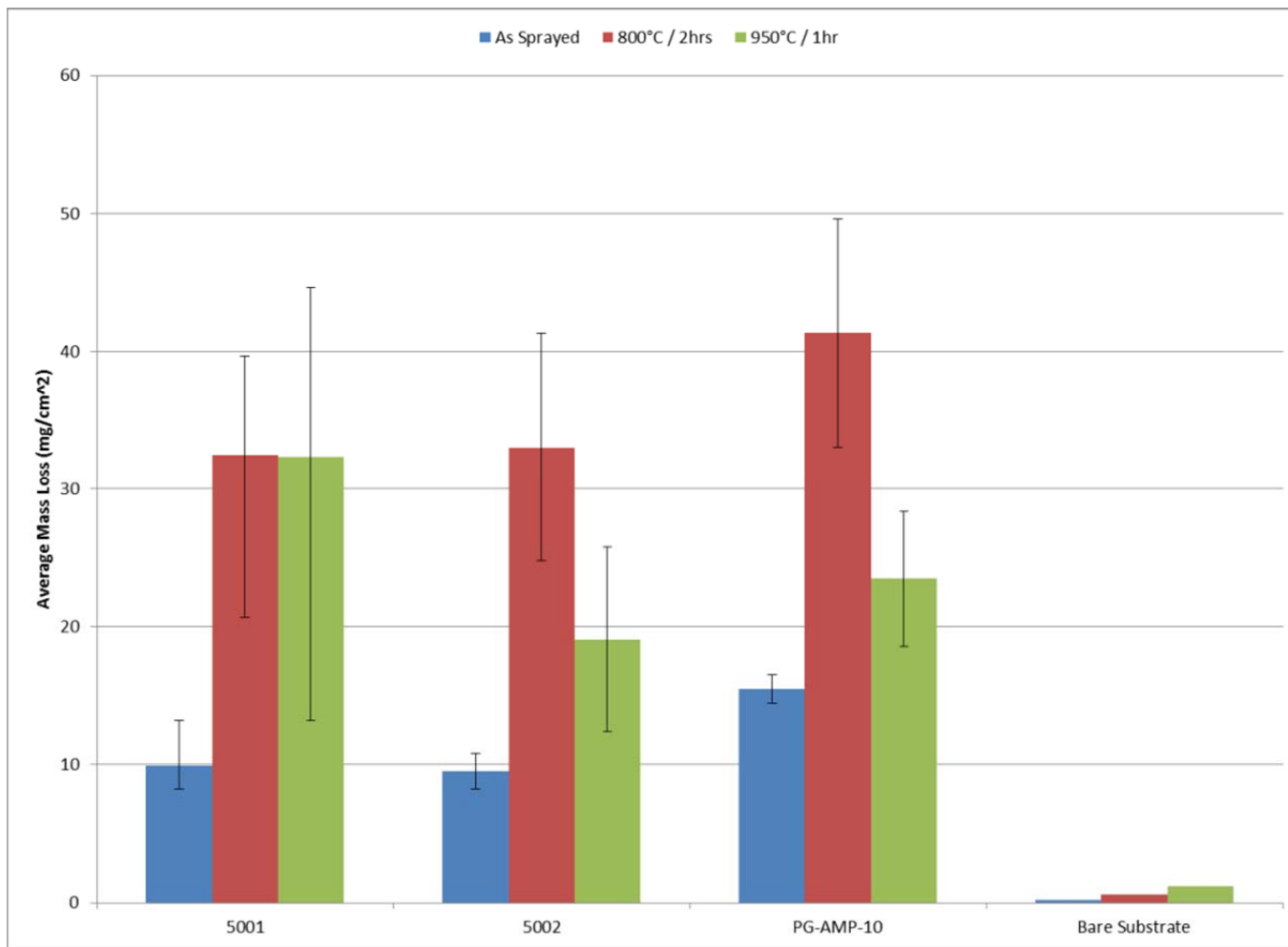


Figure 38. Mass loss measured after 1000 hrs salt fog exposure and cleaning of samples with 10% nitric acid

Error bars represent maximum and minimum sample values observed within the group.

Measurement of the pitting of the samples was more complex than mass loss measurements. The optical profiler system generated a digital model of the surface, however it was still necessary to quantify the pitting measured on the profile. This was conducted using a ‘texture’ function within the profiler software. This function identified any regions of the scan lying outside of a reference band set at 0.2 μm and centered on the sample surface. Any regions above this band were noted as peaks, and those below valleys. The system identified the size of each individual region and provided an output of the overall number found on each sample. These values were then used to compute the area fraction of pits, numeric density, average pit size and maximum measured pit depth. For the all measurements except those following cleaning with 10% nitric acid both the peaks and valleys identified by the system were assumed to represent pits; the peaks were assumed to be caps that formed over pits, thus the area fraction, numeric density and average size represent statistics from both peak and valley measurements combined. Maximum pit depth was determined solely from the maximum valley depth identified by the system and was only computed for the final profile following cleaning with nitric acid. The maximum pit depth seen on any sample was used as the maximum pit depth for that group of samples rather than taking an average of the individual sample maximum pit depths. For samples cleaned with nitric acid only the valleys identified were used to compute the pitting measurements as caps over the pits should have been removed by the exposure to nitric acid and hence all pits should have been identified as valleys. Examples profiler output is shown in Figure 39. Here the upper section of the screen capture is the raw profiler output and the lower the results of the texture analysis function.

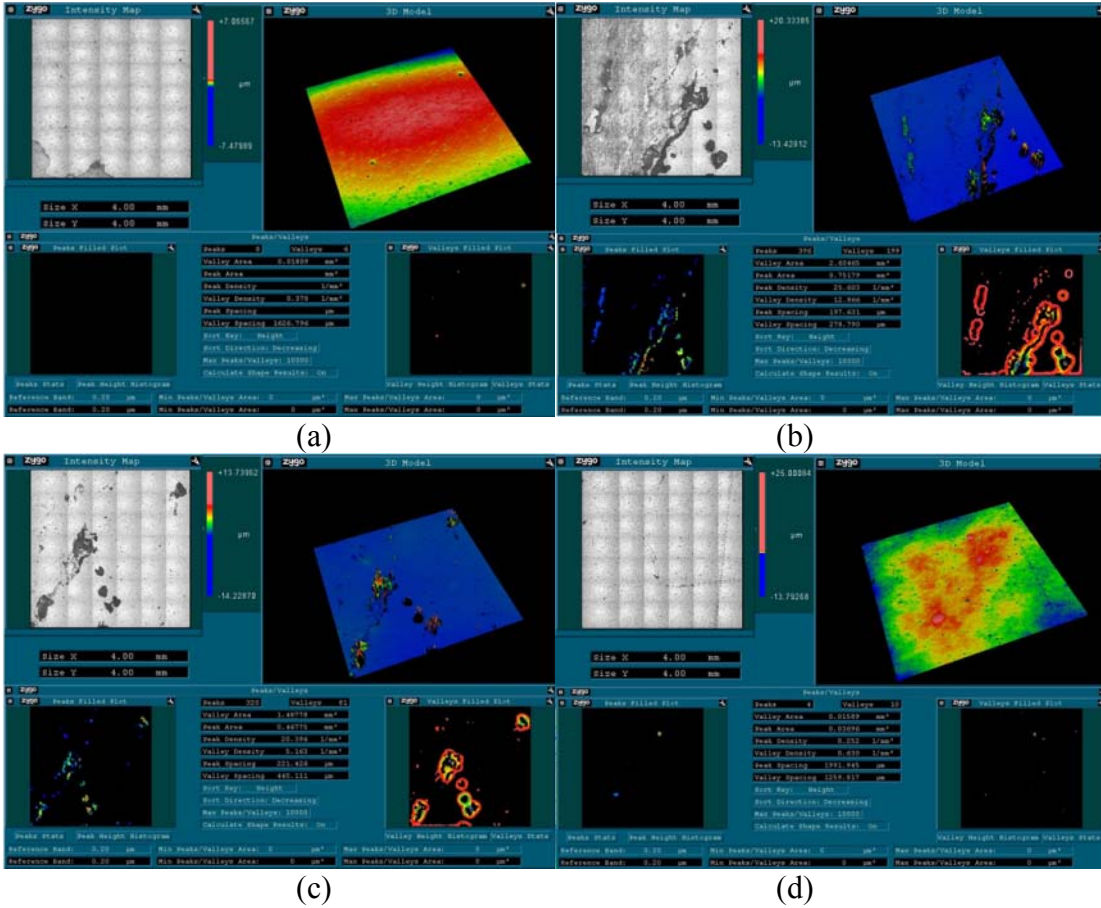


Figure 39. Example optical profiler output. (a) initial; (b) 525 hrs exposure; (c) 1005 hrs exposure, cleaned with ethanol and deionized water only; (d) 1005 hrs exposure, cleaned with 10% nitric acid. Note that color is normalized to the individual sample and varies between samples.

The pit area fraction, density and average area of each pit found from the weekly observations is shown in Figures 40–42 and the values observed following cleaning with nitric acid are shown in Figures 43–46.

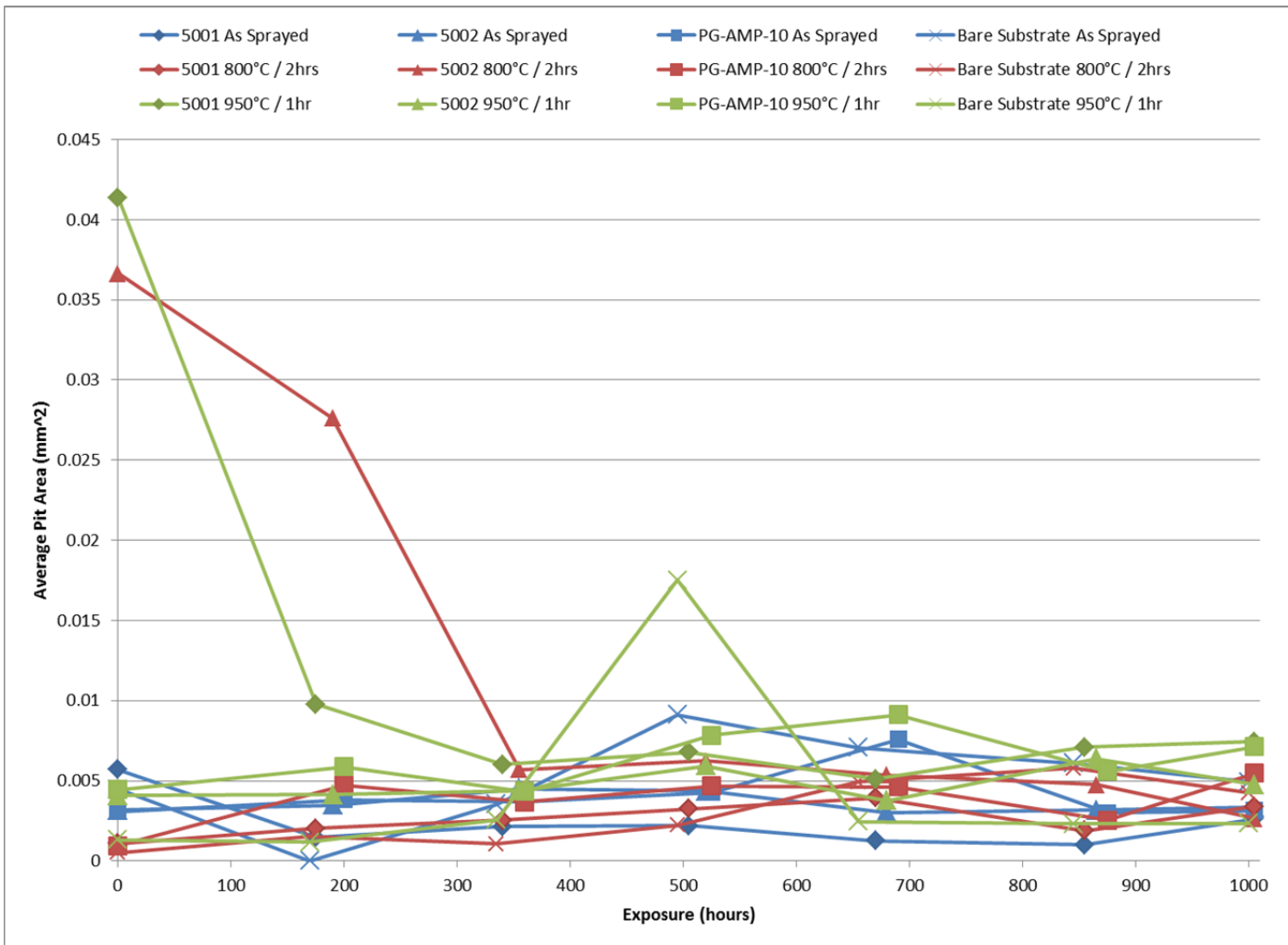


Figure 40. Observed area fraction of sample pitting during weekly sample inspection.

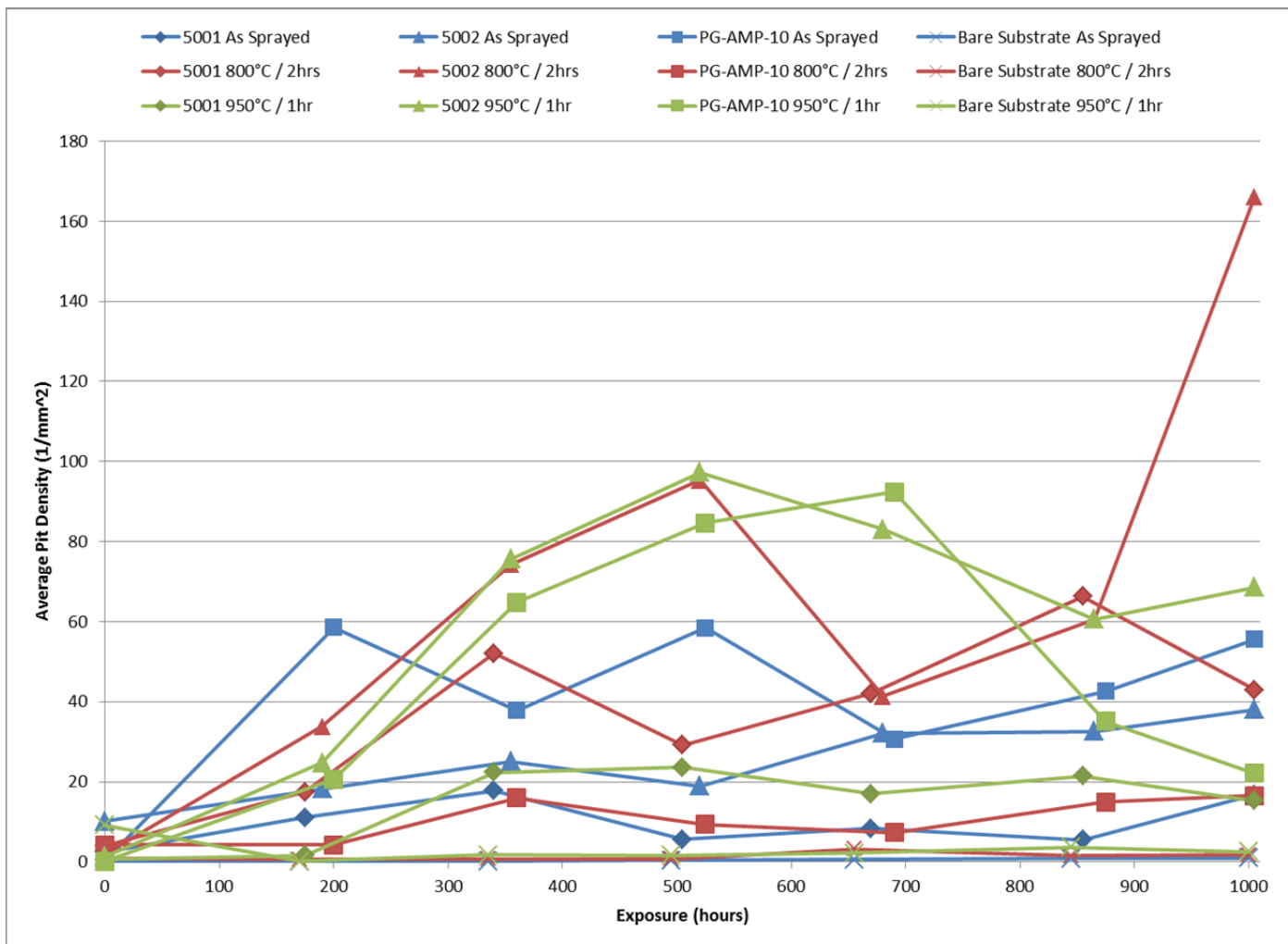


Figure 41. Observed sample pit density during weekly sample inspection.

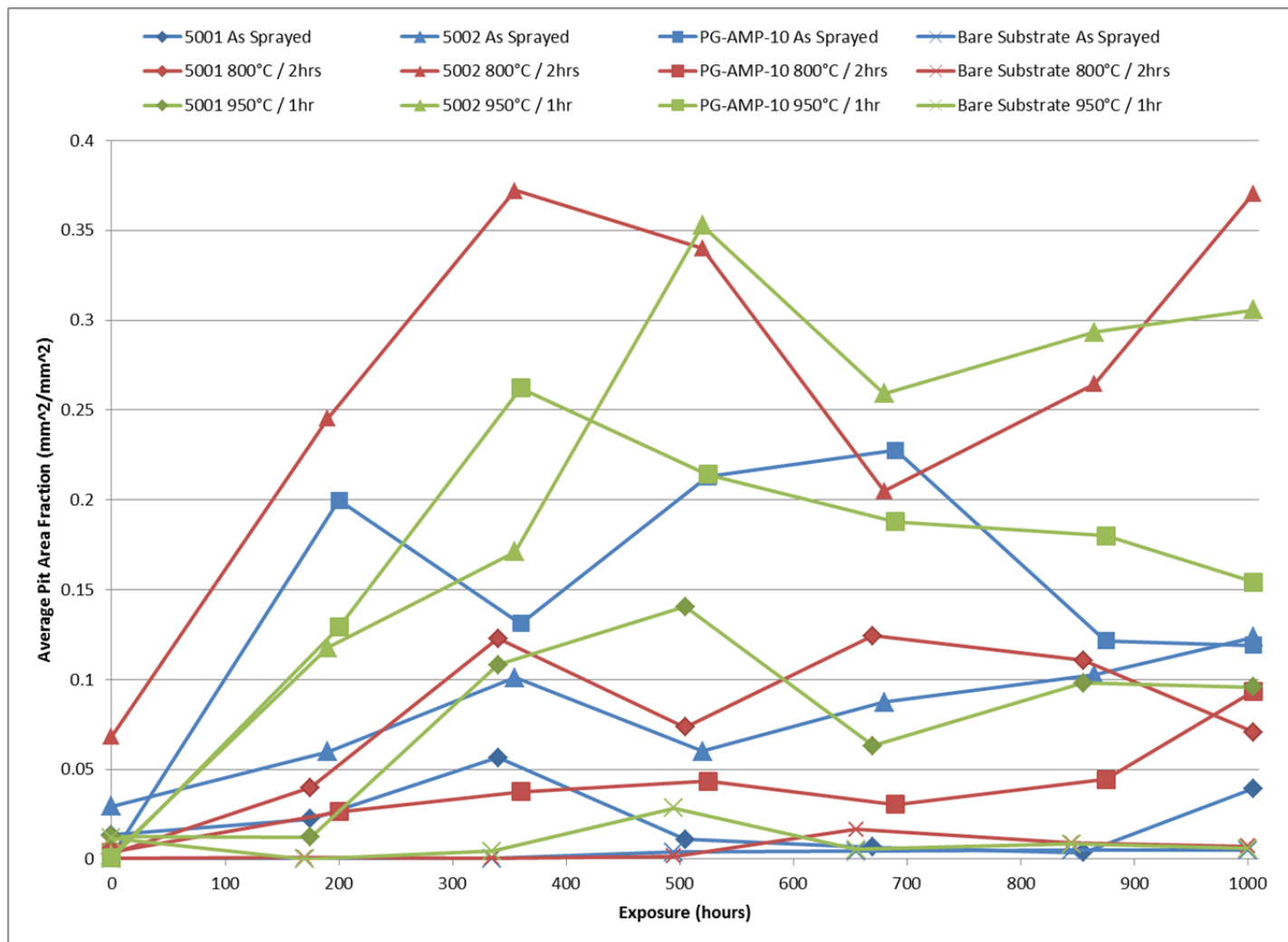


Figure 42. Observed average pit area during weekly inspection.

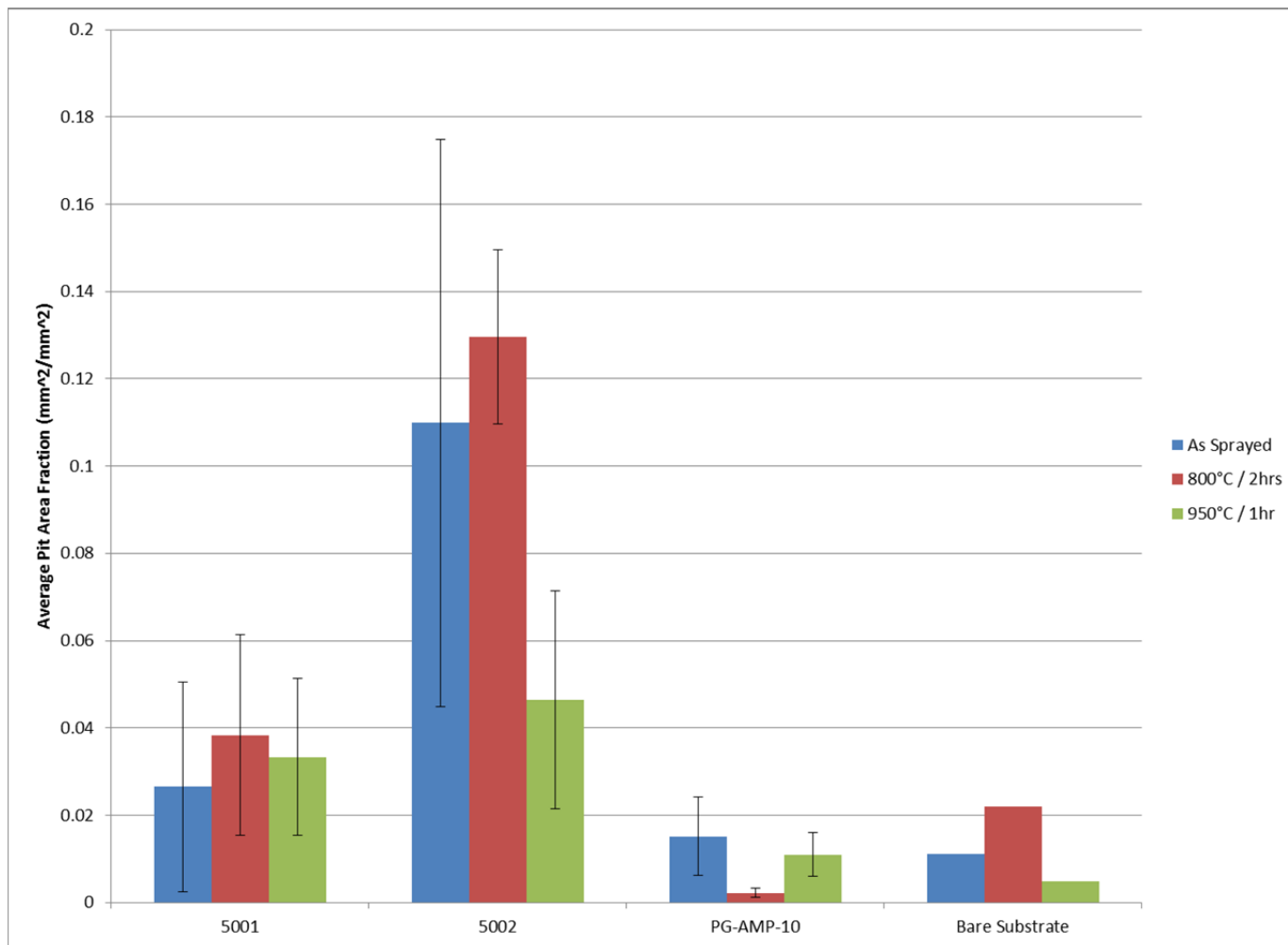


Figure 43. Pit area fraction measured after 1000 hrs salt fog exposure and cleaning with nitric acid.

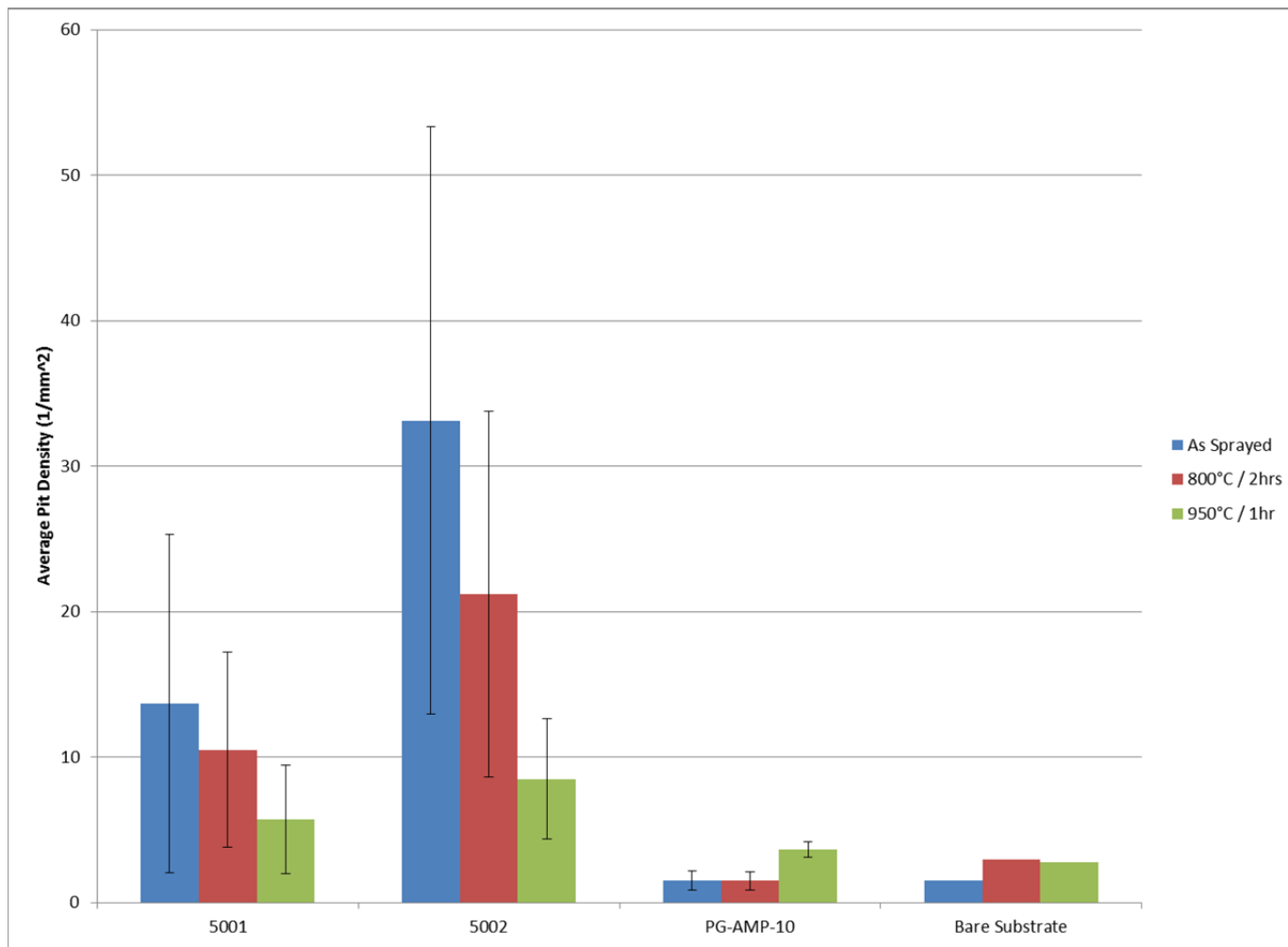


Figure 44. Pit density measured after 1000 hrs salt fog exposure and cleaning with nitric acid.

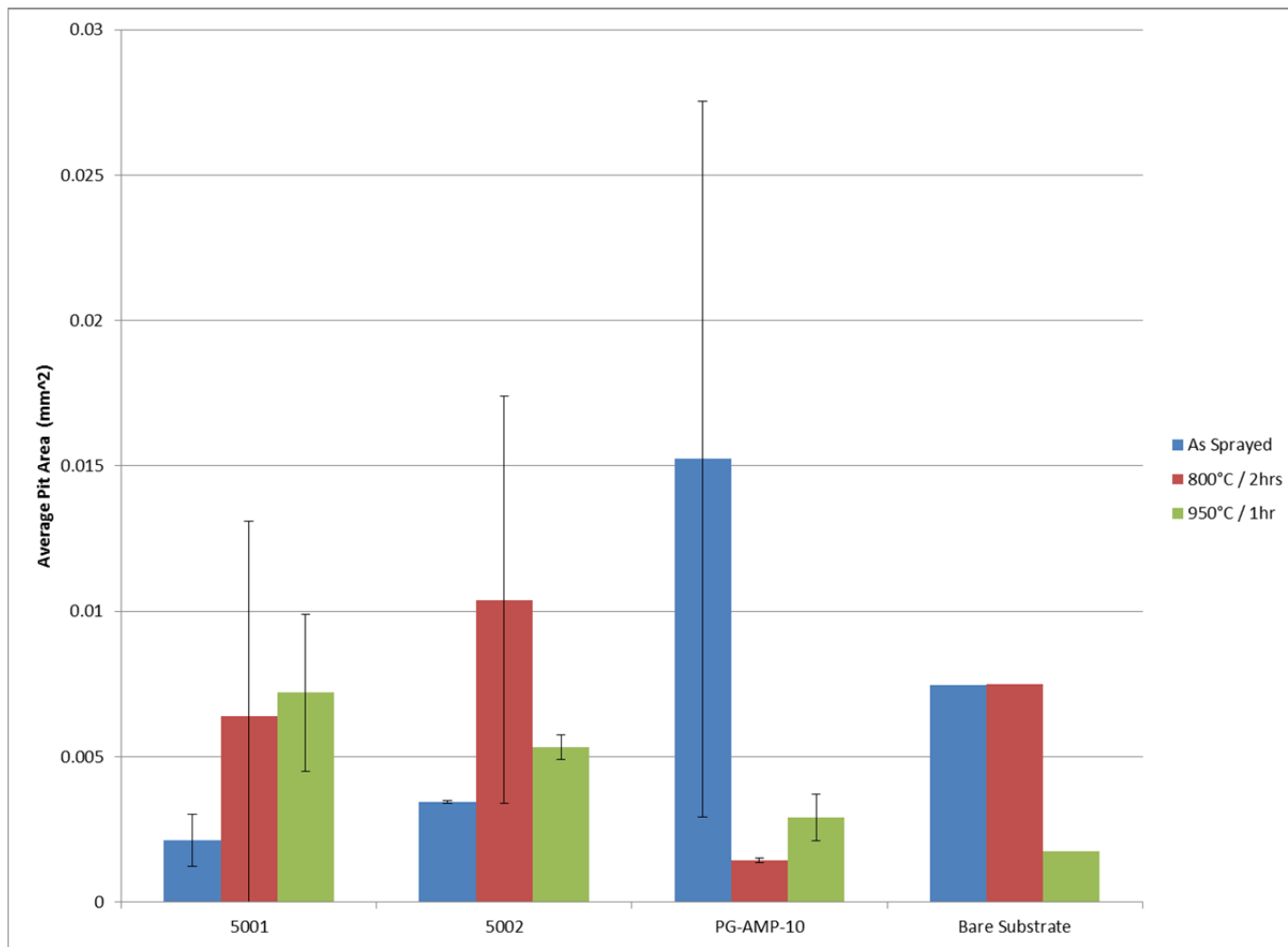


Figure 45. Average pit area measured after 1000 hrs salt fog exposure and cleaning with nitric acid.

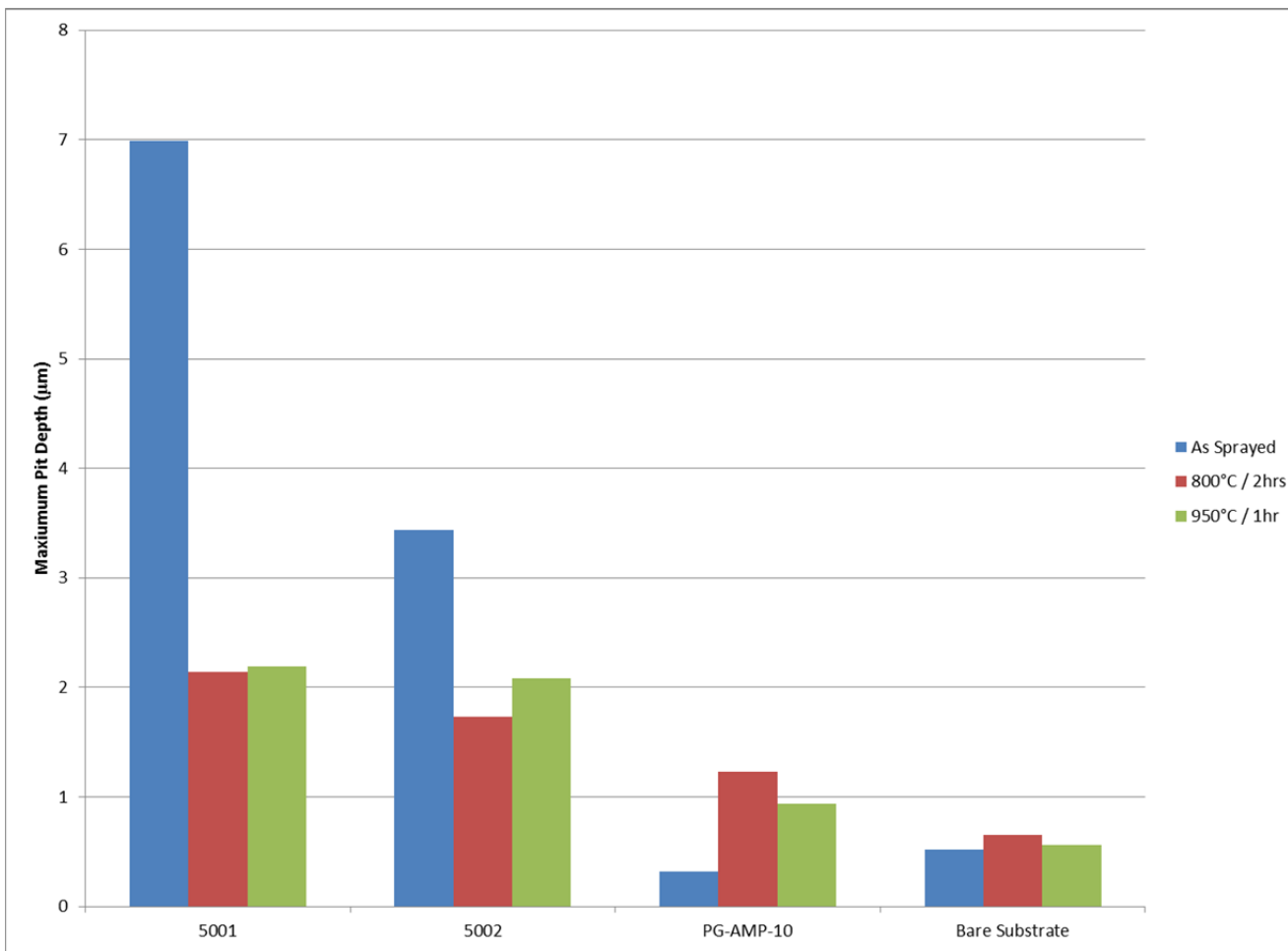


Figure 46. Maximum pit depth observed following 1000 hrs salt fog exposure and cleaning with 10 wt % nitric acid.

Mass loss and pitting data from the weekly sample observations should not be taken as definitive of sample performance but rather as evidence of a general trend in performance. The mass change in some samples, particularly during early in the testing is close to the accuracy of the balance, so a portion of the variation in mass loss could be a result of balance error rather than actual changes to the samples. Additionally, a significant amount of corrosion products deposits were observed on the sample surfaces even after cleaning. These deposits would likely add mass to the samples resulting in the measured mass loss being less than the actual amount and causing inaccuracies in the surface profile measurements and hence the pitting measurements. The heat treated samples appeared to have a greater occurrence of these deposits, possibly due to the surface oxide layer on the substrate formed during heat treatment. The surface of the coatings was polished to remove this layer and provide a flat consistent surface, but the remainder of the substrate was left with the heat treatment oxidation layer and since this entire area was exposed to the salt fog it could have caused some deviation in observed mass loss. This behavior can be seen qualitatively in photos of the samples shown in Figure 47. These photos show samples following cleaning. For these reasons, the data obtained following final cleaning with nitric acid will be assumed to represent a more definitive measurement of the material performance and this will be used primarily in further analysis.

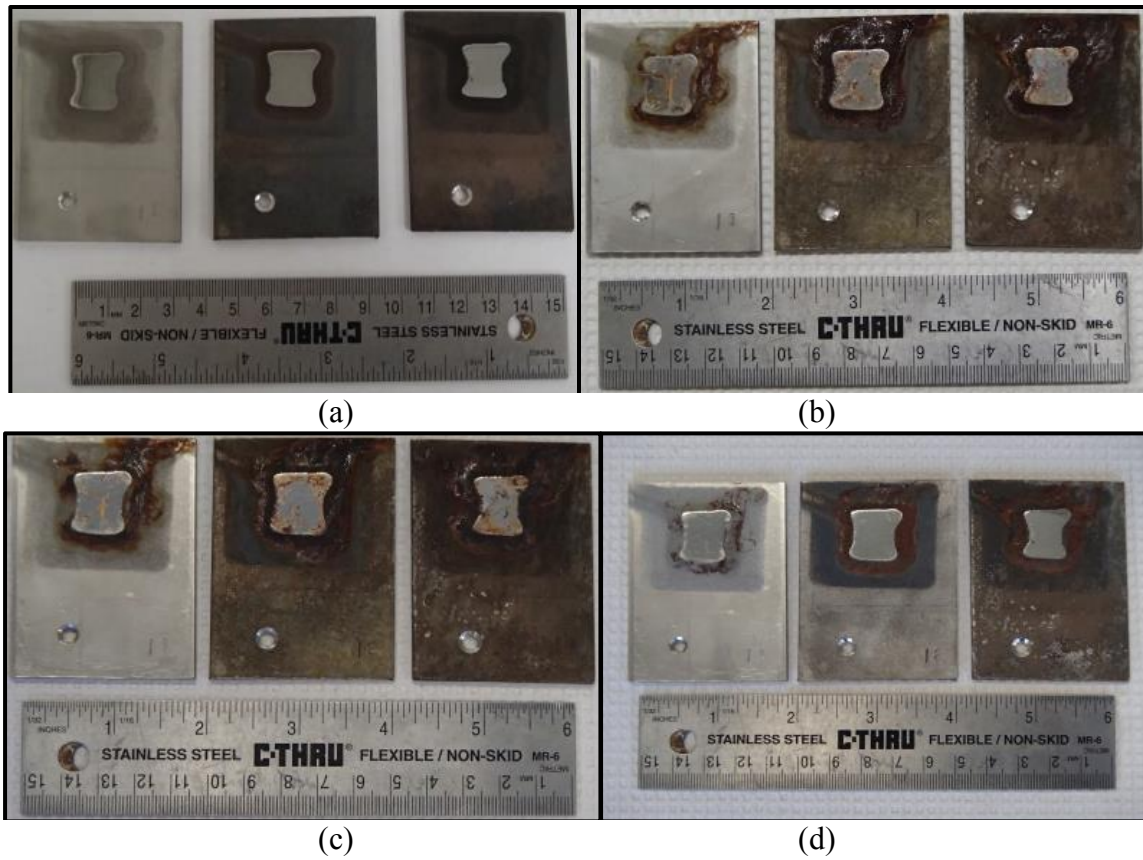


Figure 47. Photographs of samples showing corrosion deposits on sample surface. PG-AMP-10 group 1. (a) initial; (b) 495 hrs; (c) 1000 hrs, cleaned with deionized water and methanol. (d) 1000 hrs, cleaned with 10% nitric acid.

Overall performance of the powders is summarized qualitatively in Tables 12 and 13. Table 12 compares the observed performance of the three cold spray powders in the as-sprayed condition with the bare substrate while Table 13 compares performance of the heat treated coatings to that of the corresponding as-sprayed powder sample. All three coatings were observed to have substantially greater mass loss than the bare substrate, and in all cases both heat treatments also showed greater mass loss than the corresponding as-sprayed coating samples. Pitting data is more complex with no clear single overall trend apparent and will be further discussed separately.

Table 12. Qualitative corrosion performance of as-sprayed cold spray coating relative to uncoated 316 stainless steel substrate.

	5001	5002	PG-AMP-10
Pit Area Fraction	Small increase	Large increase	Slight increase
Pit Density	Moderate increase	Large increase	Identical
Average Pit Area	Moderate decrease	Moderate decrease	Moderate increase
Maximum Pit Depth	Very large increase	Large increase	Moderate decrease
Mass Loss	Moderate increase	Moderate increase	Large increase

Table 13. Qualitative corrosion performance of heat treated coatings relative to corrosion performance in the as-sprayed condition.

	5001		5002		PG-AMP-10	
	800° / 2 hrs	950° / 1 hr	800° / 2 hrs	950° / 1 hr	800° / 2 hrs	950° / 1 hr
Pit Area Fraction	Small increase	Slight increase	Small increase	Moderate decrease	Large decrease	Small decrease
Pit Density	Small decrease	Moderate decrease	Small decrease	Moderate decrease	Identical	Moderate increase
Average Pit Area	Large increase	Large increase	Large increase	Small increase	Very large decrease	Large decrease
Maximum Pit Depth	Large decrease	Large decrease	Moderate decrease	Moderate decrease	Moderate increase	Moderate increase
Mass Loss	Large increase	Large increase	Large increase	Moderate increase	Large increase	Moderate increase

The final measured mass loss (Figure 38) shows evidence of greater uniform corrosion on all of the cold spray coatings vs the uncoated substrate (rolled 316L stainless steel). It was expected that the coating would show worse corrosion performance than bulk stainless steel as the coating structure has a microstructure with a high amount of deformation, residual stress and porosity. Of these, the coating porosity is likely to have the greatest effect. Otsubo et al. investigated the corrosion properties of 304 stainless steel blasted with #24 alumina grit and found that the primary detrimental factor in corrosion performance was the surface roughness produced; residual stress in the surface had little effect [58]. In their work, corrosion resistance of blasted surfaces was determined and compared to both un-blasted and annealed blasted samples. They found very similar corrosion resistance in the blasted samples both with and without annealing

which was in both cases considerably lower than the un-blasted samples. The annealing treatment removed the residual stress resulting from the blasting process but without significantly changing the roughened surface profile thus it can be concluded that surface residual stress does not have significant effect on corrosion resistance. The cold spray process operates with a similar blasting mechanism, and is known to produce a compressive residual stress [33, 34] similar to the grit blasting used in the referenced experiment, thus the residual stress in the cold spray coating is likely not a major factor in corrosion performance. The porosity inherent in the cold spray coating process however could be a significant factor. Some difference between the different powders is also seen, with as-sprayed and 800°/2 hrs samples in the 5001 and 5002 samples showing similar performance that was notably better than that of the corresponding PG-AMP-10 samples. A different trend is seen in the 950°/1 hr samples, with the 5002 powder showing best performance, followed by PG-AMP-10 and 5001.

The most significant result is evidence of decreased corrosion resistance following heat treatment. In all samples both the 950°C/1 hr and 800°C/2hr treatments are observed to show substantially greater mass loss than as-sprayed samples, with the 800°C/2hr treatment appearing to have worse mass loss than the higher temperature. There is substantial difference in performance across the 3 powders as well. Notably, the base substrate samples also show a trend towards worse performance when heat treated, although interestingly the 950°C/1 hr heat treatment seems to give worse performance than the 800°C/2hr in the bare substrates whereas the opposite effect is seen in the coatings. It should be noted however that the bare substrate results represent only a single sample vs averaged data from two or three sprayed samples.

Pitting measurements paint a more complex story. ASTM G46 gives a method for concise pit rating accounting for the pit density, average size and depth in one value. The closest standard rating for all samples would be A-5, B-1, C-1 [59]. In other words, the measurements obtained show a larger number of individually small pits. This rating does little to allow comparison of the powders and treatments although it does provide an overall rating of the coating performance. Notably, the uncoated substrate samples also share the same rating.

Examination of Figures 43–46 and tables 12 and 13 show a number of trends within the individual data but without any clear overall definitive conclusion when considering all 4 pitting metrics. Both the 5001 and 5002 coatings appear to have a greater number of pits but with less individual area per pit than the uncoated substrates for both as-sprayed and heat treated samples with the exception of the 800°C/2 hrs heat treatment in the 5002 powder which showed greater area and number of pits. The PG-AMP-10 powder in contrast appeared to have a comparable number of pits with greater individual area than the bare substrate in the as sprayed and 950°C/1 hr conditions and the opposite in the 800°C/2 hrs samples. The bare substrate samples show an increased number of pits but with equal individual area with the 800°C/2 hrs heat treatment and a notably lower number and size of pits in the 950°C/1 hr heat treated samples.

The most critical parameter in pitting corrosion is the maximum pit depth since this is what ultimately leads to coating failure. The maximum depth measured in any sample is shown in figure 46. From this data, the as-sprayed samples of 5001 and 5002 powders appear to suffer worse pitting than the heat treated samples, whereas the reverse is true in PG-AMP-10 and bare substrate samples. Notably, the PG-AMP-10 as-sprayed sample shows a shallower maximum pit depth than any of the bare substrate samples, suggesting pitting resistance greater than bulk 316L stainless steel.

However, the use of optical profiling and computer texture assessment makes it probable that there is significant error reflected in these measurements. The pit density, pit area fraction and average pit area measured are all dependent upon an accurate assessment and identification of what is and is not a pit. Measurement of the initial profile is dependent upon the optical properties of the surface and is thus effected by changes in reflectivity associated with corrosion deposits and surface topography, so there is potential for the measured profile to imperfectly reflect the actual surface. Beyond that, the metrics used for pitting characterization were generated by a computerized topology function that does not always perfectly characterize the surface. A primary source of error is the definition of the reference plane used to differentiate peak and valleys. Many of the samples had a degree of curvature to the base surface, and this surface may not have been perfectly parallel to the base of the profiler resulting in an

apparent slope or curvature in the measured profile. The texture analysis software includes compensation for these errors, however this is not 100% accurate. An example of this is shown in Figure 48 where a portion of the edge of the sample is characterized as a valley due to incomplete compensation, resulting in an erroneously high value for the number of valleys and overall valley area.

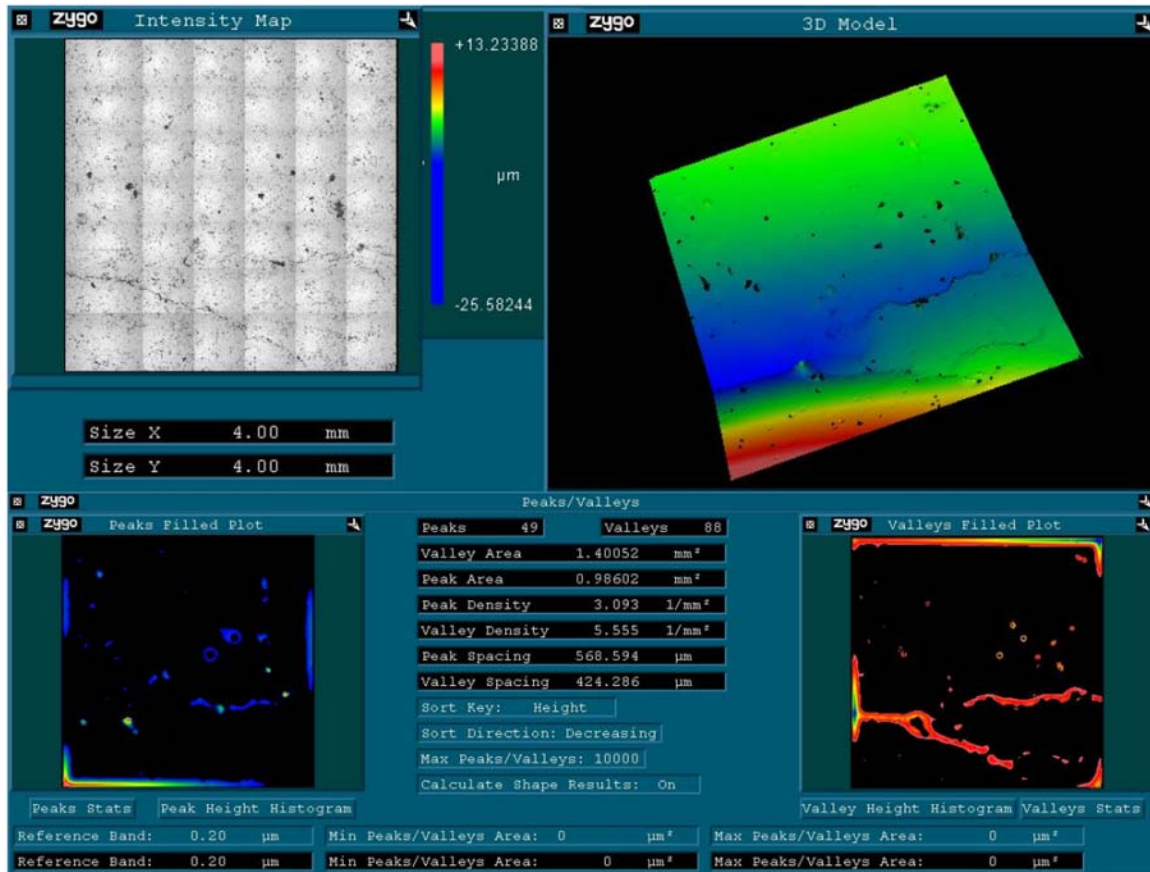


Figure 48. Profiler output and generated texture showing erroneous measurement of sample slope as peaks and valleys. 5002 powder, 800°C / 2 hrs heat treatment. Profile following 1000 hrs exposure and nitric acid cleaning

Additionally, the texture system was observed to count multiple valleys occurring within the same identifiable pit due to a rough bottom profile of the pit. Consequently it overstates the actual number of pits. Measurement of the maximum pit depth is unaffected by this error, but is effected by imperfect measurement of the pit profile

during the original scan. As mentioned previously, a major issue with this type of profiling is the variation in light intensity resulting from varied reflectivity in surfaces. The same effect occurs when measuring a deep narrow pit, with the overall result that accurate measurement of the pit depth is very difficult. Further, pit shape is notoriously complex and irregular, so the actual deepest penetration of the pit may not be visible from the surface. This error is evident in the profile shown in Figure 49, where several circular valleys with a black center are seen. These likely represent pits and the black center section is the deep center region that was not properly profiled in the original scan.

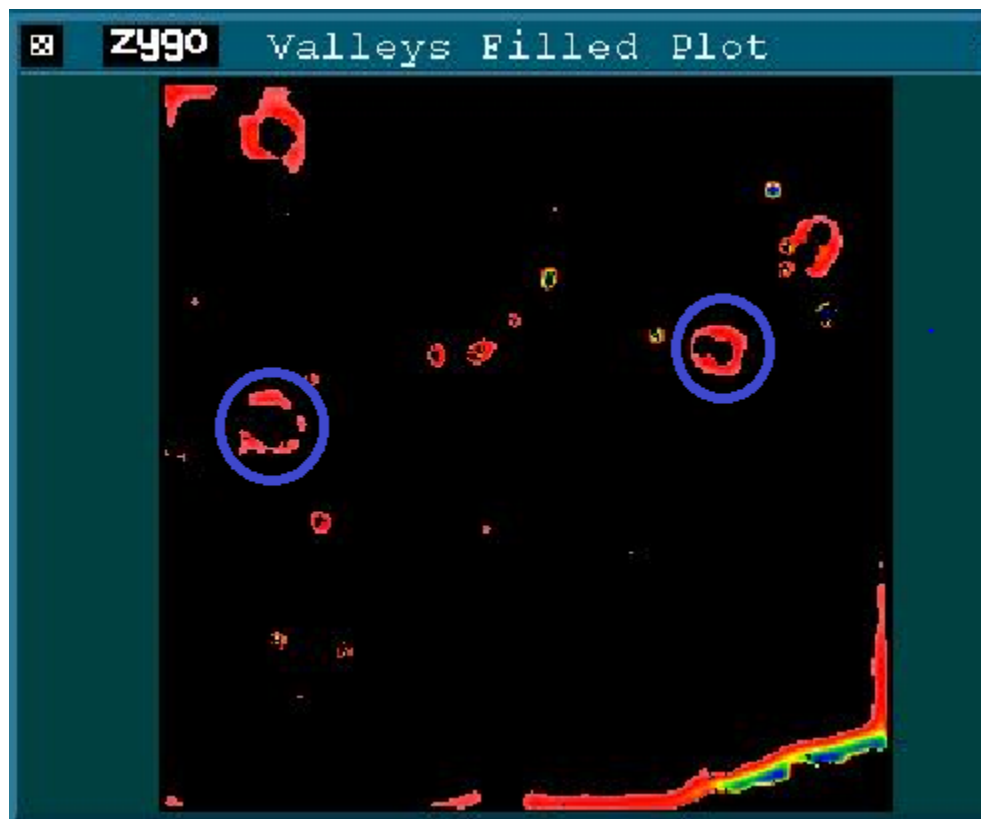


Figure 49. Example resolved valley profile showing pitted regions with unresolved centers (blue circled regions). 5002 powder, 950°C / 1 hr heat treatment. Profile following 1000 hrs exposure and nitric acid cleaning.

All of these errors are inherent concerns in the use of the optical profiling process, and can be compensated to a degree by careful configuration and manipulation of software settings to obtain the optimal results from each sample. This process is time

consuming however, and the degree to which it is required is difficult to determine until the final data is analyzed. In this work the decision was made that the time required to obtain the best quality data from the profiling was not justified, although that decision was made before the full impact on the quality of result obtained was realized. Consequently, the data obtained should not be taken as absolute metrics of expected performance, but can still be used for relative comparisons of the coatings and heat treatments used.

D. POLARIZATION TESTING RESULTS

Polarization curves for 5001, 5002 and PG-AMP-10 samples are shown in Figures 50–52, respectively. The same data is also plotted for each heat treatment as shown in figures 53–55. Each of these includes curves from as-sprayed samples as well as both heat treatments and the non heat-treated 316L substrate. These results clearly show significant differences in corrosion behavior between the cold spray coatings and bulk 316L stainless steel as well as large changes in behavior with heat treatment. In all cases the as-sprayed coating has a much lower pitting potential and hence narrower region of passive behavior than bulk 316L. All three powders also show nearly an order of magnitude higher current in the passive region which would lead to substantially greater corrosion even within when the sample is behaving passively. All samples also show essentially a complete lack of passive behavior when heat treated. Changes in the open circuit potential (OCP) are also seen. Both the 5001 and 5002 as-sprayed samples show an OCP nearly identical to the substrate while the PG-AMP-10 as-sprayed coating shows a nearly -0.2V difference. With heat treatment the OCP in the 5001 and 5002 samples decreased (became more active) while in the PG-AMP-10 sample it increased. Both heat treatments in the PG-AMP-10 and the 950°C/1 hr treatment in the 5002 powder showed a similar OCP roughly 0.1V anodic to the substrate while both heat treatments in the 5001 and 800°C/2 hrs in the 5002 powder showed an OCP approximately 0.15v anodic to the substrate. The greatest OCP difference was in the as-sprayed PG-AMP-10 with a roughly 0.2v difference. This difference could cause corrosion between the coating and substrate, in service with the coating being anodic to the substrate and potentially suffering

accelerated corrosion. Notably in all cases where a difference in the open circuit potential was seen, the coating was anodic to the substrate. While a difference in OCP is not desirable due an increased propensity for localized corrosion, it is desirable that the coating be anodic to the substrate if there is a potential difference. The reason for this is due to large area difference between the coating surface and any small substrate sections exposed due to porosity, coating damage, etc. If the substrate was anodic, this large area difference would cause a high corrosion rate on the exposed substrate area [26].

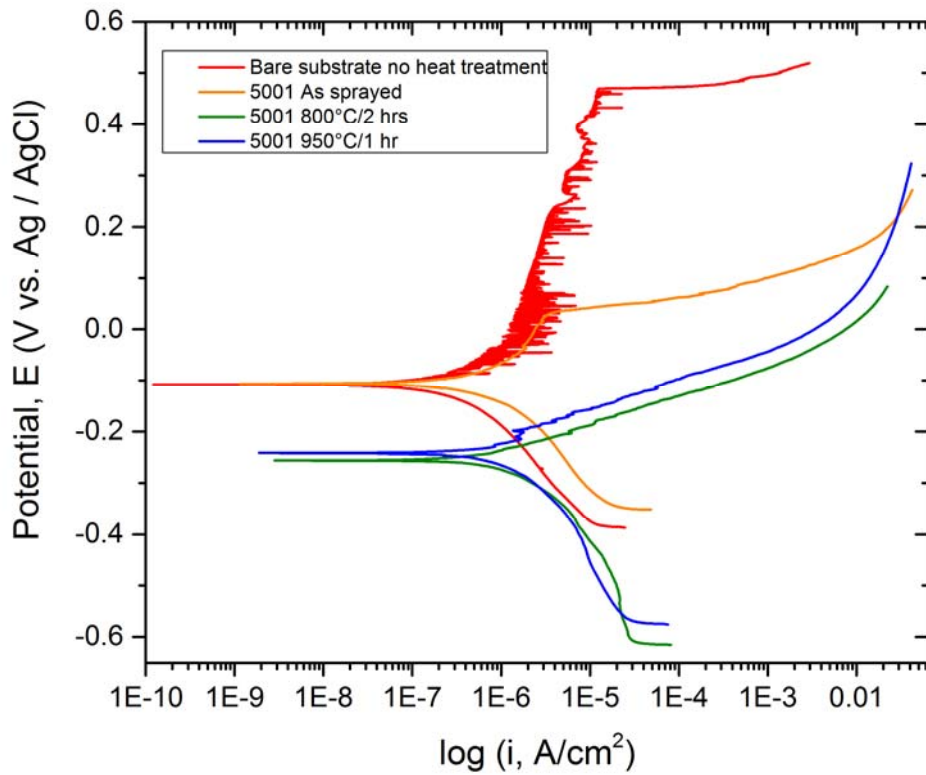


Figure 50. Anodic polarization curves for 5001 powder samples.

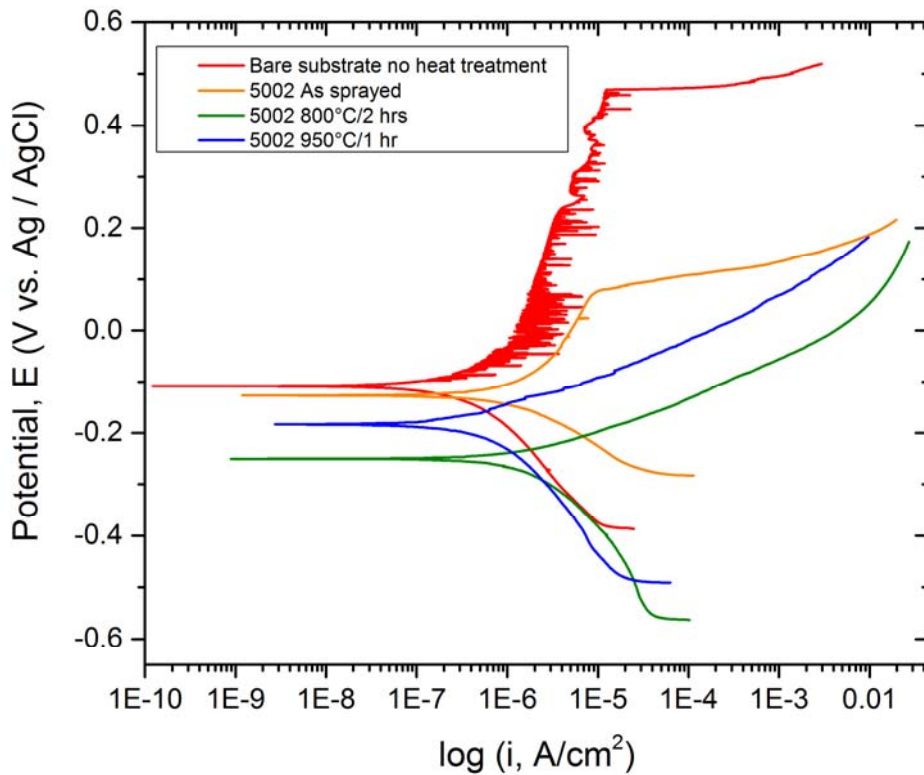


Figure 51. Anodic polarization curves for 5002 powder samples.

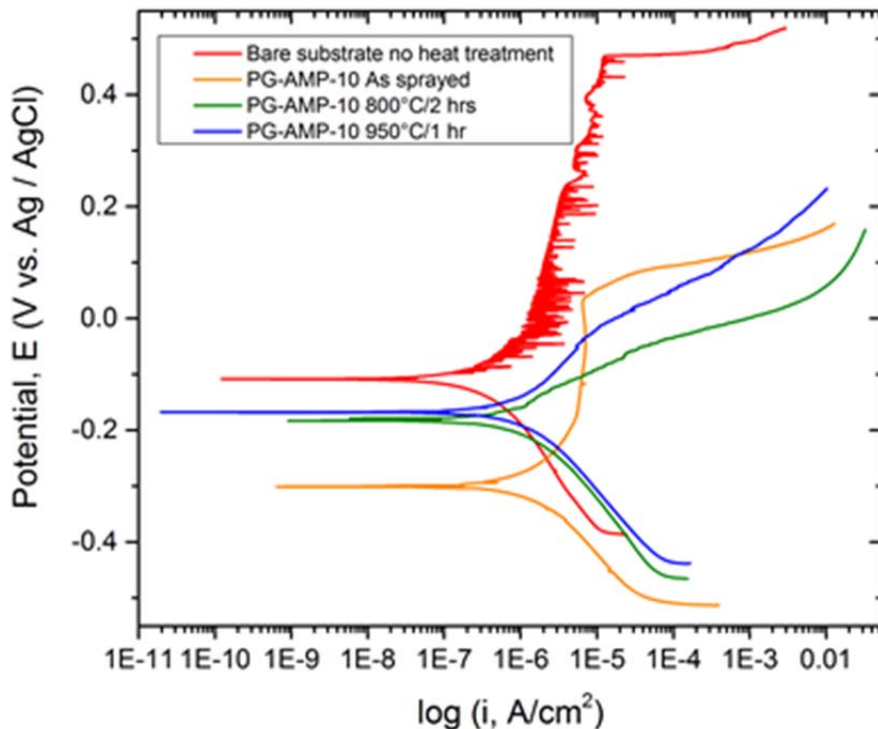


Figure 52. Anodic polarization curves for PG-AMP-10 powder samples.

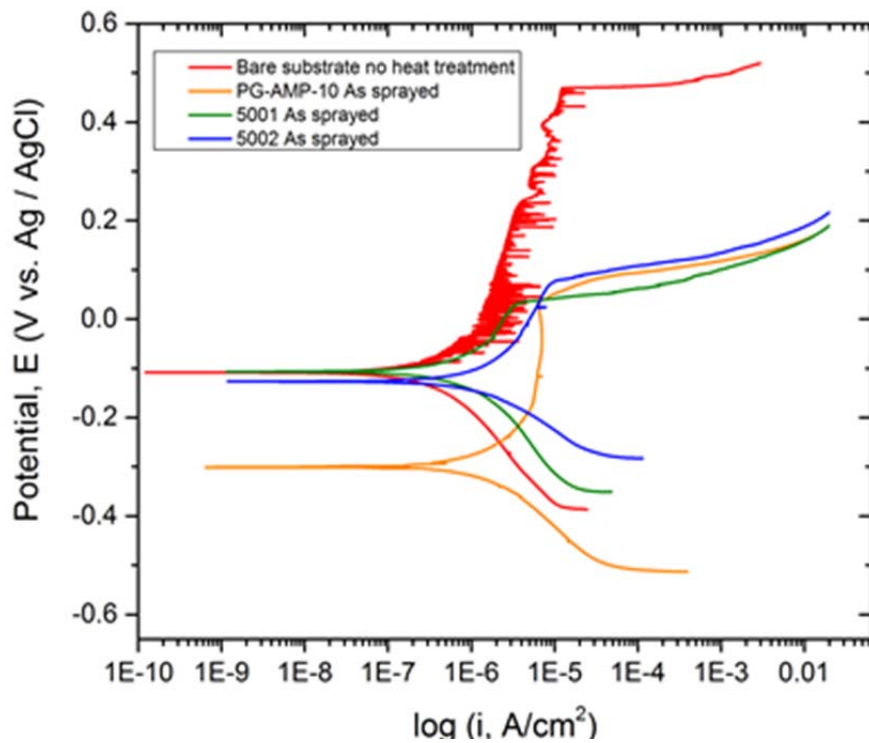


Figure 53. Anodic polarization curves for as-sprayed samples.

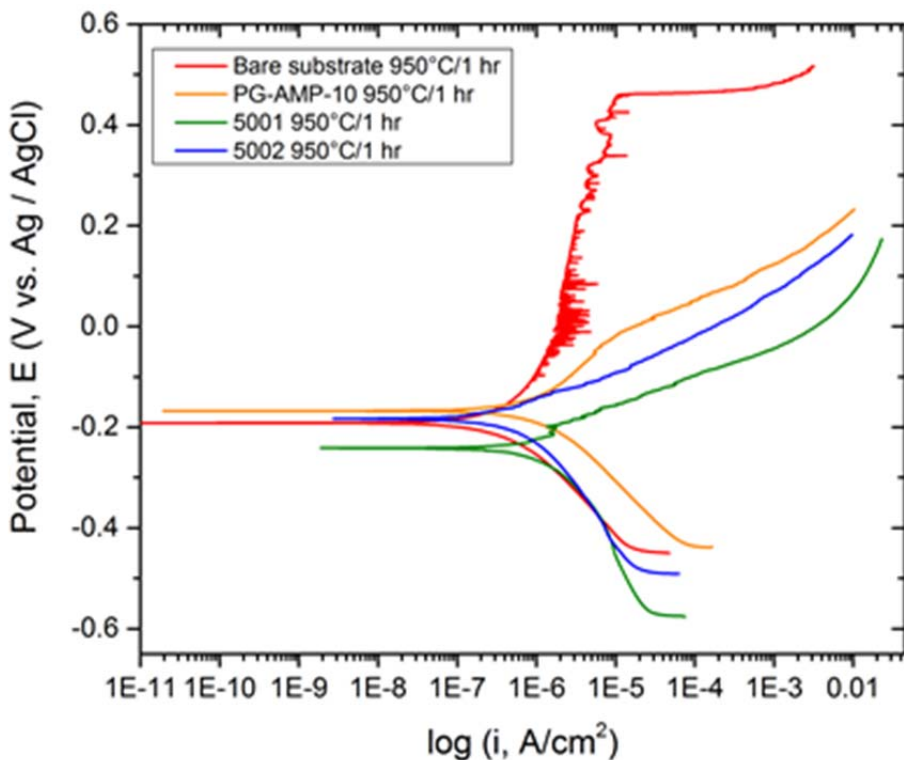


Figure 54. Anodic polarization curves for 950°C/1 hr heat treated samples.

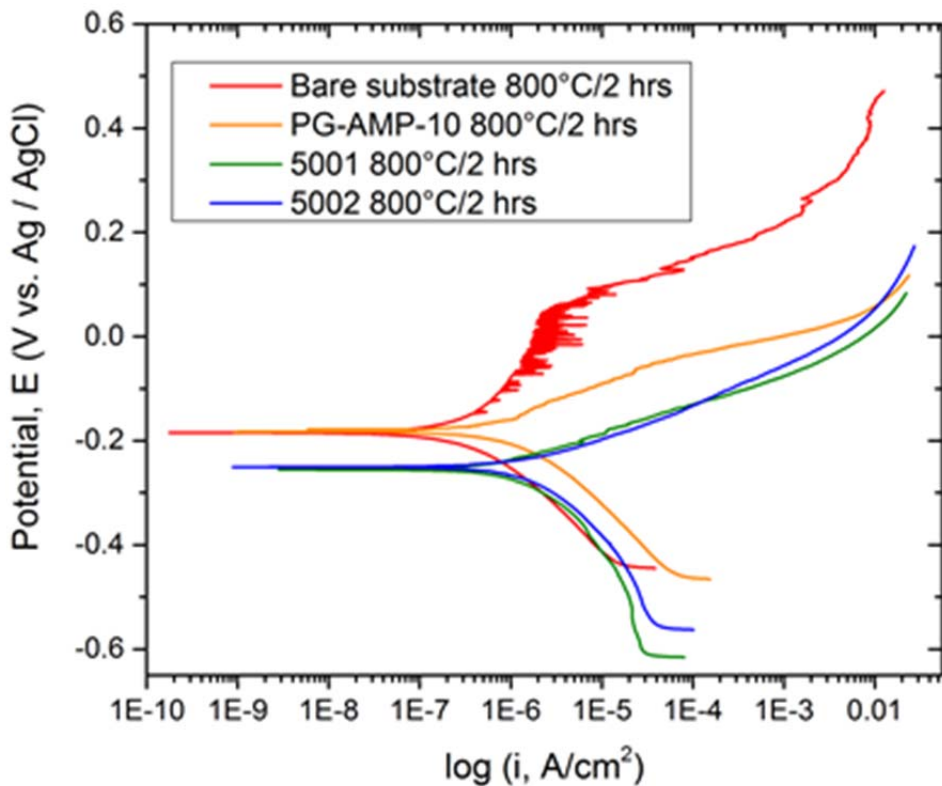


Figure 55. Anodic polarization curves for 800°C/2 hrs heat treated samples.

It was noted that the 800°C/2hrs substrate showed no clear pitting potential. To examine the behavior of the bulk 316L stainless steel, the three substrate polarization curves are plotted in Figure 56.

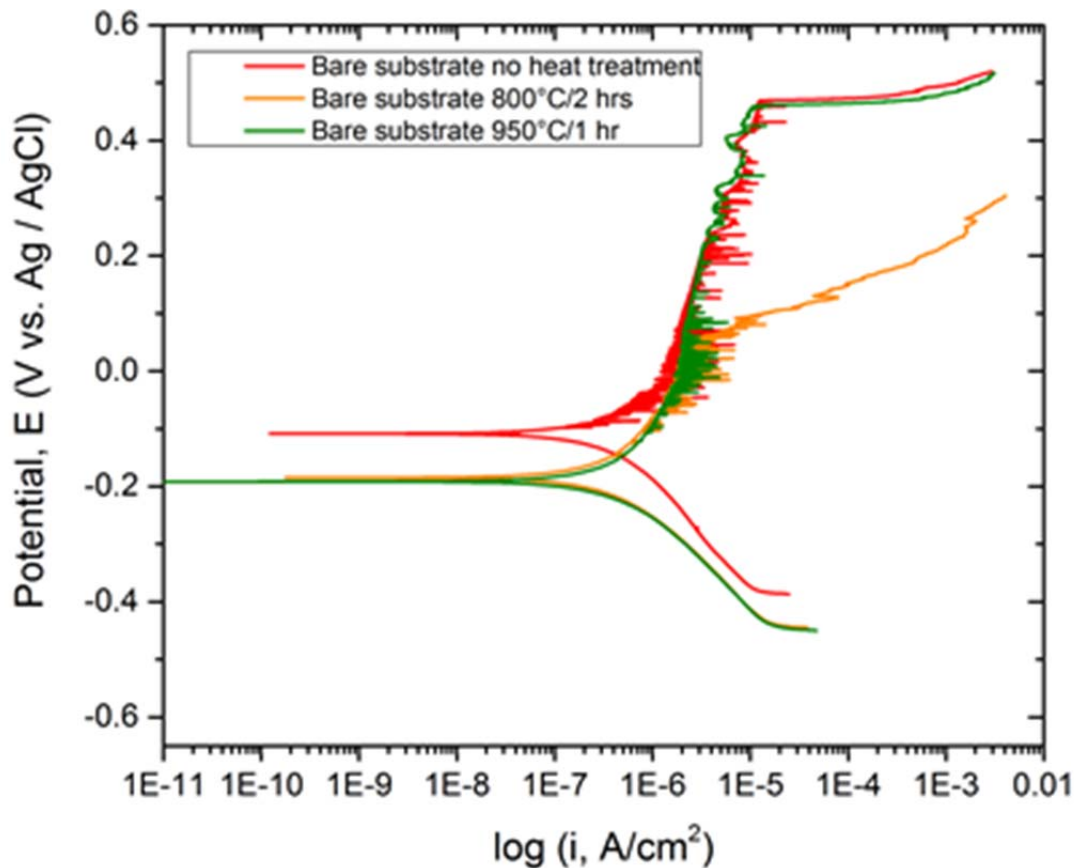


Figure 56. Polarization curves for bulk 316L substrates.

Comparison of the curves in this plot showing interesting behavior of the bulk 316L steel. The 800°C/2 hrs heat treatment shows a much lower pitting potential than the non-heat treated sample while the 950°C/1 hr samples shows a restoration of the non-heat treated corrosion resistance but with a slightly more active OCP. This behavior suggests sensitization is occurring in the 800°C/2 hrs heat treatment but the time and/or temperature in the 950°C/1 hr treatment is sufficient to mitigate this problem. The OCP is also lower in both heat treated samples. The open circuit potential and pitting potential values obtain are tabulated in Table 14.

Table 14. Measured open circuit and pitting potential voltages from coating and substrate polarization testing.

	5001			5002			PG-AMP-10			Bare Substrate		
	As sprayed	800°C/2 hrs	950°C/1 hr	As sprayed	800°C/2 hrs	950°C/1 hr	As sprayed	800°C/2 hrs	950°C/1 hr	Untreated	800°C/2 hrs	950°C/1 hr
Corrosion potential ($V_{Ag/AgCl}$)	-0.107	-0.256	-0.241	-0.127	-0.250	-0.183	-0.301	-0.183	-0.168	-0.109	-0.185	-0.192
Pitting potential ($V_{Ag/AgCl}$)	0.019	-	-	0.066	-	-	0.035	-	-	0.469	0.092	0.460

E. DISCUSSION

The results from salt fog testing tend to follow the expected behavior from assessment of the polarization testing. Polarization tests clearly show that all of the coatings have a much lower pitting potential than the substrate, and hence would be expected to show higher corrosion rates in service. Likewise the heat-treated samples have essentially no passive region and hence would be expected to have even worse corrosion resistance than as-sprayed coatings. Except for the PG-AMP-10 950°C/1 hr sample, the curve shape and pitting potential (as-sprayed samples) is nearly identical between powders with the same heat treatment, so roughly the same corrosion rate should be expected. The observed salt fog data does show greater mass loss for coatings vs the substrate and heat treated coatings versus the as-sprayed coatings, which correlates with the results expected from polarization testing. The as sprayed PG-AMP-10 sample does show the greatest mass loss of any of the as-sprayed samples which could correlate with this coating having the greatest OCP difference between the coating and substrate and hence greatest potential for galvanic corrosion.

The first possible source of different behavior is a difference in the elemental composition and distribution between the materials and changes to the distribution following heat treatment. Chromium is the primary elemental addition associated with the corrosion resistance of stainless steel, and there are several known processes in austenitic stainless steels that can result in local depletion of chromium and thus increased local corrosion. Sensitization is the most likely of these to have occurred here. As discussed in Section (III.C.2), sensitization occurs due to the precipitation of chromium carbides resulting in a local area of low chromium. A characteristic of this occurrence is that a

longer and/or higher temperature annealing treatment will reduce the detrimental effect through bulk chromium diffusion eliminating the local low chromium region. The low carbon type stainless steel alloys as used here are generally considered to be insensitive to sensitization although there is some literature reporting this occurrence in 316L stainless steels [38, 40, 42–44]. While no evidence of this occurrence was found during characterization work as reported in section III, the behavior seen in the substrate heat treatments strongly suggest this is occurring. The notable decrease in corrosion resistance as seen from the lower pitting potential in the 800°C/2 hrs treatment combined with the restoration of the high original pitting potential in the 950°C/1hr sample follows the characteristic behavior of sensitization.

Evidence of sensitization occurring in the substrate does not necessarily mean that this is occurring in the coating. This behavior is highly dependent on the carbon content of the alloy, and at least two of the powders are specified to have a carbon content much lower than the 316L specification: 0.014% in 5001 and 0.017% in 5002. As seen by the TTT diagram, (Figure 25) the kinetics of the precipitation slow greatly with even a small decrease in carbon content, so low carbon content in the coating would greatly reduce the likelihood of sensitization occurring if in fact the actual carbon content follows that specified. Conversely, a higher than specified carbon content or a local carbon concentration for some reason would greatly increase the likely hood of sensitization.

The poor performance of the 950°C/1 hr treatment in all three cold spray samples is harder to explain and casts potential doubt on grain boundary sensitization being the sole reason for poor performance in the 800°C/2 hrs samples. Reference literature [47] and the behavior of the substrate sample suggest that even if sensitization occurred in the 800°C/2 hrs treatment, it should have been at least partially mitigated at the higher temperature. P. Atanda et al. [47] studied sensitization in 316L steel by examining the degree of desensitization resulting from normalizing of sensitized samples at various temperatures. Sensitization was carried out by soaking at 750-850°C for 0.5-2 hours. When fully sensitized samples were normalized for 1 hours at 950°C, the sensitization was found to be almost completely healed. Thus at least partial restoration of non-

sensitized corrosion resistance is expected following the 950°C/2 hrs treatment. Further, the investigation referenced started with fully sensitized samples resulting from extended soaking while the samples in this work only experienced a short transient heating in the critical 600-850°C range and thus are likely to have a much lower degree of sensitization to begin with; thus complete desensitization is likely with the heat treatment used.

It is possible that differences in carbon content and microstructure could of course change the kinetics of the process, however in both cases recrystallization appears to have occurred in all samples, thus reducing any differences resulting from the highly strained small grained microstructure in the coatings. An increase in carbon content would be expected to increase the susceptibility to sensitization at lower temperatures but would not make the effect persist at higher temperatures. It is possible for sensitization to occur during cooling if the rate is sufficiently low that the material spends sufficient time within the critical temperature range of roughly 600–850°C. The critical cooling rate that causes this to occur is highly dependent on carbon content of the material. H. D. Solomon conducted work to determine this rate for a wide variety of carbon contents in 304 stainless steel [60]. He found the critical rate is roughly 0.08°C per second for a 0.03 wt% carbon content, and less than 0.01°C per second for 0.017 wt% carbon [60].

A simple ANSYS© model of a sample was constructed to estimate the cooling rate. In this model the sample was modeled as a 86 x 52 x 3.1 mm rectangular plate with a convective cooling coefficient of 5 W/m²·K on one face and no heat transfer on the other faces. The convective cooling coefficient was chosen as a conservative estimate of the coefficient for free convection in air, and assuming no heat transfer from any other faces or radiation makes the model further conservative. An initial temperature of 950°C was used with the air at 20°C. The cooling rate in this model at the face furthest removed from the convective cooling was found to be approximately 0.3°C per second at 750°C which is the nose of the cooling curve and hence where the cooling rate is most critical. Thus, with a very conservative cooling model the slowest cooling rate in the sample is found to be roughly 4 times faster than that required for sensitization for the highest

carbon content possible under the 316L specification (0.03 wt%). As such, it seems unlikely that the samples treated at 950°C resensitized during cooling.

Coating powder material and phase morphology could also have an impact. The 5001 powder is a 304L stainless steel alloy whereas the 5002 and PG-AMP-10 are 316L. The primary difference between the two alloys is the addition of 2–3 wt% molybdenum in order to increase the pitting resistance of the 316 type steel. Consequently, worse pitting corrosion would be expected in the 5001 coating as compared with the other two coatings. Observed maximum pit depth does support this to a degree, with the as-sprayed 5001 coating having a maximum pit depth twice that of the 5002 and more than ten times that of the PG-AMP-10 and 316L substrate. However, the maximum pit depth in both heat treated samples in the 5001 powder is equal to that of the 5002. Differences in pit depth were also observed between the PG-AMP-10 and 5002 powders both of which are 316 thereby making a conclusive observation of the differences between 304L and 316L behavior difficult. Additionally, other pitting metrics show better pitting performance in the 5001 coating than the 5002, although worse performance than PG-AMP-10 is suggested. The polarization data also shows little difference. In both as sprayed and heat treated conditions the pitting potential or lack thereof is nearly identical for all three powders. The open circuit potential of the 304L powder (5001) is observed to differ but no meaningful difference in pitting resistance is observed.

The initial step in the formation of a pit is nucleation of the pit in which the very first beginnings of a pit form on an otherwise flat surface [26]. Once the pit has been nucleated it allows the formation of a locally acid region and the pit begins to propagate as discussed in the introduction to this section. For this to occur however, the pit must be initially nucleated, and hence pit nucleation is a critical step in pitting corrosion. In these coatings there is a high degree of surface roughness due to porosity, so in effect there is no need for pit nucleation to occur at all since there are numerous existent regions that are essentially already pits. Given this, one would expect that the cold spray coating would show a high susceptibility to severe pitting which is not seen here. Interestingly it may be that the high density of ‘proto-pits’ from exposed porosity may actually help prevent the growth of these to large deep pits. The pitting mechanism requires a certain surface

region to act as a cathode to balance the anodic reaction in the pit. Given the limited solubility of oxygen in aerated salt solutions, a relatively large cathode area is required, and pit initiation within this area is suppressed by cathodic protection [26]. Thus this mechanism may effectively prevent any of the porosity regions from growing into larger pits.

Differences in powder phase distribution are known to exist as well. The 5001 powder is entirely austenite, while both 5002 and PG-AMP-10 powders have roughly 50% ferrite content at a microscopic level although the distribution of the ferrite is different between the powders. The ferrite phase is known to persist through the spraying process, so at least the as-sprayed PG-AMP-10 and 5002 have a substantial two phase composition. [3]. Data obtained in this work (III.C) shows that a substantial amount of ferrite is also present in heat treated samples. In the 5001 powder the ferrite content appears to increase, while in the other two it decreases. Pitting is known to preferentially occur in the ferrite phase in duplex stainless steels and austenitic stainless steels with significant ferrite composition [31]. Ferrite has also been shown to be associated with micro-segregation of chromium and hence lower corrosion resistance in that area. Ferrite/austenite grain interfaces are particularly prone to pit initiation [31]. While both the PG-AMP-10 and 5002 powders have roughly 50% ferrite, the PG-AMP-10 was shown to possess a large number of small ferrite grains intermixed within austenite grains while the 5002 has particles with a largely homogenous austenite or ferrite phase. Consequently, the PG-AMP-10 powder is expected to have a much larger amount of ferrite/austenite grain interfaces and hence could be more prone to pitting. Looking strictly at phase structure then, it would be expected that as-sprayed PG-AMP-10 would be the least corrosion resistant coating followed by 5002 as sprayed and then 5001 and heat treated powders. In fact the pitting potential observed in the 5002 powder is slightly higher than PG-AMP-10, but the difference is very minimal and thus not a significant finding.

There is a significant change in the coating porosity during heat treatment which could affect corrosion behavior. Surface roughness is known to affect uniform corrosion and pitting, with a rougher surface having worse performance [58]. Both heat treatments

have been shown to reduce sample porosity and hence would be expected to decrease corrosion rate. Examination of salt fog data for both the 5001 and 5002 powders produced evidence of better pitting performance in the heat treated powders correlating to the porosity reduction. Both powders show clear reduction in porosity as shown in Figures 10 and 11, and both heat treated samples show decreased pit density and depth, apt with increased pit area fraction and average area. The PG-AMP-10 powder shows generally opposite behavior with increased pit density and depth alongside decreased pit area fraction and average area following heat treatment. This powder exhibits the same trend toward decreased porosity with heat treatment, so its contradictory behavior makes a conclusion more difficult. Likewise, the polarization testing results show no clear difference in behavior between heat treatments and the decrease in porosity resulting from heat treatment does not correlate with the decreased corrosion resistance seen.

Evidence of substantial corrosion on the sides of the coating area was also noted on most samples following salt fog testing. This is believed to be a result of salt water condensing and standing upon these surfaces but could also reflect galvanic corrosion between the substrate and coating. Significant differences in open circuit potential between bare substrate and coated samples were observed in polarization testing with the substrate samples being more noble relative to the sprayed coatings. This could lead to galvanic corrosion occurring in the salt fog chamber with the relatively anodic coating suffering greater corrosion. The PG-AMP-10 as-sprayed sample shows the greatest open circuit potential difference from the substrate, with 5001 950°C/1 hr and 5001 and 5002 800°C/2 hrs heat treated samples also showing a notable difference. Other samples showed an open circuit potential nearly identical to that of the substrate so galvanic corrosion is unlikely in there samples. There is also likely crevice corrosion occurring at the substrate/coating interface due to poor adhesion leaving gaps and open areas here. Examination of the samples does not show any clear conclusion whether the observed corrosion correlates with these galvanic differences although there is evidence of crevice corrosion occurring. This can be seen in Figure 57.



Figure 57. Photographs of samples following 1000 hours salt fog chamber exposure and cleaning with deionized water/methanol showing evidence of corrosion on coating sides. Top 5001; middle 5002; bottom PG-AMP-10.

THIS PAGE INTENTIONALLY LEFT BLANK

V. CONCLUSION

All three of the austenitic cold spray coatings investigated were found to show worse corrosion performance than bulk 316L stainless steel with a significantly lower pitting potential, greater current in the passive region, and greater mass loss during exposure testing. The best performance was observed in non heat treated 304L coatings. Heat treatments of 800°C for 2 hours and 950°C for 1 hour both resulted in a significant further decrease in corrosion performance compared to bulk 316L stainless steel in all three powders. Both treatments in all three powders exhibited little or no passivation behavior during polarization testing and increased mass loss during exposure testing. Uniform corrosion rates of 4-6.5 mills per year (MPY) were observed in as-sprayed samples with as high as 18 MPY observed in the heat treated samples. With typical coating thicknesses of 1.6-4.8 mm (0.025-0.075"), this high of rate means coating failure could occur quite rapidly in service. The open circuit potential was also found to vary from bulk 316L stainless steel for some of the coatings both as sprayed and following heat treatment. In all cases the coatings were anodic to bulk 316L stainless steel. Pitting corrosion measurements obtained from exposure testing showed evidence of numerous small shallow pits occurring in the coatings, with the greatest pit depth measured following 1000 hours of salt fog exposure being 7 μm . Evidence of instrument/analysis error in pitting measures was seen however making these results useful primarily for relative comparison rather than absolute measurements. Evidence of grain boundary sensitization in samples heat treated at 800°C for 2 hours was found, however comparably poor behavior was also observed in samples treated at 950°C for 1 hour that are unlikely to have suffered sensitization. The reason for this behavior could not be conclusively determined although the formation of sigma phase may be a cause. Overall, the corrosion behavior of the sold spray samples appears to be controlled by a combination of porosity and ferrite content. Heat treatment may actually help stabilizing the ferrite and thus further contribute to poor corrosion resistance. Minimization of the ferrite content in the powders is thus suggested to improve corrosion resistance. Carbon

contamination in the powder could also be an added reason for a higher chance of sensitization in cold sprayed coatings.

Previously published results indicating the successful use of the low pressure cold spray process to produce an austenitic stainless steel coating were verified and some improvement in coating quality was observed with an increased standoff distance. An interesting phenomena was observed in which the coating would completely detach from the substrate in some cases during spraying of an additional layer. It was concluded that this may be caused by residual stresses in the coating combined with a weak coating/substrate bond. This phenomena has serious potential impact on the ability to produce a useable coating and should be investigated further. Heat treatment of applied coatings was observed to produce a decrease in porosity and changes in the phase distribution. Evidence of a significant amount of ferrite was found in all samples. No significant changes in elemental distribution were observed with heat treatment. Evidence of recrystallization heat treatment was observed and the recrystallization temperature determined to lie between 600°C and 800°C. Further mechanical testing of annealed coatings may be worthwhile to investigate and improvement in mechanical properties and determine what the optimal balance is between improved mechanical properties (if any) and decreased corrosion resistance resulting from heat treatment.

APPENDIX A. CHARACTERIZATION

A. COATING MICROGRAPHS

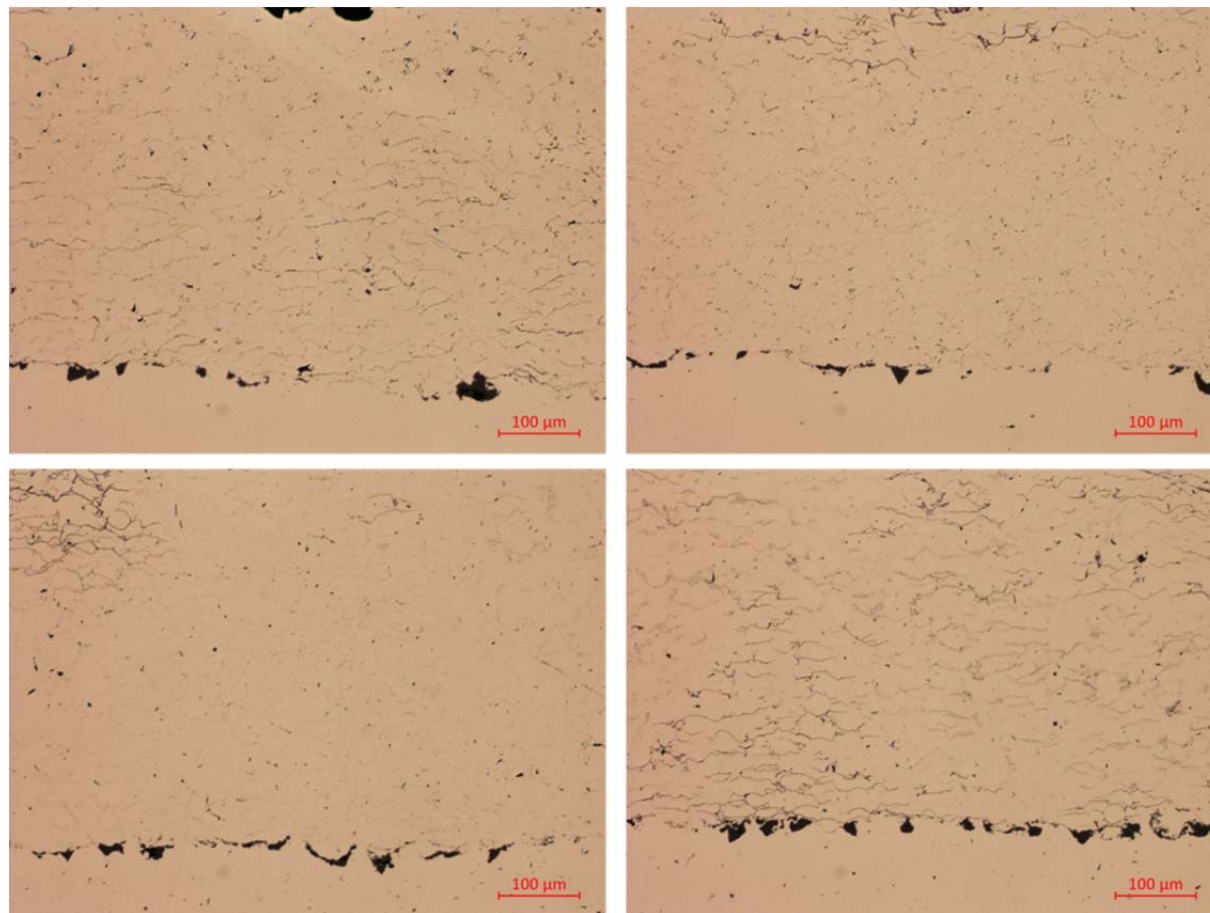


Figure 58. Low resolution optical micrographs of 5001 coating: As sprayed (top left); 950°C/1 hr (top right); 800°C/2 hrs (bottom left); 600°C/8 hrs (bottom right).

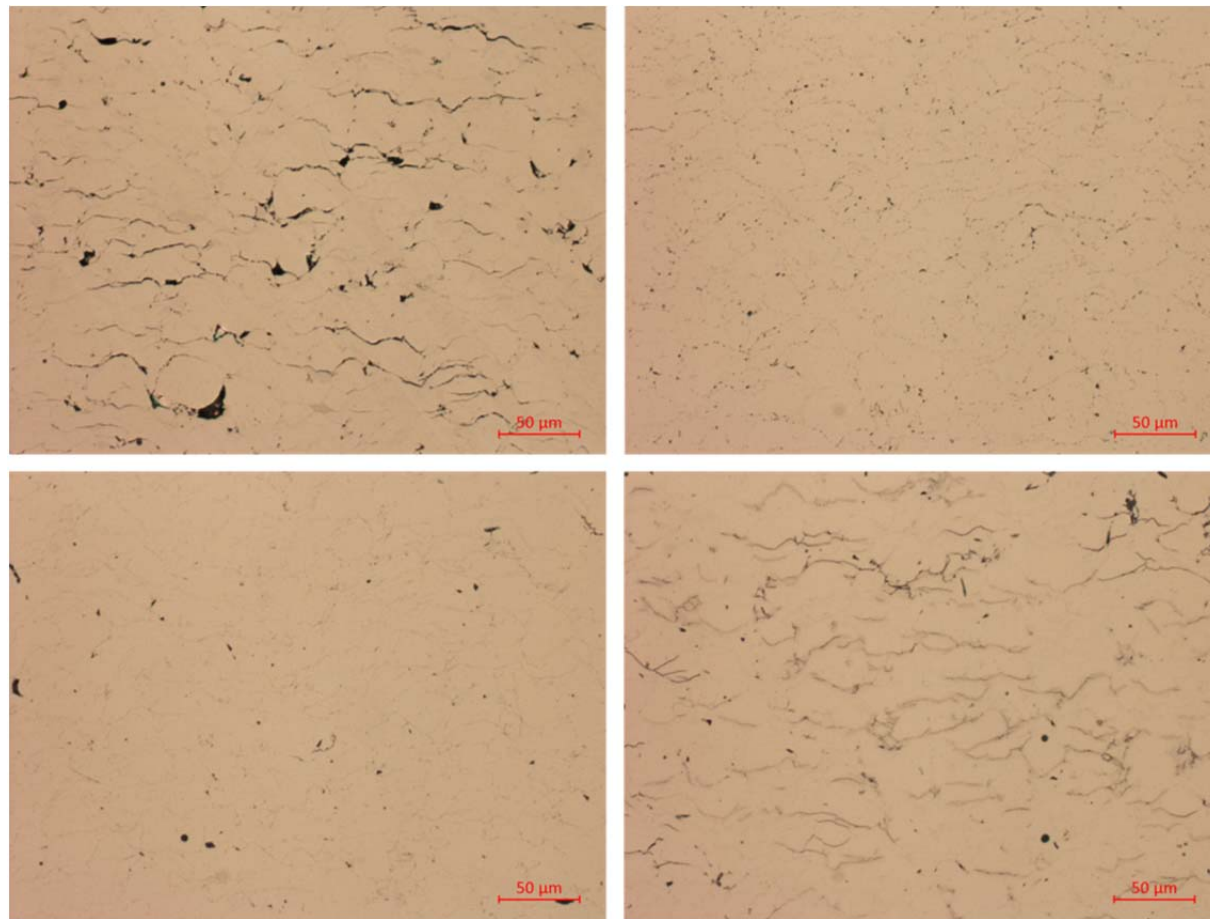


Figure 59. High resolution optical micrographs of 5001 coating: As sprayed (top left); 950°C/1 hr (top right); 800°C/2 hrs (bottom left); 600°C/8 hrs (bottom right).

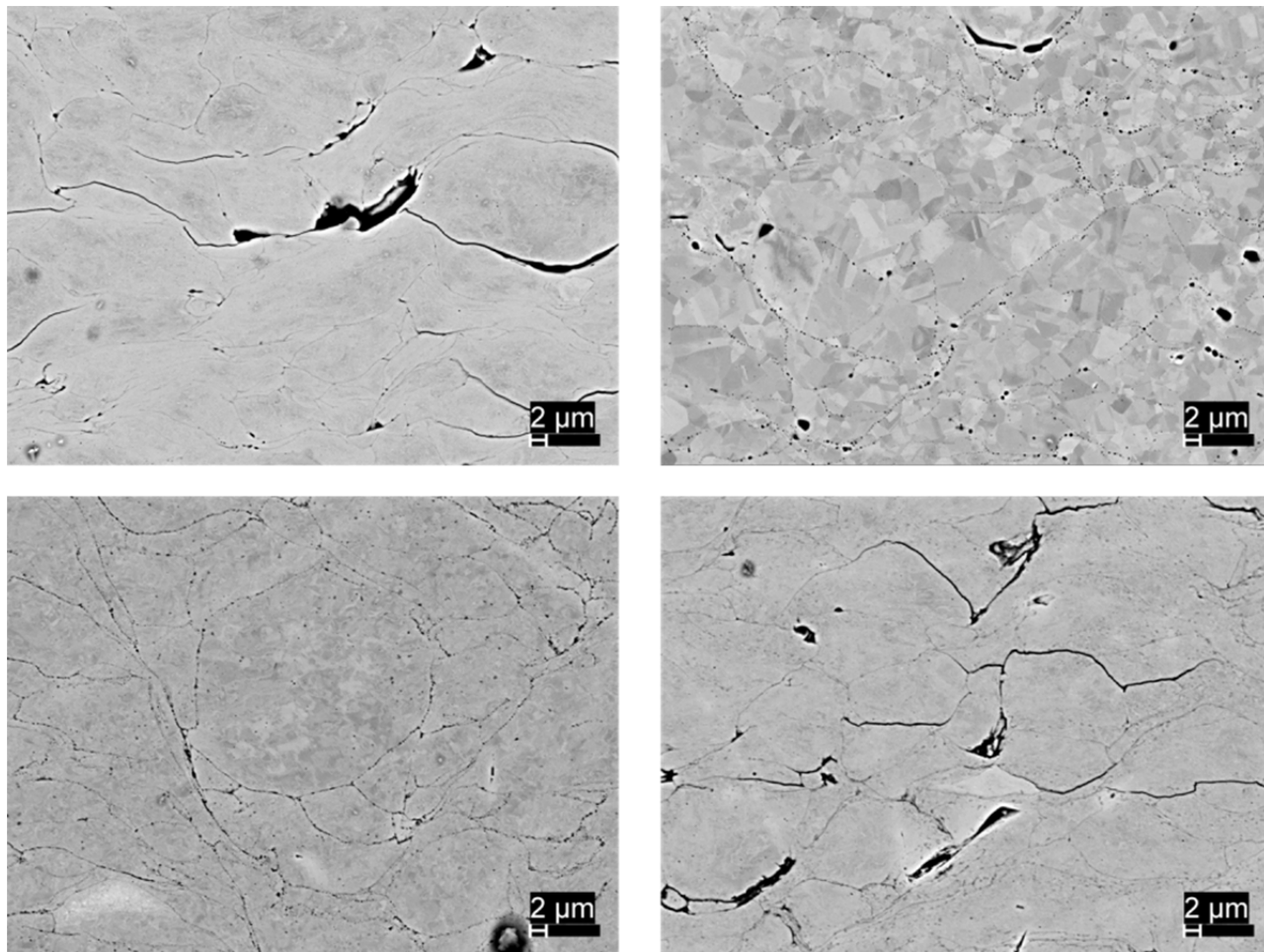


Figure 60. Low resolution SEM micrographs of 5001 coating, backscatter mode: As sprayed (top left); 950°C/1 hr (top right); 800°C/2 hrs (bottom left); 600°C/8 hrs (bottom right).

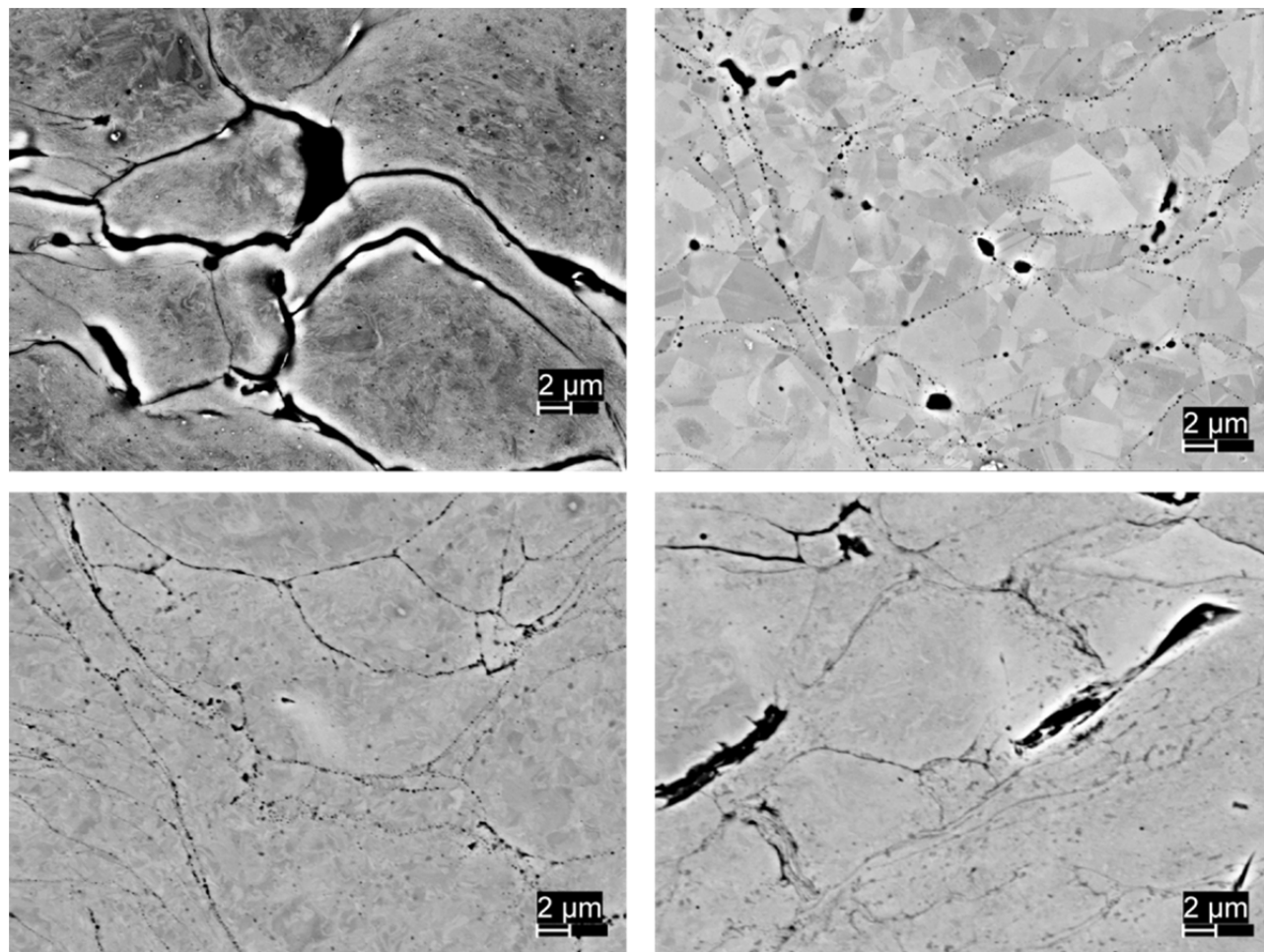


Figure 61. High resolution SEM micrographs of 5001 coating, backscatter mode: As sprayed (top left); 950°C/1 hr (top right); 800°C/2 hrs (bottom left); 600°C/8 hrs (bottom right).

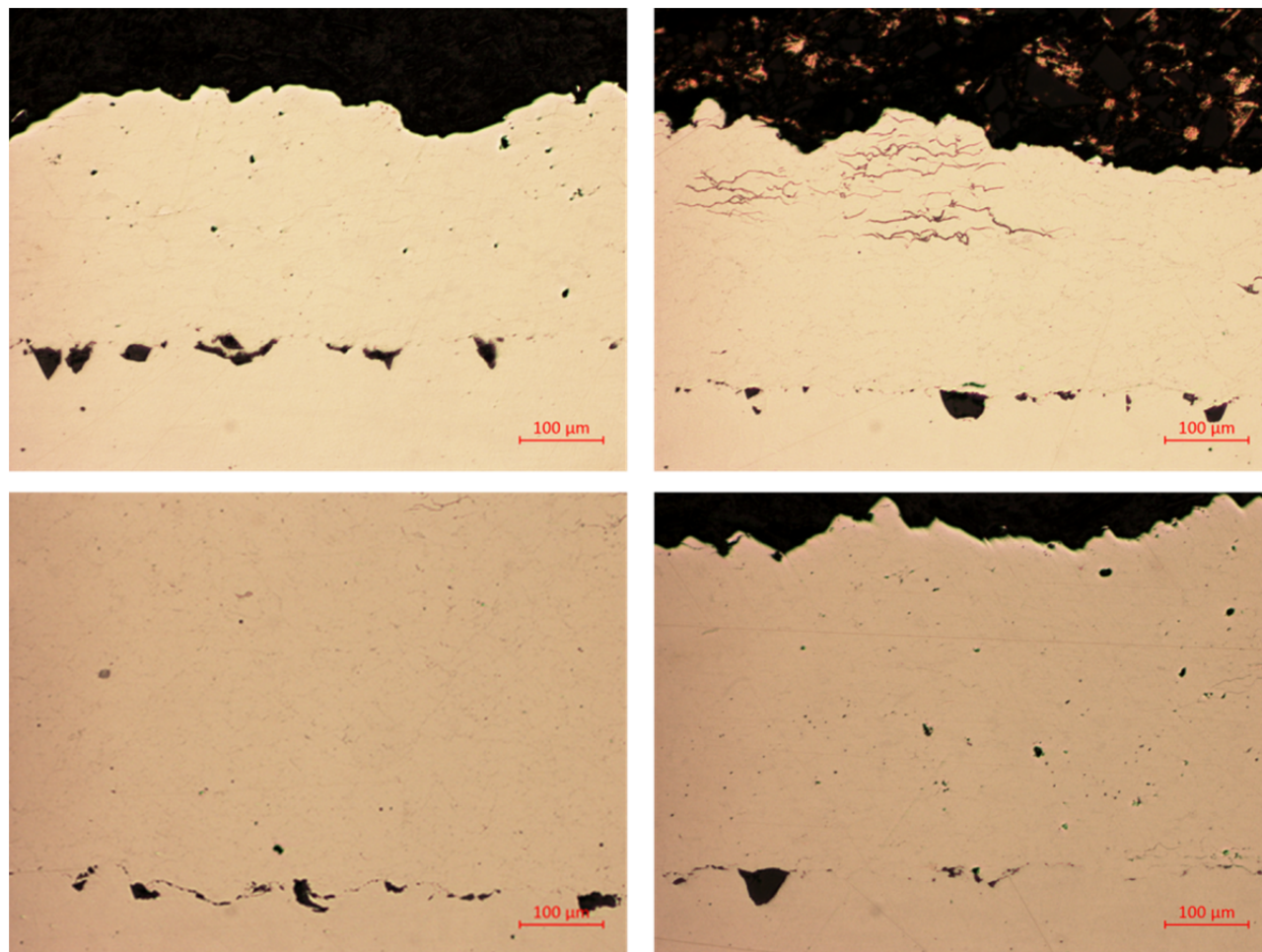


Figure 62. Low resolution optical micrographs of 5002 coating: As sprayed (top left); 950°C/1 hr (top right); 800°C/2 hrs (bottom left); 600°C/8 hrs (bottom right).

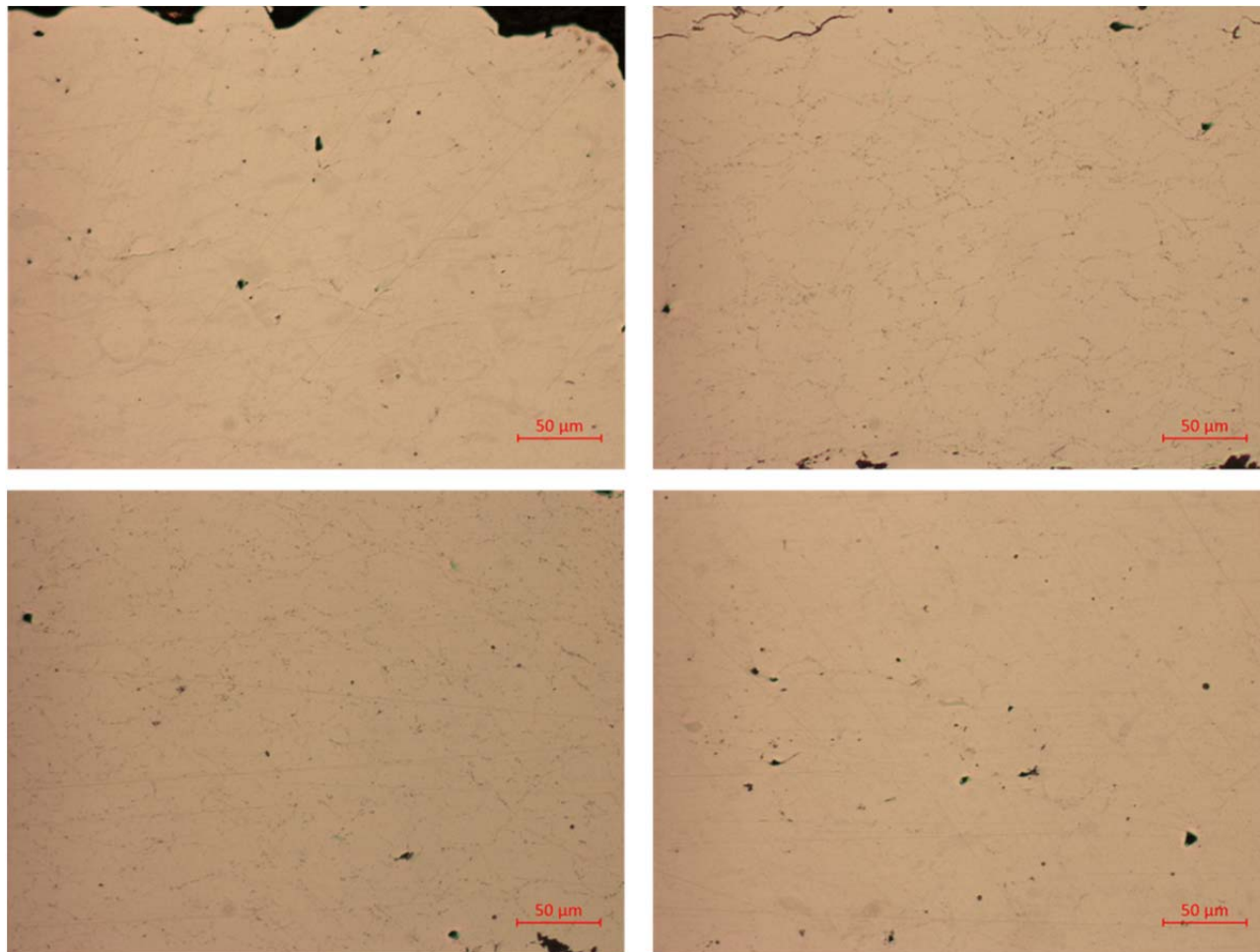


Figure 63. High resolution optical micrographs of 5002 coating: As sprayed (top left); 950°C/1 hr (top right); 800°C/2 hrs (bottom left); 600°C/8 hrs (bottom right).

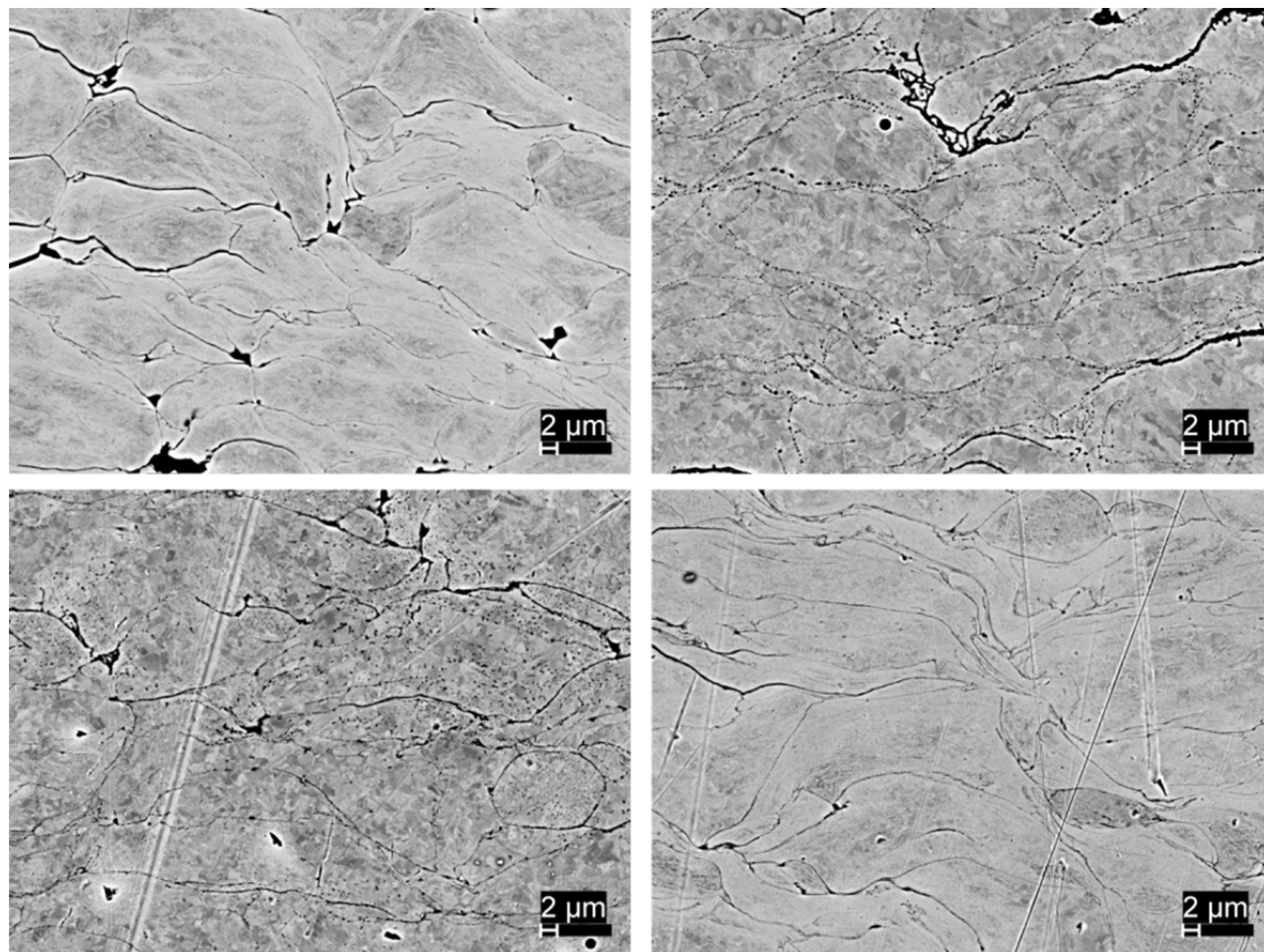


Figure 64. Low resolution SEM micrographs of 5002 coating, backscatter mode: As sprayed (top left); 950°C/1 hr (top right); 800°C/2 hrs (bottom left); 600°C/8 hrs (bottom right).

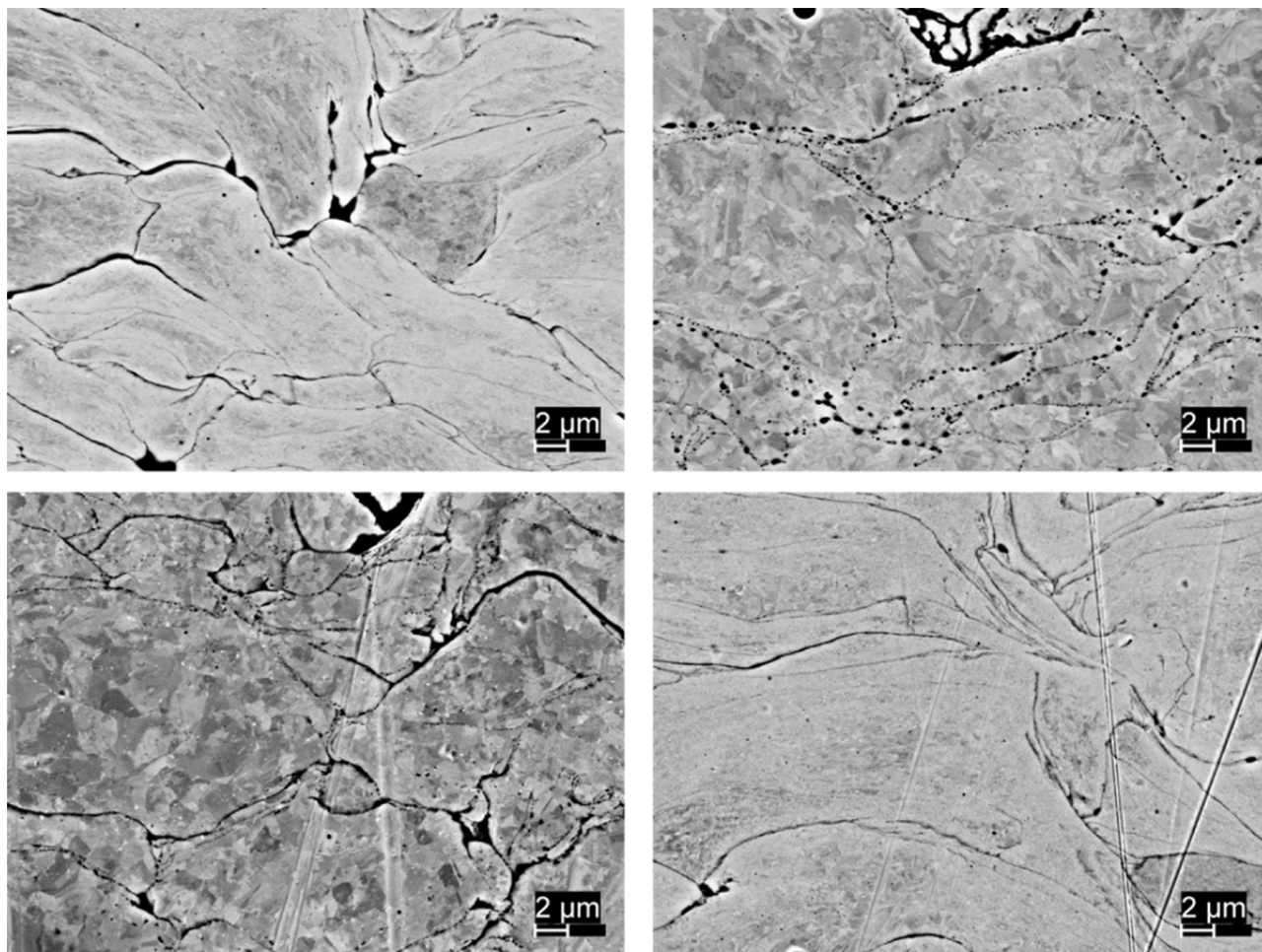


Figure 65. High resolution SEM micrographs of 5002 coating, backscatter mode: As sprayed (top left); 950°C/1 hr (top right); 800°C/2 hrs (bottom left); 600°C/8 hrs (bottom right).

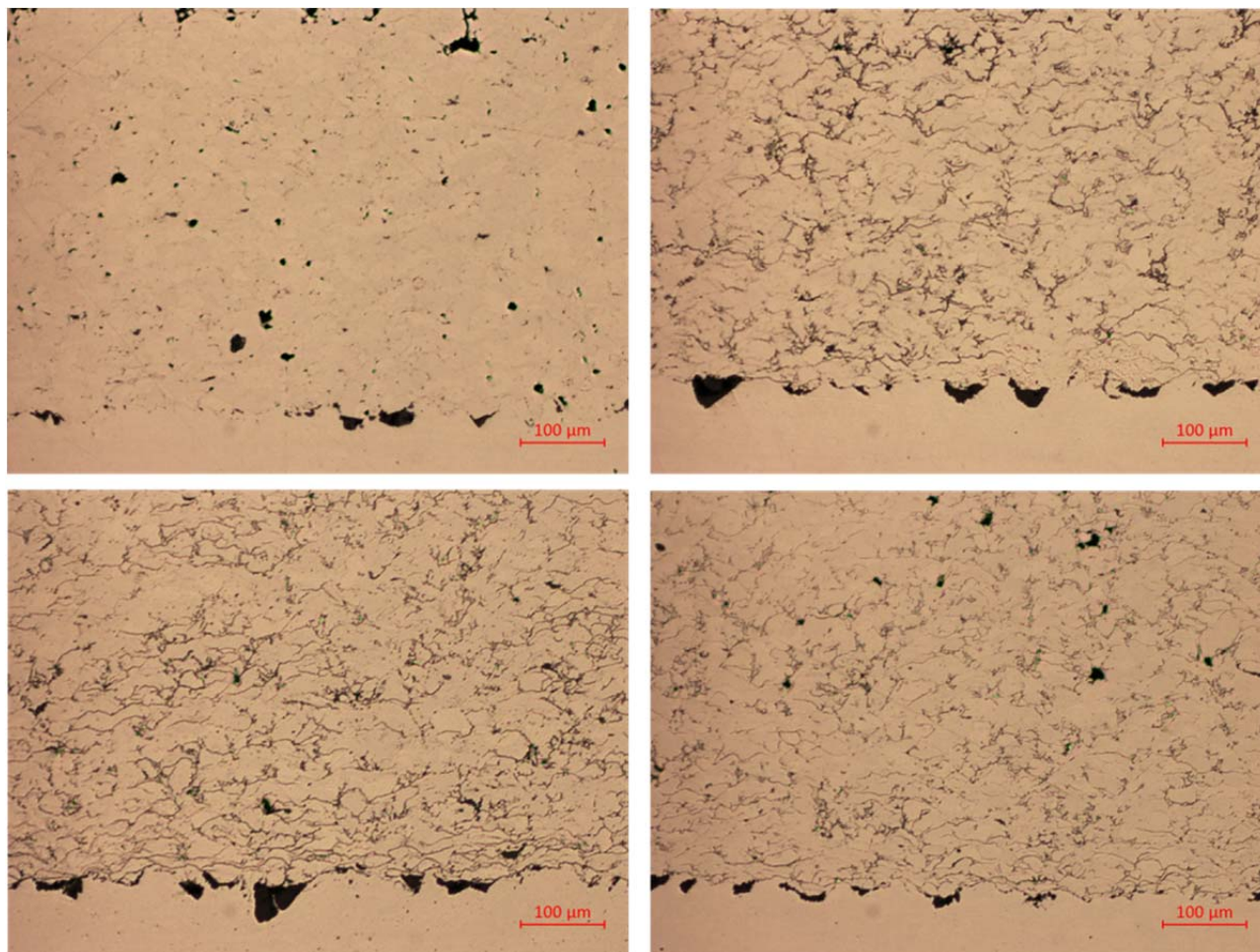


Figure 66. Low resolution optical micrographs of PG-AMP-10 coating: As sprayed (top left); 950°C/1 hr (top right); 800°C/2 hrs (bottom left); 600°C/8 hrs (bottom right).

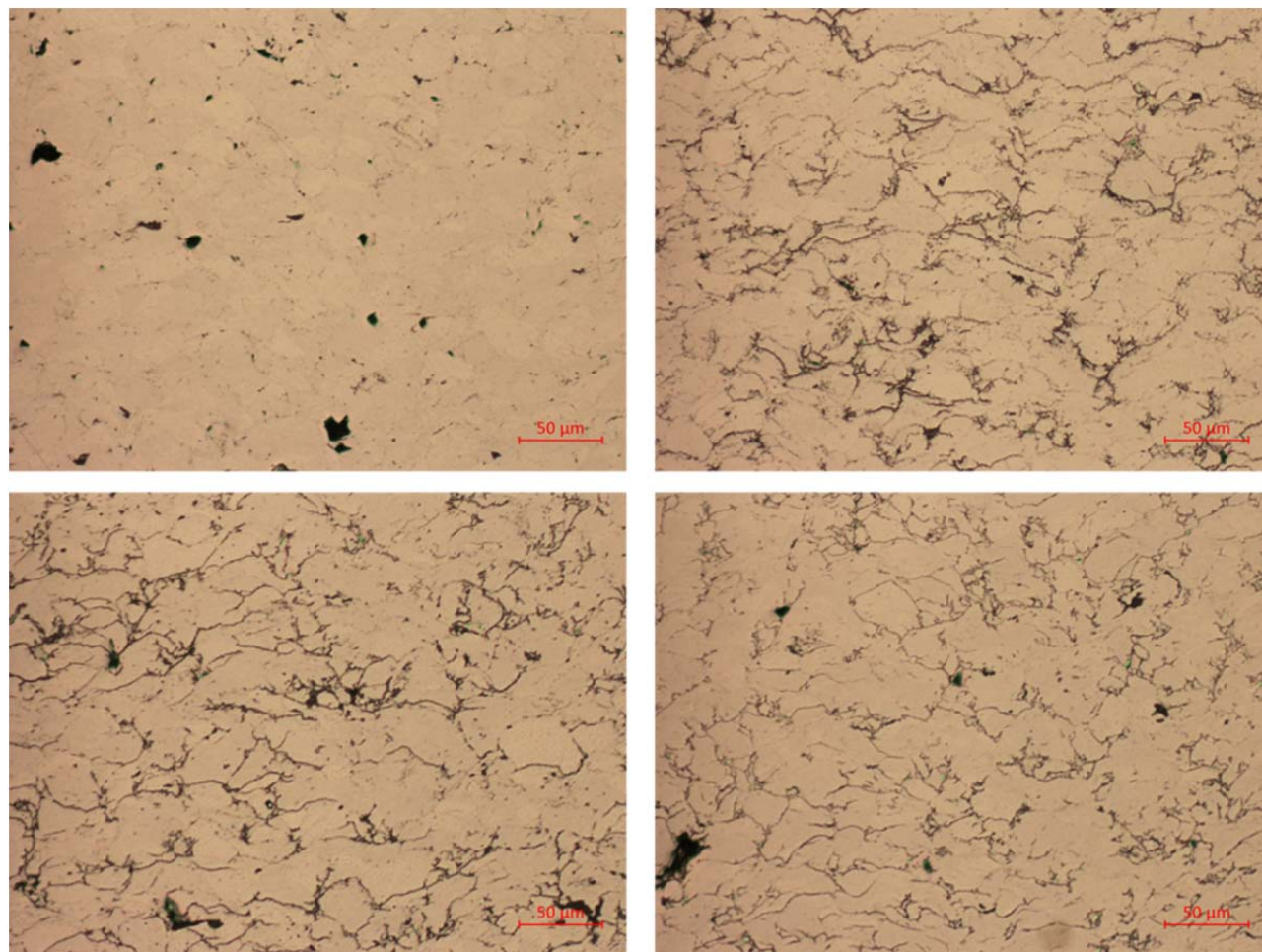


Figure 67. High resolution optical micrographs of PG-AMP-10 coating: As sprayed (top left); 950°C/1 hr (top right); 800°C/2 hrs (bottom left); 600°C/8 hrs (bottom right).

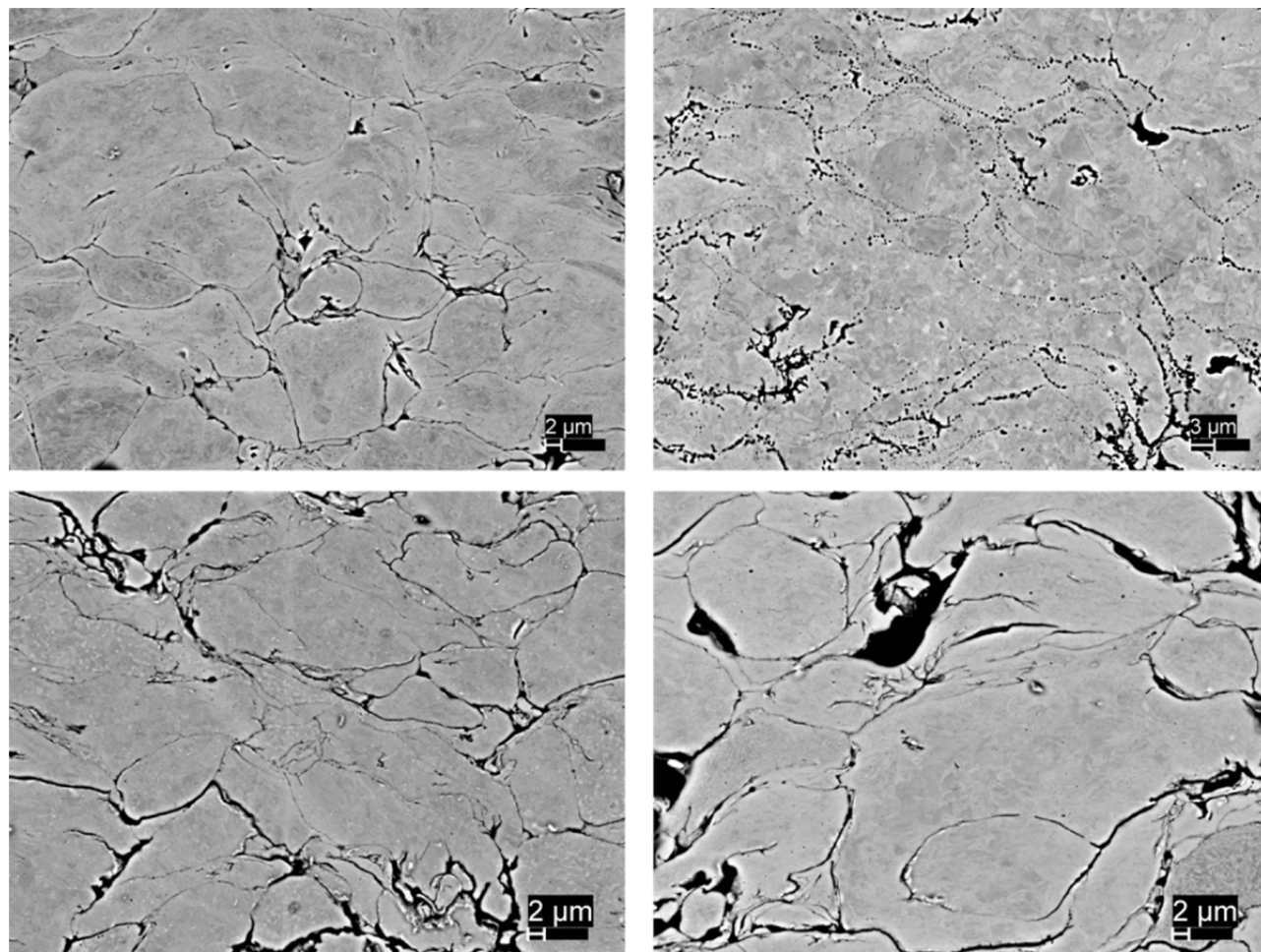


Figure 68. Low resolution SEM micrographs of PG-AMP-10 coating, backscatter mode: As sprayed (top left); 950°C/1 hr (top right); 800°C/2 hrs (bottom left); 600°C/8 hrs (bottom right).

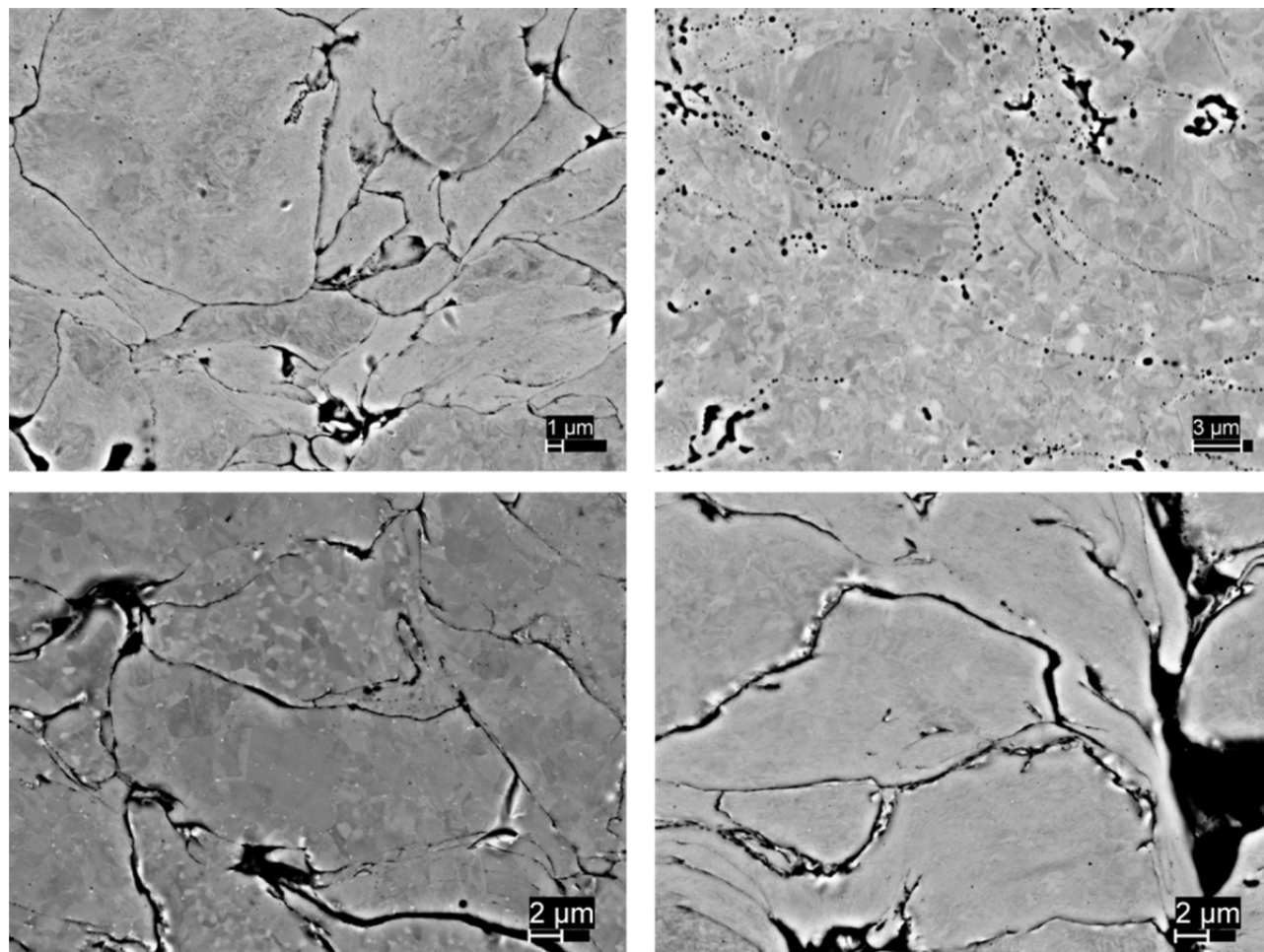


Figure 69. High resolution SEM micrographs of PG-AMP-10 coating, backscatter mode: As sprayed (top left); 950°C/1 hr (top right); 800°C/2 hrs (bottom left); 600°C/8 hrs (bottom right).

B. EDS MAPS

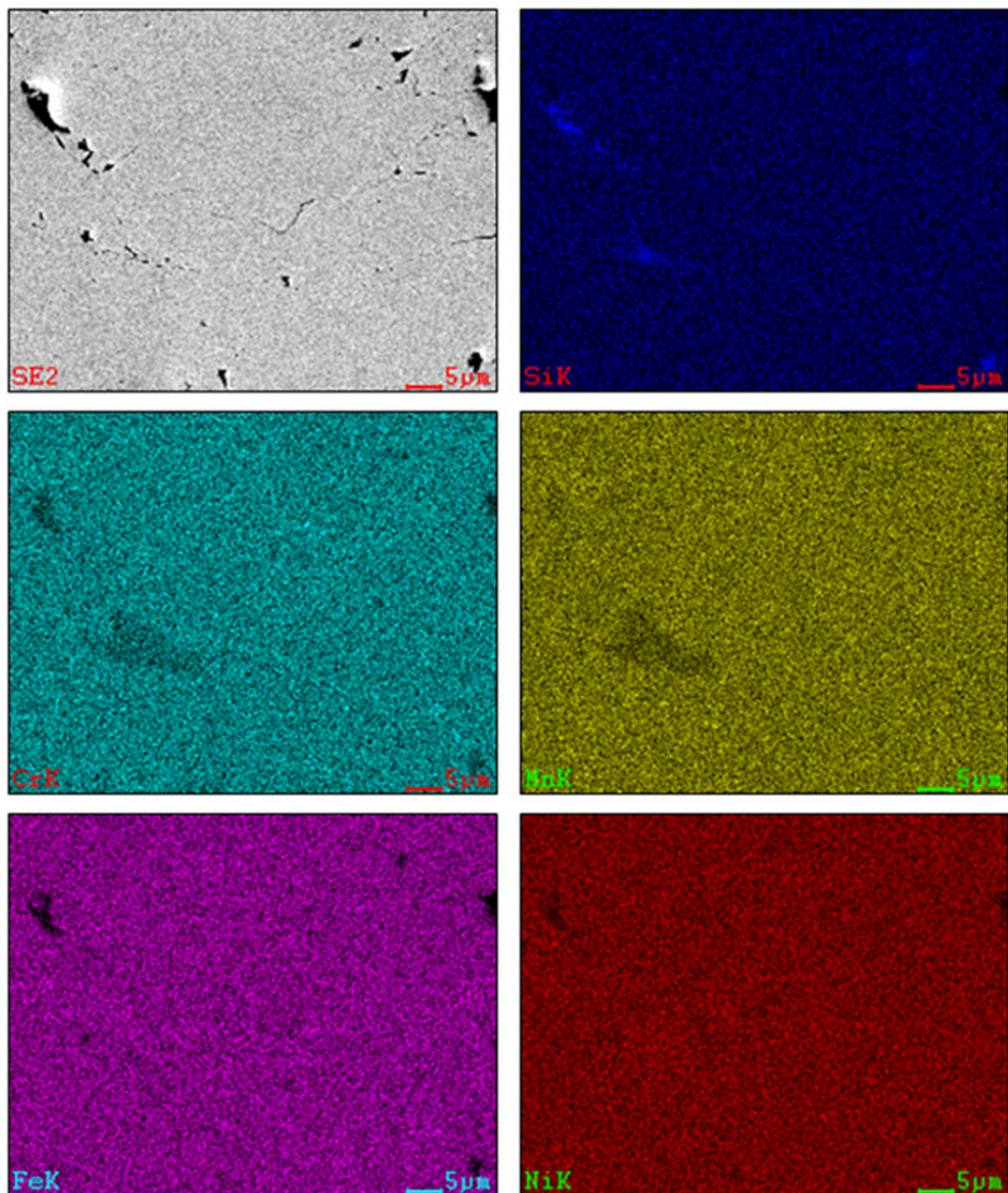


Figure 70. EDS Maps of 5001 powder as sprayed.

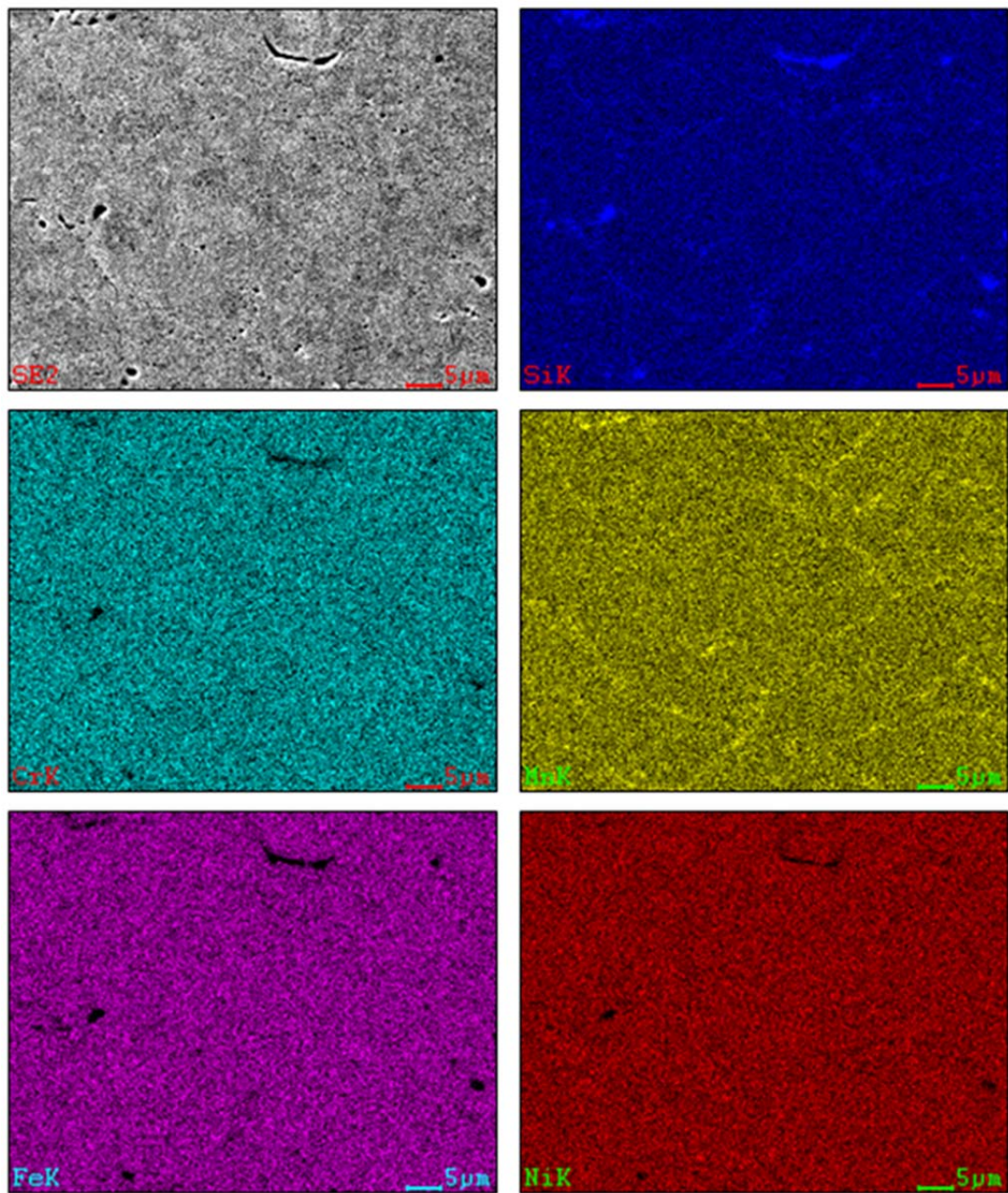


Figure 71. EDS Maps of 5001 powder, 950°C/1 hr heat treatment.

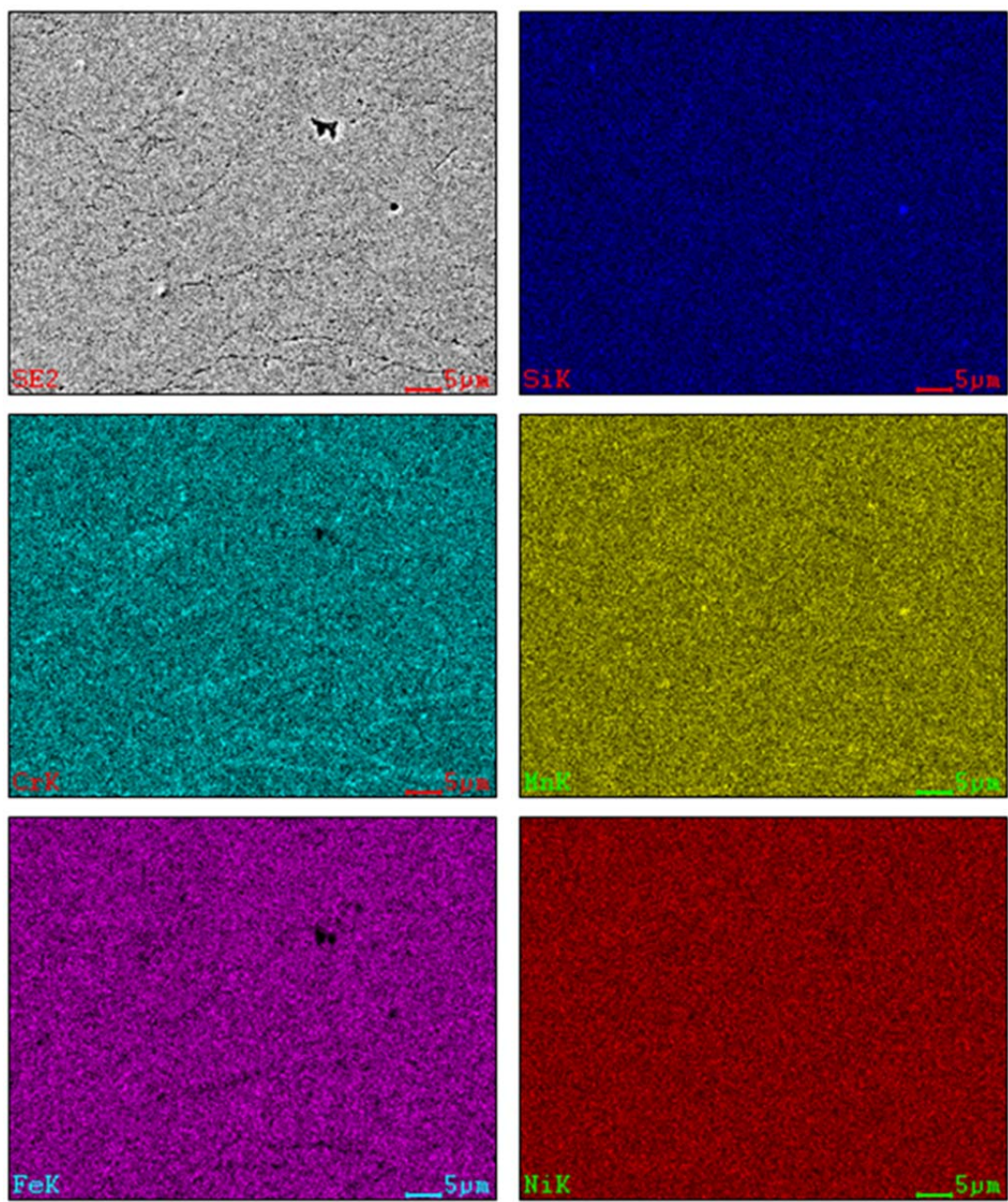


Figure 72. EDS Maps of 5001 powder, 800°C/2 hrs heat treatment.

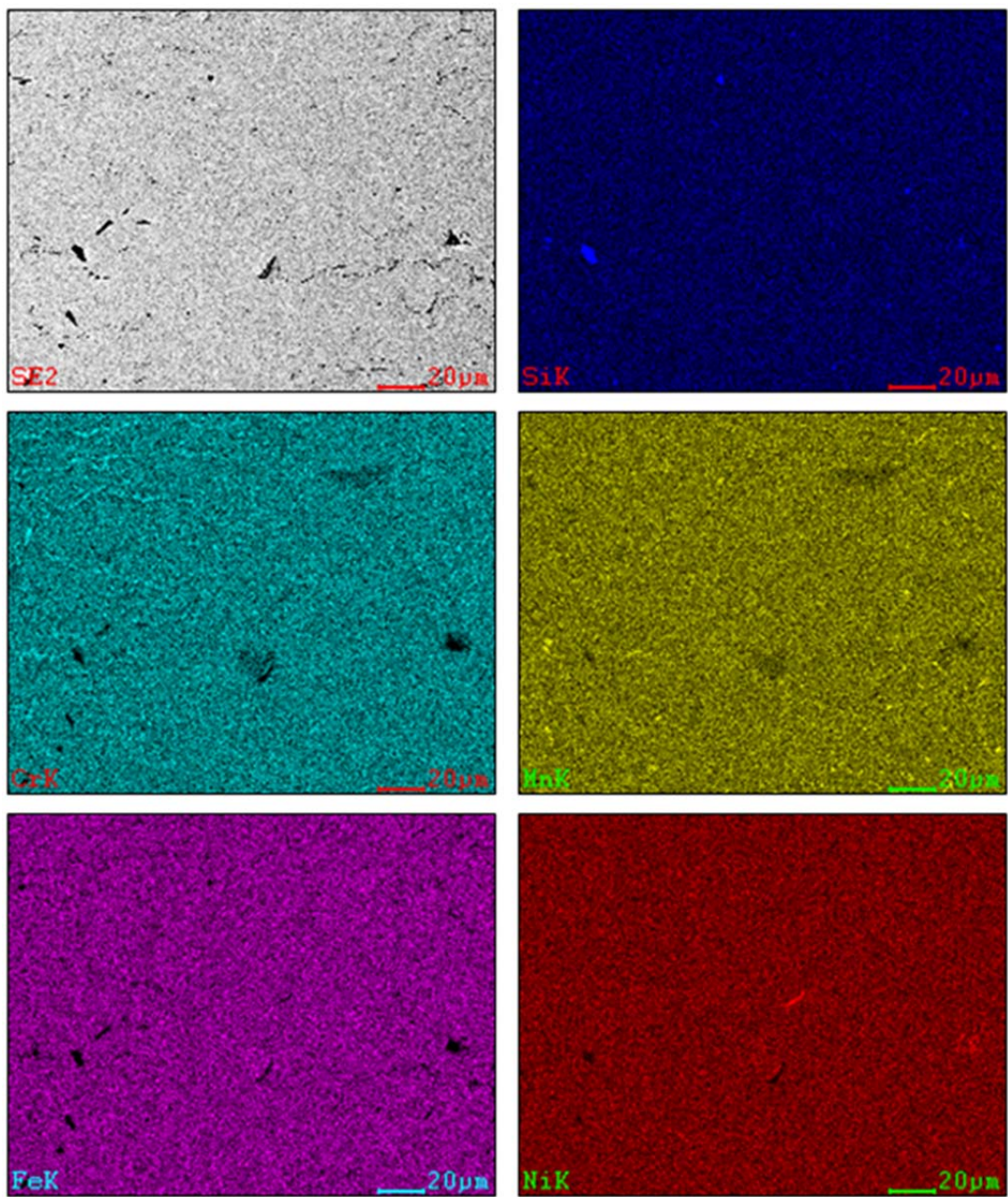


Figure 73. EDS Maps of 5001 powder, 600°C/8 hrs heat treatment.

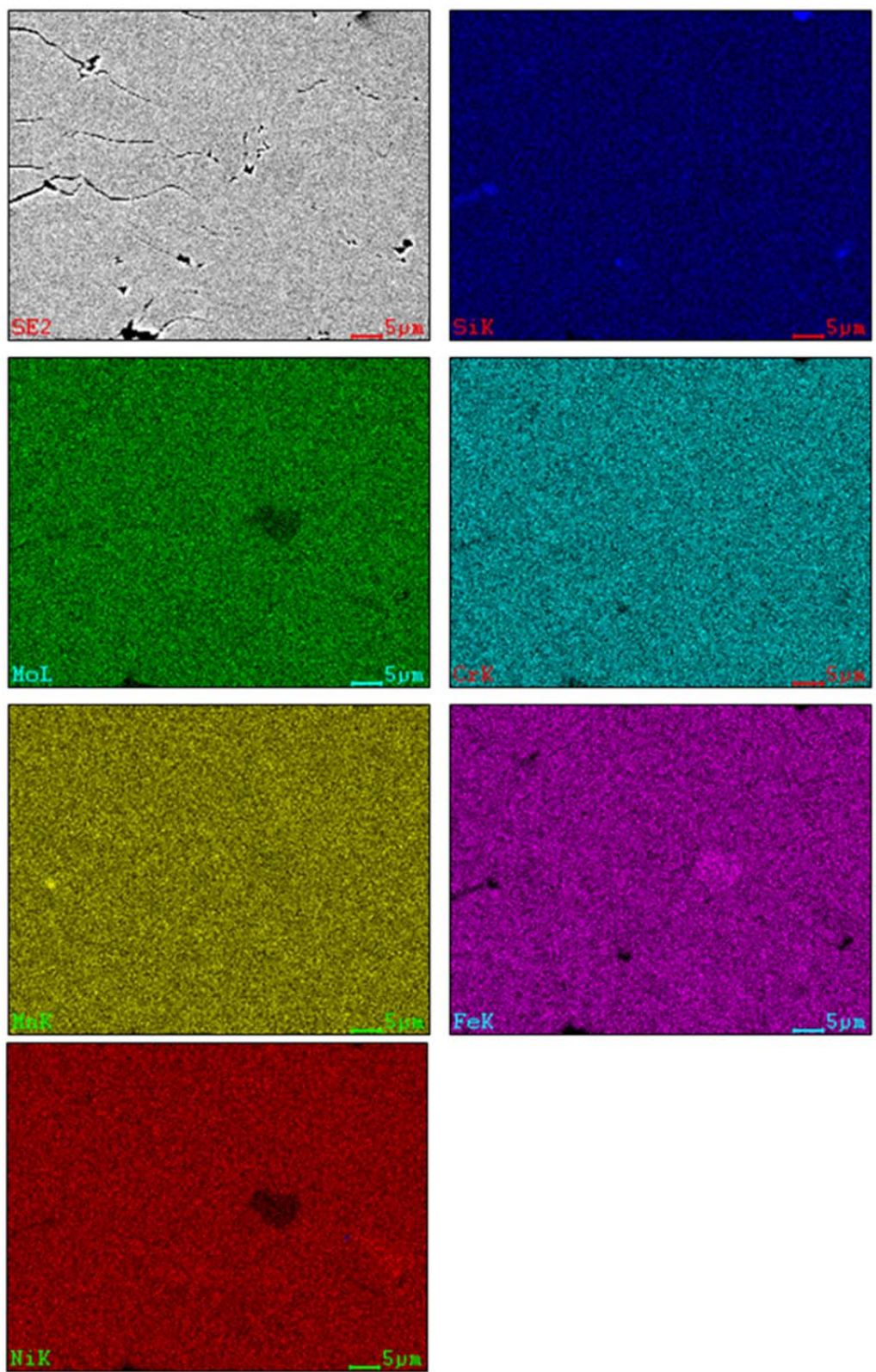


Figure 74. EDS Maps of as sprayed 5002 powder.

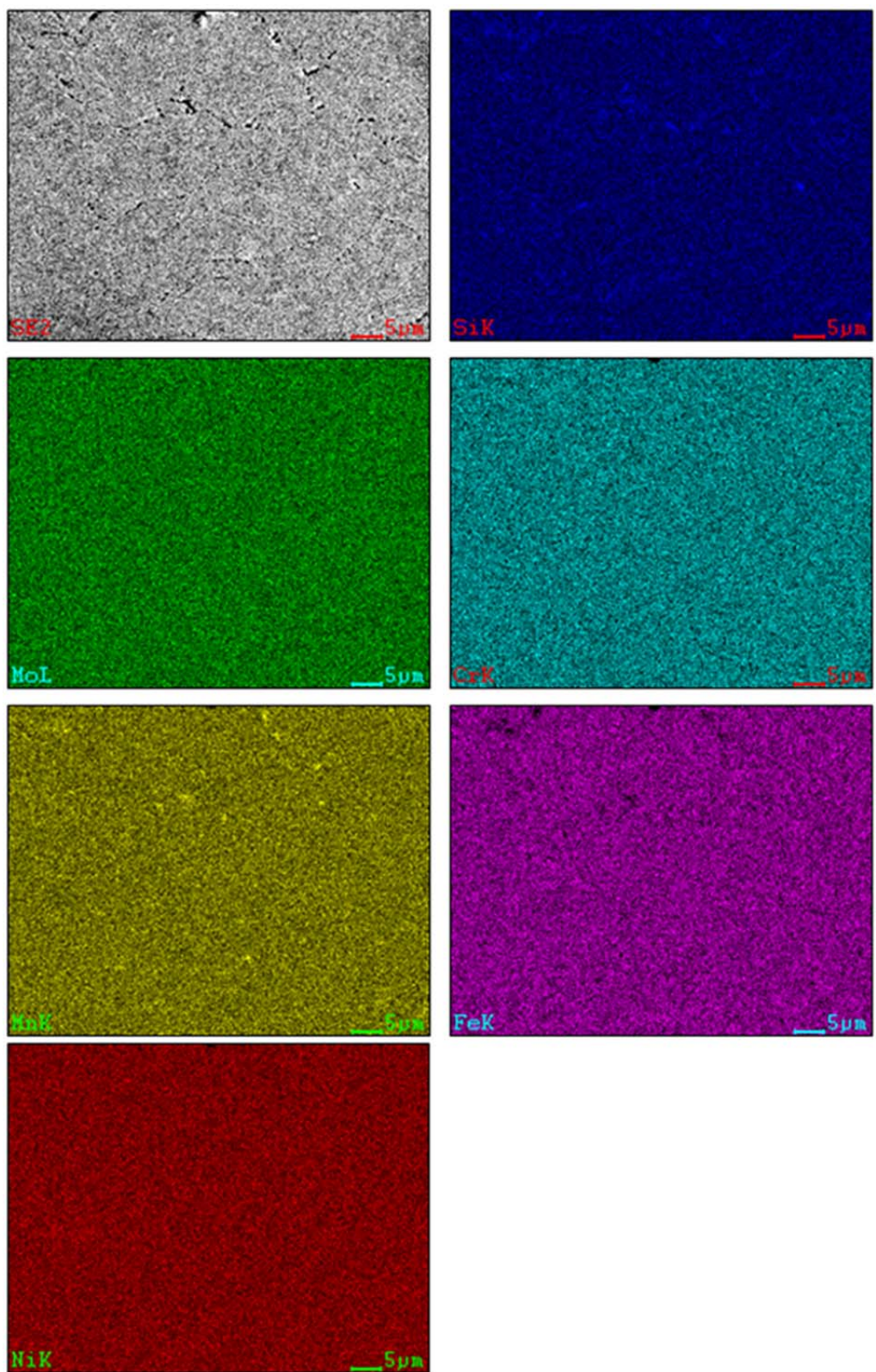


Figure 75. EDS Maps of 5002 powder, 950°C/1 hr heat treatment.

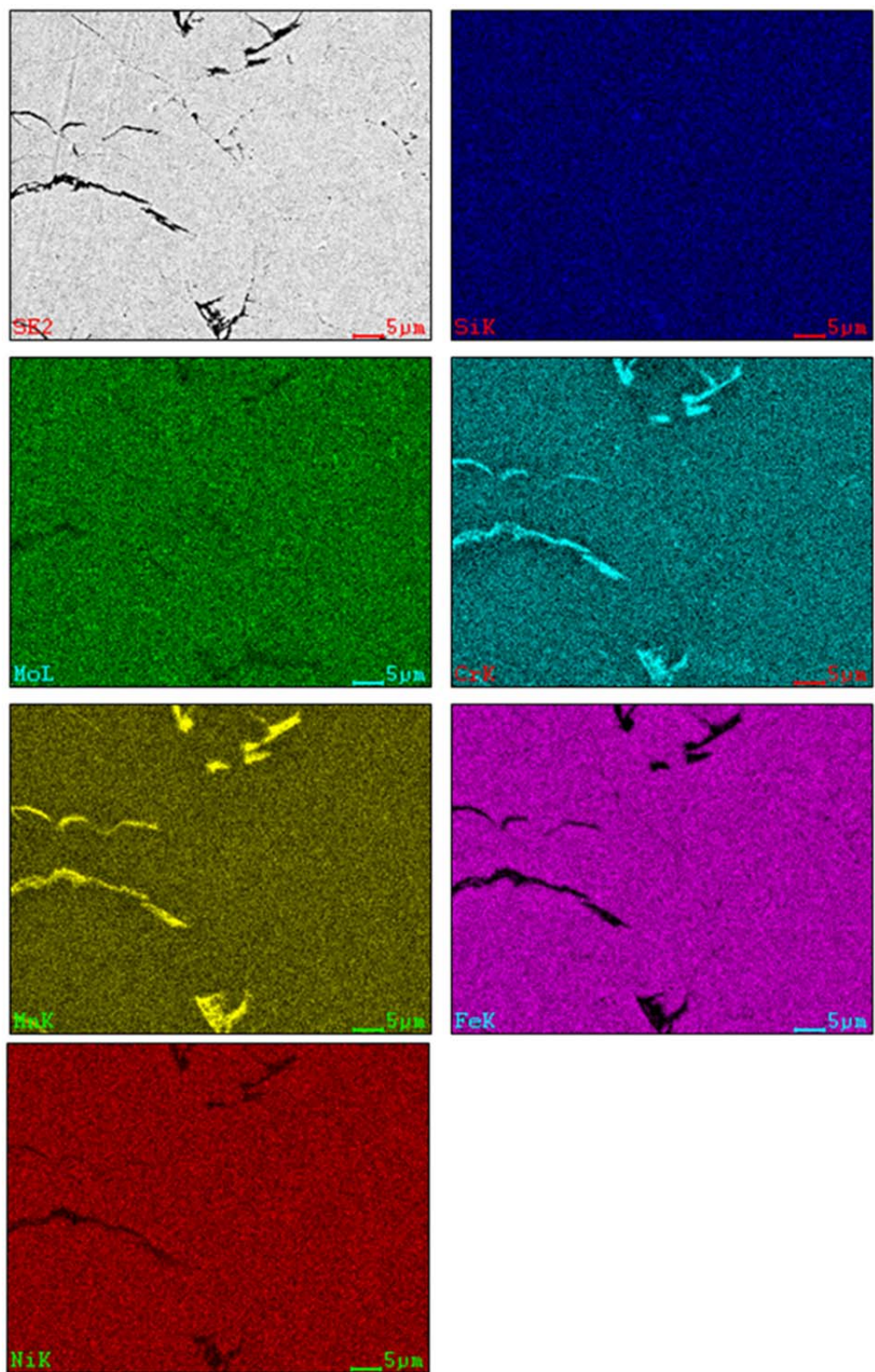


Figure 76. EDS Maps of 5002 powder, 800°C/2 hrs heat treatment.

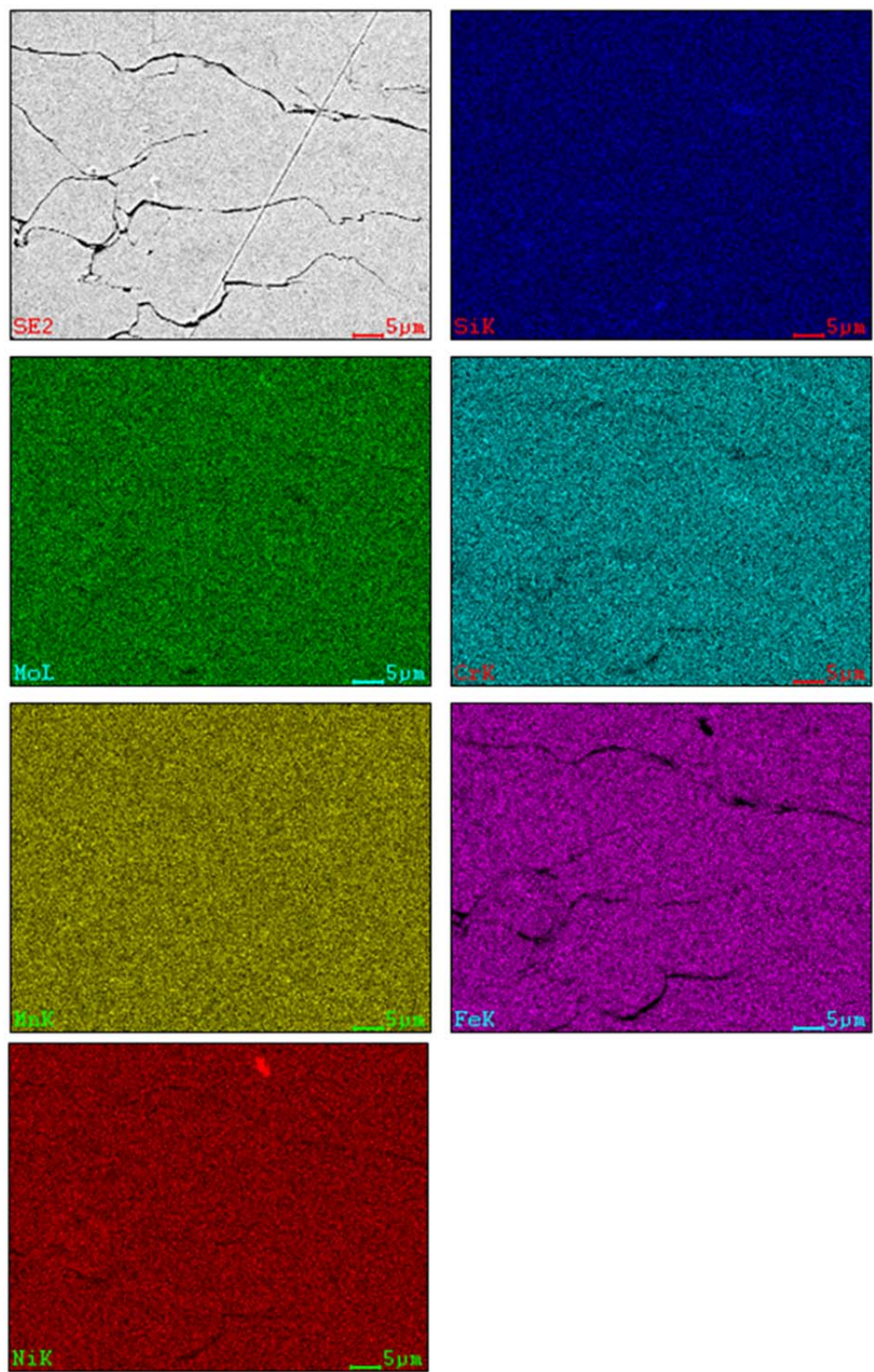


Figure 77. EDS Maps of 5002 powder, 600°C/8 hrs heat treatment.

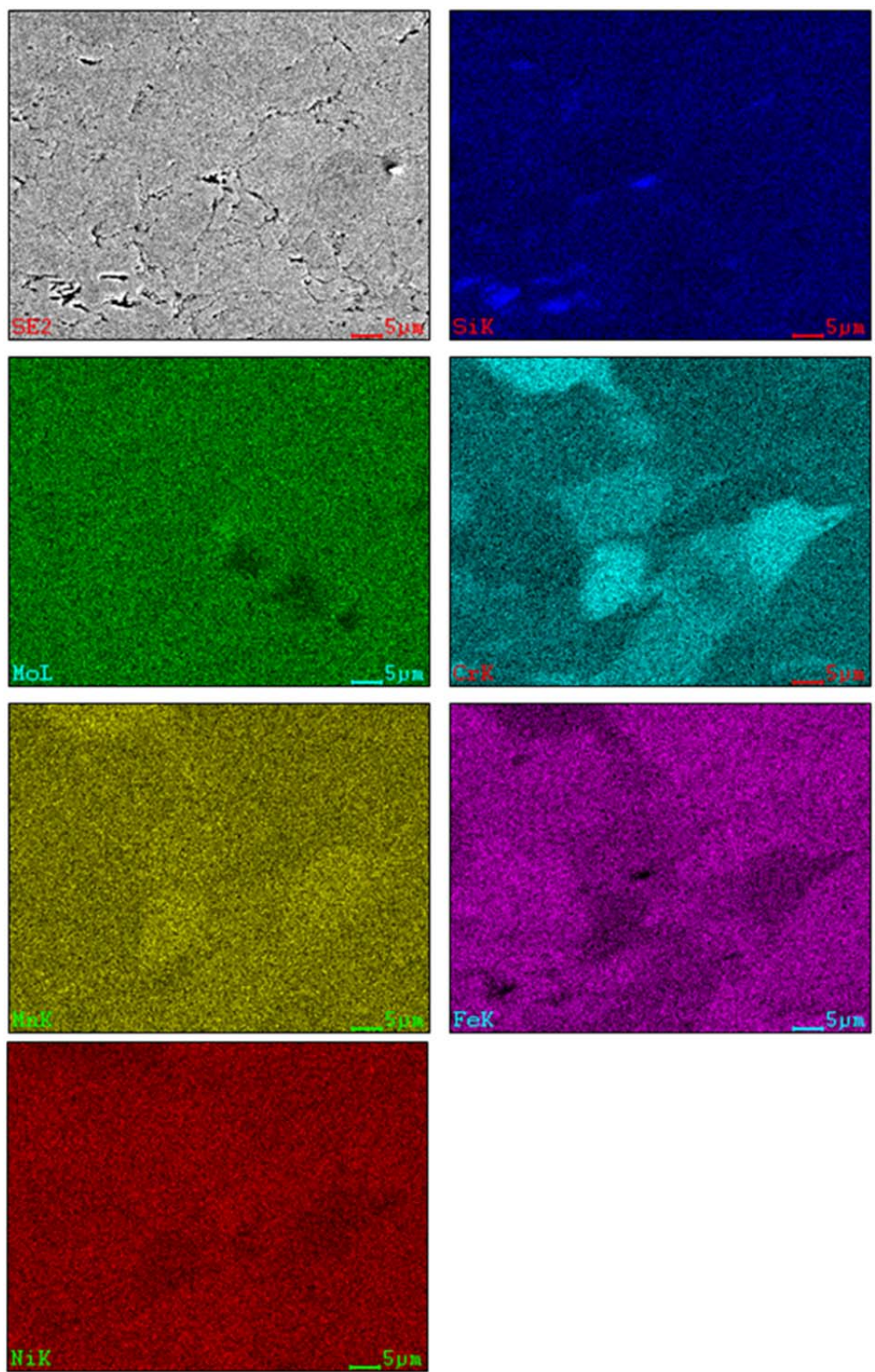


Figure 78. EDS Maps of as sprayed PG-AMP-10 powder.

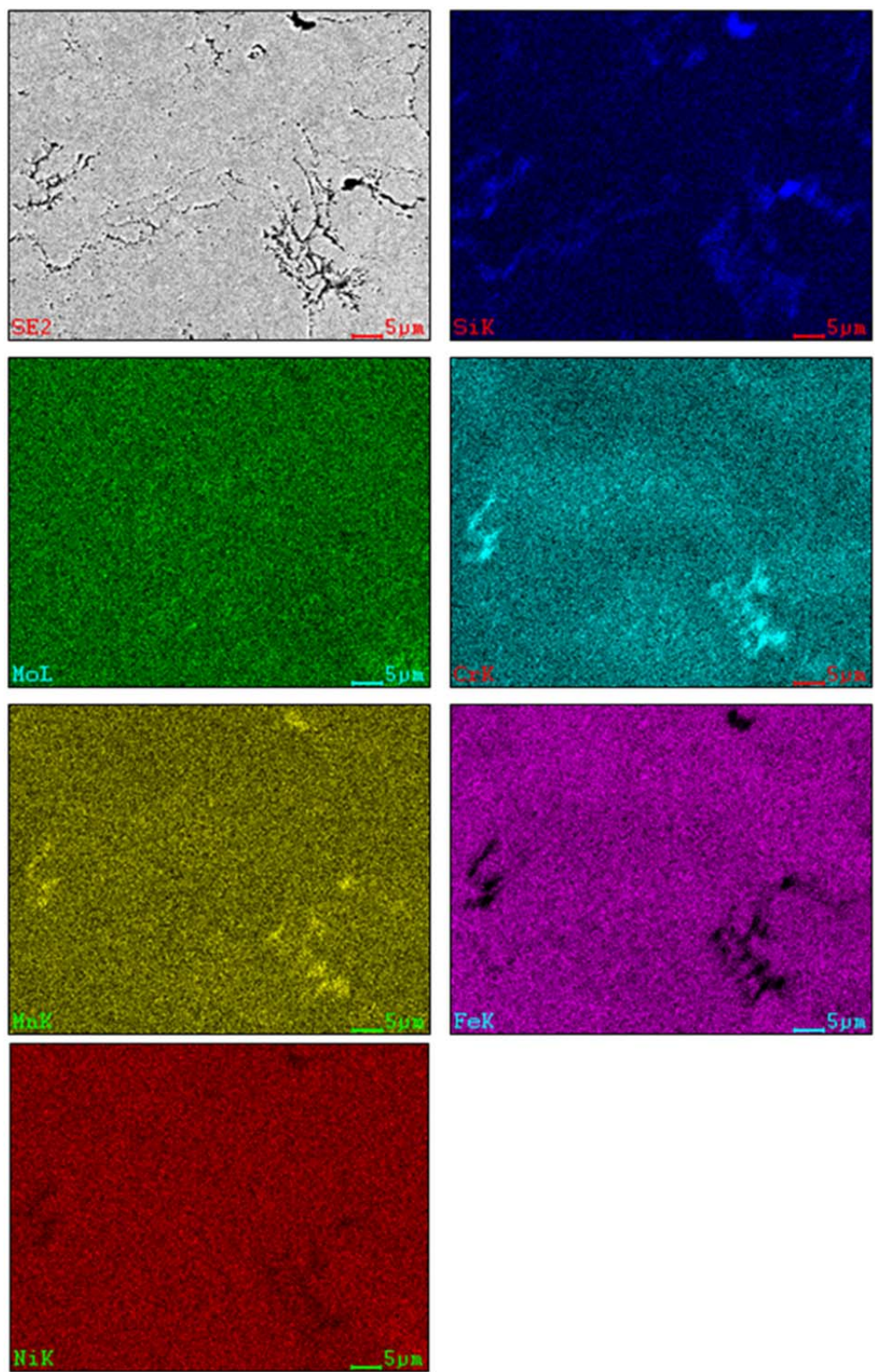


Figure 79. EDS Maps of PG-AMP-10 powder, 950°C/1 hr heat treatment.

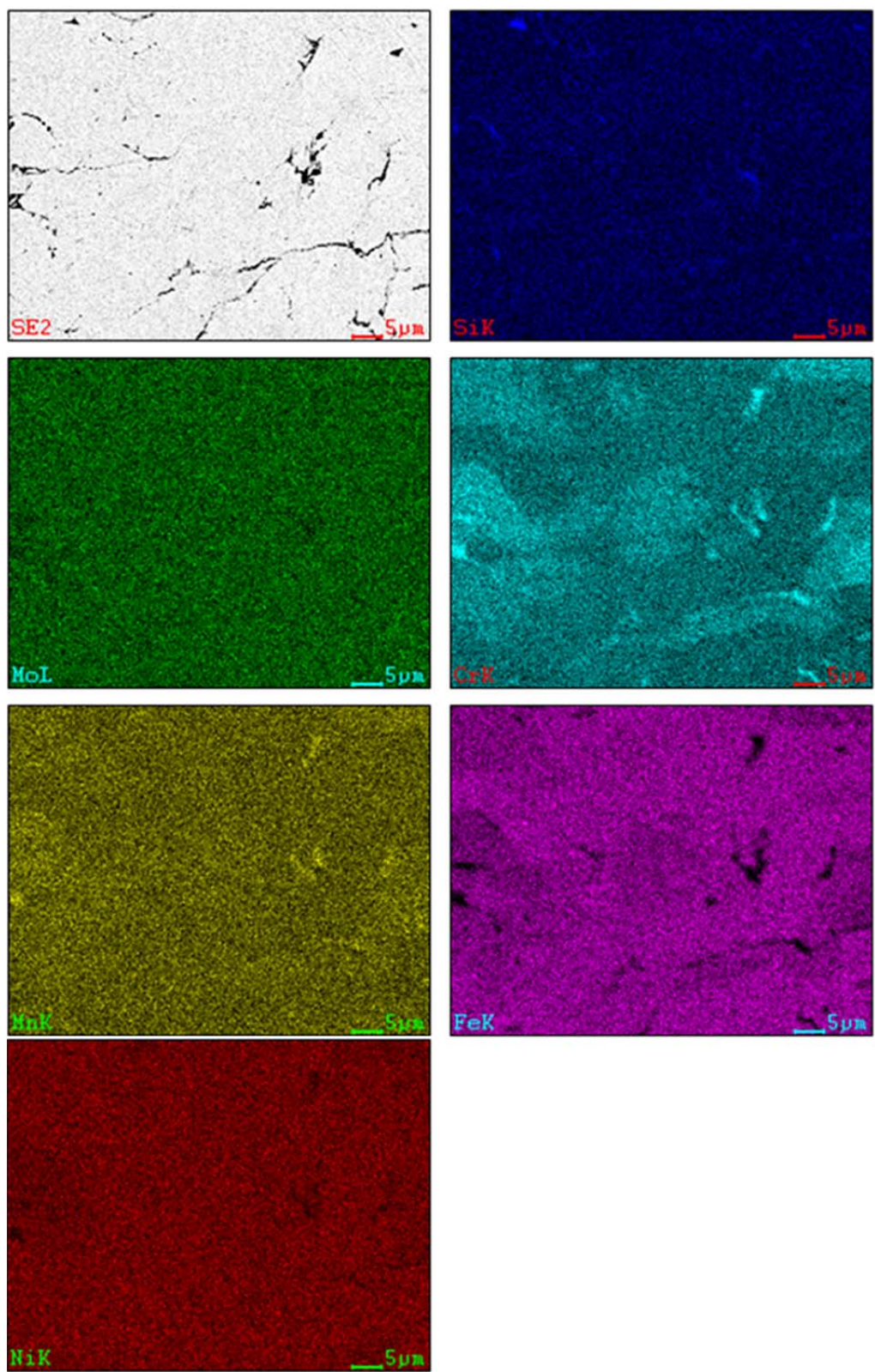


Figure 80. EDS Maps of PG-AMP-10 powder, 800°C/2 hrs heat treatment.

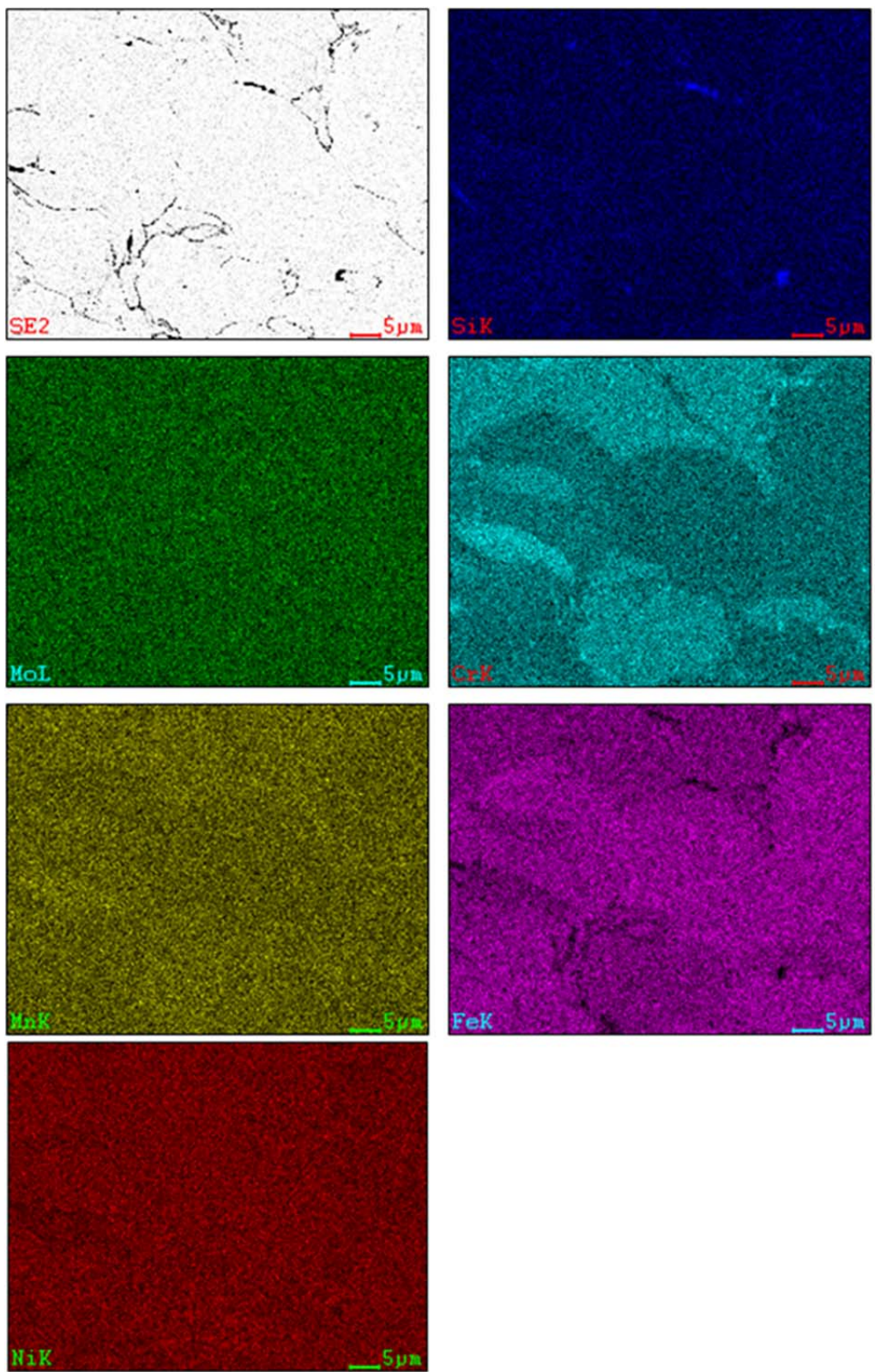


Figure 81. EDS Maps of PG-AMP-10 powder, 600°C/8 hrs heat treatment.

APPENDIX B. FOG CHAMBER RESULTS

A. SAMPLE PHOTOGRAPHS



Figure 82. 5001 Group 1 Photographs. As sprayed (left), 950°C/1 hr (center), 800°C/2 hrs (right).



Figure 83. 5001 Group 2 Photographs. As sprayed (left), 950°C/1 hr (center), 800°C/2 hrs (right).



Figure 84. 5001 Group 3 Photographs. As sprayed (left), 950°C/1 hr (center), 800°C/2 hrs (right).



Figure 85. 5002 Group 1 Photographs. As sprayed (left), 950°C/1 hr (center), 800°C/2 hrs (right).

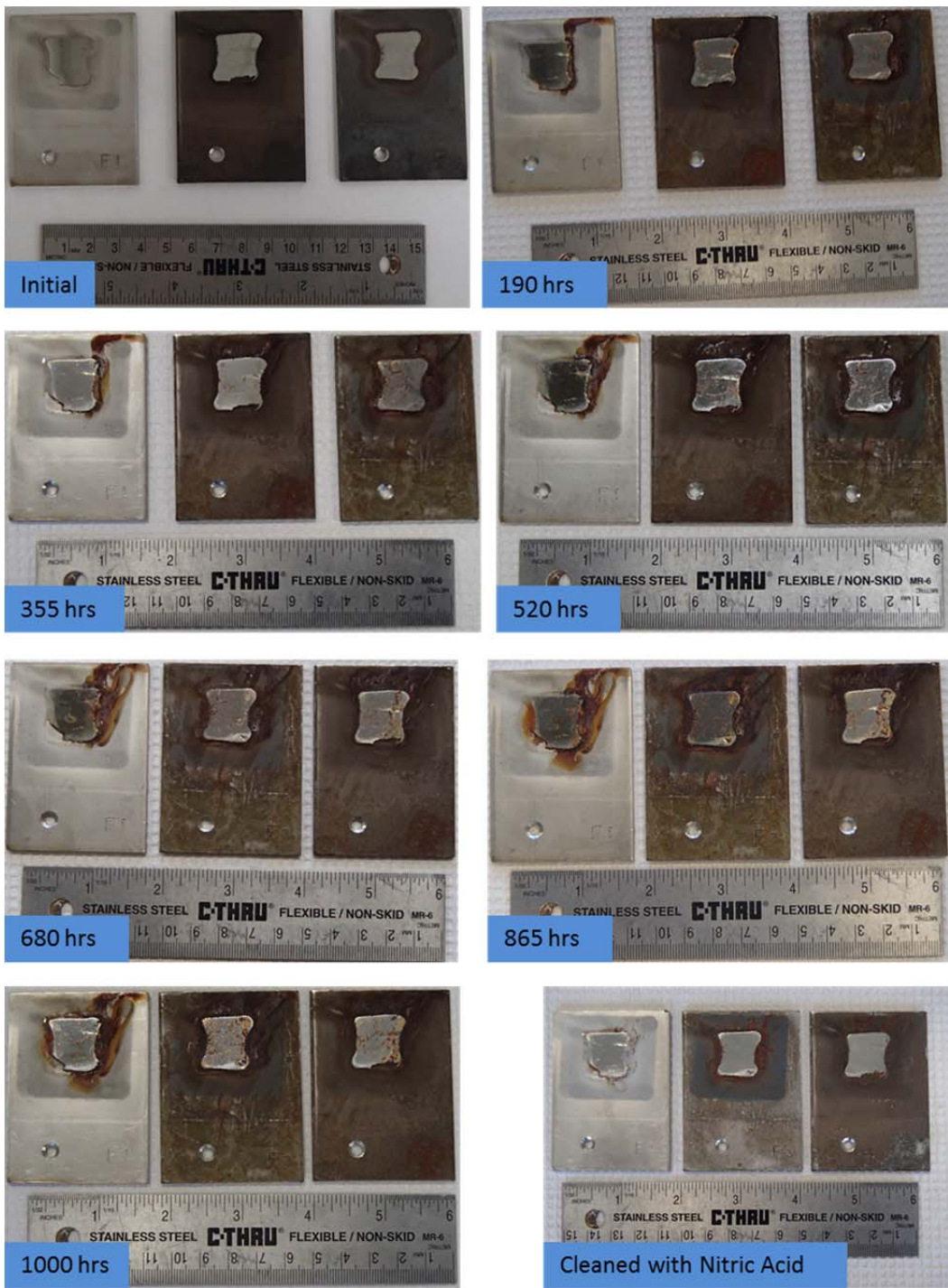


Figure 86. 5002 Group 2 Photographs. As sprayed (left), 950°C/1 hr (center), 800°C/2 hrs (right).



Figure 87. PG-AMP-10 Group 1 Photographs. As sprayed (left), 950°C/1 hr (center), 800°C/2 hrs (right).



Figure 88. PG-AMP-10 Group 2 Photographs. As sprayed (left), 950°C/1 hr (center), 800°C/2 hrs (right).



Figure 89. Bare Substrate Photographs. As sprayed (left), 950°C/1 hr (center), 800°C/2 hrs (right).

B. SURFACE PROFILES

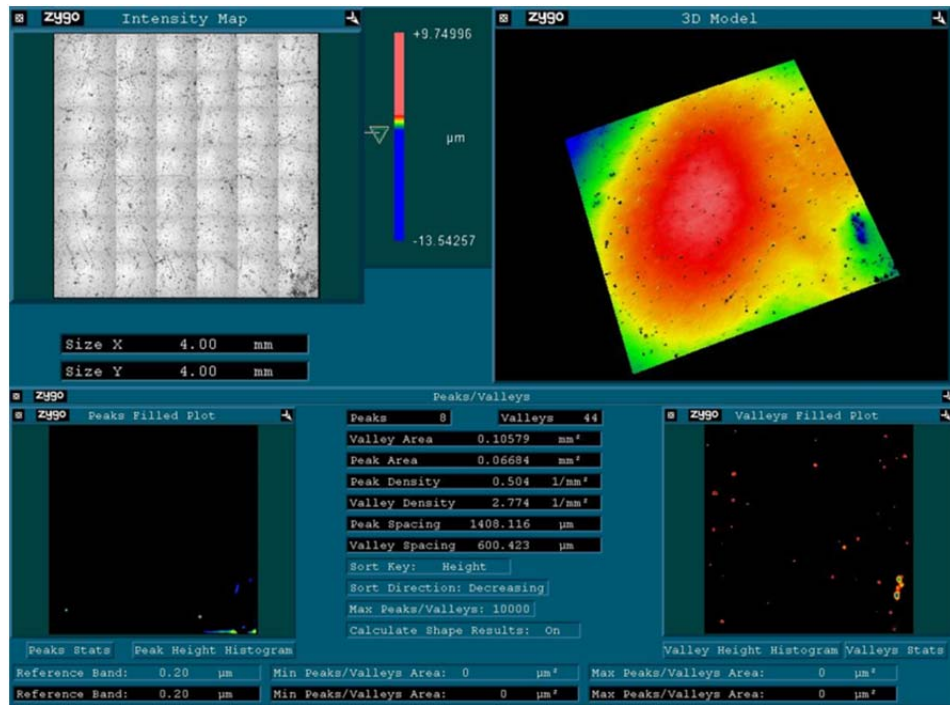


Figure 90. 5001 As-sprayed sample #1 surface profile and texture analysis.

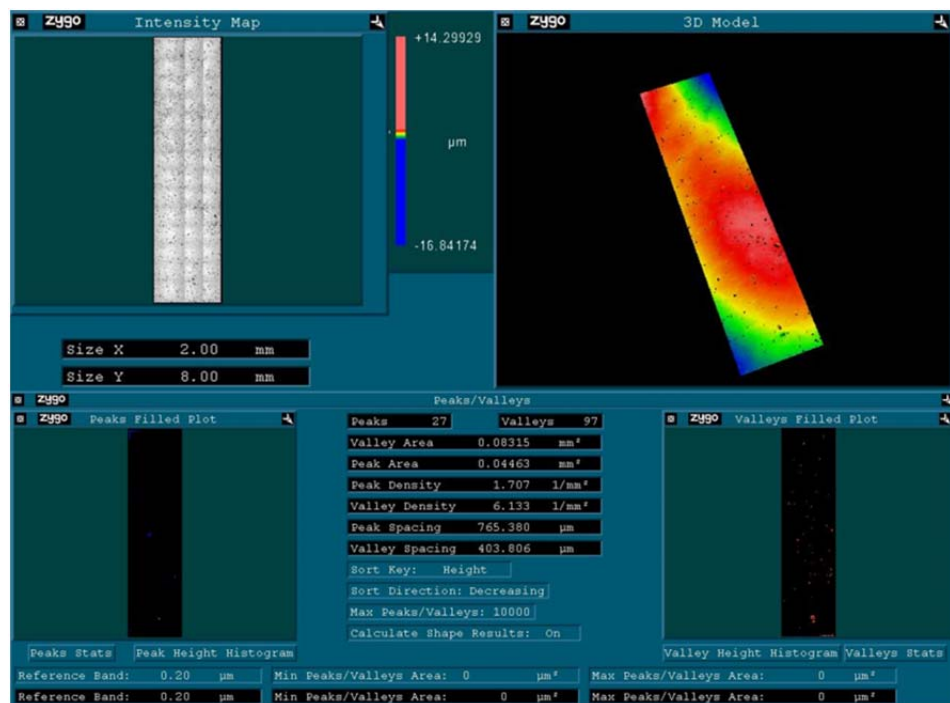


Figure 91. 5001 As-sprayed sample #2 surface profile and texture analysis.

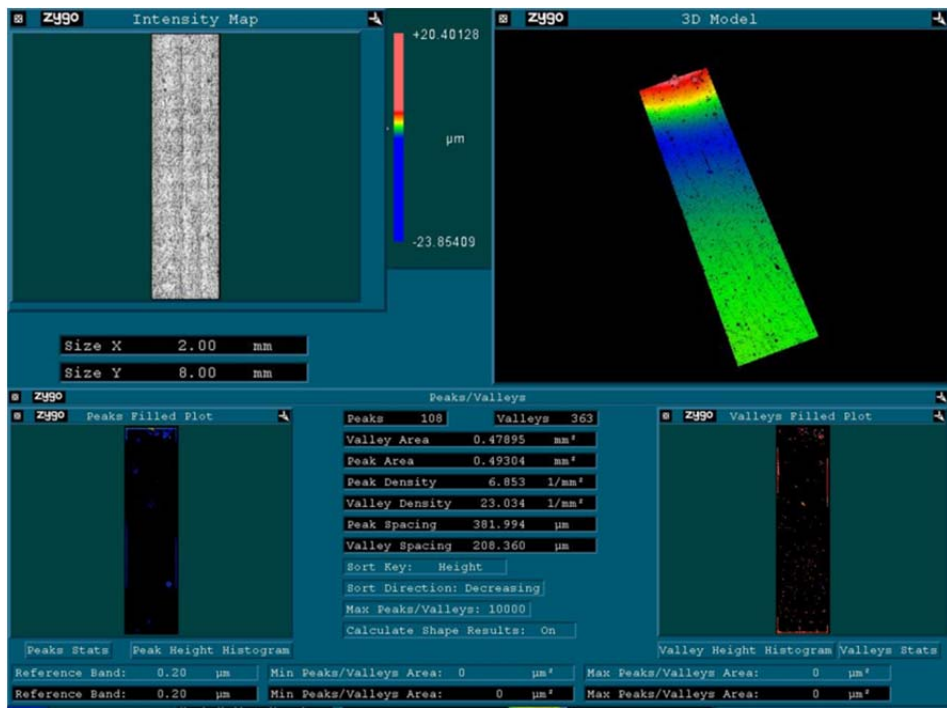


Figure 92. 5001 As-sprayed sample #3 surface profile and texture analysis.

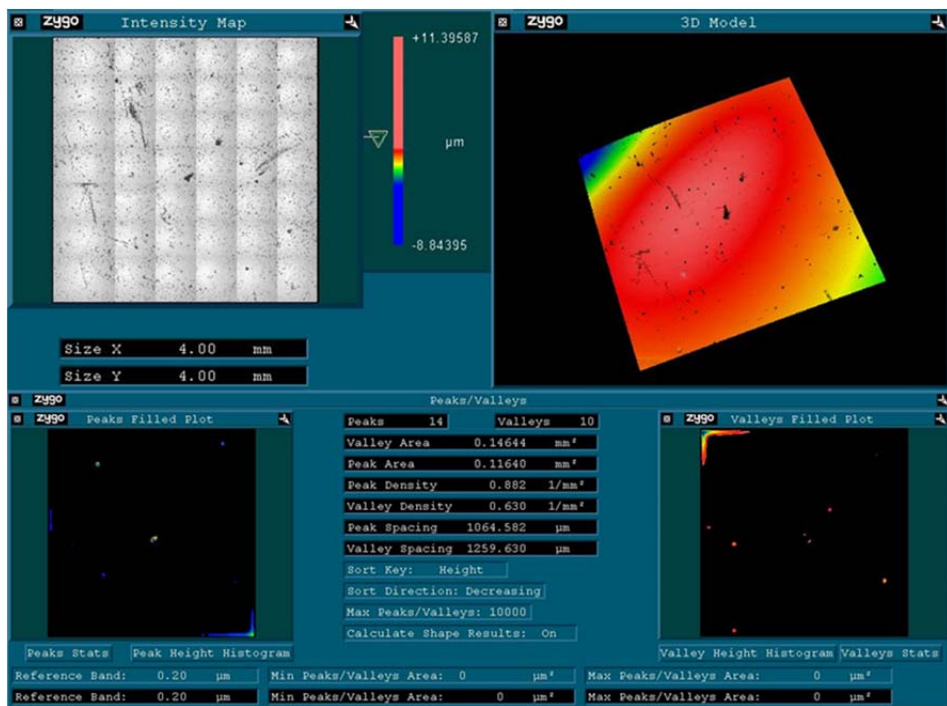


Figure 93. 5001 950°C/1 hr sample #1 surface profile and texture analysis.

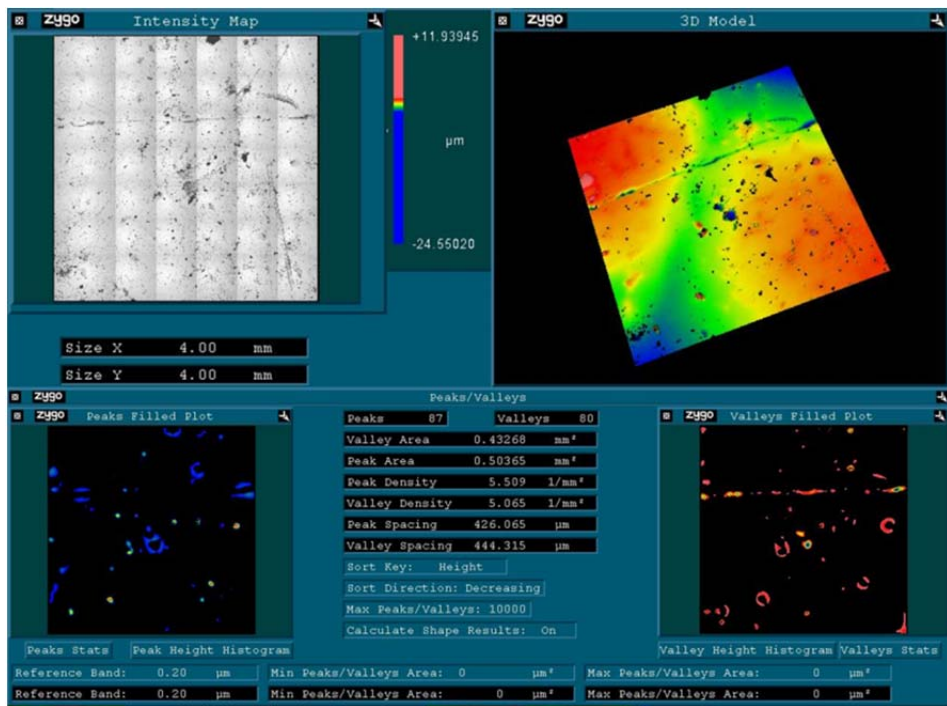


Figure 94. 5001 950°C/1 hr sample #2 surface profile and texture analysis.

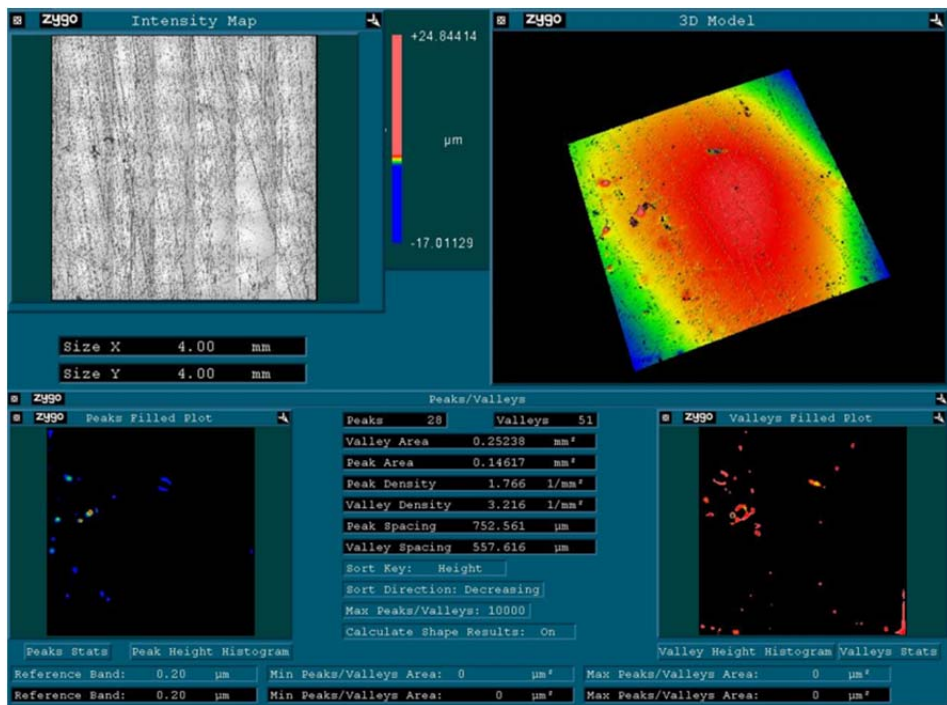


Figure 95. 5001 950°C/1 hr sample #3 surface profile and texture analysis.

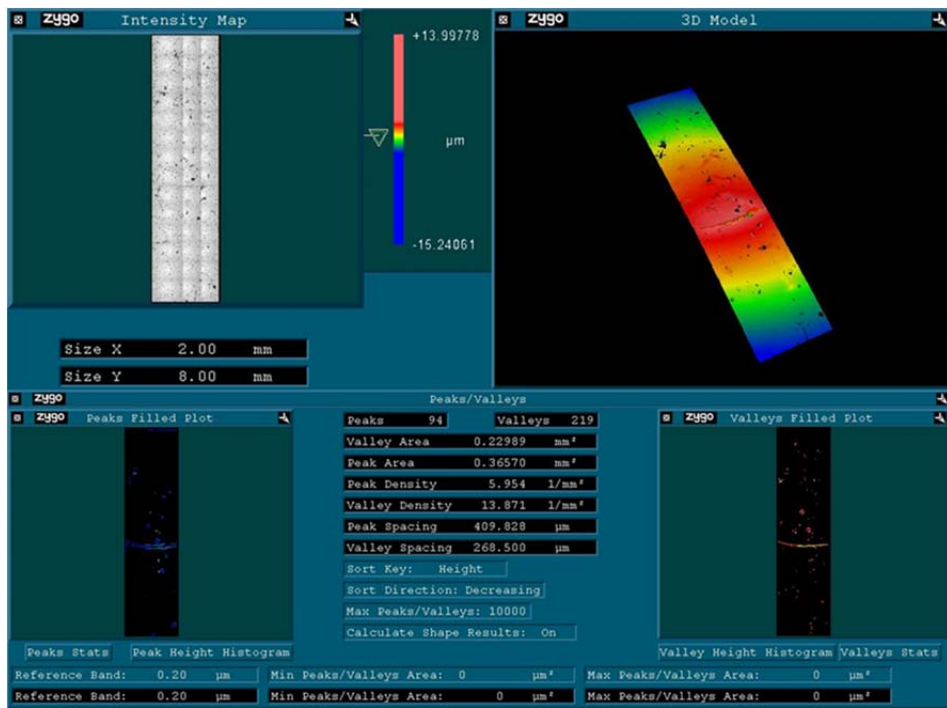


Figure 96. 5001 800°C/2 hrs sample #1 surface profile and texture analysis.

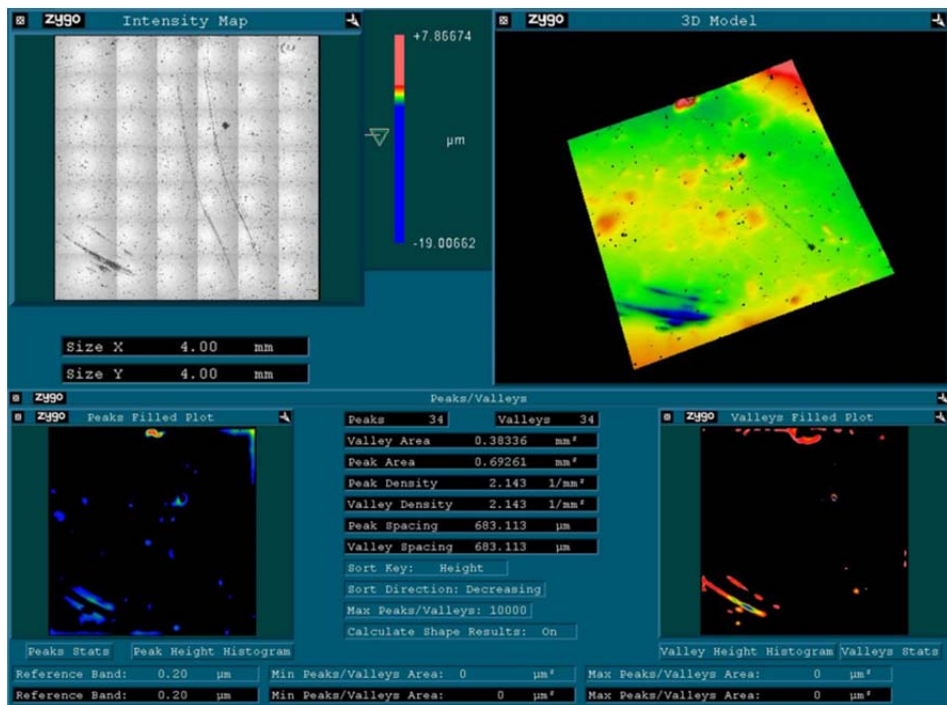


Figure 97. 5001 800°C/2 hrs sample #2 surface profile and texture analysis.

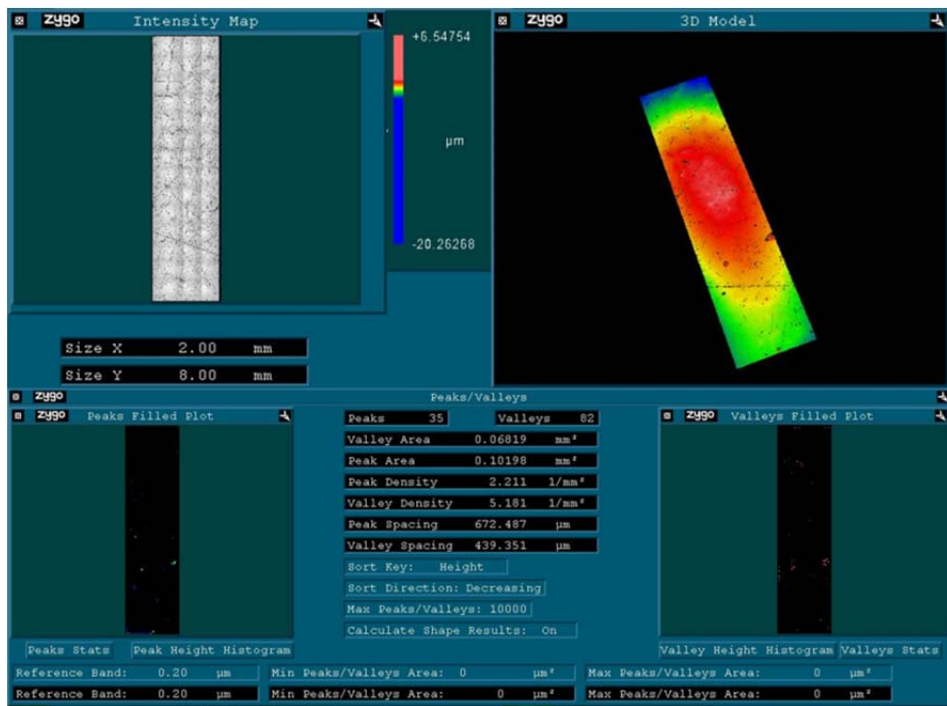


Figure 98. 5001 800°C/2 hrs sample #3 surface profile and texture analysis.

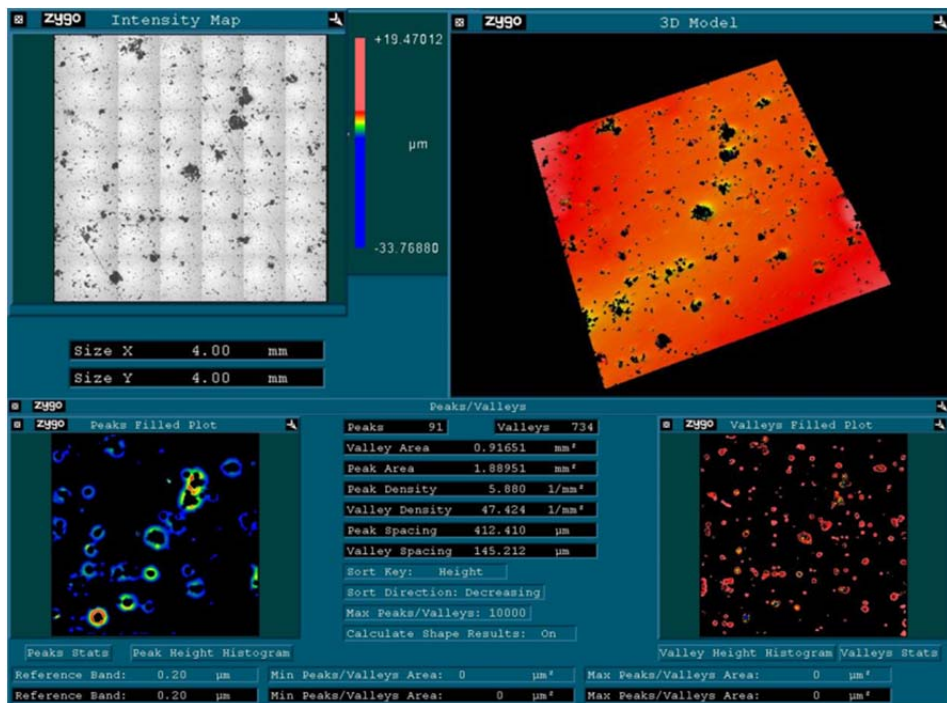


Figure 99. 5002 As-sprayed sample #1 surface profile and texture analysis.

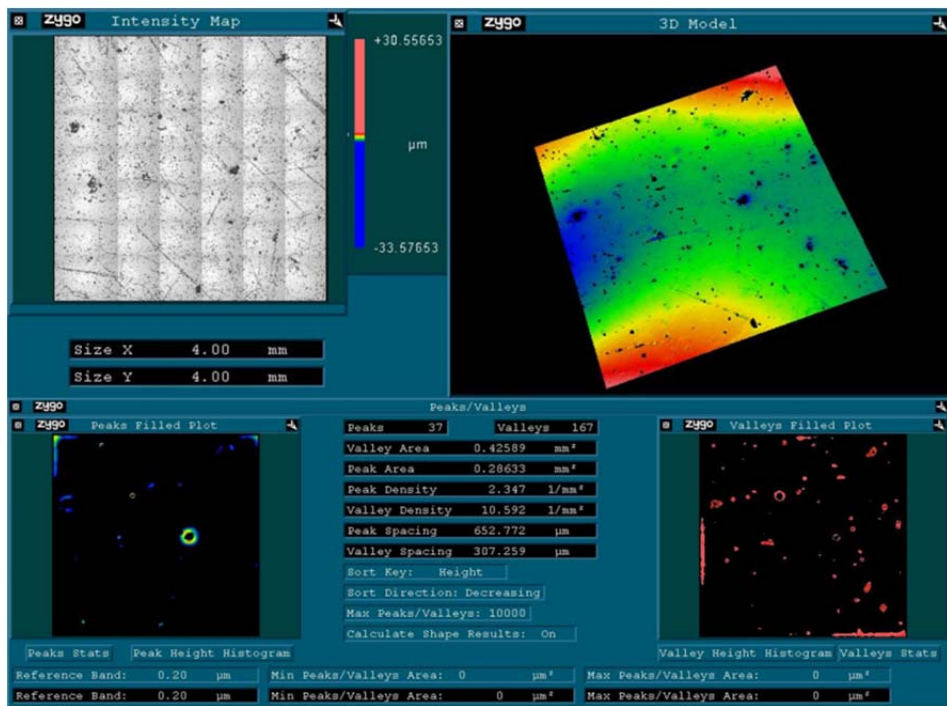


Figure 100. 5002 As-sprayed sample #2 surface profile and texture analysis.

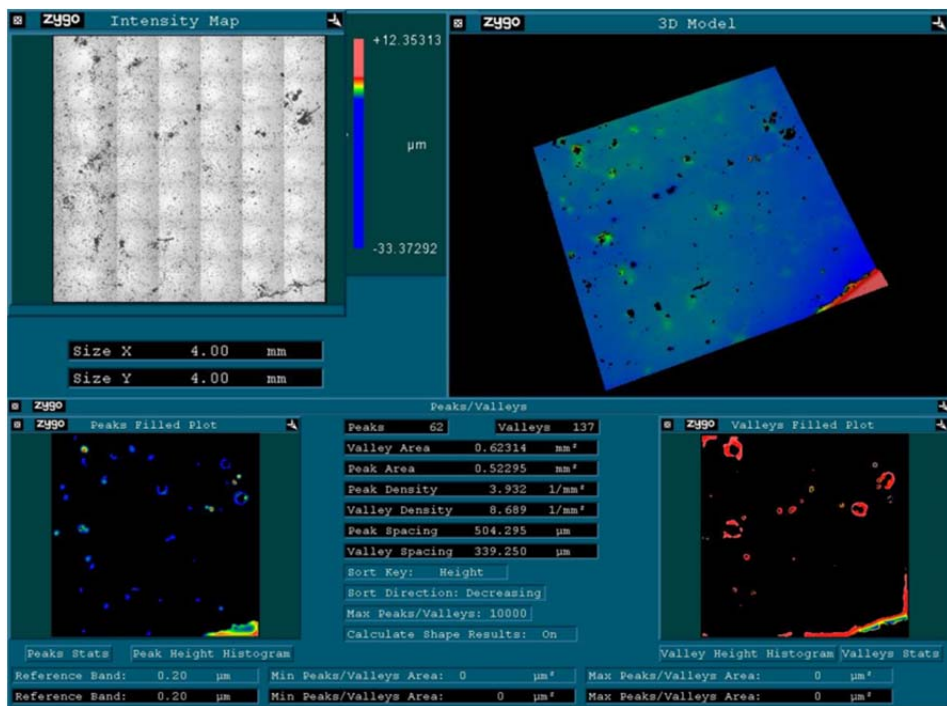


Figure 101. 5002 950°C/1 hr sample #1 surface profile and texture analysis.

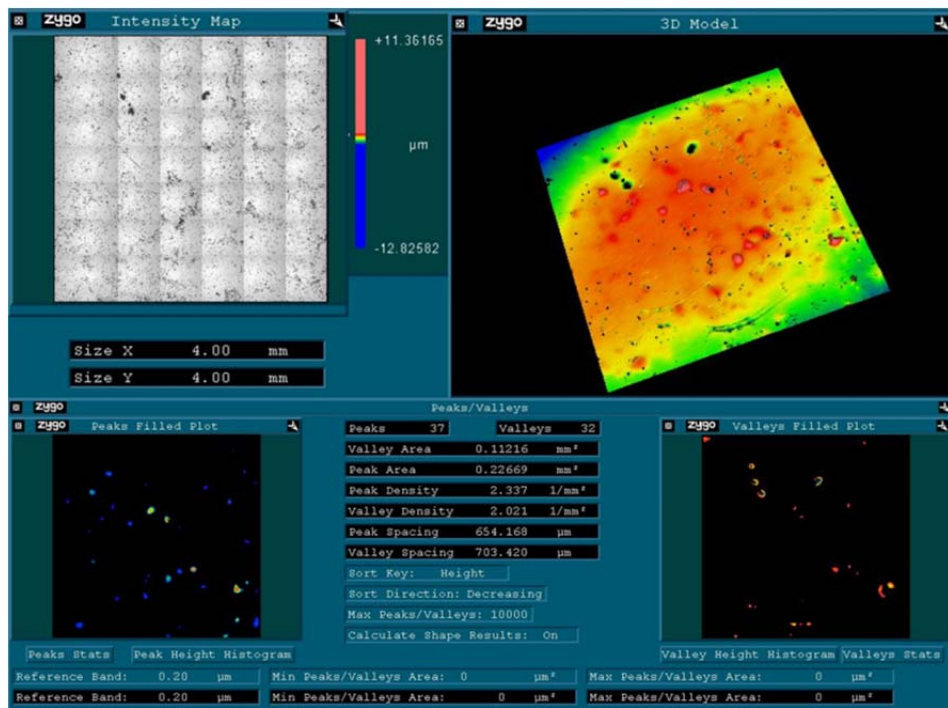


Figure 102. 5002 950°C/1 hr sample #2 surface profile and texture analysis.

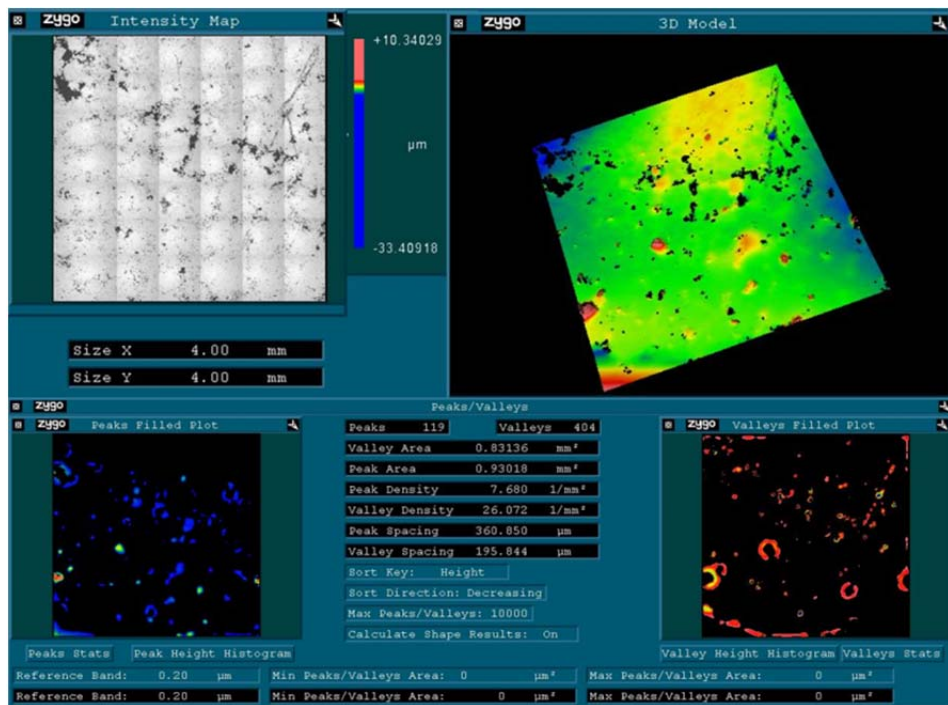


Figure 103. 5002 800°C/2 hrs sample #1 surface profile and texture analysis.

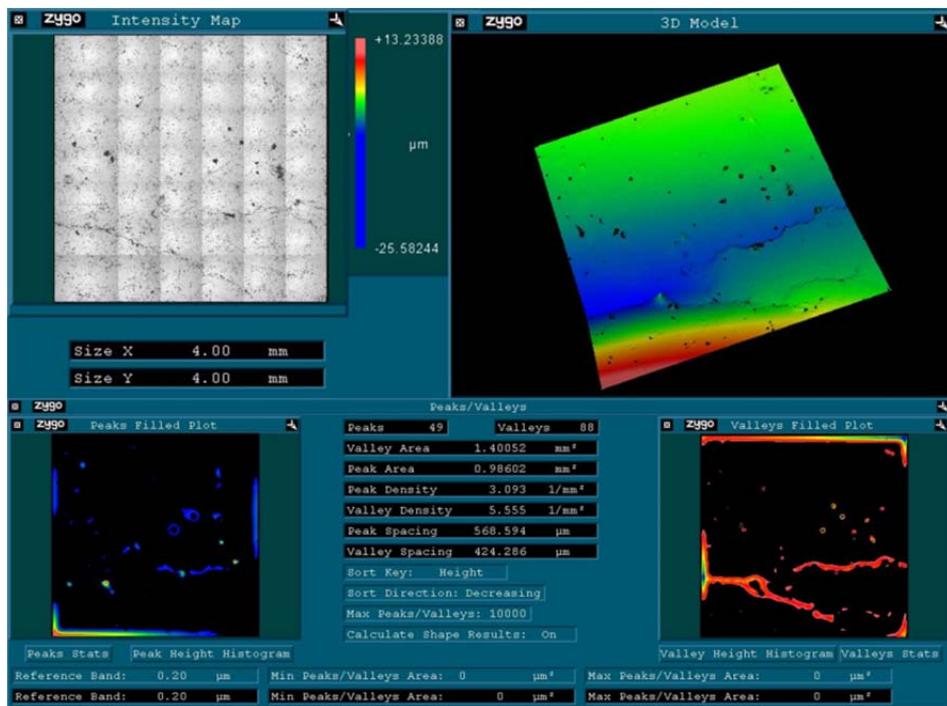


Figure 104. 5002 800°C/2 hrs sample #2 surface profile and texture analysis.

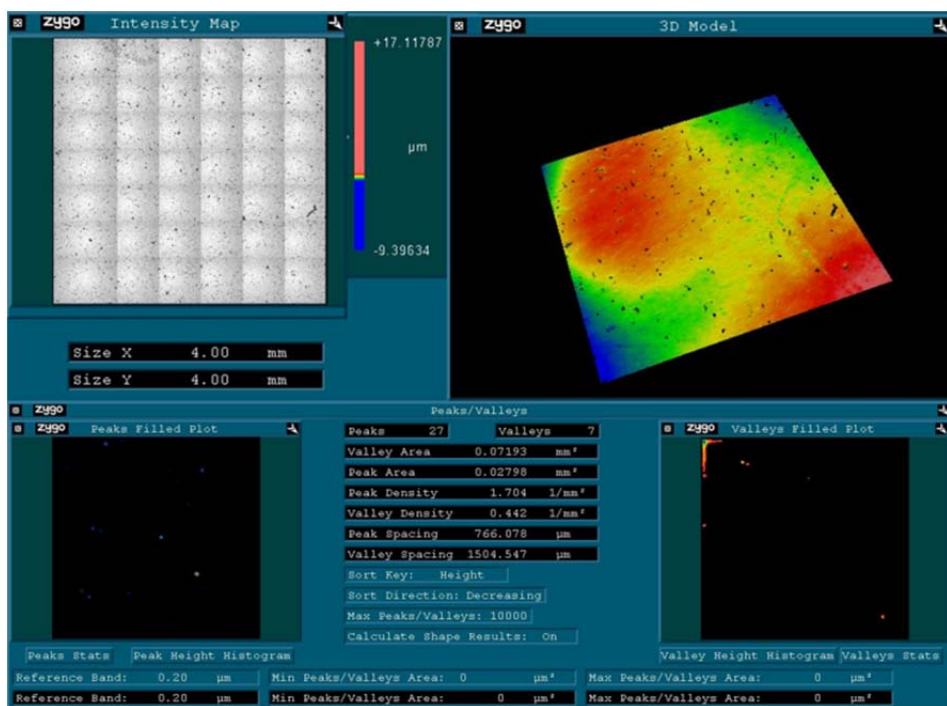


Figure 105. PG-AMP-10 As-sprayed sample #1 surface profile and texture analysis.

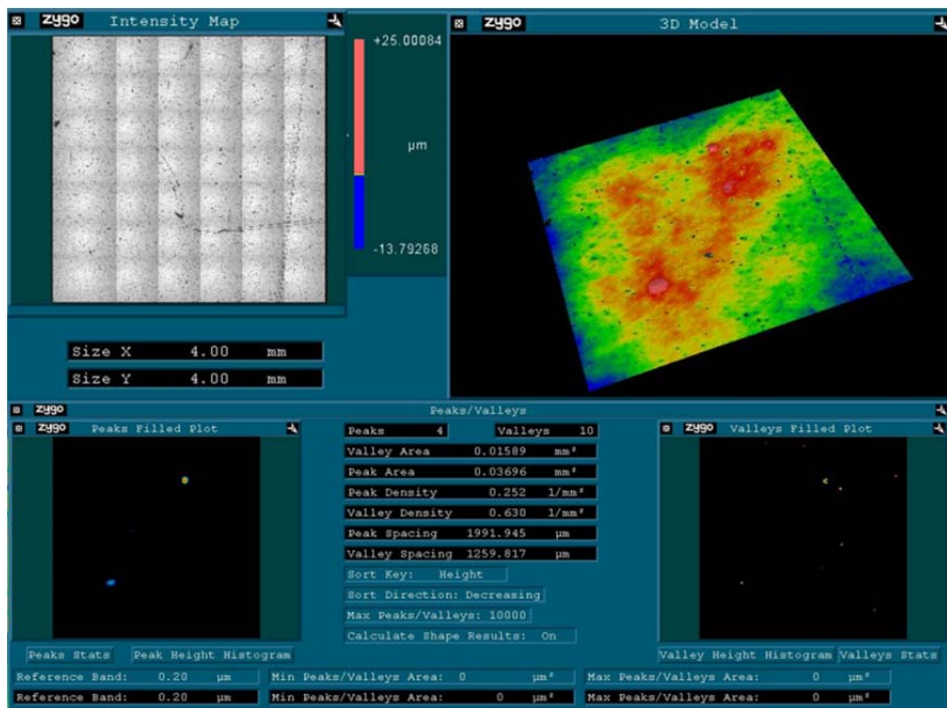


Figure 106. PG-AMP-10 As-sprayed sample #2 surface profile and texture analysis.

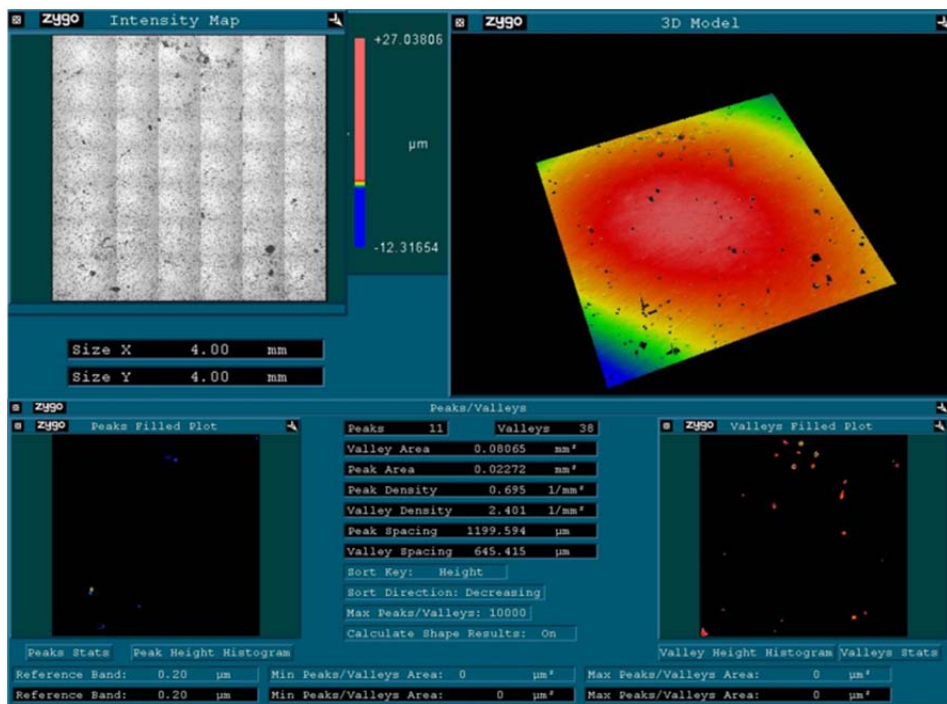


Figure 107. PG-AMP-10 950°C/1 hr sample #1 surface profile and texture analysis.

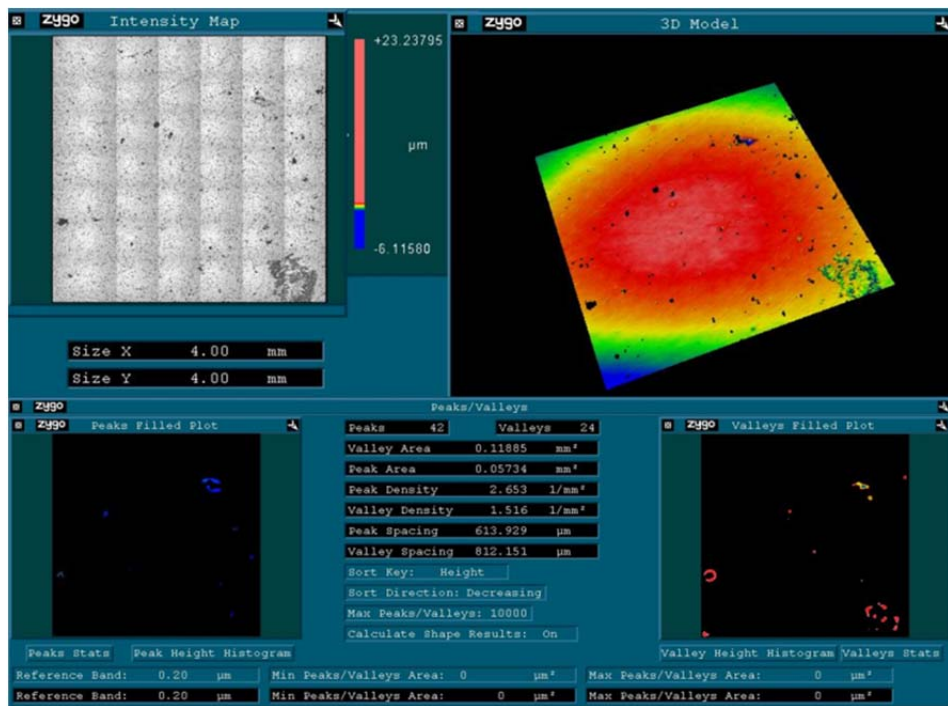


Figure 108. PG-AMP-10 950°C/1 hr sample #2 surface profile and texture analysis.

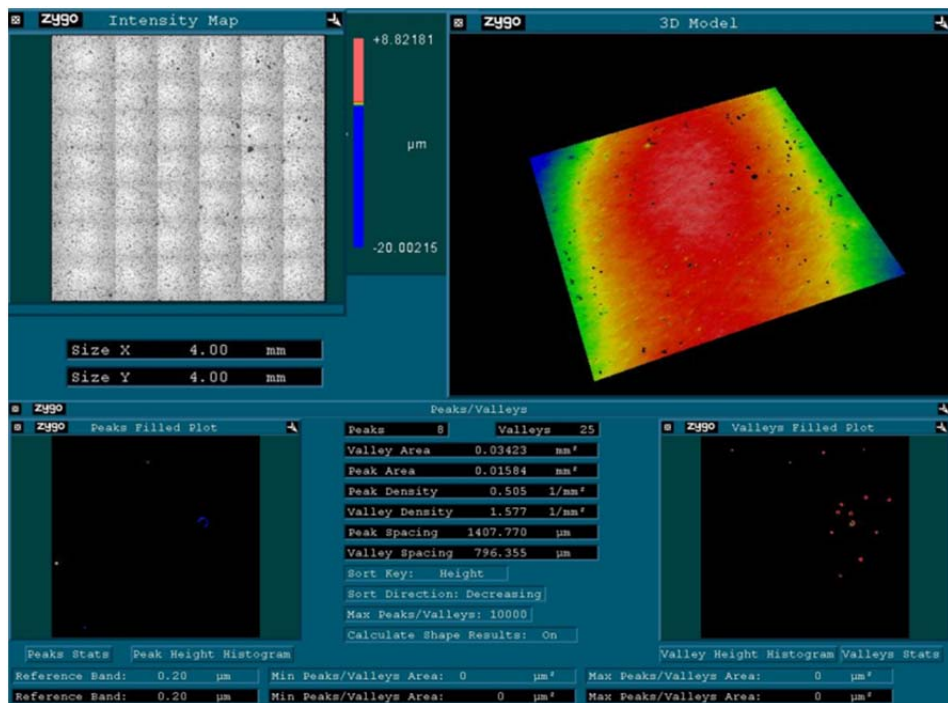


Figure 109. PG-AMP-10 800°C/2 hrs sample #1 surface profile and texture analysis.

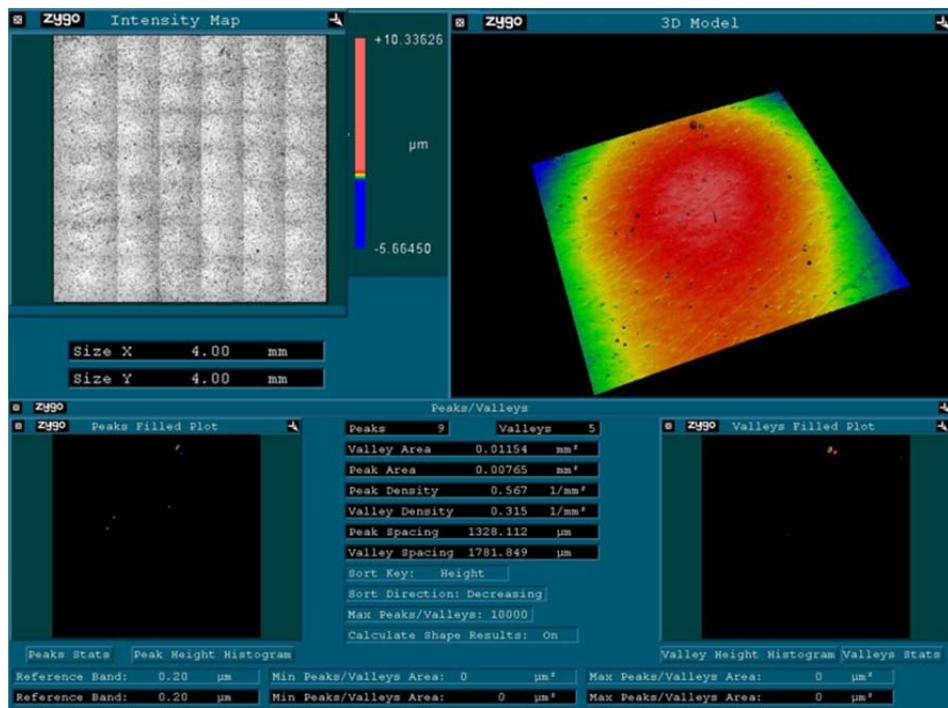


Figure 110. PG-AMP-10 800°C/2 hrs sample #2 surface profile and texture analysis.

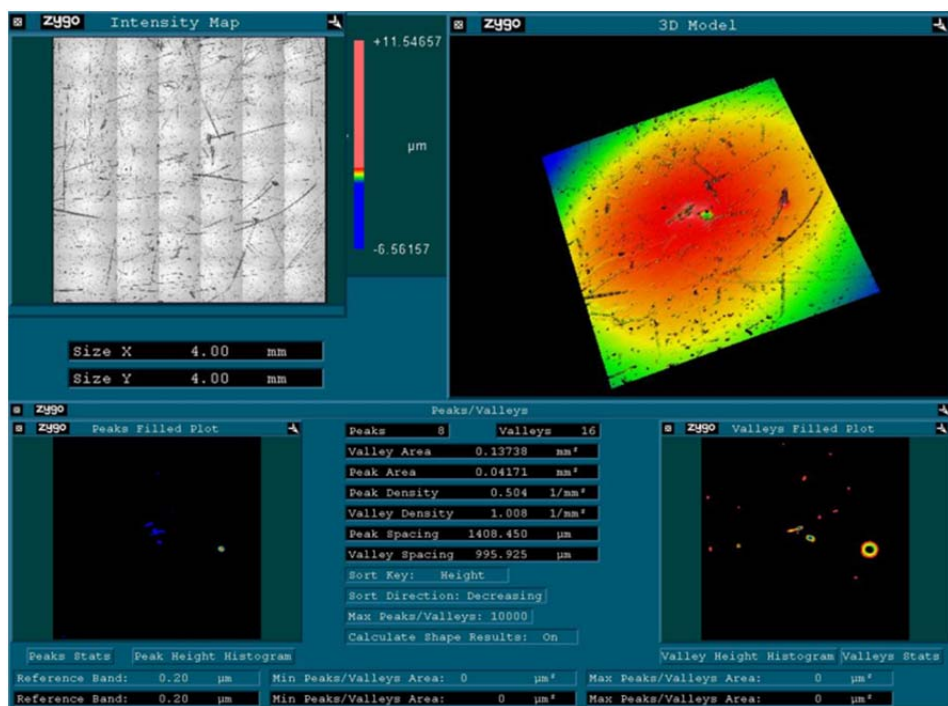


Figure 111. Bare substrate as-sprayed sample surface profile and texture analysis.

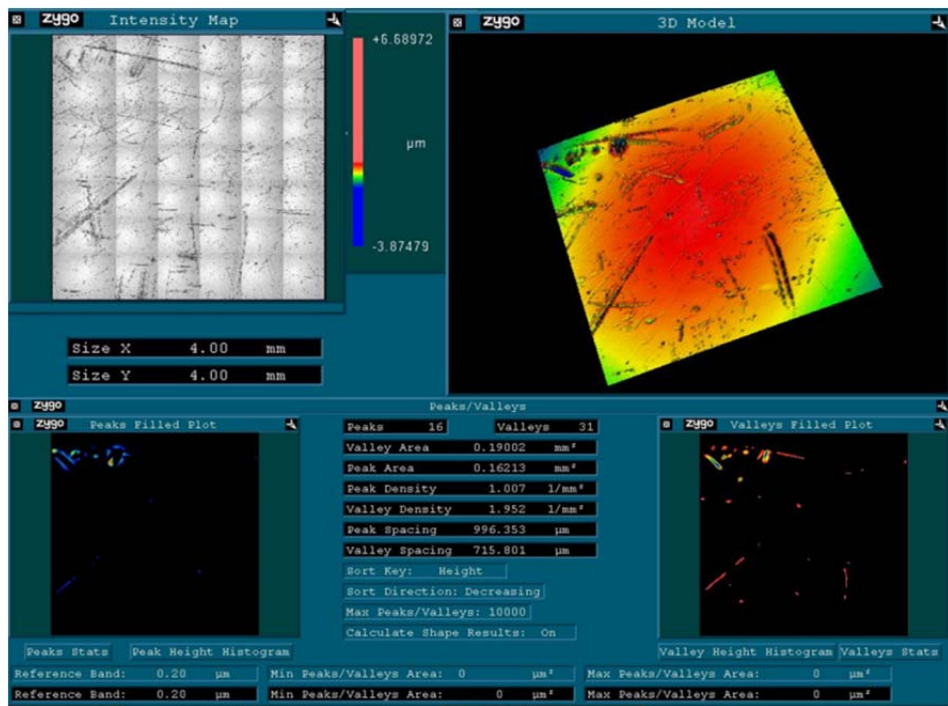


Figure 112. Bare substrate 950°C/1 hr sample surface profile and texture analysis.

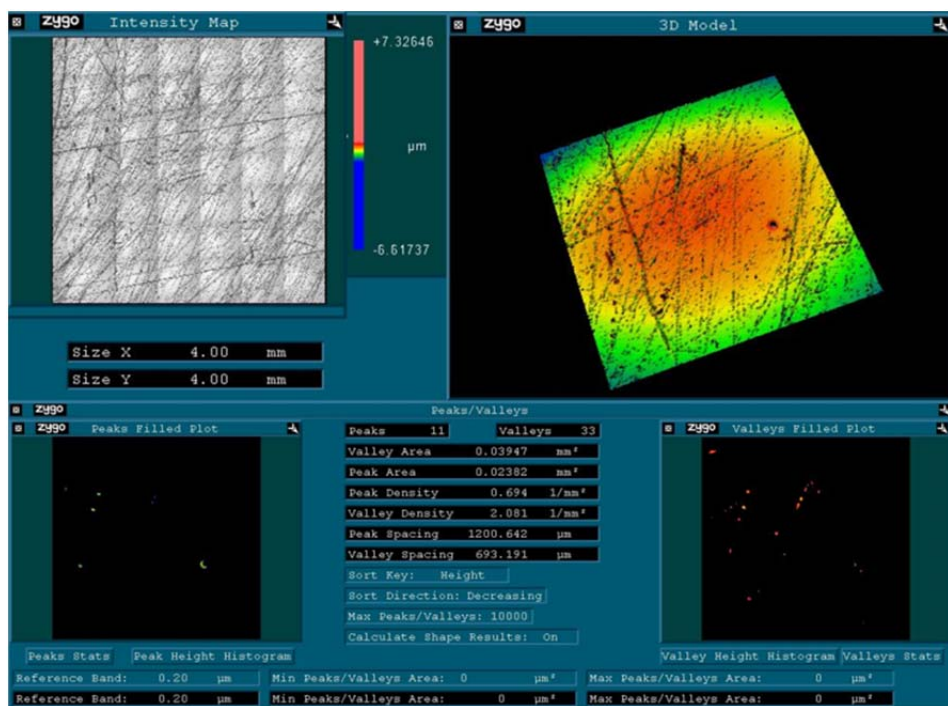


Figure 113. Bare substrate 800°C/2 hrs sample surface profile and texture analysis.

LIST OF REFERENCES

- [1] Thomas, D., 2012, “Cost of corrosion for ships, submarines and naval aviation,” presented at the Department of Defense Maintenance Symposium & Exhibition, Grand Rapids, MI, http://www.sae.org/events/DoD/presentations/2012/cost_of_corrosion_for_ships_submarines_and_naval.aviation.pdf.
- [2] Smith, M. F., 2007, “Comparing cold spray with thermal spray coating technologies,” in *The Cold Spray Materials Deposition Process: Fundamentals and Applications*, Champagne, V. K., Ed., Woodhead, Boca Raton, FL Chap. 3.
- [3] Schiel, J. F., 2014, “The cold gas-dynamic spray and characterization of microcrystalline austenitic stainless steel,” M.Eng. thesis, Department of Mechanical and Aeronautical Engineering, Naval Postgraduate School, Monterey, CA.
- [4] Spencer, K. and Zhang, M. -X., 2011, “Optimization of stainless steel cold spray coatings using mixed particle size distributions,” *Surface and Coatings Technology*, **205**(21), pp. 5135–5140.
- [5] Tao, Y., Xiong, T., Sun, C., Kong, L., Cui, X., Li, T., and Song, G., 2010, “Microstructure and corrosion performance of a cold sprayed aluminum coating on AZ91D magnesium alloy,” *Corrosion Science*, **52**(10), pp. 3191–3197.
- [6] DeForce, B. S., Eden, T. J., and Potter, J. K., 2011, “Cold Spray Al-5% Mg coatings for the corrosion protection of magnesium alloys,” *Journal of Thermal Spray Technology*, **20**(6), pp. 1352–1358.
- [7] AL-Mangour, B., Mongrain, R., Irissou, E., and Yue, S., 2013, “Improving the strength and corrosion resistance of 316L stainless steel for biomedical applications using cold spray,” *Surface and Coatings Technology*, **216**, pp. 297–307.
- [8] Leyman, P. F., and Champagne, V. K., 2009, “Cold spray process development for the reclamation of the apache helicopter mast support,” Technical Report ARL-TR-4922, Army Research Laboratory, Aberdeen Proving Ground, MD.
- [9] Villafuerte, J., and Wright, D., 2010, “Practical cold spray success: Repair of Al and Mg alloy aircraft components,” *Advanced Materials and Processes*, **168**(5), pp. 53–55.

[10] Jones, R., Matthews, N., Rodopoulos, C. A., Cairns, K., and Pitt, S., 2011, "On the use of supersonic particle deposition to restore the structural integrity of damaged aircraft structures," *International Journal of Fatigue*, **33**(9), pp 1257–1267.

[11] Matthews, N., Jones, R., and Sih, G. C., 2014, "Application of supersonic particle deposition to enhance the structural integrity of aircraft structures," *Science China-Physics, Mechanics, and Astronomy*, **57**(1), pp 12–18.

[12] Jones, R., Matthews, N., Green, R., and Peng, D., 2015, "On the potential of supersonic particle deposition to repair simulated corrosion damage," *Engineering. Fracture. Mechanics.*, **137**, pp. 26–33.

[13] Jones, R., Molent, L., Barter, S., Matthews, N., and Tamboli, D., 2014, "Supersonic particle deposition as a means for enhancing the structural integrity of aircraft structures," *International Journal of Fatigue*, **68**, pp. 260–268.

[14] Papyrin, M., 2007, "The development of the cold spray process," in *The Cold Spray Materials Deposition Process: Fundamentals and Applications*, Champagne, V. K., Ed., Woodhead, Boca Raton, FL Chap. 2.

[15] Han, W., Meng, X. M., Zhang, J. B., and Zhao, J., 2012, "Elastic modulus of 304 stainless steel coating by cold gas dynamic spraying," *Journal of Iron and Steel Research International*, **19**(3), pp 73–78.

[16] Han, W., Meng, X. M., Zhao, J., and Zhang, J. B., 2012, "Effect of heat treatment on microstructure and bending behavior of 304 stainless steel coating by cold gas dynamic spraying," *Materials Research Innovations*, **16**(2), pp. 109–114.

[17] Meng, X., Zhang, J., Han, W., Zhao, J., and Liang, Y., 2011, "Influence of annealing treatment on the microstructure and mechanical performance of cold sprayed 304 stainless steel coating," *Applied Surface Science*, **258**(2), pp. 700–704.

[18] Pattison, J., Celotto, S., Morgan, R., Bray, M., and O'Neil, W., 2007, "Cold gas dynamic manufacturing: A non-thermal approach to freeform fabrication," *International Journal of Machine Tools and Manufacture*, **47**(9), pp. 627–634.

[19] Sova, A., Grigoriev, S., Okunkova, A., and Smurov, I., 2013, "Potential of cold gas dynamic spray as additive manufacturing technology," *International Journal of Advanced Manufacturing Technologies*, **69**(3), pp 2269–2278.

[20] Spencer, K., Fabijanic, D. M., and Zhang, M. –X., 2012, "The influence of Al₂O₃ reinforcement of the properties of stainless steel cold spray coatings," *Surface and Coating Technology*, **206**(14), pp. 3275–3282.

- [21] Sundarara, G., Chavan, N. M., and Kumar, S., 2013, “The elastic modulus of cold spray coatings: Influence of inter-splat boundary cracking,” *Journal of Thermal Spray Technologies*, **22**(8), pp. 1348–1357.
- [22] Grujicic, M., 2007, “Particle/substrate interaction in the cold-spray bonding process,” in *The Cold Spray Materials Deposition Process: Fundamentals and Applications*, Champagne, V. K., Ed., Woodhead, Boca Raton, FL Chap. 9
- [23] Steenkiste, T. V., 2007, “The role of particle temperature and velocity in cold spray coating formation,” in *The Cold Spray Materials Deposition Process: Fundamentals and Applications*, Champagne, V. K., Ed., Woodhead, Boca Raton, FL Chap. 8.
- [24] Champagne, V. K., 2007, “Introduction” in *The Cold Spray Materials Deposition Process: Fundamentals and Applications*, Champagne, V. K., Ed., Woodhead, Boca Raton, FL Chap. i.
- [25] Celotto, S., Pattison, J., Ho, J. S., Johnson A. N., and O’Neil, W., 2007 “The economics of the cold spray process,” *The Cold Spray Materials Deposition Process: Fundamentals and Applications*, Champagne, V. K., Ed., Woodhead, Boca Raton, FL Chap. 5.
- [26] Jones, D., 1996, *Principles and Prevention of Corrosion*, 2nd ed., Prentice Hall, Upper Saddle River, NJ.
- [27] Washko, S. D., and Aggen, G., 1990, “Wrought Stainless Steels,” in *ASM Handbook: Volume 1: Properties and Selection: Irons, Steels and High-Performance Alloys*, 10th ed., J. R. Davis et al. eds., ASM International, Metal Park OH, pp 841-907.
- [28] Grubb, J. F., DeBold, T., and Fritz, J. D., 2005 “Corrosion of Wrought Stainless Steels,” in *ASM Handbook: Volume 13B :Corrosion: Materials*, S. D. Cramer and B. S. Covino, Jr.. eds., ASM International, Metal Park OH, pp 54-77.
- [29] Fon-Yuan Ma, 2012, “Corrosive Effects of Chlorides on Metals,” in *Pitting Corrosion*, Bensalah, N., ed., InTech, Shanghai, pp 143.
- [30] Askeland, D., 1989, *The Science and Engineering of Materials*, 2nd ed. PWS-KENT publishing company, Boston MA, Chap. 7.
- [31] Wang, Y. Q., Li, N., and Yang, B., 2015, “Effect of Ferrite on Pitting Corrosion of Fe20Cr9Ni Cast Austenite Stainless Steel for Nuclear Power Plant Pipe,” *Corrosion Engineering, Science and Technology*, **50**(4), pp 330–337.

[32] Brewer, L. N., and Fields, C. C., 2009. "Mapping and assessing plastic deformation using EBSD," in *Electron Backscatter Diffraction in Material Science*, Schwartz, A. J., Kumar, M., Adams, B. L., and Fields, D. P., Eds., Springer, New York NY, Chap. 18.

[33] Luzin, V. Spencer, K., Zhang, M., and Matthews, N., 2014, "Residual stress in coatings produced by cold spray," *Material Science Forum*, **772**, pp. 155–159.

[34] Saleh, M., Luzin, V., and Spencer, K., 2014, "Analysis of the residual stress and bonding mechanism in the cold spray technique using experimental and numerical methods," *Surface and Coatings Technology*, **252**, pp. 15–28.

[35] Meng, X. M., Zhang, J. B., Han, W., and Zhao, J., 2012, "Influence of annealing treatment on cold rolling behavior of 304SS coating by cold spraying," *Materials Research Innovations*, **16**(1), pp. 73–78.

[36] Meng, X., Zhang, J., Han, W., Zhao, J., and Liang, Y., 2011, "Influence of annealing treatment on the microstructural and mechanical performance of cold sprayed 304 stainless steel coating," *Applied Surface Science*, **258**, pp. 700–704.

[37] Sundararajan, G., Phani, P. S., Jyothirmayi, A., and Gundakaram, R. C., 2009, "The influence of heat treatment on the microstructural, mechanical and corrosion behavior of cold sprayed 316SS coatings," *Journal of Materials Science*, **44**(9), pp. 2320–2326.

[38] Kou, S., 2003, *Welding Metallurgy*, 2nd ed. John Wiley & Sons, Inc., Hoboken, NJ.

[39] Davis, J. R., ed., 2006, *Corrosion of Weldments*, ASM International, Materials Park, OH, pp 43-66.

[40] David, S. A., and Vitek, J. M., 1986, "The Sigma Phase Transformation in Austenitic Stainless Steels," *Welding Journal*, **65**, pp. S106-S111.

[41] Lancaster, J. F., 1993, *Metallurgy of Welding*, 5th ed. Chapman & Hill, London, UK, pp 278–279.

[42] Weiss, B., and Stickler, R., 1972, "Phase Instabilities During High Temperature Exposure of 316 Austenitic Stainless Steel," *Metallurgical Transactions*, **3**, pp 851–866.

[43] Douthett, J., 1991, "Heat Treating of Stainless Steels," in *ASM Handbook: Volume 4: Heat Treating*, 10th ed., ASM International, Metal Park, OH, pp. 769–792.

[44] Roberge P. R., 2012, *Handbook of Corrosion Engineering*, 2nd ed. McGraw-Hill, New York, NY, pp. 611.

[45] Solomon H. D., and Lord, D. C., 1980, "Influence of Strain During Cooling on the Sensitization of Type 304 Stainless Steel," *Corrosion*, **36**, pp 395–399.

[46] Solomon, H. D., 1978, "Continuous Cooling Sensitization of Type-304 Stainless Steel," *Corrosion*, **34**(6), pp. 183-193.

[47] Atanda, P., Fatudimu, A., and Oluwole, O., 2010, "Sensitization Study of Normalized 316L Stainless Steel," *Journal of Minerals & Material Characterization & Engineering*, **9**(1), pp 13–23.

[48] Wright, R. N., Bae, J. C., Kelly, T. F., Flinn, J. E., and Worth, G. E., 1988, "The Microstructure and Phase Relationships in Rapidly Solidified Type 304 Stainless Steel Powders," *Metallurgical Transactions A*, **19**(10), pp. 2399-2405.

[49] Culley, B. D., 1978, *Elements of X-Ray Diffraction*, 2nd ed., Addison-Westley Publishing Company, Reading, PA, Chap. 14.

[50] Roberge, P. R., 2012, *Handbook of Corrosion Engineering*, 2nd ed. McGraw Hill, New York, NY, pp 530.

[51] *Operating Practice for Operating Salt Spray (Fog) Apparatus*, ASTM Standard B117–11, 2011

[52] *Standard Practice for Preparing, Cleaning and Evaluating Corrosion Test Specimens*, ASTM Standard G1–03, 2011.

[53] de Groot, P. J., 2015, "Interference Microscopy for Surface Structure Analysis," in *Handbook of Optical Metrology: Principles and Application*, 2nd ed. Yoshizama, T., ed., CRC Press, Boca Raton, FL, Chap. 34.

[54] Johnson, R. T., 2015, "The Effect of Applied Tensile Stress on Localized Corrosion in Sensitized AA5083," M. S. thesis, Department of Mechanical and Aeronautical Engineering, Naval Postgraduate School, Monterey, CA.

[55] Fontana, M. G., 1986, *Corrosion Engineering*, 3rd ed., McGraw-Hill Book Company, New York, NY, Chap. 2.

[56] Fattah-Alhosseini, A., Saatchi, A., Golozar, M. A., and Raeissi, K., 2010, "The passivity of AISI 316L stainless steel in 0.05 M H₂SO₄," *Journal of Applied Electrochemistry*, **40**, pp. 457–461.

[57] *Standard Reference Test Method for Making Potentiodynamic Anodic Polarization Measurements*, ASTM Standard G5–13, 2013.

[58] Otsubo, F., Kishitake, K., Akiyama, T., and Terasaki, T., 2003, "Characterization of Blasted Austenitic Stainless Steel and its Corrosion Resistance," *Journal of Thermal Spray Technology*, **12**, pp 555–55.

- [59] *Standard Guide for Examination and Evaluation of Pitting Corrosion*, ASTM Standard G46-94, 2013.
- [60] Solomon, H. D., 1984, “Influence of Composition on the Continuous Cooling Sensitization of Type 304 Stainless Steel,” *Corrosion*, **40**(2), pp 51–60.

INITIAL DISTRIBUTION LIST

1. Defense Technical Information Center
Ft. Belvoir, Virginia
2. Dudley Knox Library
Naval Postgraduate School
Monterey, California